

Numerical Modeling of the Nonlinear Propagation of Ultrashort Laser Pulses in Transparent Materials

Thesis by
Paris Panagiotopoulos

In Partial Fulfillment of the Requirements
for the Degree of
Doctor of Philosophy



Department of Physics
University of Crete
Heraklion

December 2012

©2012
Paris Panagiotopoulos
All Rights Reserved

“Somewhere, something incredible is waiting to be known.”

- Carl Sagan

Acknowledgments

First and foremost I thank my supervisor Stelios Tzortzakis for his guidance and valuable advice he provided in the 5 years of my PhD studies. Science is about facts, proofs and logic. These things must always be in the mind of a researcher, and Stelios did remind me of them every time I got carried away. In addition Stelios always cared for me and all the members of our team (UNIS), doing his best about providing funding, material supplies and most importantly a healthy working environment. It was a honor for me.

I thank Arnaud Couairon for providing me the basic numerical tool which was used as the starting point of all my work. In the process of my PhD I extended this tool writing large amounts of code, to investigate new phenomena and ideas. Arnaud's help was invaluable for me throughout this whole process. He was always ready to answer my questions concerning either theoretical or technical issues. Even though he was physically absent most of the time, our long and often phone calls were always enlightening and helpful. Thank you for all the help and patience.

I also want to thank the person who sparked my interest in optics in the first place, Dimitris Papazoglou. Dimitris was always ready to invest endless hours in helping me in both technical and theoretical problems that came up. I will always remember the numerous eureka-moments I had in front of the whiteboard in his office with joy. After all, science has to be enjoyable, and time is never free; I appreciate all the help.

I want to thank my fellow PhD students and coworkers in the UNIS team Daryoush Abdollahpour, Jean-Michele Manceau, Mathieu Bellec, Mixalis Loulakis, Tasos Koulouklidis, Mixalis Galanakis, Maria Massauti, and Cristina Daskalaki for all the support and the laughs we had throughout these years. From these people I want to especially thank Daryoush and Matthieu for their great collaboration, making the direct comparison of simulations and experiments possible. I also want to especially thank Mixalis Galanakis for saving my hard disk with all my work up to the 3rd year, when a power failure fried it.

I want to thank the collaborators of the UNIS team in Italy, Antonio Lotti, Danielle Faccio, and the rest of the people that attended the STELLA school in 2007. The interaction with so many people from different countries, all focusing on the same goal was a great inspiration for me.

Also many thanks to Ritsa Karali and L. Papadopoulos for their great help with administrative issues, and the organization of the most awesome parties at FORTH.

I thank Manos Giatromanolakis for his constant help with computer network related and printing issues that arose during the years. He also provided a problem free cluster at which a big part of the simulation were done.

I want to thank all my friends in Heraklion for all the fun time we spent together. In particular Mixalis Semertzakis who always had a new joke to tell. Especially, I want to thank Eleni Poulere for the quality time we spend together, the trips we made, and for making me want to be a better person.

Last but not least I want to thank my brother, mother and father which supported me throughout my whole life.

Abstract

This thesis is focused on the study and control of femtosecond light filaments in transparent materials. Since filamentation is a complex phenomenon in which multiple physical effects take place, the understanding and modeling of the whole process is of great importance. The thesis starts with a brief introduction of the linear and nonlinear effects that take place in the filamentation process. It is followed by the description of the numerical model used in the simulations and the main limitations and approximations are stated. Throughout this work numerical simulation will be used in conjuncture with laboratory experiments to study and ultimately control the nonlinear propagation of filaments. The control of the attributes of light filaments, or else filamentation tailoring, is investigated in mainly two different ways; by the use of optical periodic lattices and second by use of various non-diffracting waves.

It is shown that photonic periodic lattices can be used to spatially tailor a light filament in respect to its peak intensity and beam waist. In addition it is shown that the stabilizing effect of the lattice can result in the generation of intense dynamic light bullets. The tailoring properties of multiple lattice geometries are explored in materials as water, fused silica glass and BK7 glass both through simulations and experiments.

The use of nondiffracting beams as driving pulses for filaments reveals never seen before light structures in the nonlinear regime. The use of Bessel beams is demonstrated to increase the length and homogeneity of filaments in air. In addition Bessel filaments are shown to generate linear X-waves through means of cross-phase modulation in fused silica glass. The propagation dynamics of 2D high power nonlinear Airy beams is investigated in great detail in both air and water. In one spatial dimension the existence of a stationary nonlinear Airy solution in the presence of high nonlinear losses is presented. Finally the use of a new type of abruptly autofocusing wavepacket is studied in the nonlinear regime, revealing that it can overcome intensity clamping issues which are observed in all Gaussian filaments. In addition it is shown that the nonlinear focus shift of autofocusing waves cannot be described by Marburgers formula as in the case of Gaussians, and a new semi-empirical formula is given. Finally the creation of a nonlinear quazi-light bullet structure is reported for abruptly autofocusing waves carrying multiple critical powers.

Table of Contents

Acknowledgments	5
Abstract	7
Table of Contents	8
1. Introduction and motivation.....	13
1.1 The Gaussian spatio-temporal wavepacket	13
1.2 Linear propagation regime	19
1.2.1 Beam diffraction.....	19
1.2.2 Dispersion of femtosecond pulses.....	23
1.3 Nonlinear femtosecond laser pulse propagation	27
1.3.1 Optical Kerr effect and self-focusing	28
1.3.2 Optical field ionization.....	35
1.3.3 Plasma defocusing and absorption	37
1.3.4 Self-phase modulation and white light generation	39
1.3.5 Self-steepening	41
1.3.6 Filamentation: an equilibrium of linear and nonlinear effects	43
1.4 Main attributes of femtosecond filaments	44
1.4.1 Robustness.....	44
1.4.2 Long range propagation	45
1.4.3 Intensity clamping	46
1.4.4 Modulation instability and multiple filamentation.....	48
1.4.5 Spectral broadening - White light generation.....	49
1.4.6 Conical emission	50
1.4.7 Pulse self-compression	51
1.4.8 THz radiation generation.....	53
1.5 Applications	54

1.5.1	White light LIDAR.....	54
1.5.2	Remote LIBS.....	55
1.5.3	Electric discharge triggering and guiding	56
1.5.4	Nano-fabrication.....	57
1.6	Uncontrollable attributes of filaments.....	58
1.6.1	Beam waist - Peak intensity and plasma channel uniformity.....	59
1.6.2	Pulse shape and spectrum.....	60
1.6.3	Nonlinear losses	61
1.7	Thesis outline	62
2.	Nonlinear wave propagation equation and its solution.....	65
2.1	The nonlinear propagation equation.....	65
2.1.1	Analytic derivation from the Maxwell equations.....	67
2.2	Numerical implementations of the propagation equation	87
2.2.1	Numerical implementation of diffraction.....	87
2.2.2	Addition of nonlinear effects.....	103
2.2.3	Addition of time and temporal effects.....	108
2.2.4	"Frozen time" scheme (XYZ).....	113
2.2.5	Uniform and non-uniform grids	114
2.2.6	Boundary conditions	117
2.2.7	Checking for numerical errors.....	118
2.3	Typical simulation results	119
2.3.1	Linear diffraction.....	119
2.3.2	Addition of time and dispersion	120
2.3.3	Addition of the optical Kerr effect	122
2.3.4	Addition of saturating mechanisms.....	125
2.3.5	Addition of self-steepening	128

3.	Filamentation tailoring with photonic lattices	130
3.1	Classical approaches	130
3.2	Radial symmetric lattice in air	130
3.3	Soliton to filament transition and superposition	140
3.4	Temporal solitons and nonlinear light bullets	143
3.4.1	Previous works in the literature.....	144
3.4.2	Intense dynamic bullets in a periodic lattice	146
3.4.3	The effect of random noise.....	152
3.5	Increasing the power of tailored filaments using cylindrical lattices.....	154
3.5.1	Addition of a diverging lens to the cylindrical lattice.....	157
3.5.2	Addition of an anti-waveguide to the cylindrical lattice.....	159
3.5.3	Addition of a miniature lattice to the cylindrical lattice.....	161
3.6	Square lattices in the single filamentation regime	163
3.6.1	Filamentation tailoring in air with square lattices.....	163
3.6.2	Filamentation in fused silica	165
3.6.3	Filamentation in water.....	172
3.6.4	Dependence on setup parameters	176
3.7	Permanent elliptical waveguide lattice in BK7 glass	180
3.8	Filamentation tailoring in Bessel-like plasma lattices in water.....	190
3.9	Multi filamentation control with 2D lattices in fused silica.....	196
3.9.1	Bravais lattices	196
3.9.2	Discrete cylindrical lattices	200

4. Filamentation tailoring with non-diffracting beams	206
4.1 Finite energy Bessel beams	206
4.1.1 Generation with an axicon.....	208
4.1.2 Stationary UV Bessel filaments in air	208
4.1.3 X-waves.....	216
4.2 Finite energy Airy beams	225
4.2.1 Airy beams in the literature.....	227
4.2.2 Generation techniques	228
4.2.3 The Linear Airy beam	231
4.2.4 Nonlinear Airy beams	235
4.2.5 Autofocusing waves	268
5. Appendix.....	284
6. List of Electronic Files.....	290
7. Index of Symbols	291
8. Index of Abbreviations	295
9. Physical Parameters and coefficients.....	298
10. List of Publications	301
11. References.....	302

1. Introduction and motivation

1.1 The Gaussian spatio-temporal wavepacket

Most commercial laser sources have a spatial intensity distribution (TEM₀₀ mode that develops in within the resonator) that can be approximated by a Gaussian function [1]. As a Gaussian beam is interacting with lenses and mirrors, it is transformed into another Gaussian with different parameters, which makes them a convenient way to describe laser beams in optics. The Gaussian function $f(x) = e^{-x^2}$, is a solution to the Helmholtz Eq. (1.1-1):

$$\nabla^2 E + k^2 E = 0 \quad (1.1-1)$$

which is the simplest way to describe the propagation of an electromagnetic wave with electric field E in space. The spatial electric field amplitude, or envelope $\mathcal{E}(r)$, of a laser beam with a Gaussian spatial distribution is given by Eq. (1.1-2):

$$\mathcal{E}(r) = \sqrt{I_0} \exp\left[-\frac{r^2}{w_0^2}\right] \quad (1.1-2)$$

where I_0 ($\equiv |\mathcal{E}_0|^2$) is the peak intensity of the beam corresponding to the square of the peak amplitude of the electric field envelope \mathcal{E}_0 , w_0 is the beam width at $1/e^2$ radius (at roughly 13.5% of I_0), and r is the radial coordinate. In optics there are many other ways to characterize the width of Gaussian beams. The other norm that is often used in optics is the full width at half maximum (FWHM), which measures the beam diameter at the point where the amplitude has dropped to half of the maximum value I_0 . In this thesis w_0 is always referring to $1/e^2$ radius if not stated otherwise, which can be easily converted to FWHM using Eq. (1.1-3):

$$w_0 = 0.85 \times FWHM \quad (1.1-3)$$

We can see a plot of a Gaussian distribution in Fig 1-1, where both $1/e^2$ radius and FWHM are shown with the red and blue lines respectively.

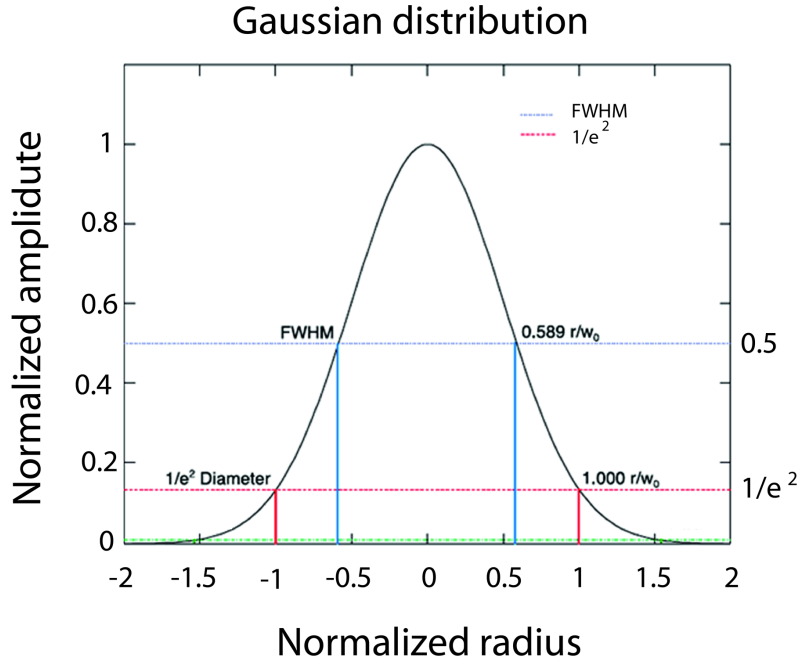


Fig 1-1 Normalized Gaussian distribution indicating the two typical width used in optics. FWHM in blue, and $1/e^2$ diameter in red.

In case the wavefront has an initial curvature induced by a refracting element like a lens, Eq. (1.1-2) is modified by the addition of the phase term. In the case of an ideal achromatic spherical lens the phase term can be written as $-i \frac{kr^2}{2f}$, and electric field envelope is given by Eq. (1.1-4)

$$\mathcal{E}(r) = \sqrt{I_0} \exp \left[-\frac{r^2}{w_0^2} - i \frac{kr^2}{2f} \right] \quad (1.1-4)$$

$k \equiv \frac{2\pi}{\lambda}$ corresponds to the wavenumber of the beam with wavelength λ , and initial curvature f . The intensity profile is given by the square of the electric field envelope $\mathcal{E}(r)$, and is shown in Fig 1-2 for a typical two dimensional Gaussian beam with $I_0 = 1 W / cm^2$ and $w_0 = 500 \mu m$.

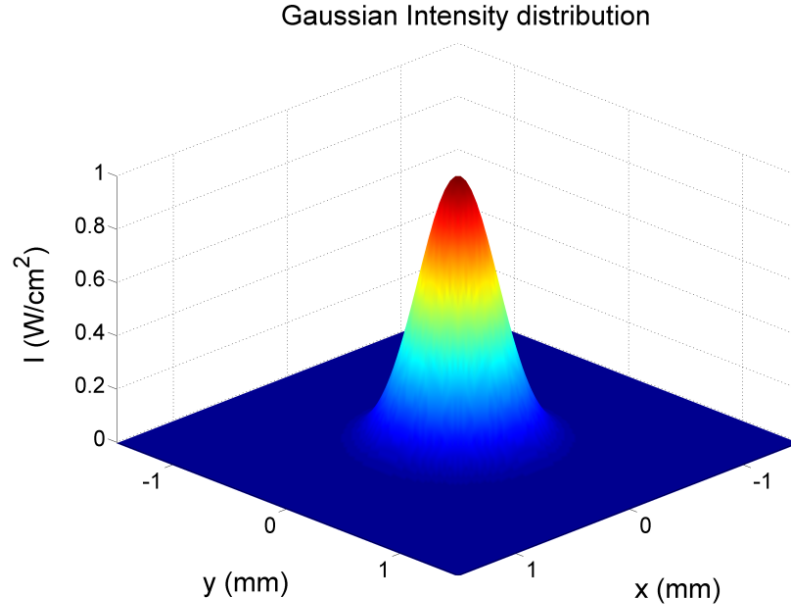


Fig 1-2 Two dimensional Gaussian intensity distribution with peak intensity $I_0 = 1 W / cm^2$ and $w_0 = 500 \mu m$.

In case of laser pulse, the temporal dimension must be taken into account. The rapidly oscillating electric field of a point source is given by Eq. (1.1-5):

$$E(t) = \text{Re} \left\{ \mathcal{E}(t) \exp \left[i(-\omega_0 t + \varphi(t)) \right] \right\} \quad (1.1-5)$$

where $\mathcal{E}(t)$ is the temporal complex envelope of the electric field of the pulse, $\omega_0 \equiv \frac{2\pi c}{\lambda_0}$ is the central frequency, λ_0 the central wavelength, and $c = 299792458 \text{ m / s}$ is the speed of light in vacuum, while $\varphi(t) = \arg[\mathcal{E}(t)]$.

The temporal intensity profile is given (as in the spatial coordinate) by $I(t) = |\mathcal{E}(t)|^2$. Today many different pulse shapes can be generated, like Lorentzian $I(t) \propto 1/[1+(t/t_p)^2]$, hyperbolic $I(t) \propto \sec^2(t/t_p)$ and Gaussian profiles. Gaussian pulses are of particular interest since they are readily available in the femtosecond (fs) time scale, and as such will be used extensively in this thesis. To include the Gaussian pulse shape in Eq. (1.1-4), the factor $-t^2/t_p^2$ is added in the exponential and the field envelope is now a function of both space and time as written in Eq. (1.1-6):

$$\mathcal{E}(r,t) = \sqrt{I_0} \cdot \exp\left[-\frac{r^2}{w_0^2} - i\frac{kr^2}{2f} - \frac{t^2}{t_p^2}\right] \quad (1.1-6)$$

where t_p is the pulse duration at $1/e^2$ radius of the electric field amplitude. In analogy to the beam curvature in the spatial dimension, we can introduce a temporal phase term in Eq. (1.1-6) with a quadratic dependence on time $\varphi(t) = Ct^2$, which is called pulse chirp with parameter C.

The approximation of the rapidly oscillating electric field $E(t)$ with its envelope $\mathcal{E}(t)$ simplifies the modeling of laser pulses significantly. However the approximation is valid only if the envelope is slowly varying (both amplitude and phase) in time compared to the wavelength, and hence it is called the *slowly varying envelope approximation* (SVEA). Effectively this simplification constrains the physical model to pulses that cannot be shorter than one wavelength [2]. A graphical representation of the electric field and envelope can be seen in Fig 1-3, for two laser pulses with 35 and 5 fs duration. The negative times correspond to the leading part of the pulse, while the positive to the trailing part.

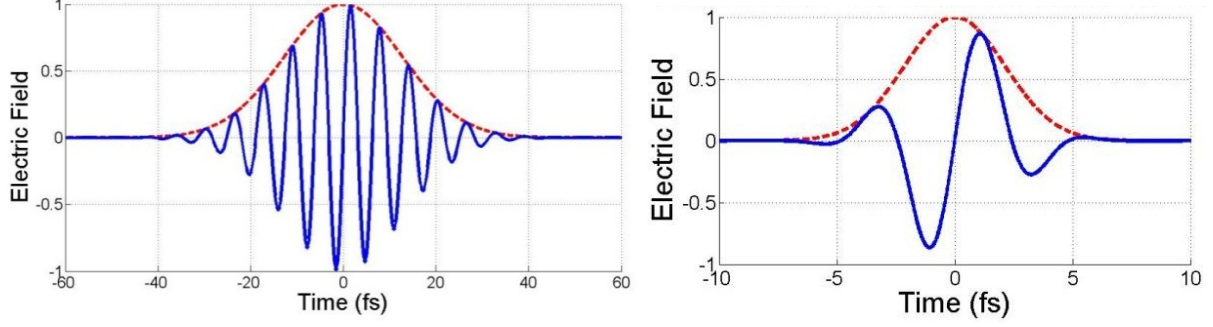


Fig 1-3 Graphical representation of the electric field (blue) and envelope (red) of a Gaussian laser pulse with 35 fs duration (left), and 5 fs duration (right). Central wavelength is $\lambda_0 = 800 \text{ nm}$. Propagation from right to left.

From the above we can clearly define the spatio-temporal wavepacket with peak intensity I_0 , beam waist w_0 , curvature f , pulse duration t_p , and chirp parameter C with Eq. (1.1-7):

$$\mathcal{E}(r,t) = \sqrt{I_0} \cdot \exp \left[-\frac{r^2}{w_0^2} - i \frac{kr^2}{2f} - \frac{t^2}{t_p^2} - iCt^2 \right] \quad (1.1-7)$$

with an intensity distribution of $I(r,t) = |\mathcal{E}(r,t)|^2$

$$I(r,t) = I_0 \exp \left[-\frac{r^2}{w_0^2} - i \frac{kr^2}{2f} - \frac{t^2}{t_p^2} - iCt^2 \right]^2 \quad (1.1-8)$$

A three dimensional representation of such a wavepacket with beam waist $w_0 = 850 \mu\text{m}$ and pulse duration of $t_p = 200 \text{ fs}$ is shown in Fig 1-4.

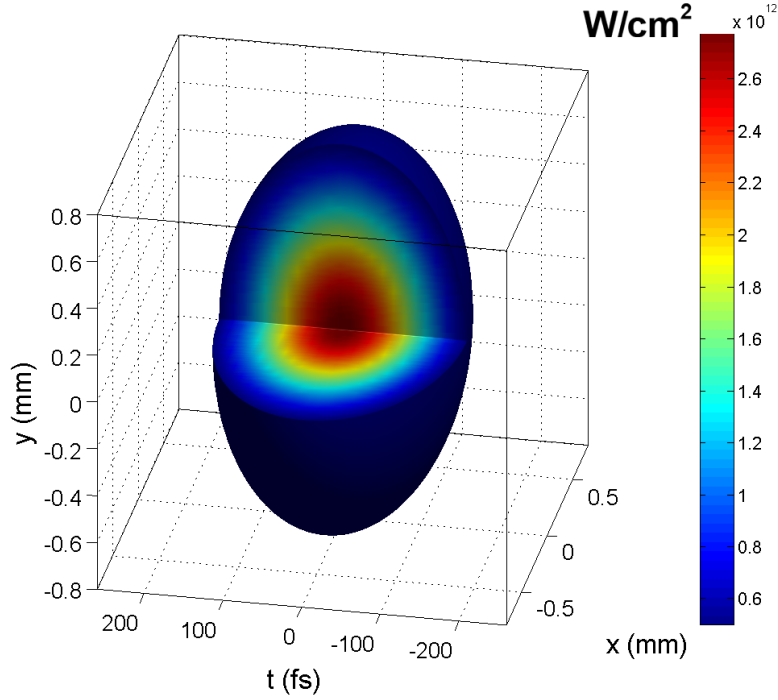


Fig 1-4 Three dimensional Gaussian intensity profile with $w_0 = 850 \mu m$, $t_p = 200 fs$ and

$$I_0 = 2.8 \times 10^{12} W / cm^2 .$$

The pulse energy and power of a Gaussian spatio-temporal wavepacket is given by Eqs. (1.1-9) and (1.1-10):

$$P_{in} = \frac{\pi w_0^2 I_0}{2} \quad (1.1-9)$$

$$E_{in} = P_{in} \frac{t_p}{\sqrt{\pi/2}} \quad (1.1-10)$$

The spectral representation of a laser pulse is defined by the Fourier transformation $F\{ \}$ of the temporal electric field from Eq. (1.1-5) is given by Eq. (1.1-11):

$$E(\omega) = F\{E(t)\} = \int_{-\infty}^{+\infty} E(t) e^{-i\omega t} dt = |E(\omega)| \exp[i\phi(\omega)] \quad (1.1-11)$$

Experimentally the spectral representation of laser pulses is measured with spectrometers, which measure the spectral intensity $I(\omega) = |E(\omega)|^2 = |\mathcal{E}(\omega)|^2$. Since the Fourier transform of a Gaussian results in another Gaussian, $E(\omega)$ is a Gaussian distribution which is centered on the central frequency $\omega_0 = \frac{2\pi c}{\lambda_0}$ of the laser pulse. λ_0 is the central wavelength and $\varphi(\omega)$ is the spectral phase.

Generally the electric field of any spatio-temporal wavepacket propagating in the z direction can be written in the form:

$$E(r, t, z) = \frac{1}{2} \mathcal{E}(r, t, z) \exp[i(k_0 z - \omega_0 t)] + cc \quad (1.1-12)$$

where $\mathcal{E}(r, t, z)$ denotes the spatio-temporal electric field envelope with carrier envelope $\exp[i(k_0 z - \omega_0 t)]$ with central frequency ω_0 . In case of a Gaussian wavepacket in space and time the envelope is written in the form of Eq. (1.1-7). This however is not constricting since other profiles are possible, like super-Gaussians, top-hats, etc.

1.2 Linear propagation regime

Before we investigate the nonlinear dynamics observed in femtosecond pulse propagation it is vital that we describe the linear effects which are the basis of any propagation model. In the case of laser pulse propagation in a transparent medium there are mainly two linear effects to consider: diffraction and dispersion.

1.2.1 Beam diffraction

Diffraction is a fundamental linear property of finite size waves, causing them to spread in space as they propagate. Diffraction always occurs, even in vacuum. The laws of Gaussian optics

predict that any beam with a Gaussian intensity profile that has a flat spatial phase (no initial wavefront curvature) will double the area of illumination after propagating one Rayleigh length. The doubling of the area corresponds in an increase of the beam radius by a factor $\sqrt{2}$. The Rayleigh length is given by Eq. (1.2-1):

$$L_{Diff} = \frac{kw_0^2}{2} = \frac{\pi n_0 w_0^2}{\lambda_0} \quad (1.2-1)$$

where λ_0 is the central wavelength in vacuum, n_0 is the refraction index of the medium at wavelength λ_0 , while $k = n_0 k_0$ and $k_0 = \frac{2\pi}{\lambda_0}$ are the wavenumbers in the medium and in vacuum respectively. Since L_{Diff} is a function of w_0^2 , diffraction becomes increasingly important as the beam width becomes smaller. To give an example, a Gaussian beam with $\lambda_0 = 800 \text{ nm}$ and $w_0 = 100 \text{ }\mu\text{m}$ propagating in vacuum has a Rayleigh length of $L_{Diff} = 3.93 \text{ cm}$. However if the beam has a width of one inch (2.54 cm) instead, the Rayleigh length will be over 2.5 km long.

The spreading of a Gaussian beam after one and two Rayleigh lengths, as well as the associated drop in intensity, can be seen in Fig 1-5

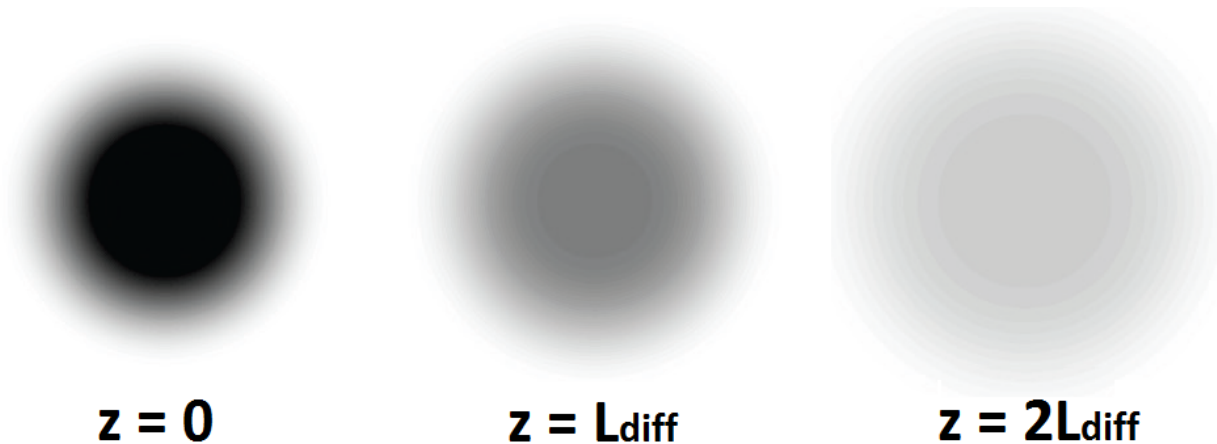


Fig 1-5 Normalized intensity of a Gaussian beam after propagation of one (middle) and two (left) Rayleigh lengths.

By applying the paraxial approximation we can obtain the functions describing the beam waist along z and the divergence angle θ .

$$w(z) = w_0 \cdot \left(1 + \frac{z^2}{L_{Diff}^2} \right)^{1/2} \quad (1.2-2)$$

$$\theta = \frac{\lambda}{\pi w_0} \quad (1.2-3)$$

Which in turn give us an analytic function of the intensity along propagation distance z :

$$I(r, z) = I_0 \left[\frac{w_0}{w(z)} \right]^2 \exp \left[2 \left(\frac{r}{w(z)} \right)^2 \right] \quad (1.2-4)$$

The electric field of the beam at position (r, z) in space can be written in the form:

$$E(r, z) = \mathcal{E}_0 \frac{w_0}{w(z)} \exp \left[-\frac{r^2}{w^2(z)} \right] \exp \left[-ik \frac{r^2}{2R(z)} \right] \exp \left[-ikz + i\zeta(z) \right] \quad (1.2-5)$$

where:

$$R(z) = z \left[1 + \left(\frac{L_{Diff}}{z} \right)^2 \right] \quad (1.2-6)$$

$$\zeta(z) = \tan^{-1} \frac{z}{L_{Diff}} \quad (1.2-7)$$

The paraxial propagation equation for diffraction, which is the basis of the whole computational model used in this thesis, is the following:

$$\frac{\partial \mathcal{E}}{\partial z} = \frac{i}{2k_0} \nabla_{\perp}^2 \mathcal{E} \quad (1.2-8)$$

where $\nabla_{\perp}^2 = \Delta_{\perp} = \frac{\partial^2}{\partial x^2} + \frac{\partial^2}{\partial y^2}$ denotes the transverse (spatial) Laplacian operator, and z is the propagation axis. Eq. (1.2-8) can be numerically solved through a computational scheme on a computer. More importantly, it serves as the basic equation for all linear and nonlinear effects studied in this thesis. A graphical representation of the diffraction of a laser beam with waist w_0 propagating along the z direction can be seen in Fig 1-6

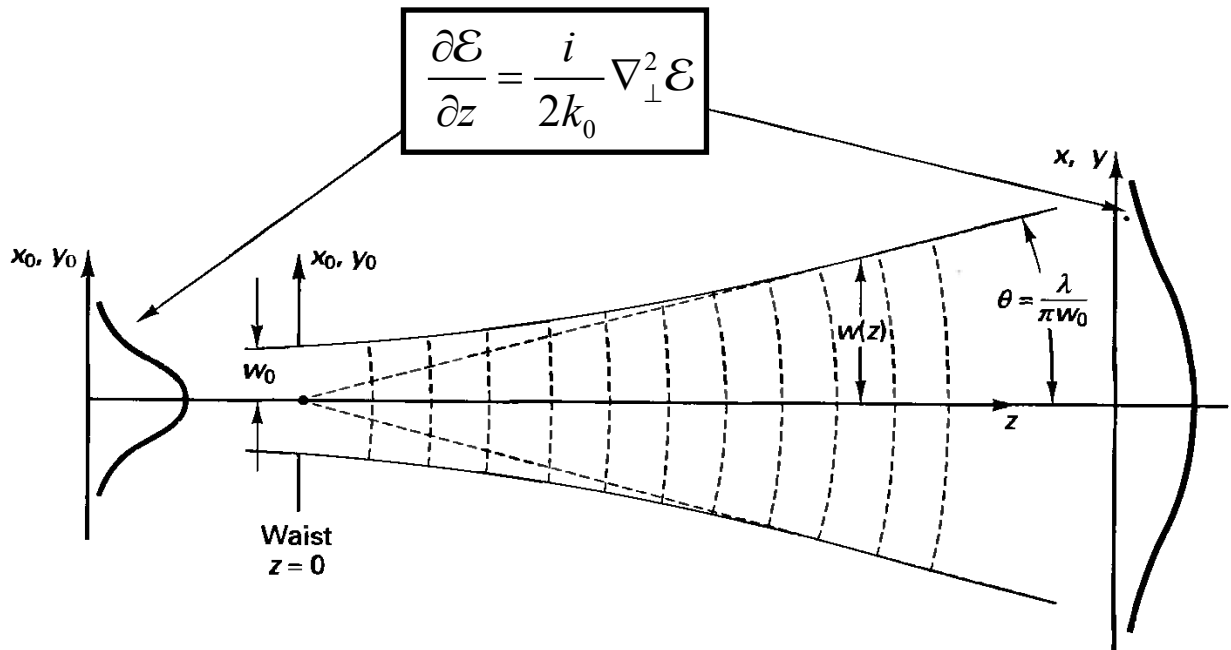


Fig 1-6 Graphical representation of diffraction of a beam with initial waist w_0 and no initial curvature.

Eq. (1.2-8) is directly derived from the Maxwell equations for a non-magnetic medium without free charges ($\rho = 0$) and currents ($\vec{J} = 0$) as it is shown in the Appendix.

1.2.2 Dispersion of femtosecond pulses

The second linear effect that will be analyzed is the material chromatic dispersion. Dispersion describes the spreading of polychromatic waves as they propagate in a transparent medium. It originates from the wavelength dependence of the refractive index $n(\lambda)$ observed in dispersive materials, which results in different wavelengths propagating at different speeds $v = \frac{c}{n(\lambda)}$. Dispersion is a temporal phenomenon, thus it is meaningless for continuous laser beams. However, for laser pulses in the femtosecond time scale, which are by definition polychromatic, dispersion becomes increasingly important, effectively distorting the initial shape of the pulse envelope as it propagates.

At this point the group and phase velocity have to be defined. The velocity of propagation of the electric field envelope \mathcal{E} is called group velocity $v_{group} = \frac{\partial \omega(k)}{\partial k}$, where $k = n(\omega) \frac{\omega}{c}$. The phase velocity $v_{phase} = \frac{\omega(k)}{k}$ is the velocity at which the phase fronts propagate in the medium. In vacuum both phase and group velocity are equal to c , and all frequency components $\omega = \omega(k)$ propagate with the same speed c . Consequently the pulse shape remains undistorted. The same is true if the refractive index n is independent of wavelength λ (or frequency ω), since both $v_{group} = v_{phase} = \frac{c}{n}$. However, in a dispersive material each frequency component propagates at its own speed, resulting in a difference between v_{group} and v_{phase} , which will change the pulse shape. Most transparent materials exhibit the so called "normal dispersion", in which longer wavelengths propagate at higher velocities than shorter ones (red frequencies are faster than blue frequencies). Equivalently, the refractive index of normal dispersion materials is a decreasing function of wavelength. This however is not true for the whole spectral region, since close to the materials absorption lines, dispersion becomes anomalous and the refractive index is increasing with wavelength. A graphical representation of the wavelength dependence of the refractive index and absorption can be seen in Fig 1-7 (taken from [3]).

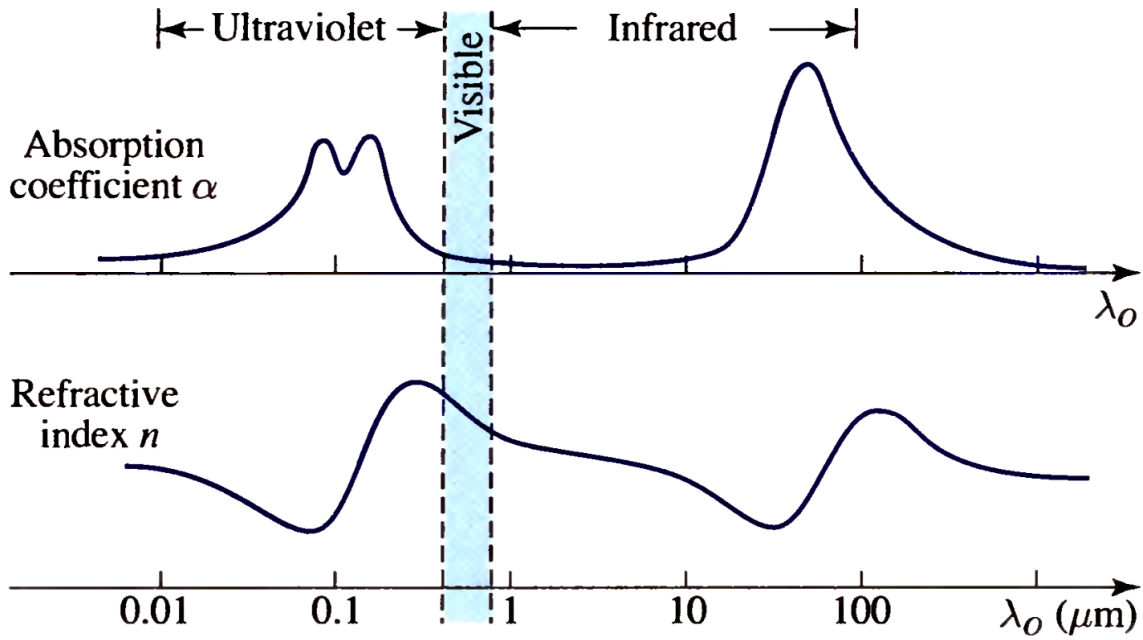


Fig 1-7 Graphical representation of the absorption (top) and refractive index (bottom) as a function of wavelength.

To model both normal and anomalous dispersion, a single empirical equation was proposed by Sellmeier in 1871 [4], called the Sellmeier dispersion formula:

$$n^2(\lambda) = 1 + \sum_i \frac{B_i \lambda^2}{\lambda^2 - \lambda_i^2} \quad (1.2-9)$$

where B_i are experimentally determined Sellmeier coefficients, and $\lambda_i = 1, 2, 3, \dots$ correspond to the absorption lines. The Sellmeier equation can be found in many different forms in the literature, some of which are extended versions of the original, specialized to better describe specific materials. In this thesis three different version of the Sellmeier dispersive relation are used to describe the dispersion of i) air with Eq. (1.2-10) [5], ii) noble gases with Eq. (1.2-11) [6], and iii) liquids and condensates materials with Eq. (1.2-12).

$$n(\lambda)-1=10^{-6}\left(A+\frac{B}{C-\lambda^{-2}}+\frac{D}{E-\lambda^{-2}}\right) \quad (1.2-10)$$

$$n^2(\lambda)-1=A+\frac{B}{\lambda^2}+\frac{C}{\lambda^4}+\frac{D}{\lambda^6}+\frac{E}{\lambda^8}+\frac{F}{\lambda^{10}} \quad (1.2-11)$$

$$n^2(\lambda)=A+\frac{B_1\lambda^2}{\lambda^2-\lambda_1^2}+\frac{B_2\lambda^2}{\lambda^2-\lambda_2^2}+\frac{B_3\lambda^2}{\lambda^2-\lambda_3^2}+D\lambda^2+F\lambda \quad (1.2-12)$$

where the wavelength λ is given in μm . The coefficients in Eqs. (1.2-10) - (1.2-12) for various materials can be found in section 9.

Most femtosecond laser sources have a relative narrow spectrum, which is centered on the central frequency ω_0 . In these cases dispersion can adequately be described mathematically by the Taylor expansion of the wavenumber $k(\omega)$ around the central frequency ω_0 :

$$k(\omega)=k_0+\frac{\partial k(\omega)}{\partial \omega}(\omega-\omega_0)+\frac{1}{2!}\frac{\partial^2 k(\omega)}{\partial \omega^2}(\omega-\omega_0)^2+\frac{1}{3!}\frac{\partial^3 k(\omega)}{\partial \omega^3}(\omega-\omega_0)^3+\dots \quad (1.2-13)$$

where $k_0=n(\omega_0)\frac{\omega_0}{c}$. The term $\frac{\partial k(\omega)}{\partial \omega}=k'$ corresponds to the inverse of the group velocity

$k' \equiv \frac{1}{v_{group}}$, or else group delay per unit length. The third term of the RHS is the second order

dispersive term, containing the change of the group delay per unit length, also called group

velocity dispersion (GVD): $\frac{\partial^2 k(\omega)}{\partial \omega^2}=\frac{\partial}{\partial \omega}\left(\frac{1}{v_{group}}\right)=k''$. Higher dispersive term like k''', k'''' ,...

are rarely used since the validity of the Taylor expansion is lost, and the full Sellmeier dispersion relation is preferred instead.

In analogy to diffraction in the spatial domain we can define the characteristic length of dispersion in the temporal domain:

$$L_{GVD}=\frac{t_p^2}{2k''} \quad (1.2-14)$$

which defines the distance over which the pulse duration will increase by a factor $\sqrt{2}$. Typical values for k'' are $0.2 \text{ fs}^2 / \text{cm}$ for air, $248 \text{ fs}^2 / \text{cm}$ for water, and $360 \text{ fs}^2 / \text{cm}$ for fused silica glass for an 800 nm pulse. For a Fourier limited pulse duration of 35 fs and without initial chirp the dispersive length which correspond to these materials are $L_{GVD(\text{air})} = 30.65 \text{ m}$, $L_{GVD(\text{water})} = 2.47 \text{ cm}$, $L_{GVD(\text{SiO}_2)} = 1.7 \text{ cm}$ respectively. The broadening of a pulse with two frequency components over $1 \times L_{GVD}$ due to normal dispersion can be seen in Fig 1-8

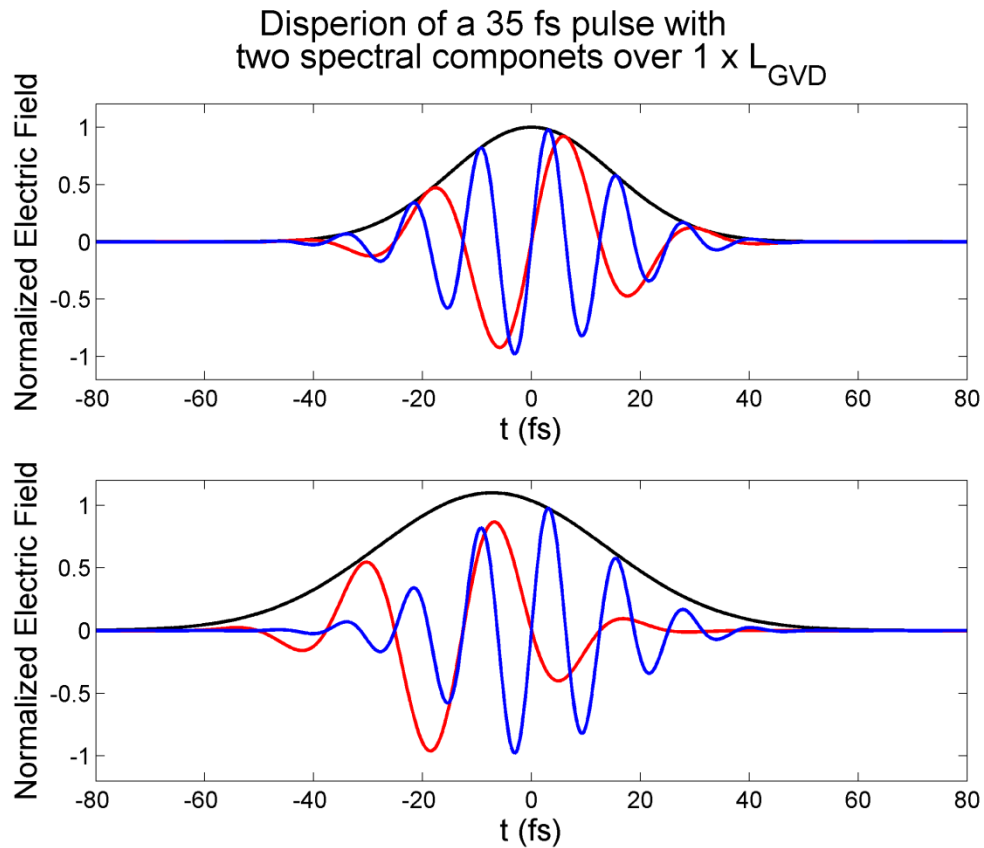


Fig 1-8 Electric field of two in phase frequency components (blue and red) of a 35 fs laser pulse, and the corresponding envelope, before (first row) and after the effect of normal dispersion (second row) over one dispersive length. Propagation from right to left.

In case the pulse has an initially negative chirp, the propagation through a normal dispersion material will lead to a shortening of the duration through the accumulation of positive chirp. This way it is possible to deliver very short pulses inside dispersive materials (normal or anomalous), by inducing the appropriate chirp (negative or positive) in the initial pulse. This is possible because the difference in propagation speed of the various spectral components will eventually lead to an increase of the pulse duration after the minimum duration is reached.

Note that the use of t_p in Eq. (1.2-14) can be misleading, since the dispersive length is dependent on the spectrum bandwidth. Thus t_p is referring to the Fourier limited pulse duration obtained from the Fourier transformation of the spectrum with a flat spatial phase (no initial phase difference between spectral components).

1.3 Nonlinear femtosecond laser pulse propagation

Up to this point only linear optical phenomena have been discussed. Linear optical phenomena are "linear" in the sense that they depend in a linear manner on the strength of the optical field. In other words, the optical properties of the material are independent of the light intensity. However, when the optical field becomes strong enough the linear dependence is lost and the light itself is modifying the optical properties of the material. The change of the optical properties of the material will in turn modify the propagation of the optical field which is seeding this process, giving rise to the so called "nonlinear self-action effects". The first reported nonlinear optical phenomenon was the generation of the second harmonic (SHG) in 1961 by Franken *et al.* [7], shortly after the invention of the laser by Maiman in 1960 [8], [9]. 50 years later, the field of nonlinear optics has evolved into one of the most active research communities in science, boasting numerous research laboratories around the world with an extensive theoretical and experimental background [10]. Nowadays, optical pulses in the femtosecond time scale are generated by commercially available tabletop laser sources through the chirped pulse amplification technique (CPA) [11]. The availability of femtosecond laser pulses sparked multidisciplinary research activities in fields like biology, material science and medicine leading to important practical applications.

1.3.1 Optical Kerr effect and self-focusing

1.3.1.1 The nonlinear optical susceptibility

The material response to optical fields is the dipole moment per unit of volume, also called electric polarization $\vec{P}(t)$. $\vec{P}(t)$ is dependent on the electric field of the light that is propagating through the material. In the linear regime, the electric polarization $\vec{P}(t)$ is a linear function of the electric field strength $\vec{E}(t)$, which for simplicity can be written in scalar form as:

$$P(t) = \varepsilon_0 \chi^{(1)} E(t) \quad (1.3-1)$$

where $\chi^{(1)}$ is the linear optical susceptibility of the material. However in the nonlinear regime, where the optical field strength is comparable to the interatomic field, Eq. (1.3-1) is not valid anymore. In order to properly describe the nonlinear response of the material we express Eq. (1.3-1) as a power series of $E(t)$:

$$P(t) = \varepsilon_0 \left[\chi^{(1)} E(t) + \chi^{(2)} E^2(t) + \chi^{(3)} E^3(t) + \dots \right] \quad (1.3-2)$$

or else

$$P(t) = P^{(1)}(t) + P^{(2)}(t) + P^{(3)}(t) + \dots \quad (1.3-3)$$

where $\chi^{(2)}$ and $\chi^{(3)}$ are the second and third order optical susceptibilities of the medium respectively. $P^{(2)}(t) = \varepsilon_0 \chi^{(2)} E^2(t)$ and $P^{(3)}(t) = \varepsilon_0 \chi^{(3)} E^3(t)$ are the second and third order nonlinear polarizations. The above formulation is standard in the field of nonlinear optics, and can be found in numerous textbooks in the literature [12], [13], [14]. Note that Eqs. (1.3-1) and (1.3-2) are written in scalar form, however in general, the polarization and electric field are vector functions of time, and the constants $\chi^{(1)}$, $\chi^{(2)}$, $\chi^{(3)}$ are tensors depending on the material

properties and the frequency of the applied optical field. Eq. (1.3-2) also assumes that the material response is instantaneous, or at least much faster than the pulse duration. This assumption is valid for femtosecond pulses and nonlinearities with electronic origin [15].

It is known that second order nonlinear optical interactions are possible ($\chi^{(2)} \neq 0$) only in noncentrosymmetric nonlinear crystals [12], which are crystals that do not display inversion symmetry. Materials, like gases, amorphous solids (glasses) and liquids, which exhibit inversion symmetry, have no second order susceptibility. In these materials the first nonlinear effect that comes into play is associated with the third order susceptibility $\chi^{(3)}$, and Eq. (1.3-2) can be simplified to:

$$P(t) \approx \varepsilon_0 \chi^{(1)} E(t) + \varepsilon_0 \chi^{(3)} E^3(t) \quad (1.3-4)$$

which gives the electric polarization of materials exhibiting only third order nonlinear interaction. The study of second order nonlinear interaction is out of the scope of this thesis.

The third order nonlinear polarization for a monochromatic wave $E(t) = \mathcal{E} \cos(\omega t)$ with frequency ω is given by:

$$\left. \begin{aligned} P^{(3)}(t) &= \varepsilon_0 \chi^{(3)} [\mathcal{E} \cos(\omega t)]^3 \\ \cos^3(x) &= \frac{3}{4} \cos(x) + \frac{1}{4} \cos(3x) \end{aligned} \right\} \Rightarrow P^{(3)}(t) = \frac{3}{4} \varepsilon_0 \chi^{(3)} \mathcal{E}^3 \cos(\omega t) + \frac{1}{4} \varepsilon_0 \chi^{(3)} \mathcal{E}^3 \cos(3\omega t) \quad (1.3-5)$$

The last term on the RHS of Eq. (1.3-5) corresponds to the generation of a new wave with frequency 3ω , a phenomenon called third harmonic generation (THG). In the THG process, three photons of frequency ω are converted into one photon with frequency 3ω , as it is depicted in Fig 1-9.

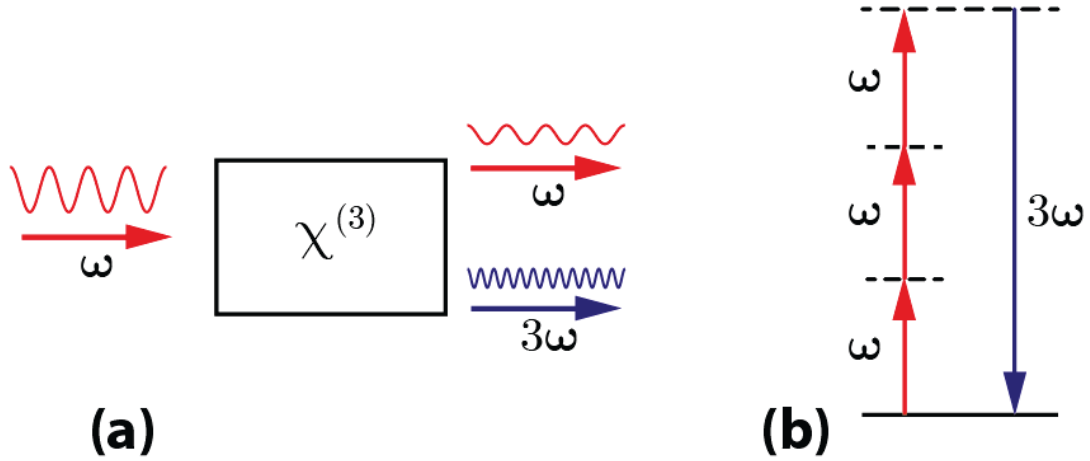


Fig 1-9 Third harmonic generation. a) Schematic representation of the interaction geometry, and b) energy level diagram.

We can now write the polarization for only the frequency ω (neglecting 3ω) in the form:

$$P(t) \approx \epsilon_0 \left(\chi^{(1)} + \frac{3}{4} \chi^{(3)} |\mathcal{E}|^2 \right) \mathcal{E} \cos(\omega t) \quad (1.3-6)$$

or else:

$$P(t) \approx \epsilon_0 \chi \mathcal{E} \cos(\omega t) \quad (1.3-7)$$

where:

$$\chi = \chi^{(1)} + \chi_{\text{nonlinear}} = \chi^{(1)} + \frac{3}{4} \chi^{(3)} |\mathcal{E}|^2 \quad (1.3-8)$$

The term $\frac{3}{4} \epsilon_0 \chi^{(3)} \mathcal{E}^3 \cos(\omega t)$ of Eq. (1.3-6) describes the nonlinear contribution to the polarization at frequency ω of the driving optical field. Eq. (1.3-8) defines the total susceptibility of the material for frequency ω , from both linear and nonlinear origin.

1.3.1.2 Intensity dependent refractive index

The optical susceptibility χ is related to the refractive index of the medium with the relation:

$$n = \sqrt{1 + \chi} \quad (1.3-9)$$

which can be written as:

$$n = \sqrt{1 + \chi^{(1)} + \chi_{nonlinear}} \approx n_0 + \frac{1}{2n_0} \chi_{nonlinear} \quad (1.3-10)$$

where n_0 is the linear refractive index of the medium at frequency ω :

$$n_0 = \sqrt{1 + \chi^{(1)}} \quad (1.3-11)$$

and

$$\chi = \chi^{(1)} + \chi_{nonlinear} \quad (1.3-12)$$

By substituting $\chi_{nonlinear} = \frac{3}{4} \chi^{(3)} |\mathcal{E}|^2$ from Eq. (1.3-8) in Eq. (1.3-10) we can write the total refractive index as a function of the optical intensity of the incident wave

$$n = n_0 + n_2 I \quad (1.3-13)$$

where $n_2 I$ is the nonlinear contribution of $\chi^{(3)}$ to the total refractive index for frequency ω .

n_2 (cm^2 / W) is called the nonlinear refractive index of the medium and depends on the frequency of the incident wave and the material properties:

$$n_2 = \frac{3}{4\varepsilon_0 n_0^2 c} \chi^{(3)} \quad (1.3-14)$$

The intensity of the envelope \mathcal{E} is given by:

$$I = \frac{\varepsilon_0 n_0 c}{2} |\mathcal{E}|^2 \quad (1.3-15)$$

The dependence of the refractive index of a material to the strength of an applied static electric field was first reported in 1877 by John Kerr [16]. In the field of nonlinear optics, where the static electric field is replaced by a rapidly oscillating optical electric field from a laser, the same phenomenon is observed and is called the optical Kerr effect. It is the driving effect of femtosecond filamentation and the origin of rich nonlinear phenomena. Typically the nonlinear refractive index n_2 is of the order of $10^{-19} \text{ cm}^2 / W$ in gases and $10^{-16} \text{ cm}^2 / W$ in amorphous solids and liquids. Therefore nonlinear phenomena can only be observed when the term $n_2 I$ becomes large enough and is able to compete with the linear phenomena of diffraction and dispersion. For a 35 fs laser pulse at 800 nm, the nonlinear refractive index is typically positive and of the order of $3.2 \times 10^{-19} \text{ cm}^2 / W$ in air [17], [18], $1.6 \times 10^{-16} \text{ cm}^2 / W$ in water [19], [20], and around $\sim 3 \times 10^{-16} \text{ cm}^2 / W$ in fused silica glass [21]. Experimentally, both real and imaginary parts of n_2 can be measured using the z-scan technique [22].

1.3.1.3 Self-focusing of Gaussian beams

Since most transparent materials have positive n_2 , the total refractive index is increasing with beam intensity according to Eq. (1.3-13). Since laser beam profiles are in general not homogeneous, the total refractive index will be a function of the spatial intensity profile $I(r)$:

$$n(r) = n_0 + n_2 I(r) \quad (1.3-16)$$

This means that the refractive index acting on any beam propagating in a nonlinear medium is dependent on the intensity profile of the beam itself. As a direct result a beam with a Gaussian intensity profile will induce a Gaussian refractive index modulation as it propagates. This refractive index modulation resembles a positive lens and will cause the beam to focus as it is shown in Fig 1-10. The focusing of the beam due to self-action effects (without any initial beam curvature), called self-focusing, was first investigated by P. L. Kelly in 1965 [23] and has been extensively studied thereafter [24].

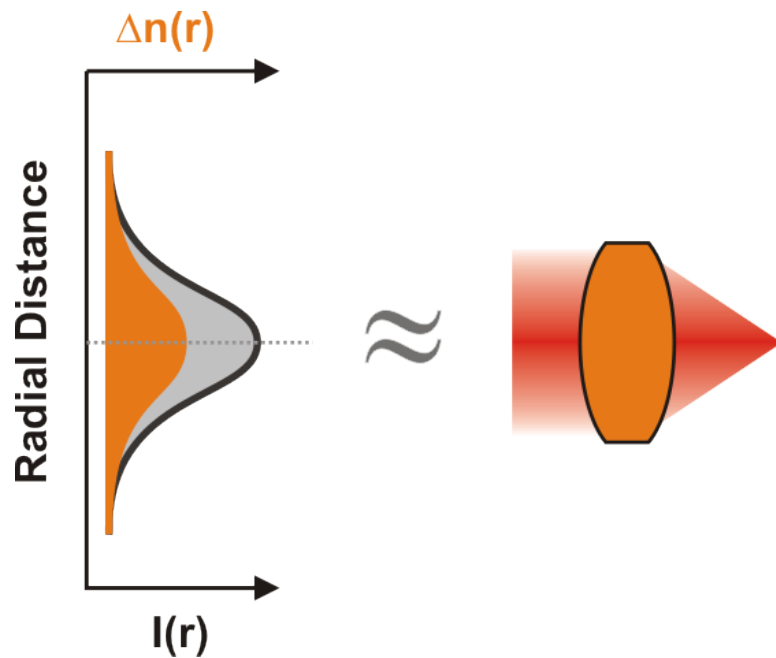


Fig 1-10 Schematic representation of the self-focusing of a Gaussian beam. Black line: Intensity distribution. Yellow: refractive index modulation.

Self-focusing of Gaussian beams is always happening in positive n_2 nonlinear media, even at very low intensities. However in order to be observable self-focusing must overcome diffraction. This is possible only if the power carried by the beam is above a critical value which depends on the beam shape. For Gaussian beams the critical power is given by Eq. (1.3-17) [25], [26]:

$$P_{cr} = \frac{3.77\lambda_0^2}{8\pi n_0 n_2} \quad (1.3-17)$$

Note that Eq. (1.3-17) is referring to the critical power value for collimated Gaussian beams only, and is independent of intensity. Typically the critical power for an 800 nm laser pulse is about ~3.2 GW in air and ~4 MW in water.

Self-focusing is a self-fueling process, since the increasing intensity will only strengthen self-focusing further, eventually leading to a catastrophic collapse of the beam on itself. The collapse distance can be approximated by a semi-empirical formula [25], [27]:

$$L_C = \frac{0.367L_{Diff}}{\sqrt{(\sqrt{Pin / Pcr} - 0.852)^2 - 0.0219}} \quad (1.3-18)$$

Eq. (1.3-18) is called the Marburger's formula, and is widely used in the literature to estimate the collapse distance of collimated Gaussian laser beams. For Gaussians with initial curvature (focal length f), the collapse distance is given by $L_{C,f}$:

$$\frac{1}{L_{C,f}} = \frac{1}{L_C} + \frac{1}{f} \quad (1.3-19)$$

In reality however the beam collapse is arrested by saturating mechanisms like ionization and nonlinear absorption losses, which will be mentioned in detail later on.

In analogy to the characteristic lengths of diffraction and dispersion, which were introduced previously, we can define the characteristic length for self-focusing [28] with:

$$L_{Kerr} = \frac{c}{\omega_0 n_2 I} \quad (1.3-20)$$

1.3.2 Optical field ionization

Optical field ionization (OFI), or else called photo-ionization, is one of the main saturating mechanisms that arrest the beam collapse from self-focusing. Close to the point of collapse, the optical intensity is high enough to ionize the medium through the simultaneous absorption of multiple photons. The number K of photons required depends on the ionization potential of the material U_i and the frequency of the optical field:

$$K = \left\langle \frac{U_i}{E_{photon}} \right\rangle + 1 \quad (1.3-21)$$

where $\hbar = 6.58211928 \times 10^{-16} \text{ eV} \cdot \text{s}$ is the reduced Plank constant, and E_{photon} is the photon energy given by:

$$E_{photon} = \hbar\omega \quad (1.3-22)$$

The brackets $\langle . \rangle$ in Eq. (1.3-21) denote the integer part. For an 800 nm laser pulse, which is the reference wavelength that will be used throughout this thesis, the energy is $E_{800nm} = 1.5498 \text{ eV}$. If the process is taking place in air, the number of photons needed to liberate an electron are $K = 8$, for $U_i = 12.063$ taking into account only oxygen [29]. In liquids and condensed materials K is in general smaller than in gases. For the same 800 nm laser we need $K = 5$ photons in water, and 6 in fused silica glass in order to generate an electron.

This nonlinear process, called Multi-Photon Ionization (MPI) and depicted in Fig 1-11(a), is extremely improbable to happen at low intensities. The MPI rate is given by

$$W_{MPI} = \sigma_K I^K \quad (1.3-23)$$

where σ_K denotes the MPI coefficient depending on the material.

The generation of free electron plasma through the simultaneous absorption of multiple photons (MPA) leads to a decrease of the intensity. MPA scales with I^K , therefore it will be

strongest at the most intense points of the beam, namely closest to the position of collapse. Since MPA (scales with I^K) is a higher order nonlinear process than self-focusing (scales with I) it will dominate as intensity increases, ultimately arresting the collapse of the beam. The exact intensity at which the collapse is arrested by MPA is dependent on the focusing geometry, beam power and the material parameters. For paraxial beams it is generally between $10^{13} - 10^{14} \text{ W/cm}^2$. The characteristic length of MPA is given by Eq.(1.3-24):

$$L_{MPA} = \frac{1}{2\beta_K I^{K-1}} \quad (1.3-24)$$

where β_K denotes the MPA coefficient given from:

$$\beta_K = K\hbar\omega_0\rho_{at}\sigma_K \quad (1.3-25)$$

At higher intensity levels ($I > 10^{15} \text{ W/cm}^2$) and shorter optical frequencies, OFI occurs mainly through tunneling ionization, in which the electron tunnel escapes under the combined strength of the optical field and the coulomb potential. A schematic representation of tunnel ionization is depicted in Fig 1-11(b).

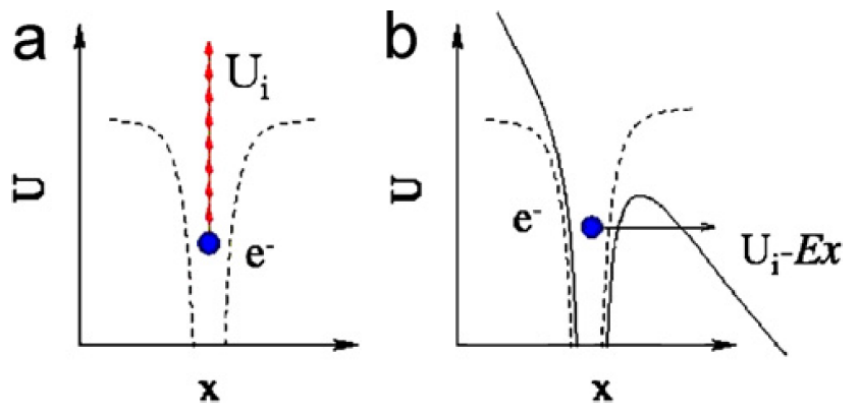


Fig 1-11 Schematic diagram of: (a) multiphoton and (b) tunnel ionization.

1.3.3 Plasma defocusing and absorption

The generated through MPI electron plasma will locally decrease the refractive index of the medium and therefore interact with the laser pulse. The modified refractive index is given by Eq. (1.3-26) [30]:

$$n \approx n_0 - \frac{\rho}{2\rho_c} \quad (1.3-26)$$

where ρ is electrons density of the generated plasma and ρ_c the critical plasma density at which the medium becomes opaque, given from:

$$\rho_c \equiv \frac{\epsilon_0 m_e \omega_0^2}{e^2} \quad (1.3-27)$$

$m_e = 9.1093829140 \times 10^{-31} \text{ kg}$, and $e = -1.602176565 \cdot 10^{-19} \text{ C}$ are the electron mass and charge. For 800 nm we get $\rho_c \approx 1.7 \times 10^{21} \text{ cm}^{-3}$.

The modification of the refractive index due to the presence of plasma will influence the propagation of light, depending on its shape and density. Specifically, if a self-focusing laser pulse with spatial intensity distribution $I(r)$ is used to generate the plasma, the shape of the plasma will be $\sim I^K(r)$. In most cases the shape of the generated plasma will resemble a bubble, since most laser profiles $I(r)$ are more intense at the center (Gaussian, Lorentzian, hyperbolic secant, etc). Since the densest plasma is located on-axis, the effect of the plasma will resemble a defocusing lens much like an air bubble in water. As already mentioned, the strength of the plasma lens is dependent not only on the shape of the plasma but also on the peak electron density, which ultimately depends on the peak intensity I_0 of the driving laser. Consequently plasma defocusing becomes increasingly important close to the position of the collapse, and is able to locally overcome self-focusing and arrest the collapse. The reason behind this is the same as in the case of MPA; plasma defocusing is a higher order nonlinear process than self-focusing,

and therefore it will eventually dominate given high enough intensity values. A schematic representation of plasma defocusing is shown in Fig 1-12.

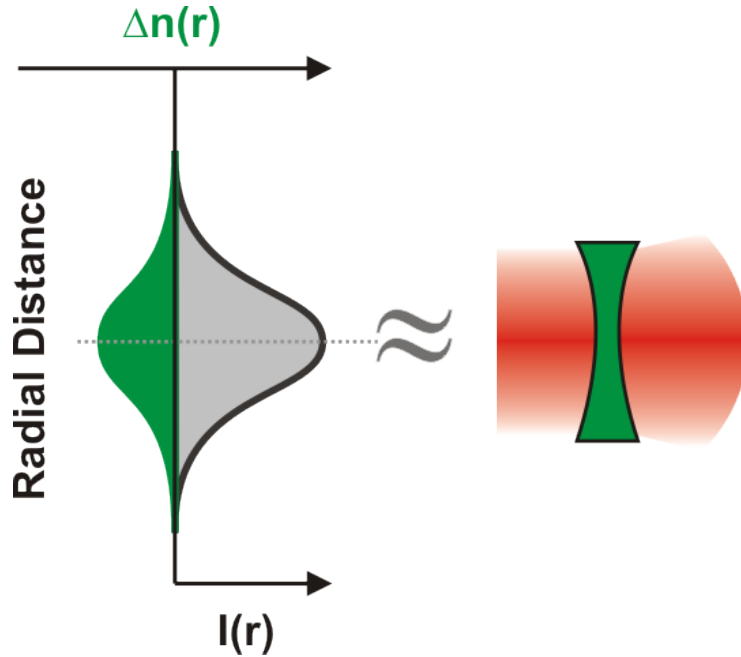


Fig 1-12 Schematic representation of plasma defocusing. Black line: intensity distribution. Green: Refractive index modulation.

In addition to its defocusing effect, plasma is also able to absorb photons and deplete the energy of the laser pulse that is propagating through it. In this process existing free electrons (possibly generated by OFI) are accelerated by the electric field of the pulse. The accelerated electrons collide with other atoms and molecules, and given enough kinetic energy, will generate new electrons in an avalanche like process. This phenomenon, also known as inverse Bremsstrahlung effect, is especially strong for pulses with long durations.

Both plasma defocusing and plasma absorption are saturating mechanisms of the intensity. The characteristic lengths of plasma defocusing (L_{Plasma}) and absorption (L_{ABS}) are given by:

$$L_{Plasma} = \frac{2}{\sigma\omega_0\rho\tau} \quad (1.3-28)$$

and

$$L_{ABS} = \frac{2}{\sigma\rho} \quad (1.3-29)$$

where σ the cross section for inverse Bremsstrahlung is given by Eq. (1.3-30) [31]:

$$\sigma \equiv \frac{e^2\tau_c}{\varepsilon_0 m_e c n_0 (1 + \omega^2\tau_c^2)} \quad (1.3-30)$$

where τ_c is the characteristic time for electron collisions depending on the material.

Here it must be noted that both the defocusing and absorption effects of the plasma are mainly affecting by the trailing part of the pulse, since most of the plasma is generated at the center time slice where intensity is highest. A more detailed description of the space-time coupling found in filamentation will be given later on.

1.3.4 Self-phase modulation and white light generation

Self-Phase Modulation (SPM) is the phenomenon where the phase of a pulse is changing due to a self-induced modulation of the refractive index in time. The time varying phase will cause the spectrum to change, leading to spectral broadening and white light generation. The modulation of the refractive index $n = n_0 + n_2 I$ can generally be associated to both its linear and nonlinear parts, since in the filamentation process both of these quantities are changing in time. The phase of the carrier wave $e^{i(\vec{k}\vec{r} - \omega_0 t)}$ is given by $\varphi(t) = \vec{k}\vec{r} - \omega_0 t$. For simplicity we assume that the propagation direction is along the z axis, so we can write: $\varphi(t) = nk_0 z - \omega_0 t$. In general the new frequencies that are generated are given by the simple relation:

$$\omega(t) = -\frac{\partial\varphi(t)}{\partial t} \quad (1.3-31)$$

So by substitution we have:

$$\left. \begin{aligned} \omega(t) &= -\frac{\partial \varphi(t)}{\partial t} = -\frac{\partial}{\partial t} [nk_0 z - \omega_0 t] = \omega_0 - k_0 z \frac{\partial n(t)}{\partial t} \\ n(t) &= n_0(t) + n_2 I(t) = n_0 - \frac{\rho(t)}{2\rho_c} + n_2 I(t) \end{aligned} \right\} \Rightarrow \omega(t) = \omega_0 - k_0 z \frac{\partial}{\partial t} \left(n_0 - \frac{\rho(t)}{2\rho_c} + n_2 I(t) \right) \quad (1.3-32)$$

The term $n_2 I(t)$ is associated with the optical Kerr effect, which is increasing the refractive index when intensity is increased. The term $-\frac{\rho(t)}{2\rho_c}$ is associated with plasma defocusing, i.e. the reduction of the linear part of the refractive index due to the presence of plasma. The calculation of the derivative gives us finally the relation that links the spectrum with the time dependent intensity $I(t)$ and electron density $\rho(t)$:

$$\left. \begin{aligned} \omega(t) &= \omega_0 + \frac{n_0 k_0 z}{2\rho_c} \frac{\partial \rho(t)}{\partial t} - n_2 k_0 z \frac{\partial I(t)}{\partial t} \\ \text{where: } k_0 &= \frac{\omega_0}{c} \end{aligned} \right\} \Rightarrow \omega(t) = \omega_0 + \frac{n_0 \omega_0 z}{2c\rho_c} \frac{\partial \rho(t)}{\partial t} - \frac{n_2 \omega_0 z}{c} \frac{\partial I(t)}{\partial t} \quad (1.3-33)$$

On the RHS of Eq.(1.3-33), only the two partial derivatives in time are varying quantities, everything else is constant. This means that the new frequencies that are nonlinearly generated depend on these two derivatives. When intensity is increasing ($\partial_t I(t) > 0$) as in the leading part of the laser pulse, lower frequencies are generated (red shift). Likewise when intensity is decreasing ($\partial_t I(t) < 0$) as in the trailing part of the pulse, higher frequencies are generated (blue shift). The plasma contribution is working in a similar fashion. When the electron density is increasing ($\partial_t \rho(t) > 0$) the spectrum is blue shifted, while red shifted in the opposite case. Note

here that since electron recombination is on much longer time scale (ps) than the typical pulse duration of fs lasers pulses, the latter case is rarely observable with ultrashort pulses. This means that plasma will almost exclusively produce blue frequencies in femtosecond filaments.

1.3.5 Self-steepening

Self-steepening is the formation of a steep edge in the trailing part of an intense laser pulse due to nonlinear self-action effects in a medium with positive n_2 [32]. The edge is formed because the most intense part (peak) of the pulse is propagating at a smaller speed than the trailing part. This speed difference makes it possible for the trailing part to catch up to the rest of the pulse, resulting in the formation of the sharp edge. The effect of self-steepening on a pulse profile is shown in Fig 1-13.

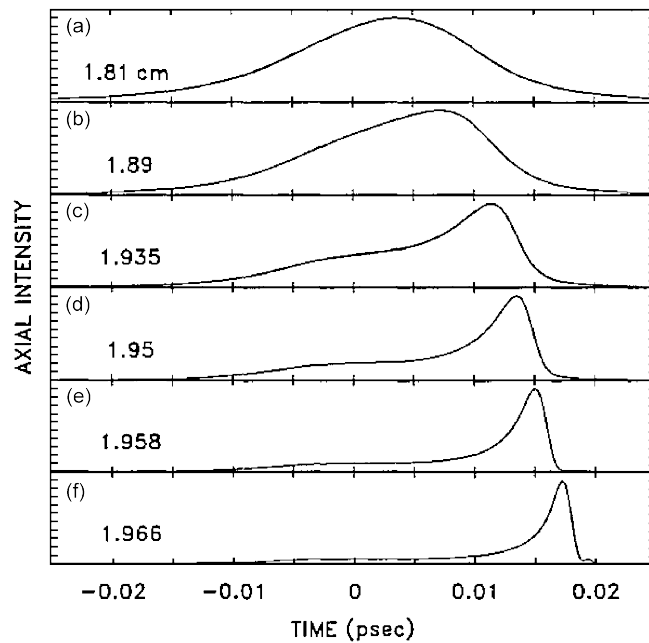


Fig 1-13 Numerical simulated pulse reshaping due to self-steepening taken from [33].

The origin behind this phenomenon is once again the intensity dependent refractive index $n(t) = n_0 + n_2 I(t)$, which is high at the intense parts (peak) and low at the less intense parts (tails). The difference in refractive index results in a difference in propagation speed according to:

$$v(t) = \frac{c}{n(t)} = \frac{c}{n_0 + n_2 I(t)} \quad (1.3-34)$$

By looking at Eq. (1.3-34) it becomes clear that in the nonlinear regime all different pulse slices with different intensities propagate at different speeds. This will lead to a form of pulse dispersion, which however is fundamentally different than the material chromatic dispersion analyzed in section 1.2.2.

The modification of the pulse shape will in turn lead to an increase of the generation of bluer frequencies [33] from SPM in the trailing part due to the term $\frac{\partial I(t)}{\partial t}$ in Eq. (1.3-33) becoming smaller. In addition the increase of the intensity in the trailing part of the pulse will lead to a local increase of self-focusing, eventually forcing asymmetric pulse splitting [34], [35] as it is shown in Fig 1-14.

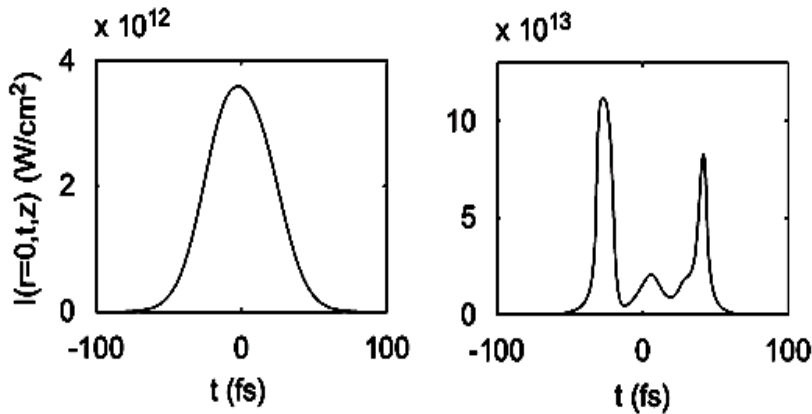


Fig 1-14 Numerical simulated pulse reshaping highlighting asymmetric pulse splitting, taken from [29].

1.3.6 Filamentation: an equilibrium of linear and nonlinear effects

The goal of this section is to give a qualitative understanding of the filamentation phenomenon.

Filamentation is the result of the dynamic equilibrium of numerous linear and nonlinear effects acting on intense ultrashort laser pulses when they propagate through transparent media. The effects that create and sustain filaments were described individually in sections 1.2 and 1.3.1-1.3.5, however their combination and interplay will be described in detail here:

Imagine an above critical power collimated laser pulse with a noise-free Gaussian spatiotemporal profile propagating in a transparent medium with positive n_2 . Initially only diffraction, dispersion and self-focusing are acting on the wavepacket, and given enough power the beam will start to self-focus. Self-focusing will lead to an increase of the intensity, which will in turn accelerate the self-focusing process further. As the pulse is propagating, self-steepening will reshape the pulse shape and Kerr SPM will generate new frequencies in the wake of the pulse. Close to the point of collapse the intensity of the pulse is high enough to ionize the medium through MPI and generate plasma arresting the collapse. MPA will locally drop the intensity, while plasma defocusing will defocus the trailing part of the pulse widening the beam. The plasma related SPM will generate additional frequencies, broadening the spectrum of the pulse even more. The length of this process depends on beam geometry and the material. At its end it leaves the wavepacket defocused in space and split in time. The energy that was contained in the initial wavepacket has been reduced due to multi-photon and plasma absorption, while the spectrum is significantly broader.

The above described nonlinear process will repeat itself if the wavepacket has enough power left to initiate a second self-focusing stage. In fact the process repeats itself multiple times, up to the point where the power carried by the wavepacket is not high enough to re-initiate a new self-focusing stage and linear effects will finally disperse the wavepacket. The light-material interactions of each refocusing cycle are depending on the output of the previous one, which makes the whole process very complex. The schematic representation of the refocusing cycles taking place in filamentation is shown in Fig 1-15.

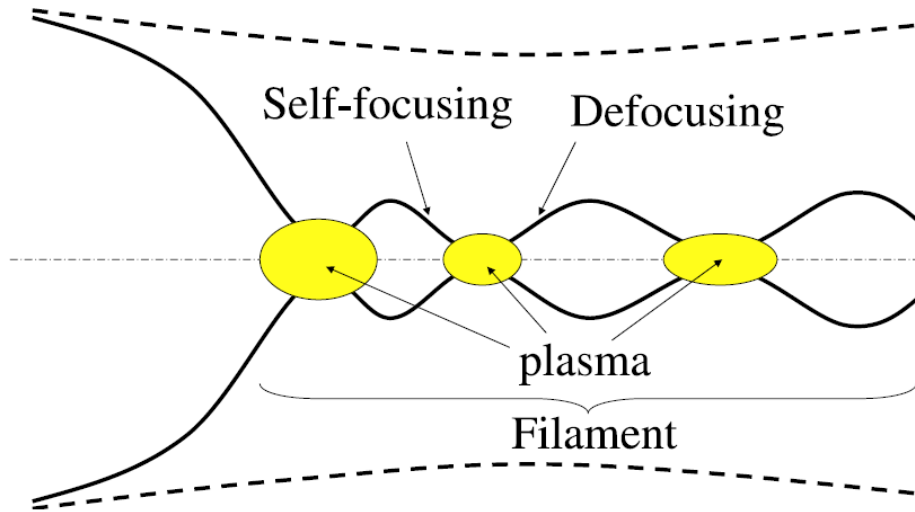


Fig 1-15 Schematic representation of refocusing cycles of an intense laser beam undergoing filamentation.

For detailed information on filamentation and the field of nonlinear pulse propagation consult the reviews found in [10], [36], [37].

1.4 Main attributes of femtosecond filaments

1.4.1 Robustness

Macroscopically filaments are very robust in the sense that they are very durable to perturbations. Once formed, filaments are able to regenerate themselves even after the central part has been blocked by an opaque object [38], [39], [40], [41], an ability called self-healing [39] or self-reconstruction [40] in the literature. The reason behind this peculiar behavior is the energy reservoir that surrounds the intense core of the beam, which is constantly feeding energy to the center [42]. The demonstration of self-reconstruction of a filament in water can be seen in Fig 1-16.

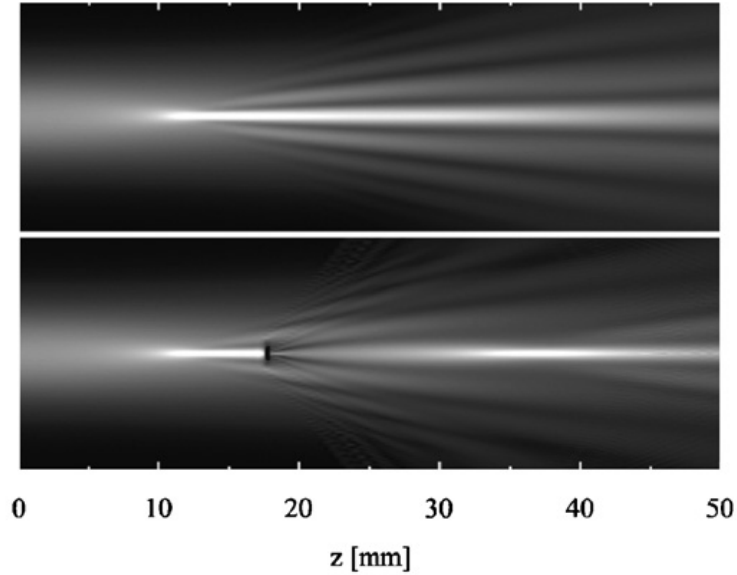


Fig 1-16 Numerical results for (top) free and (bottom) blocked at $z = 18$ mm filament propagation in water. Self-reconstruction takes place at $z = 35$ mm. Taken from [40].

1.4.2 Long range propagation

As already mentioned, high power laser pulses can undergo multiple refocusing cycles until they finally disperse. Given enough power, filaments can stretch out over extremely long distances, even reaching several km in the atmosphere [43], [44], [45]. Over this range, the filament diameter remains very narrow (about $\sim 100 \mu\text{m}$ in air), while intensity is sufficiently high to generate extremely long plasma channels. An experimental demonstration of the long range propagation of filaments can be seen in Fig 1-17.

This very impressive phenomenon is possible because of the relatively low energy losses that occur in the atmosphere with fs pulses, since inverse Bremsstrahlung and MPA is relatively limited.

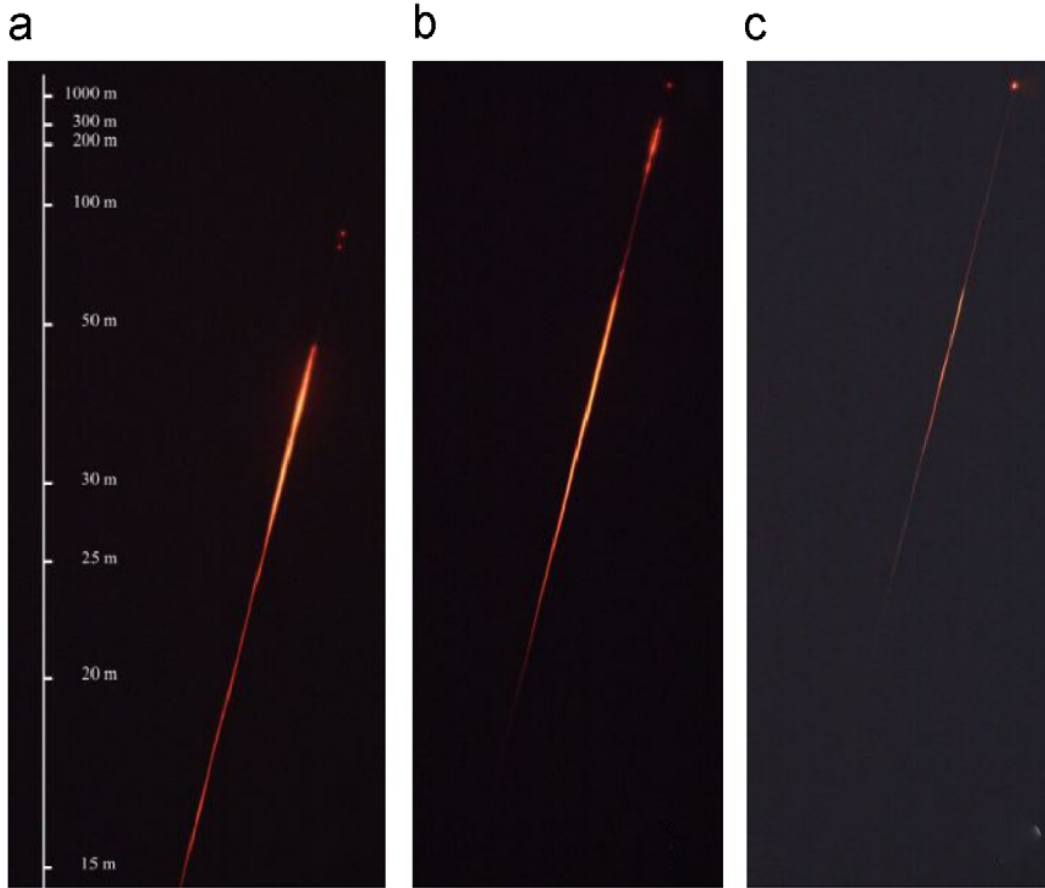


Fig 1-17 Long range propagation of light filaments in the atmosphere for different laser pulses. (a) 100 fs, (b) 1 ps, and (c) 2 ps. Taken from [45].

1.4.3 Intensity clamping

Close to the position of collapse, filamentation is mainly driven by the competition of self-focusing and MPA. Self-focusing will tend to increase the intensity while on the other hand; MPA will work towards the opposite direction, depleting the pulse energy and decreasing the intensity. As already mentioned, MPA will always dominate over self-focusing over certain intensity values because it is a higher order nonlinear process. Once the intensity is increased above this threshold value, MPA will rapidly deplete the pulse energy and intensity will drop. This threshold value is called the intensity clamping value, given by [46], [47], [48]:

$$n_2 I = \frac{\rho(I)}{2\rho_c} \quad (1.3-35)$$

If the propagation is taking place in air we can estimate the electron density of the plasma to be about:

$$\rho(I) \sim \sigma_K I^K \rho_{at} t_p \quad (1.3-36)$$

where ρ_{at} is the density of neutral atoms and σ_K is the ionization cross section for K photons. By substitution we obtain the clamping value of the intensity:

$$I \sim \left(\frac{2n_2\rho_c}{\sigma_K t_p \rho_{at}} \right)^{1/(K-1)} \quad (1.3-37)$$

Typically for an 800 nm laser pulse with 100 fs duration propagating in air the clamping intensity is about $I \sim 2 \times 10^{13} \text{ W/cm}^2$. Intensity clamping was demonstrated through numerical simulation in [46], as shown in Fig 1-18.

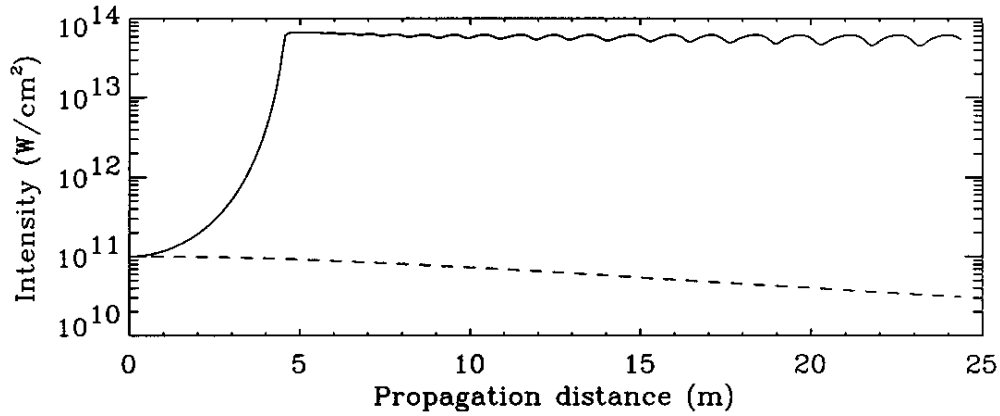


Fig 1-18 Peak intensity of a simulated filament in air, demonstrating intensity clamping. Taken from [46].

1.4.4 Modulation instability and multiple filamentation

In section 1.3.6 we assumed that the initial wavepacket was noise-free. However this is hardly the case in real life laser sources, since beam inhomogeneities are always present. These inhomogeneities will evolve into separate filament cores under the effect of self-focusing, given that the total beam power is high enough [49]. In the multi-filamentation regime each individual filament carries approximately one critical power, while the intensity remains clamped along propagation. The number of individual filaments is slightly less than the number of critical power contained in the whole wavepacket.

Once the nonlinear losses deplete the power of an individual filament, it will disperse restoring energy to the extended energy reservoir which surrounds the whole beam. The change in the intensity distribution of the energy reservoir will lead to the generation of new filaments in a seemingly random fashion. As the beam propagates in space, nonlinear losses will eventually deplete the pulse energy and the number of individual filaments will decrease. The multi-filamentation pattern of a 100 fs laser pulse is shown in Fig 1-19 after propagation of (a) 50 m, and (b) 600 m in air.

The spatial control of multi-filamentation is possible through a number of different approaches, like air turbulence [42], the insertion of a mesh into the beam [50], induced beam astigmatism [51], initial beam ellipticity [52], or amplitude masks [53].

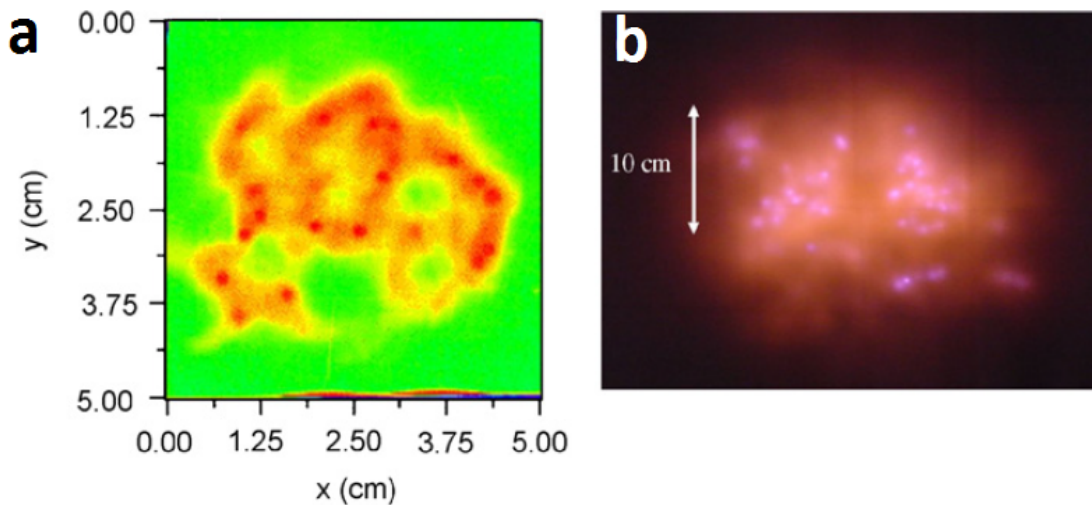


Fig 1-19 Multiple filamentation pattern after (a) 50 m, and (b) 600 m propagation. Taken from [54].

It is evident that the theoretical study of the propagation of pulses in the multi-filamentation regime cannot be done with radially symmetric models. All three spatial dimensions plus time must be taken into account in order to properly describe the dynamics.

1.4.5 Spectral broadening - White light generation

Spectral broadening is commonly observed in laser pulses undergoing filamentation. The new frequency components are mainly generated through self-steepening [32], [55], and SPM associated with Kerr and plasma as it was described in detail in section 1.3.4. As we can see in Eq. (1.3-32) the generated frequencies depend on the partial derivatives of the temporal shapes of the pulse and the generated plasma in respect to time $\left(\frac{\partial I(t)}{\partial t}, \frac{\partial \rho(t)}{\partial t}\right)$. As already mentioned, both longer and shorter wavelengths will be generated by SPM. In case a near infrared input laser pulse is used (like 800 nm), the newly generated frequencies will span over the whole visual region and even reach UV wavelengths, as can be seen in Fig 1-20. They will thus appear as white light to the human eye, which is why the phenomenon is called white light supercontinuum generation. The conversion rate of the narrow bandwidth spectrum into white light is strongly dependent on the numerical aperture (NA) of the setup, given by [56]:

$$NA = \frac{w_0/2}{f} n \quad (1.3-38)$$

The stronger the focusing (higher NA) the more white light is generated.

White light supercontinuum generation is observed in most transparent nonlinear materials, like in gases, liquids [57], and transparent solids [58]. However since most condensed materials have relatively low transmittance at the extreme ends of the spectrum, experimentally measuring the spectral broadening accurately is problematic.

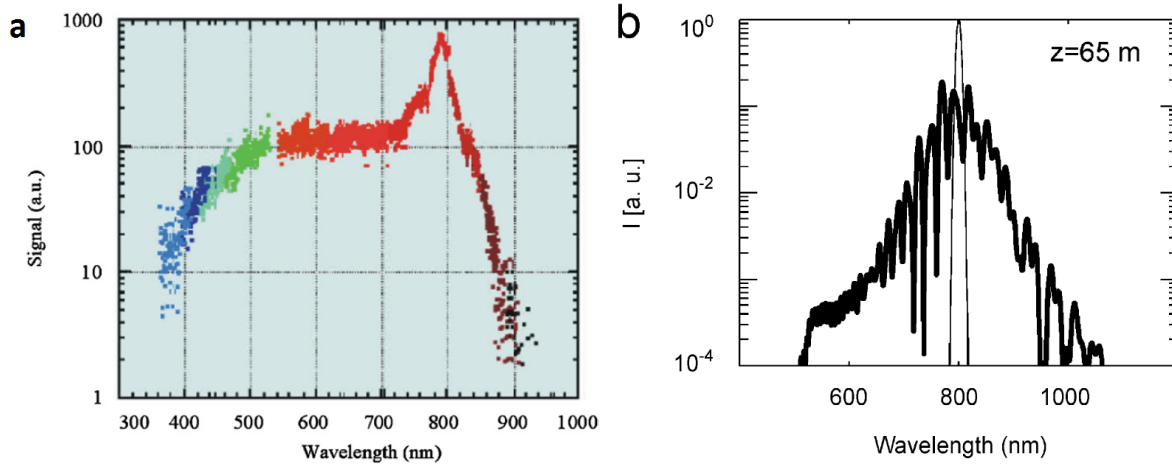


Fig 1-20 (a) Experimentally measured spectral broadening of a 3 TW 70 fs laser pulse with central wavelength of 800 nm after the propagation of 10 m in air. The drop between 800 to 900 nm corresponds to the fall of the detectivity of the measuring apparatus. Taken from [59]. (b) Simulated spectral broadening of a 100 fs, 800 nm pulse with 3 mJ energy after propagation of 65 m in air. Taken from [10].

1.4.6 Conical emission

The white light generated in laser filaments is mostly located on-axis. This white spot is surrounded by conical emission in the form of multicolored rings, as can be seen in Fig 1-21. The radial order of the colored rings is inverse of the one we would expect from pure diffraction, with red frequencies located closer to the center and bluer ones on the outer part.

The last two decades several mechanisms have been proposed to explain the conical emission associated with laser filaments, like Cerenkov radiation [60], [61], SPM [62], [63], four-wave mixing [64], [65], and nonlinear X-waves [66], [67], [68]. For more details on conical waves consult the text book by D. Faccio *et al.* [69].

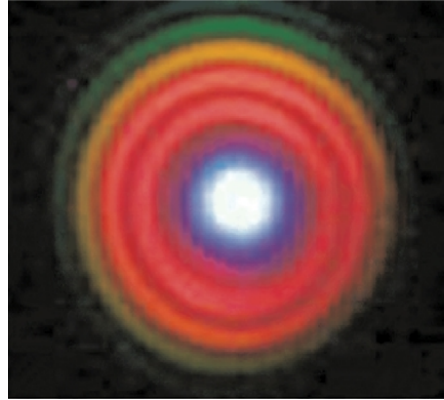


Fig 1-21 Conical emission of a 5 mJ, 45 fs, 800 nm laser pulse after 25 m of propagation in air. Taken from [70].

1.4.7 Pulse self-compression

As already mentioned the nonlinear effects taking place during femtosecond laser filamentation are strongly reshaping the wavepacket. It is possible, by carefully tuning the focusing conditions and material parameters (pressure, temperature, etc), to shorten the initial laser pulse close to the single-cycle limit [71], [72]. The numerical study of the spatiotemporal dynamics that are reshaping a wavepacket during filamentation in argon gas was investigated in [73], and is shown in Fig 1-22.

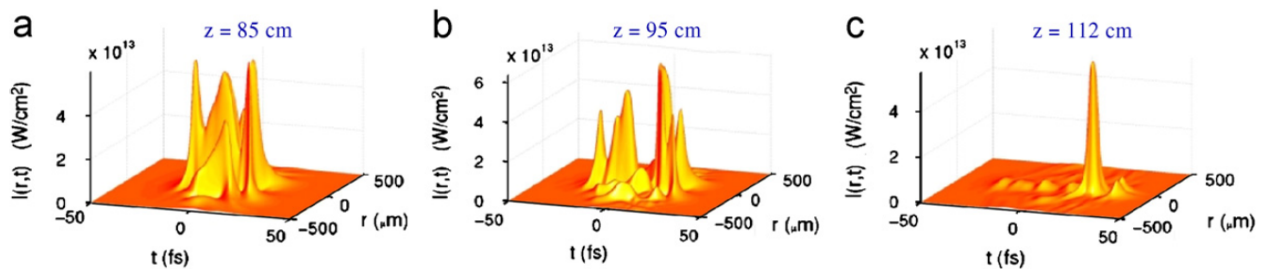


Fig 1-22 Pulse reshaping of 25 fs , 800 nm laser pulse carrying 1.1 mJ energy from filamentation in argon at various propagation distances. Taken from [73].

Approaches like filamentation in anomalous dispersion [74], and pressure gradients in noble gases [75] have also been proposed. In addition, it is possible to flatten the spectral phase of the supercontinuum through dispersion compensation to reach even shorter pulse durations. A very impressive demonstration of this technique was able to reach 5.7 fs carrier-envelope phase-locked pulses carrying 0.38 mJ energy [76]. The setup used in [76] is shown in Fig 1-23. It utilizes two successive gas tanks filled with argon for the supercontinuum generation and chirped mirrors to synchronize the spectral components.

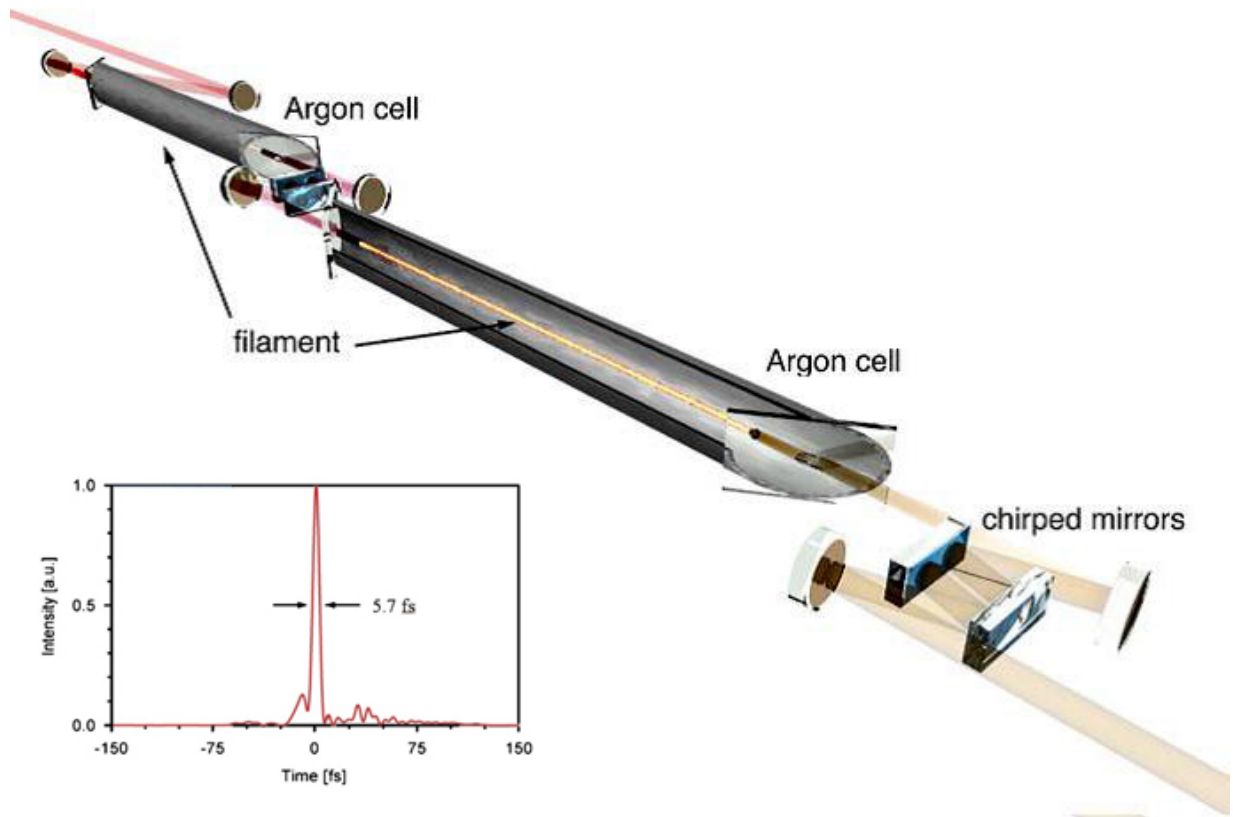


Fig 1-23 Experimental setup of [76] containing two low pressure argon gas cells and a set of chirped mirrors for dispersion compensation. The pulse is compressed from 43 fs down to 5.7 fs while containing 0.38 mJ of energy (inset).

The self-compressed laser pulses from femtosecond filamentation can be used as driving lasers sources for attosecond XUV pulse generation through high-harmonic generation [77], [76], [78].

1.4.8 THz radiation generation

The plasma channels generated in femtosecond filamentation can act as sources for THz radiation [79]. The generation of THz radiation is especially strong in the case of 2-color filamentation setups [80], in which the fundamental and the second harmonics (generated by a frequency doubling crystal) are focused collinearly in order to generate a plasma channel in air or other gas. The typical 2-color filamentation setup used for THz generation is schematically shown in Fig 1-24.

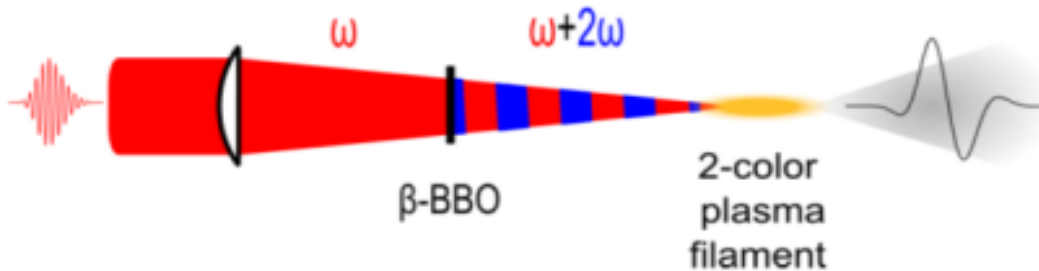


Fig 1-24 Schematic representation of a 2-color filament setup used for THz radiation generation.

The discovery of this phenomenon is very important since the ways to generate intense THz radiation with tabletop setups are extremely limited. On the other hand the high demand on intense THz sources in multiple research fields like chemical biology [81], genetic analysis [82], non-destructive imaging [83], and materials science (metamaterials) [84], has made THz generation one of the most active field in nonlinear optics [85].

Furthermore the emitted THz radiation can be tailored by the control of the filament itself and the plasma channel left in its wake. Such approaches are for instance: the elongation of the plasma channel through concatenation [86], and the tailoring of the plasma string geometry with the help of an axicon [87].

1.5 Applications

1.5.1 White light LIDAR

The robustness and long range propagation [44] of filaments are making them excellent tools for the study of remote targets high in the atmosphere with remote ranging and sensing [88], [89]. In white light detection and ranging (white light LIDAR), the white light generated from filaments is used to perform atmospheric diagnostics by measuring the atmospheric absorption spectrum at various altitudes, giving information about air pollution, aerosols, and the concentration of gaseous and solid particles [90]. The altitude at which the filament is generated is controlled by a negative chirp in the initial laser pulse.

Filament based LIDAR techniques have many advantages when compared to conventional LIDAR systems. Filament based LIDAR gives a much stronger signal and is therefore able to operate over longer distances [91]. In addition by utilizing the broad spectrum of filaments, single-shot multi-species measurements are possible. In comparison, classical monochromatic LIDAR systems must scan over an extended frequency range in order to obtain similar results. A schematic representation of white light LIDAR setup is shown in Fig 1-25.

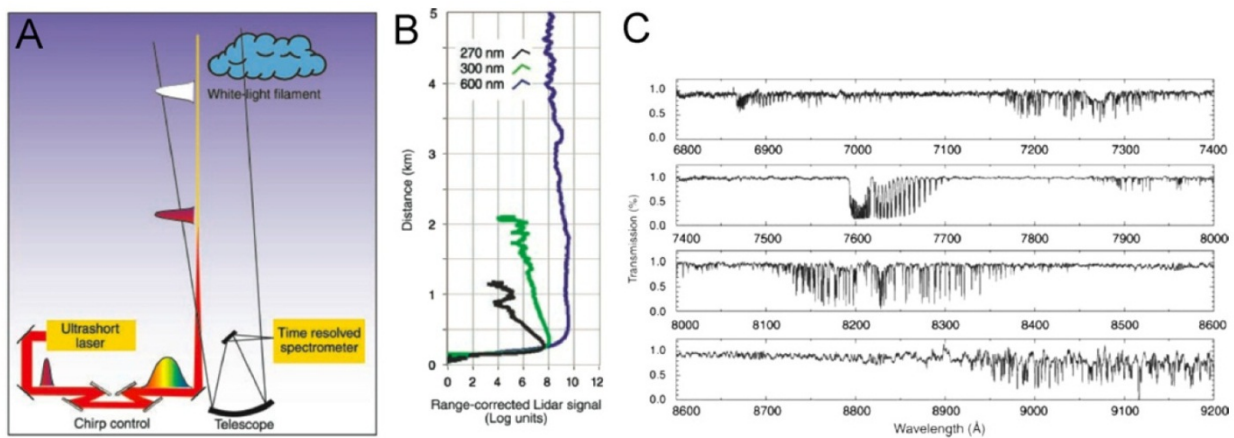


Fig 1-25 (A) Graphical representation of a white light LIDAR system. (B) Vertical white light LIDAR at three different wavelengths. (C) Atmospheric absorption spectrum measured at 4.5 km altitude. From [89].

In addition, filament based LIDAR techniques can be applied in meteorology and cloud microphysics. Cloud characteristics, like droplet size and density, and meteorological values like temperature and humidity, can be measured at various altitudes [92]. In [93] femtosecond laser-induced nonlinear spectroscopy was used for the remote sensing of methane gas. The condensation of supersaturated water vapor in the presence of filamentation generated plasma was demonstrated in [89].

1.5.2 Remote LIBS

In Laser Induced Breakdown Spectroscopy (LIBS) an intense beam is used to ablate the surface of an object and produce a plasma plume. The spectral analysis of the plasma gives information about the composition of the ablated material. The technique has proved to be very successful in the quantitative and qualitative detection of elements in paintings, glasses and generally materials with unknown chemical composition.

In remote LIBS an intense filament is used to create the plasma plume on the surface of the sample. The main advantage of this technique is that the distance between the setup and the sample can be much longer than in classical tabletop LIBS systems, even reaching a distance of 90 m [94], [95], [96]. The large working distance of remote LIBS has been proven to be of great importance for the mapping of large monuments [97].

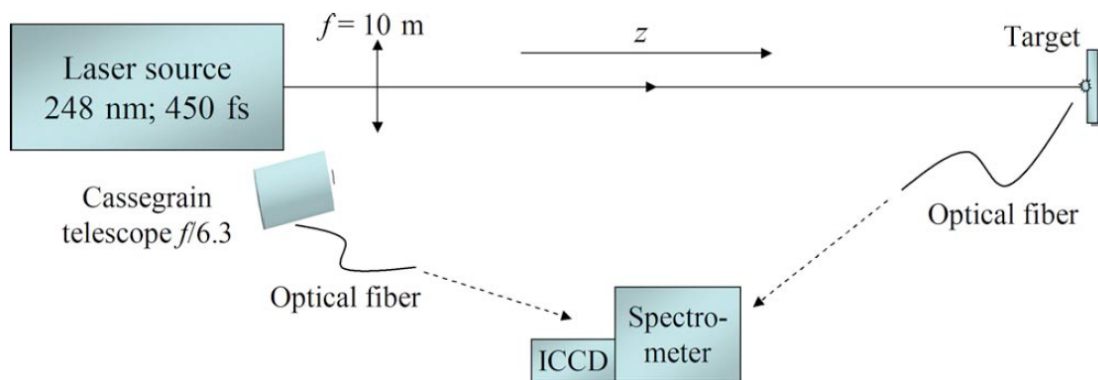


Fig 1-26 Schematic representation of the remote LIBS setup, taken from [97].

1.5.3 Electric discharge triggering and guiding

Since filaments generate an extended plasma channel along propagation, they can be used in order to trigger and,-or guide electric discharges, as can be seen in Fig 1-27.

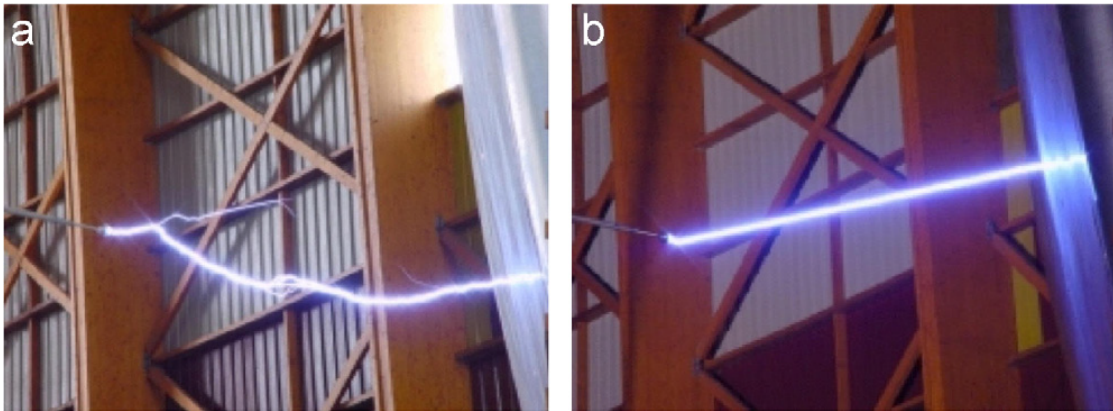


Fig 1-27 Experimental demonstration of the electric discharge guiding with filamentation. Taken from [98].

An impressive application of a this principle is the laser induced lightning rod, which was proposed in [99], [100], [101], [98]. An artistic view of the possible lightning triggering and guiding schemes is shown in Fig 1-28.

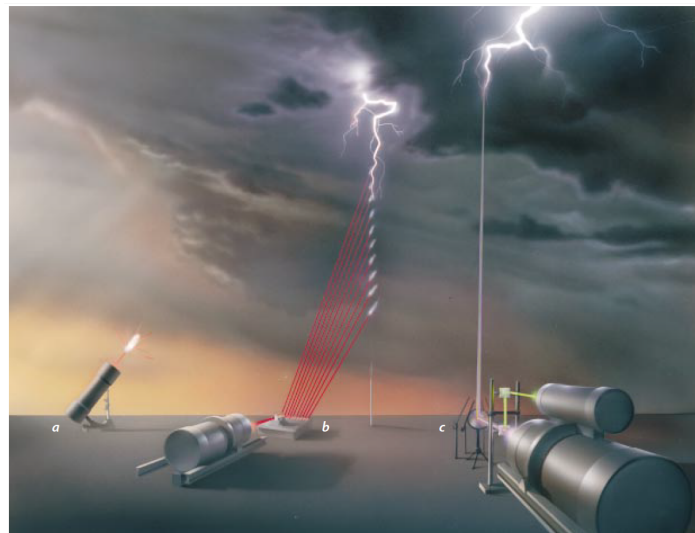


Fig 1-28 Artistic view of possible lightning triggering and guiding techniques. Taken from [102].

1.5.4 Nano-fabrication

Filaments are used for the fabrication of miniature structures inside the bulk of glasses [103]. The damage suffered by the dielectric can be exploited to produce waveguides [104], [105], [106], transmission gratings [107], [108], and even 3D optical storage devices [109]. By controlling the intensity and beam size it is possible to induce a permanent refractive index modulation in the bulk of glasses while at the same time avoiding structural damage (like cracks). The waveguides that are produced this way are of very high quality [108], [110], as can be seen in Fig 1-29.

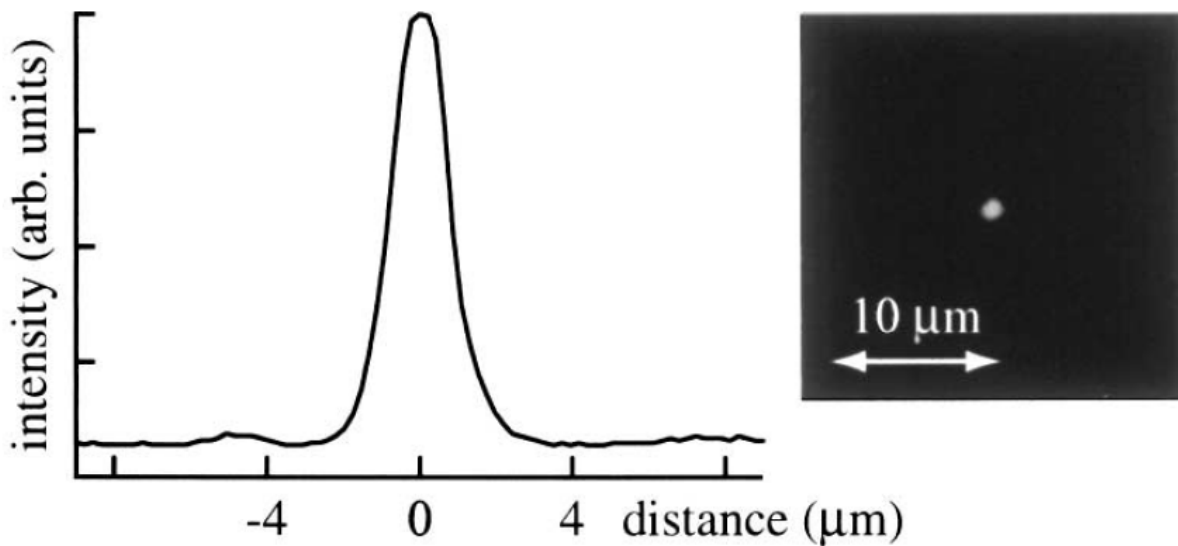


Fig 1-29 Left: waveguide output profile at 633 nm inside the bulk of fused silica glass. Right: near field. Taken from [110].

An interesting phenomenon is observed when high numerical apertures are used to focus the fs laser pulses inside the bulk of fused silica glass. Under the right conditions, the formation of periodic nanostructures is observed [111], [112], also called nanogratings. The nanogratings arrangement in space depends on the writing electric field polarization, as can be seen in Fig 1-30.

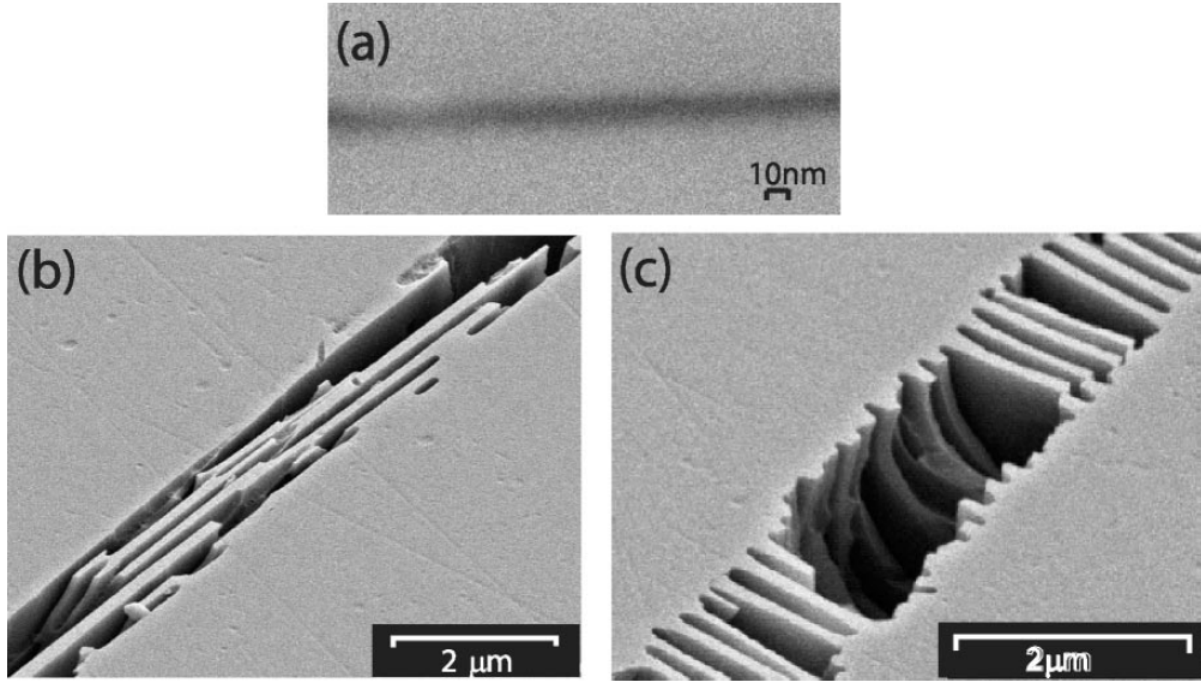


Fig 1-30 Scanning electron microscope images of chemically etched laser-modified regions. (a) High resolution image of a weakly etched structure. (b) and (c) are arrayed nanostructures written with $E \perp S$ and $E \parallel S$, respectively, after extensive etching. Taken from [112].

1.6 Uncontrollable attributes of filaments

Even though many different approaches have been proposed to control the attributes of filaments, the degree of control obtained by those techniques is quite limited. Thus filamentation still remains an essentially self-regulated process. The major problem all attempts have to consider is the extreme intensity of filaments which makes the use of conventional optical elements like lenses and prisms impossible. In addition the filament size is on the micrometer scale, which makes any attempt of controlling them even more difficult. The varying attributes of femtosecond filaments are presented in this section.

1.6.1 Beam waist - Peak intensity and plasma channel uniformity

Although the spatial characteristics of a filament are generally on the micrometer scale, they cannot be characterized as uniform or homogeneous. As already mentioned in section 1.3.6, after the first nonlinear focus the filament diameter will increase mainly due to MPA and plasma defocusing, while at the same time the peak intensity and plasma density will drop. In more complex cases however, multiple refocusing cycles will constantly reshape the spatial shape of and consequently the intensity and generated plasma will greatly vary along propagation. This can be clearly seen in Fig 1-31, where the beam waist, peak intensity, plasma density and fluence of two laser pulses (UV and IR) are plotted along propagation in logarithmic scale.

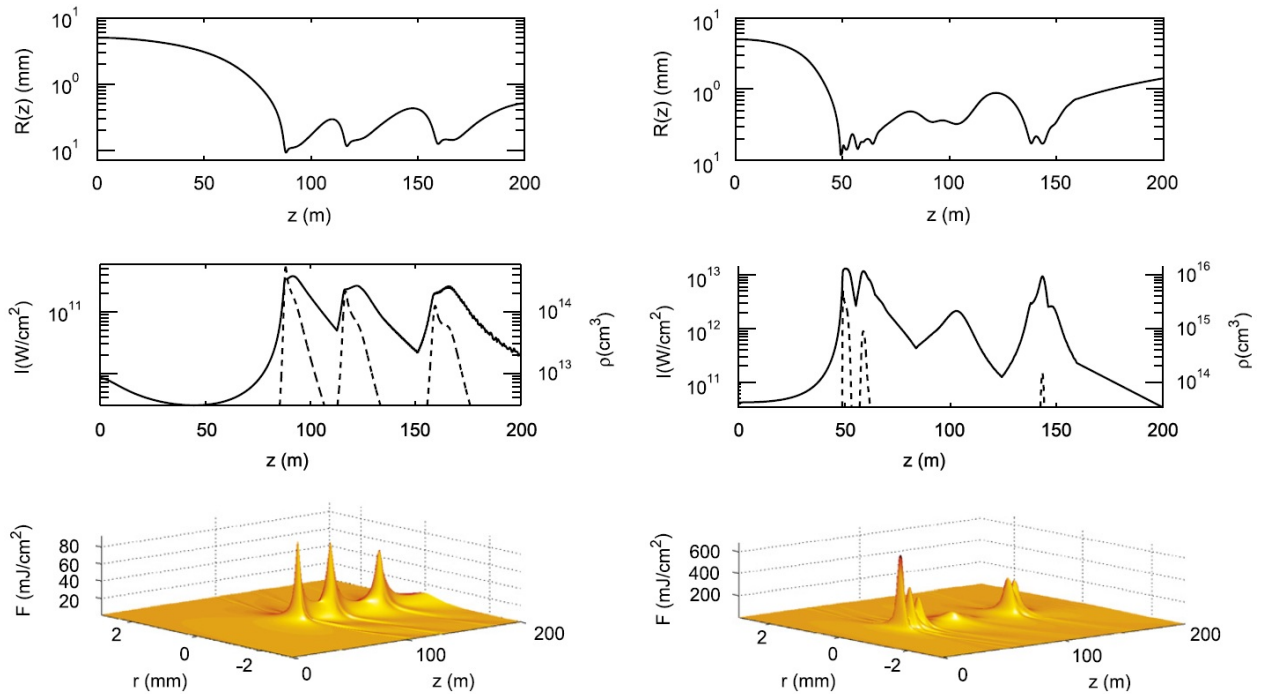


Fig 1-31 Spatial reshaping of collimated laser beams in air. Left: UV laser pulse with $\lambda = 248$ nm, 100 fs duration, and 1 mJ total energy. Right: IR laser pulse with $\lambda = 800$ nm, 100 fs duration, and 3 mJ total energy. First line: Beams waist at FWHM along z . Second line: Peak intensity (left axis) and electron density (right axis) along z . Third line: Fluence distribution along z . Taken from [113].

In the multi-filamentation regime the dynamics are even more complex, since new filaments are constantly forming and dispersing at different positions in space. The control of these spatial characteristics is very difficult, and is still regarded as an open challenge today.

1.6.2 Pulse shape and spectrum

The temporal shape (and the corresponding spectrum) of a laser pulse undergoing filamentation is constantly being reshaped, mainly due to Kerr and plasma related SPM. The pulse profile is undergoing multiple asymmetric splitting during subsequent refocusing cycles. The spatiotemporal reshaping of the IR laser pulse used in the right column of Fig 1-31 can be seen in Fig 1-32.

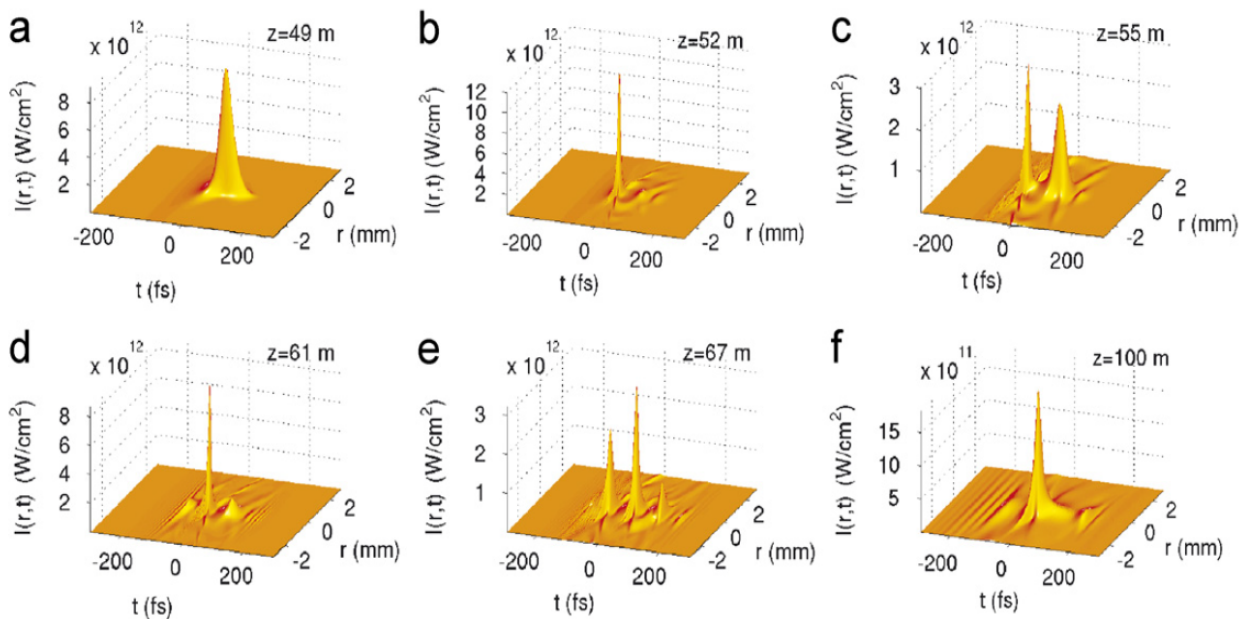


Fig 1-32 Evolution of the temporal profile of the pulse during the nonlinear propagation of the same IR pulse as in Fig 1-31. The initial pulse (a) undergoes contraction in the transverse diffraction plane (b) plasma defocusing of its trailing part (c) which is subsequently refocused by the optical Kerr effect (apparent splitting beyond the nonlinear focus) (d,e,f) During the propagation in the form of a filament, successive focusing–defocusing cycles reinforce and accentuate the shortening and the stiffening of the pulse beyond the nonlinear focus. From [113].

The control of the temporal shape of pulses in undergoing filamentation is mostly limited to dispersion compensation, since the temporal dynamics of the filamentation process are completely self-regulated.

1.6.3 Nonlinear losses

The most complex nonlinear processes are found in the multi-filamentation regime. Although the position of individual filaments can be controlled reasonably well [43], [114], as shown in Fig 1-33, many open problems remain unsolved.

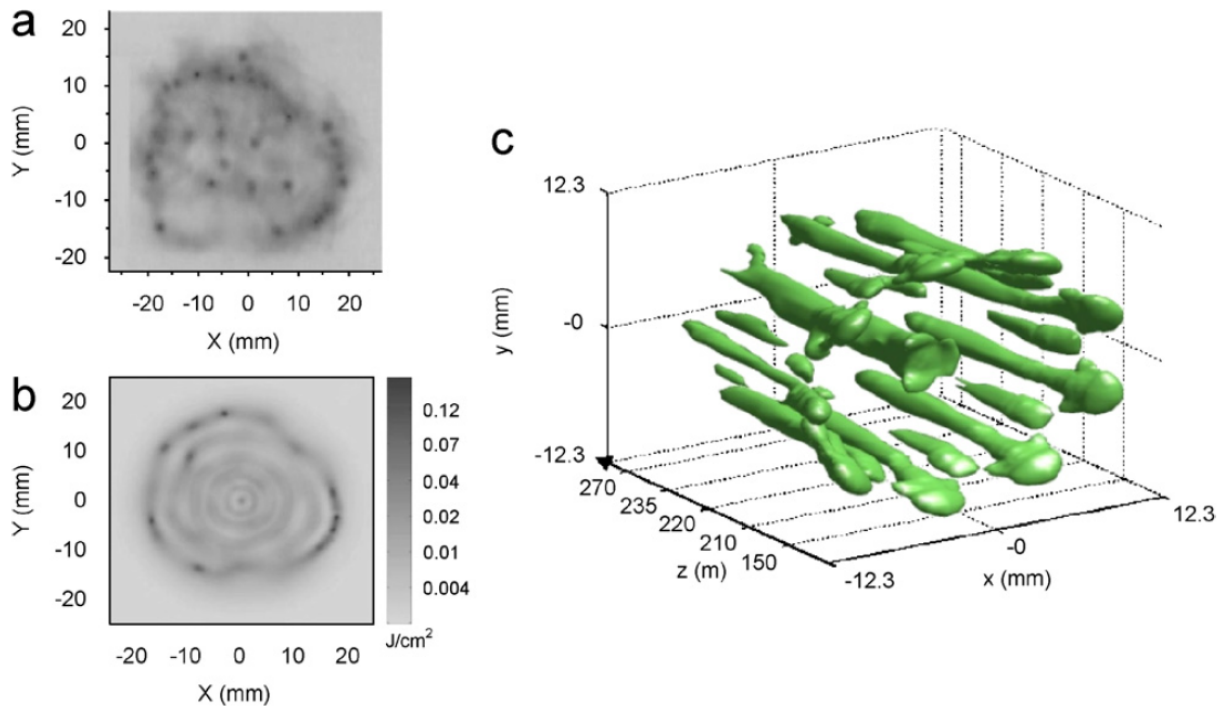


Fig 1-33 Spatial control of multiple filaments. (a) and (b): Comparison between the multiple filamentation patterns obtained in (a) experiments and (b) (3+1)D simulations after propagation over 68 m of a 190 mJ, 800 nm laser pulse stretched to 1.2 ps by a negative chirp. (c) Multiple filaments predicted by (3+1)D simulations. The iso-surfaces for the fluence distribution are shown for a 150 mJ, chirped 500 fs, 800 nm input pulse whose initial beam includes azimuthal perturbations of order 10. Taken from [43], [114].

In the multi-filamentation regime, the high intensity of individual filaments is generating multiple plasma stings in the medium through MPI. This way the energy of the initial laser pulse is rapidly depleted, making lossless long range energy transfer very difficult. Since filamentation is mainly driven by the competition of self-focusing and MPA, high nonlinear losses can only be avoided by maintaining the filament intensity below the MPI threshold. This would demand the presence of a different intensity saturating mechanism than MPA, which must be able to stop the collapse of the beam before ionization sets in. At relatively low input powers various approaches were proposed utilizing materials with anomalous higher order dispersion [115], competing higher order nonlinearities [116], and materials with saturating nonlinearities from the photorefractive effect of electro-optic materials [117]. However the lossless long range propagation of extremely high power laser pulses in gases, fibers, or liquids still remains an open challenge up to this day.

1.7 Thesis outline

The study of nonlinear propagation of ultrashort laser pulses in the filamentation regime has been extensively studied in the last decades. However many questions about the interplay of physical effects and their interaction with the material still remain unanswered. The numerous linear and nonlinear effects that are driving femtosecond filaments are constantly competing with each other as the wavepacket propagates. This competition is resulting in a dynamic equilibrium that is very difficult to predict and control.

Over the years many different approaches have been proposed to harness filaments and control their attributes, mostly by controlling the shape of the initial wavepacket and the properties of the propagation medium. These approaches include the spatial control of the initial beam shape, optimizing the focusing geometry, negative or positive chirp, or the propagation in controlled dispersion materials. However, controlling a filament (spatially or temporally) once it is formed is still an open challenge.

It is clear that the control of the attributes of femtosecond filaments is of fundamental importance in the field of nonlinear optics. Not only will it have a big impact on research topics

utilizing filaments (like attosecond pulse generation, and THz generation), but also benefit numerous practical applications (see section 1.5). Filamentation tailoring, which is the main axis of this thesis, consist of the selective control of specific filament attributes (like peak intensity, pulse shape and generated plasma) in order to optimize their use in research and practical applications. Two different approaches are explored in chapters 3 and 4 utilizing periodic lattices and nondiffracting beams.

Chapter 2 starts with the analytic derivation of the extended nonlinear Schrodinger equation from the Maxwell equations, which describes the propagation of the envelope of the electric field along z . The temporal evolution of the electron plasma due to MPI, avalanche ionization and recombination is taken into account and introduced into the model. The second part of the chapter explains in detail the numerical scheme that is solving the mathematical model. The numerical code described will be used for the majority of the numerical simulations throughout this thesis. The third part of the chapter presents the results of numerical simulations using the described model. Starting from simple linear effects like diffraction and dispersion, one by one additional effects are added in order to give the reader a qualitative and quantitative understanding of each mechanism and its effect on the propagation of the laser pulse.

In Chapter 3 filamentation tailoring using periodic photonic lattices is studied. The chapter is starting with an overview of previous attempts of filamentation control. The spatial control of a single filament using a cylindrical symmetric plasma lattice in air is presented. Next the transition from the moderate power soliton regime to the high power filament regime is explained and analyzed. In addition to the spatial control, the temporal control of the wavepacket by the same cylindrical lattice is shown to lead to the formation of a nonlinear dynamic light bullet in air. Multiple different approaches that target the increase of power of the tailored filament both in the single and multi-filamentation regime are numerically explored. These approaches utilize multiple lattice geometries (square, polygon, elliptical etc) and materials (air, water, fused silica glass). In addition to numerical simulations, two lab experiments were carried out in BK7 glass and water, where a permanent lattice with elliptical waveguides and a Bessel-like plasma lattice are used to tailor the filaments.

Chapter 4 is approaching filamentation tailoring through the use of non-diffracting beams. The first part of the chapter is about filamentation tailoring using Bessel beams. First the generation of a stationary UV Bessel filament in air is presented. Next the nonlinear X-wave is

introduced and the generation of a linear X-wave by cross-phase modulation through the use of a second pump pulse is reported. The second part of the chapter is studying the nonlinear propagation of Airy beams. First an overview of the linear exotic characteristics of Airy beams is given, and the main techniques used for their generation are depicted. A complete numerical study of the nonlinear propagation dynamics of 2D airy beams in air is presented. In addition, experiments in water are compared with matching simulations to verify the results. For one spatial dimension, a stationary nonlinear Airy beam solution is found in the presence of high nonlinear losses. Finally a radial variation of the Airy beam, which is a member of a family of autofocusing waves that was recently discovered, is studied in the nonlinear regime. Numerical studies in air reveal that the focus position and peak intensity of nonlinear autofocusing waves is driven by very different mechanics than the ones found in Gaussian filaments.

2. Nonlinear wave propagation equation and its solution

2.1 The nonlinear propagation equation

The nonlinear propagation of ultrashort laser pulses in transparent materials is modeled using an extended nonlinear Schrödinger equation, which describes the evolution of the slowly varying electric field envelope \mathcal{E} along z :

$$K \frac{\partial \mathcal{E}}{\partial z} = \frac{i}{2} \left[\nabla_{\perp}^2 \mathcal{E} + D \mathcal{E} \right] + k_0 \left[T^2 N_{Kerr}(\mathcal{E}) + T N_{NLL}(\mathcal{E}) + N_{Plasma}(\mathcal{E}, \rho) \right] \quad (2.1-1)$$

Eq.(2.1-1) takes into account both linear (first term on the RHS) and nonlinear effects (second term on the RHS) that are acting on the electric field envelope \mathcal{E} . $\nabla_{\perp}^2 = \Delta_{\perp} = \frac{\partial^2}{\partial x^2} + \frac{\partial^2}{\partial y^2}$ is the transverse Laplacian operator which is used to model diffraction, while D is the dispersive operator used to model the material chromatic dispersion. The operators $K = k_0 + ik_0' \frac{\partial}{\partial t}$, and $T = 1 + i\omega_0^{-1} \frac{\partial}{\partial t}$ account for space-time focusing and self-steepening of the laser pulse. The nonlinear source terms N_{Kerr} , N_{NLL} , N_{Plasma} on the RHS of Eq.(2.1-1) are associated with the optical Kerr effect, nonlinear losses from MPA and plasma related effects like plasma defocusing and absorption. They are given by:

$$N_{Kerr}(\mathcal{E}) = i \frac{\omega_0}{c} n_2 \left((1-a) |\mathcal{E}|^2 + a \int_{-\infty}^t R(t-\tau) |\mathcal{E}|^2 d\tau \right) \mathcal{E} \quad (2.1-2)$$

$$N_{NLL} = -\frac{\beta_K}{2} \left[1 - \frac{\rho}{\rho_{at}} \right] |\mathcal{E}|^{2K-2} \mathcal{E} \quad (2.1-3)$$

$$N_{Plasma}(\mathcal{E}, \rho) = -\frac{\sigma}{2}(1 + i\omega\tau_c)\rho\mathcal{E} \quad (2.1-4)$$

The optical Kerr effect described by Eq.(2.1-2) consists out of an instantaneous and a delayed component with fraction alpha. The instantaneous part is associated with the electronic response of the medium and is described by the term $i\frac{\omega_0}{c}n_2(1-a)|\mathcal{E}|^2\mathcal{E}$, while the delayed component associated with stimulated molecular Raman scattering can be written as $i\frac{\omega_0}{c}n_2a\int_{-\infty}^t R(t-\tau)|\mathcal{E}|^2 d\tau\mathcal{E}$. $R(t)$ is the function describing the delayed molecular response:

$$R(t) = R_0 \exp[-\Gamma t] \sin(\omega_R t) \quad (2.1-5)$$

where Γ and ω_R are the characteristic time and frequency of the molecular response. Eq.(2.1-2) can be re-written for instantaneous material response only ($a = 0$) in the form:

$$N_{Kerr}(\mathcal{E}) = i\frac{\omega_0}{c}n_2|\mathcal{E}|^2\mathcal{E} \quad (2.1-6)$$

The nonlinear losses term of Eq.(2.1-3) describes the losses to the field envelope due to MPA of order K.

The plasma contribution term described by Eq.(2.1-4) consists of an imaginary part describing plasma defocusing and a real part describing plasma absorption.

Eq.(2.1-1) is coupled with an electron evolution equation in order to follow the evolution of the generated plasma in time:

$$\frac{\partial\rho}{\partial t} = \sigma_K |\mathcal{E}|^{2K} (\rho_{at} - \rho) + \frac{\sigma}{U_i} \rho |\mathcal{E}|^2 - a_{rec}\rho^2 \quad (2.1-7)$$

Eq.(2.1-7) is taking into account MPI (first term on the RHS) with rate $W_{MPI} = \sigma_K I^K$, and avalanche ionization (second term on the RHS). The last term of the RHS accounts for the

electron to ion recombination with coefficient $a_{rec} = \frac{1}{\tau_{rec}}$. Since recombination time τ_{rec} is much longer than the typical femtosecond laser pulse duration, the last term of Eq.(2.1-7) can safely be neglected in most cases (gases).

The analytic derivation of the mathematical model will be shown in the next section.

2.1.1 Analytic derivation from the Maxwell equations

In this section the derivation of the nonlinear propagation equation will be analytically shown. The basic six steps are the following:

1. Starting from Maxwell's equations in a non-magnetic medium, the nonlinear wave equation is derived.
2. The material polarization is separated into linear (dispersion) and nonlinear parts (optical Kerr effect).
3. Next the wave equation will be re-written using the field envelope, along with both material polarization and current density terms.
4. The dispersive coefficient is calculated through a Taylor expansion of the wavenumber in the spectral domain.
5. Finally the evolution equation for the electric field envelope is derived by rewriting the nonlinear wave equation in the moving reference frame of the laser pulse.
6. The nonlinear source terms are calculated from the nonlinear polarization and current density.

In this process multiple approximations will be made, which are standard in the field of femtosecond filamentation optics.

Step#1: Derivation of the nonlinear wave equation from Maxwell's

Maxwell's equations in differential form for transverse electromagnetic waves can be written in SI units as shown below:

$$\nabla \vec{D} = \rho \quad (2.1-8)$$

$$\nabla \vec{B} = 0 \quad (2.1-9)$$

$$\nabla \times \vec{E} = -\frac{\partial \vec{B}}{\partial t} \quad (2.1-10)$$

$$\nabla \times \vec{H} = \vec{J} + \frac{\partial \vec{D}}{\partial t} \quad (2.1-11)$$

and:

$$\vec{D} = \epsilon_0 \vec{E} + \vec{P} \quad (2.1-12)$$

$$\vec{B} = \mu_0 \vec{H} + \vec{M} \quad (2.1-13)$$

Where:

\vec{E} : electric field

\vec{D} : electric displacement

\vec{P} : electric polarization

\vec{J} : current density

ϵ_0 : permittivity of vacuum

\vec{B} : magnetic field

\vec{H} : magnetic field strength

\vec{M} : magnetization

ρ : charge density

μ_0 : permeability of vacuum

For a non-magnetic material: $\vec{M} = 0 \Rightarrow \vec{H} = \frac{\vec{B}}{\mu_0}$, and Eq.(2.1-11) can now be written as:

$$\nabla \times \vec{H} = \nabla \times \frac{\vec{B}}{\mu_0} = \vec{J} + \frac{\partial \vec{D}}{\partial t} \Rightarrow \nabla \times \vec{B} = \mu_0 \vec{J} + \mu_0 \frac{\partial \vec{D}}{\partial t} \quad (2.1-14)$$

We will start from Eq.(2.1-10):

$$\begin{aligned}
\nabla \times \vec{E} &= -\frac{\partial \vec{B}}{\partial t} \xrightarrow{\nabla \times} \nabla \times \nabla \times \vec{E} = \nabla \times \left(-\frac{\partial \vec{B}}{\partial t} \right) \\
\Rightarrow \nabla \times \nabla \times \vec{E} &= -\frac{\partial}{\partial t} (\nabla \times \vec{B}) \xrightarrow{(2.1-14)} \nabla \times \nabla \times \vec{E} = -\frac{\partial}{\partial t} \left(\mu_0 \vec{J} + \mu_0 \frac{\partial \vec{D}}{\partial t} \right) \\
\Rightarrow \nabla \times \nabla \times \vec{E} &= -\frac{\partial}{\partial t} (\mu_0 \vec{J}) - \frac{\partial}{\partial t} \left(\mu_0 \frac{\partial \vec{D}}{\partial t} \right) = -\mu_0 \frac{\partial \vec{J}}{\partial t} - \mu_0 \frac{\partial^2 \vec{D}}{\partial t^2} \left. \vphantom{\frac{\partial}{\partial t}} \right\} \Rightarrow \\
&\quad \text{for: } \frac{\partial}{\partial t} = \partial_t \text{ and } \frac{\partial^2}{\partial t^2} = \partial_t^2 \\
\nabla \times \nabla \times \vec{E} &= -\mu_0 \partial_t \vec{J} - \mu_0 \partial_t^2 \vec{D} \\
\xrightarrow{(2.1-12)} \nabla \times \nabla \times \vec{E} &= -\mu_0 \partial_t \vec{J} - \mu_0 \partial_t^2 (\varepsilon_0 \vec{E} + \vec{P}) \\
\Rightarrow \nabla \times \nabla \times \vec{E} &= -\mu_0 \partial_t \vec{J} - \mu_0 \varepsilon_0 \partial_t^2 \vec{E} - \mu_0 \partial_t^2 \vec{P} \\
\Rightarrow \nabla \times \nabla \times \vec{E} &= -\mu_0 \partial_t \vec{J} - \mu_0 \varepsilon_0 \partial_t^2 \vec{E} - \mu_0 \partial_t^2 \vec{P} \tag{2.1-15}
\end{aligned}$$

From basic vector calculus we know that:

$$\nabla \times \nabla \times \vec{E} = \nabla (\nabla \cdot \vec{E}) - \nabla^2 \vec{E} \tag{2.1-16}$$

Also by definition:

$$\mu_0 \varepsilon_0 = \frac{1}{c^2} \tag{2.1-17}$$

By substituting Eq.(2.1-16) and Eq.(2.1-17) in Eq(2.1-15). we get:

$$\begin{aligned}
\nabla (\nabla \cdot \vec{E}) - \nabla^2 \vec{E} &= -\mu_0 \partial_t \vec{J} - \frac{1}{c^2} \partial_t^2 \vec{E} - \mu_0 \partial_t^2 \vec{P} \\
\Rightarrow \nabla^2 \vec{E} - \nabla (\nabla \cdot \vec{E}) - \frac{1}{c^2} \partial_t^2 \vec{E} &= \mu_0 (\partial_t^2 \vec{P} + \partial_t \vec{J}) \tag{2.1-18}
\end{aligned}$$

Step#2: Separating linear and nonlinear polarization

The polarization vector \vec{P} can be written as:

$$\vec{P} = \vec{P}_{linear} + \vec{P}_{nonlinear} \quad (2.1-19)$$

This way the nonlinear polarization is separated from the linear response of the medium, which can be later combined with the electric field to form the linear electric displacement:

$$\vec{D}_{linear} = \epsilon_0 \vec{E} + \vec{P}_{linear} \quad (2.1-20)$$

By substituting Eq.(2.1-19) in Eq.(2.1-18) we have:

$$\begin{aligned} \nabla^2 \vec{E} - \nabla(\nabla \cdot \vec{E}) - \frac{1}{c^2} \partial_t^2 \vec{E} &= \mu_0 \left[\partial_t^2 (\vec{P}_{linear} + \vec{P}_{nonlinear}) + \partial_t \vec{J} \right] \\ \nabla^2 \vec{E} - \nabla(\nabla \cdot \vec{E}) - \frac{1}{c^2} \partial_t^2 \vec{E} &= \mu_0 \partial_t^2 \vec{P}_{linear} + \mu_0 \left[\partial_t^2 \vec{P}_{nonlinear} + \partial_t \vec{J} \right] \\ \nabla^2 \vec{E} - \nabla(\nabla \cdot \vec{E}) - \frac{1}{c^2} \partial_t^2 \left(\vec{E} + \frac{\vec{P}_{linear}}{\epsilon_0} \right) &= \mu_0 \left[\partial_t^2 \vec{P}_{nonlinear} + \partial_t \vec{J} \right] \end{aligned} \quad (2.1-21)$$

We assume that the electric field remains linearly polarized, transverse to the propagation direction. This way the term $\nabla(\nabla \cdot \vec{E})$ can be neglected and Eq. (2.1-21) can now be written in scalar form, simplifying calculations:

$$\nabla^2 E - \frac{1}{c^2} \partial_t^2 \left(E + \frac{P_{linear}}{\epsilon_0} \right) = \mu_0 \left[\partial_t^2 P_{nonlinear} + \partial_t J \right] \quad (2.1-22)$$

We are taking in account dispersion, which means that the linear polarization P_{linear} is given by [13]:

$$P(r,t)_{linear} = \varepsilon_0 \int_{-\infty}^t \chi^{(1)}(t-t') E(r,t',z) dt' \quad (2.1-23)$$

where:

$$\varepsilon(t) = 1 + \chi^{(1)}(t) \quad (2.1-24)$$

is the instantaneous dielectric constant of the material, which can be written in the frequency domain using the Fourier transform:

$$\varepsilon(\omega) = 1 + \hat{\chi}_{(\omega)}^{(1)} \quad (2.1-25)$$

where $\hat{\chi}_{(\omega)}^{(1)}$ is the Fourier transform of the first order susceptibility of the medium in the frequency domain. The Fourier transform of a function $f(t)$ is defined by:

$$\hat{f}(\omega) = \int_{-\infty}^{+\infty} f(t) e^{-i\omega t} dt \quad (2.1-26)$$

The frequency dependent dielectric constant of Eq.(2.1-25) is complex in general. Its real and imaginary parts represent the linear refractive index $n(\omega)$ and absorption coefficient $\alpha(\omega)$, which are both frequency dependent and are given by the relations:

$$\varepsilon = \left(\frac{n + i\alpha}{2\omega} \right)^2 \Rightarrow \left\{ \begin{array}{l} n(\omega) = 1 + \text{Re} \left\{ \hat{\chi}_{(\omega)}^{(1)} \right\} \\ \alpha(\omega) = \frac{\omega}{nc} \text{Im} \left\{ \hat{\chi}_{(\omega)}^{(1)} \right\} \end{array} \right\} \quad (2.1-27)$$

By substituting Eq.(2.1-23) in Eq.(2.1-22) we get:

$$\nabla^2 E(r, t, z) - \frac{1}{c^2} \partial_t^2 \left(E(r, t, z) + \frac{\varepsilon_0 \int_{-\infty}^t \chi_{(t-t')}^{(1)} E(r, t', z) dt'}{\varepsilon_0} \right) = \mu_0 [\partial_t^2 P_{nonlinear} + \partial_t J] \quad (2.1-28)$$

but because

$$E(r, t, z) = \int_{-\infty}^{+\infty} \delta(t-t') E(r, t', z) dt' \quad (2.1-29)$$

we can write:

$$\nabla^2 E(r, t, z) - \frac{1}{c^2} \partial_t^2 \left(\int_{-\infty}^t \delta(t-t') E(r, t', z) dt' + \frac{\varepsilon_0 \int_{-\infty}^t \chi_{(t-t')}^{(1)} E(r, t', z) dt'}{\varepsilon_0} \right) = \mu_0 [\partial_t^2 P_{nonlinear} + \partial_t J] \Rightarrow$$

$$\nabla^2 E(r, t, z) - \frac{1}{c^2} \partial_t^2 \left(\int_{-\infty}^t (\delta(t-t') + \chi_{(t-t')}^{(1)}) E(r, t', z) dt' \right) = \mu_0 [\partial_t^2 P_{nonlinear} + \partial_t J] \quad (2.1-30)$$

By substituting Eq.(2.1-24) in Eq.(2.1-30) we can write:

$$\nabla^2 E(r, t, z) - \frac{1}{c^2} \partial_t^2 \int_{-\infty}^t \varepsilon(t-t') E(r, t', z) dt' = \mu_0 [\partial_t^2 P_{nonlinear} + \partial_t J] \quad (2.1-31)$$

We assume here that the absorption coefficient is small compared to the refractive index, thus $\varepsilon \approx n^2$, and we can write:

$$\nabla^2 E(r, t, z) - \frac{1}{c^2} \partial_t^2 \int_{-\infty}^t n_{(t-t')}^2 E(r, t', z) dt' = \mu_0 [\partial_t^2 P_{nonlinear} + \partial_t J] \quad (2.1-32)$$

and since:

$$\left. \begin{aligned} \nabla^2 E(r, t, z) &= \left(\frac{\partial^2}{\partial x^2} + \frac{\partial^2}{\partial y^2} + \frac{\partial^2}{\partial z^2} \right) \cdot E(r, t, z) \\ \frac{\partial^2}{\partial x^2} + \frac{\partial^2}{\partial y^2} &= \nabla_{\perp}^2 \\ r &= \sqrt{x^2 + y^2} \end{aligned} \right\} (\nabla_{\perp}^2 + \partial_z^2) E(r, t, z)$$

we can write Eq.(2.1-32) in the form:

$$\boxed{(\nabla_{\perp}^2 + \partial_z^2) E(r, t, z) - \frac{1}{c^2} \partial_t^2 \int_{-\infty}^t n_{(t-t')}^2 E(r, t', z) dt' = \mu_0 [\partial_t^2 P_{\text{nonlinear}} + \partial_t J]} \quad (2.1-33)$$

Step#3: Re-writing of the wave equation using the electric field envelope

We will now rewrite the electric field using the envelope and carrier wave:

$$E(r, t, z) = \frac{1}{2} \mathcal{E}(r, t, z) e^{i(k_0 z - \omega_0 t)} + c.c. \quad (2.1-34)$$

Now it is time to apply the envelope decomposition on all terms of Eq.(2.1-33). First we calculate the partial derivatives with respect to the propagation coordinate “z”:

$$\bullet \nabla_{\perp}^2 E = \nabla_{\perp}^2 \mathcal{E} e^{i(k_0 z - \omega_0 t)} \quad (2.1-35)$$

$$\begin{aligned}
\bullet \quad \partial_z^2 E &= \partial_z^2 \left[\mathcal{E} e^{i(k_0 z - \omega_0 t)} \right] = \partial_z \left[\partial_z \left(\mathcal{E} e^{i(k_0 z - \omega_0 t)} \right) \right] = \partial_z \left[\partial_z (\mathcal{E}) \cdot e^{i(k_0 z - \omega_0 t)} + \mathcal{E} \partial_z \left(e^{i(k_0 z - \omega_0 t)} \right) \right] \\
\Rightarrow \partial_z^2 E &= \partial_z \left[\partial_z \mathcal{E} e^{i(k_0 z - \omega_0 t)} + ik_0 \mathcal{E} e^{i(k_0 z - \omega_0 t)} \right] \\
\Rightarrow \partial_z^2 E &= \partial_z \left(\partial_z \mathcal{E} e^{i(k_0 z - \omega_0 t)} \right) + \partial_z \left(ik_0 \mathcal{E} e^{i(k_0 z - \omega_0 t)} \right) \\
\Rightarrow \partial_z^2 E &= \partial_z \left(\partial_z \mathcal{E} \right) \cdot e^{i(k_0 z - \omega_0 t)} + \partial_z \mathcal{E} \partial_z \left(e^{i(k_0 z - \omega_0 t)} \right) + ik_0 \partial_z (\mathcal{E}) \cdot e^{i(k_0 z - \omega_0 t)} + ik_0 \mathcal{E} \partial_z \left(e^{i(k_0 z - \omega_0 t)} \right) \\
\Rightarrow \partial_z^2 E &= e^{i(k_0 z - \omega_0 t)} \partial_z^2 \mathcal{E} + ik_0 e^{i(k_0 z - \omega_0 t)} \partial_z \mathcal{E} + ik_0 e^{i(k_0 z - \omega_0 t)} \partial_z \mathcal{E} + (ik_0)^2 \mathcal{E} e^{i(k_0 z - \omega_0 t)} \\
&\Rightarrow \partial_z^2 E = \left(\partial_z^2 + 2ik_0 \partial_z - k_0^2 \right) \mathcal{E} e^{i(k_0 z - \omega_0 t)} \tag{2.1-36}
\end{aligned}$$

We assume that the nonlinear terms of Eq.(2.1-33) follow the envelope of the electric field, and are given from the relations:

$$P_{nonlinear} = P_{nl}^{env} \cdot e^{i(k_0 z - \omega_0 t)} \tag{2.1-37}$$

$$J = J^{env} \cdot e^{i(k_0 z - \omega_0 t)} \tag{2.1-38}$$

By applying the envelope in the same way we calculate the partial derivatives in respect to the time coordinate “t”:

$$\begin{aligned}
\bullet \quad \partial_t^2 P_{nonlinear} &= \partial_t^2 \left[P_{nl}^{env} \cdot e^{i(k_0 z - \omega_0 t)} \right] = \partial_t \left[\partial_t \left(P_{nl}^{env} \cdot e^{i(k_0 z - \omega_0 t)} \right) \right] \\
\Rightarrow \partial_t^2 P_{nonlinear} &= \partial_t \left[\partial_t \left(P_{nl}^{env} \right) \cdot e^{i(k_0 z - \omega_0 t)} + P_{nl}^{env} \partial_t \left(e^{i(k_0 z - \omega_0 t)} \right) \right] \\
\Rightarrow \partial_t^2 P_{nonlinear} &= \partial_t \left[\partial_t P_{nl}^{env} e^{i(k_0 z - \omega_0 t)} + (-i\omega_0) P_{nl}^{env} e^{i(k_0 z - \omega_0 t)} \right] \\
\Rightarrow \partial_t^2 P_{nonlinear} &= \partial_t \left(\partial_t P_{nl}^{env} e^{i(k_0 z - \omega_0 t)} \right) + \partial_t \left((-i\omega_0) P_{nl}^{env} e^{i(k_0 z - \omega_0 t)} \right) \\
&\Rightarrow \partial_t^2 P_{nonlinear} = \partial_t \left(\partial_t P_{nl}^{env} \right) e^{i(k_0 z - \omega_0 t)} + \partial_t P_{nl}^{env} \partial_t \left(e^{i(k_0 z - \omega_0 t)} \right) \\
&\quad + (-i\omega_0) \partial_t \left(P_{nl}^{env} \right) e^{i(k_0 z - \omega_0 t)} + (-i\omega_0) P_{nl}^{env} \partial_t \left(e^{i(k_0 z - \omega_0 t)} \right)
\end{aligned}$$

$$\begin{aligned}
\Rightarrow \partial_t^2 P_{\text{nonlinear}} &= e^{i(k_0 z - \omega_0 t)} \partial_t^2 P_{nl}^{env} + (-i\omega_0) e^{i(k_0 z - \omega_0 t)} \partial_t P_{nl}^{env} \\
&\quad + (-i\omega_0) e^{i(k_0 z - \omega_0 t)} \partial_t P_{nl}^{env} + (-i\omega_0)^2 e^{i(k_0 z - \omega_0 t)} P_{nl}^{env} \\
\Rightarrow \partial_t^2 P_{\text{nonlinear}} &= e^{i(k_0 z - \omega_0 t)} \partial_t^2 P_{nl}^{env} - i\omega_0 e^{i(k_0 z - \omega_0 t)} \partial_t P_{nl}^{env} - i\omega_0 e^{i(k_0 z - \omega_0 t)} \partial_t P_{nl}^{env} - \omega_0^2 e^{i(k_0 z - \omega_0 t)} P_{nl}^{env} \\
\Rightarrow \partial_t^2 P_{\text{nonlinear}} &= \left[\frac{\partial_t^2}{\omega_0^2} - \frac{2i\partial_t}{\omega_0} - 1 \right] P_{nl}^{env} \omega_0^2 e^{i(k_0 z - \omega_0 t)} = -\omega_0^2 e^{i(k_0 z - \omega_0 t)} \left[i^2 \frac{\partial_t^2}{\omega_0^2} + 2i \frac{\partial_t}{\omega_0} + 1^2 \right] P_{nl}^{env} \\
&\Rightarrow \partial_t^2 P_{\text{nonlinear}} = -\omega_0^2 e^{i(k_0 z - \omega_0 t)} \left[1 + \frac{i}{\omega_0} \partial_t \right]^2 P_{nl}^{env} \tag{2.1-39}
\end{aligned}$$

And in the same way:

$$\begin{aligned}
\bullet \partial_t J &= \partial_t \left[J^{env} \cdot e^{i(k_0 z - \omega_0 t)} \right] = \partial_t (J^{env}) \cdot e^{i(k_0 z - \omega_0 t)} + J^{env} \cdot \partial_t (e^{i(k_0 z - \omega_0 t)}) \\
\Rightarrow \partial_t J &= e^{i(k_0 z - \omega_0 t)} \partial_t J^{env} - i\omega_0 e^{i(k_0 z - \omega_0 t)} J^{env} \\
\partial_t J &= -i\omega_0 e^{i(k_0 z - \omega_0 t)} J^{env} \left[1 + \frac{i}{\omega_0} \partial_t \right] \tag{2.1-40}
\end{aligned}$$

Let

$$T = \left[1 + \frac{i}{\omega_0} \partial_t \right] \tag{2.1-41}$$

denotes the operator responsible for self – steepening and optical shock formation. Then we can rewrite Eq.(2.1-39) and Eq.(2.1-40) in the form:

$$\partial_t^2 P_{\text{nonlinear}} = -\omega_0^2 T^2 e^{i(k_0 z - \omega_0 t)} P_{nl}^{env} \tag{2.1-42}$$

$$\partial_t J = -i\omega_0 T e^{i(k_0 z - \omega_0 t)} J^{env} \tag{2.1-43}$$

Step#4: Calculation of the dispersive coefficient

Next, the integral term on the LHS of Eq.(2.1-33) will be Fourier transformed with respect to the time coordinate, as defined by Eq.(2.1-26). Then the wavenumber $k(\omega)$ will be written as a Taylor expansion around the central frequency ω_0 , followed by an inverse Fourier transform which will bring us back to the time domain [13], [14], [12]. We represent the envelope $\mathcal{E}(r, t, z)$ in terms of the spectral content through its inverse Fourier transform:

$$\mathcal{E}(r, t, z) = \frac{1}{2\pi} \int_{-\infty}^{+\infty} \hat{\mathcal{E}}(r, \omega, z) e^{i\omega t} d\omega \quad (2.1-44)$$

Note that field and envelope can be related in the spectral domain with the relation (2.1-45) [12]:

$$\hat{E}_{(r, \omega, z)} \approx \hat{\mathcal{E}}(r, \omega - \omega_0, z) e^{ik_0 z} \quad (2.1-45)$$

The Fourier transform of the integral term reads:

$$FT \left\{ -\frac{1}{c^2} \partial_t^2 \int_{-\infty}^t n_{(t-t')}^2 \mathcal{E}(r, t', z) e^{i(k_0 z - \omega_0 t')} dt' \right\} = -\frac{1}{c^2} (i\omega_0)^2 n_{(\omega)}^2 \hat{\mathcal{E}}(r, \omega - \omega_0, z) e^{ik_0 z} \quad \left. \vphantom{FT} \right\} \Rightarrow$$

$$k_{(\omega)} = \frac{2\pi n(\omega)}{\lambda} = \frac{n(\omega) \omega_0}{c}$$

$$FT \left\{ -\frac{1}{c^2} \partial_t^2 \int_{-\infty}^t n_{(t-t')}^2 \mathcal{E}(r, t', z) e^{i(k_0 z - \omega_0 t')} dt' \right\} = k_{(\omega)}^2 \hat{\mathcal{E}}(r, \omega - \omega_0, z) e^{ik_0 z} \quad (2.1-46)$$

The Taylor expansion of $k(\omega)$ around ω_0 can be applied since $k(\omega)$ is an analytic function close to ω_0 (can be expressed by a convergent power series):

$$k(\omega) = k(\omega_0) + k'_{(\omega_0)} (\omega - \omega_0) + \frac{k''_{(\omega_0)} (\omega - \omega_0)^2}{2} + \frac{k'''_{(\omega_0)} (\omega - \omega_0)^3}{3!} + \dots$$

$$k(\omega) = \sum_{n=0}^{\infty} \frac{k_{(\omega_0)}^{(n)} (\omega - \omega_0)^n}{n!} \quad (2.1-47)$$

which for $k_0 = k(\omega_0)$, can simply be written:

$$k(\omega) = k_0 + k_0' (\omega - \omega_0) + \frac{k_0''}{2} (\omega - \omega_0)^2 + \frac{k_0'''}{3!} (\omega - \omega_0)^3 + \dots \quad (2.1-48)$$

where $k_0^{(n)} = k_{(\omega_0)}^{(n)} = \left. \frac{\partial^{(n)} k(\omega)}{\partial \omega^{(n)}} \right|_{\omega=\omega_0}$ denote the partial derivatives of the frequency dependent wavenumber with respect to ω . The physical meaning of these partial derivatives can be associated with the group velocity v_{group} for the central frequency ω_0 of the propagating wave and the group velocity dispersion, with dispersive coefficient of 2nd order and higher.

We will evaluate the term $k_{(\omega)}^2$ in Eq.(2.1-46) by using the Taylor expansion from Eq.(2.1-48). First we define:

$$\hat{K}(\omega) = k_0 + k_0' (\omega - \omega_0) \quad (2.1-49)$$

Then by using relations (2.1-49) and (2.1-48) we can write $k_{(\omega)}^2$:

$$k_{(\omega)}^2 = \left(\hat{K} + \sum_{n=2}^{\infty} \frac{k_0^{(n)} (\omega - \omega_0)^n}{n!} \right)^2 \Rightarrow$$

$$k_{(\omega)}^2 = \hat{K}^2 + 2\hat{K} \sum_{n=2}^{\infty} \frac{k_0^{(n)} (\omega - \omega_0)^n}{n!} + \left(\sum_{n=2}^{\infty} \frac{k_0^{(n)} (\omega - \omega_0)^n}{n!} \right)^2 \quad (2.1-50)$$

The last term of Eq.(2.1-50) can be neglected because its contribution is invariably small. In order to separate the dispersive from the non-dispersive terms, we define the dispersive operator D:

$$\hat{D}(\omega) = 2\hat{K} \sum_{n=2}^{\infty} \frac{k_0^{(n)} (\omega - \omega_0)^2}{n!} \quad (2.1-51)$$

so that

$$k_{(\omega)}^2 \approx \hat{K}^2 + \hat{D} \quad (2.1-52)$$

The full dispersive relation for the propagation equation is thus given by the term $\frac{\hat{D}}{2\hat{K}}$, which can be written as:

$$\frac{\hat{D}}{2\hat{K}} = \frac{k_{(\omega)}^2 - \hat{K}^2}{2\hat{K}} \quad (2.1-53)$$

By using Eqs.(2.1-48) and (2.1-49) we can easily evaluate Eq.(2.1-53):

$$\begin{aligned} \frac{k_{(\omega)}^2 - \hat{K}^2}{2\hat{K}} &= \frac{\frac{k_0''}{2}(\omega - \omega_0)^2 + \frac{k_0'''}{3!}(\omega - \omega_0)^3 + \dots + \left[2\hat{K} + \left(\frac{k_0''}{2}(\omega - \omega_0)^2 + \frac{k_0'''}{3!}(\omega - \omega_0)^3 + \dots \right) \right]}{2\hat{K}} \\ &\Rightarrow \frac{k_{(\omega)}^2 - \hat{K}^2}{2\hat{K}} \approx \frac{k_0''}{2}(\omega - \omega_0)^2 + \frac{k_0'''}{3!}(\omega - \omega_0)^3 + \dots \end{aligned}$$

The above simplification is valid if we assume that:

$$2\hat{K} \gg \sum_{n=2}^{\infty} \frac{k_0^{(n)} (\omega - \omega_0)^2}{n!} \quad (2.1-54)$$

By using Eq.(2.1-52) inside the Fourier transform of the integral term of Eq.(2.1-46) we obtain:

$$FT \left\{ -\frac{1}{c^2} \partial_t^2 \int_{-\infty}^t n_{(t-t')}^2 \mathcal{E}(r, t', z) e^{i(k_0 z - \omega_0 t')} dt' \right\} = (\hat{D} + \hat{K}^2) \hat{\mathcal{E}}(r, \omega - \omega_0, z) e^{ik_0 z} \quad (2.1-55)$$

By applying the inverse Fourier transform on Eq.(2.1-55) we return to the temporal domain. To do this we need to multiply by $e^{i(\omega - \omega_0)t}$ and integrate over all values of $\omega - \omega_0$. We finally obtain:

$$-\frac{1}{c^2} \partial_t^2 \int_{-\infty}^t n_{(t-t')}^2 \mathcal{E}(r, t', z) e^{i(k_0 z - \omega_0 t')} dt' = (K^2 + D) \mathcal{E}(r, t, z) e^{i(k_0 z - \omega_0 t)} \quad (2.1-56)$$

where D and K are now in the time domain. Here K is given by:

$$K = k_0 + ik_0' \partial t \quad (2.1-57)$$

while the operator D is accounting for all dispersive terms exactly computed by the Sellmeier dispersion relation. However D can be analytically expressed only in the frequency domain, as defined previously in Eq.(2.1-52):

$$\hat{D} \approx k_{(\omega)}^2 - \hat{K}^2 \quad (2.1-58)$$

In order to write the wave equation for the envelope, we now need to substitute all the terms we previously calculated in steps 3 and 4 into Eq.(2.1-33). These are: (2.1-35), (2.1-36), (2.1-42), (2.1-43) and (2.1-56):

$$\begin{aligned} \nabla_{\perp}^2 \mathcal{E} e^{i(k_0 z - \omega_0 t)} + (\partial_z^2 + 2ik_0 \partial_z - k_0^2) \mathcal{E} e^{i(k_0 z - \omega_0 t)} + (K^2 + D) \mathcal{E} e^{i(k_0 z - \omega_0 t)} \\ = \mu_0 \left[-\omega_0^2 T^2 e^{i(k_0 z - \omega_0 t)} P_{nl}^{env} - i\omega_0 T e^{i(k_0 z - \omega_0 t)} J^{env} \right] \Rightarrow \end{aligned}$$

$$\boxed{(\nabla_{\perp}^2 + \partial_z^2 + 2ik_0 \partial_z - k_0^2) \mathcal{E} + (K^2 + D) \mathcal{E} = -\mu_0 \left[\omega_0^2 T^2 P_{nl}^{env} + i\omega_0 T J^{env} \right]} \quad (2.1-59)$$

Eq.(2.1-59) is the spatiotemporal nonlinear wave equation in the time domain for the pulse envelope. It takes into account diffraction, dispersion, as well as the nonlinear polarization of the material and current density from nonlinear losses and plasma formation. Note that for simplicity sake the electric field envelope is written as $\mathcal{E}(r, t, z) = \mathcal{E}$.

Step#5: Re-writing the propagation equation in the reference frame of the pulse

In order to solve numerically the Eq.(2.1-59) we will now rewrite it in the reference frame of the pulse:

$$\tau = t - k_0' z, \quad \zeta = z \quad (2.1-60)$$

so that $\mathcal{E}(r, \zeta, \tau) = \mathcal{E}(r, z, t)$. The partial derivatives for the new variables are must of course be calculated by applying the chain rule of differentiation:

$$\begin{aligned} \bullet \quad \partial_z \mathcal{E}(r, z, t) &= \frac{\partial \mathcal{E}(r, z, t)}{\partial z} = \frac{\partial \mathcal{E}(r, \zeta, \tau)}{\partial \zeta} \frac{\partial \zeta}{\partial z} + \frac{\partial \mathcal{E}(r, \zeta, \tau)}{\partial \tau} \frac{\partial \tau}{\partial z} \\ \Rightarrow \partial_z \mathcal{E}(r, z, t) &= \frac{\partial \mathcal{E}(r, \zeta, \tau)}{\partial \zeta} \frac{\partial(z)}{\partial z} + \frac{\partial \mathcal{E}(r, \zeta, \tau)}{\partial \tau} \frac{\partial(t - k_0' z)}{\partial z} \\ \Rightarrow \partial_z \mathcal{E}(r, z, t) &= \frac{\partial \mathcal{E}(r, \zeta, \tau)}{\partial \zeta} \cdot 1 + \frac{\partial \mathcal{E}(r, \zeta, \tau)}{\partial \tau} \cdot (-k_0') \\ &\Rightarrow \partial_z \mathcal{E}(r, z, t) = (\partial_\zeta - k_0' \partial_\tau) \mathcal{E}(r, \zeta, \tau) \end{aligned} \quad (2.1-61)$$

$$\bullet \quad \partial_z^2 \mathcal{E}(r, z, t) = (\partial_\zeta - k_0' \partial_\tau)^2 \mathcal{E}(r, \zeta, \tau) \quad (2.1-62)$$

$$\begin{aligned} \bullet \quad \partial_t \mathcal{E}(r, z, t) &= \frac{\partial \mathcal{E}(r, z, t)}{\partial t} = \frac{\partial \mathcal{E}(r, \zeta, \tau)}{\partial \zeta} \frac{\partial \zeta}{\partial t} + \frac{\partial \mathcal{E}(r, \zeta, \tau)}{\partial \tau} \frac{\partial \tau}{\partial t} = \\ \Rightarrow \partial_t \mathcal{E}(r, z, t) &= \frac{\partial \mathcal{E}(r, \zeta, \tau)}{\partial \zeta} \frac{\partial(z)}{\partial t} + \frac{\partial \mathcal{E}(r, \zeta, \tau)}{\partial \tau} \frac{\partial \tau}{\partial t} \\ \Rightarrow \partial_t \mathcal{E}(r, z, t) &= \frac{\partial \mathcal{E}(r, \zeta, \tau)}{\partial \zeta} \cdot 0 + \frac{\partial \mathcal{E}(r, \zeta, \tau)}{\partial \tau} \cdot 1 \\ &\Rightarrow \partial_t \mathcal{E}(r, z, t) = \partial_\tau \mathcal{E}(r, \zeta, \tau) \end{aligned} \quad (2.1-63)$$

$$\bullet \partial_t^2 \mathcal{E}(r, z, t) = \partial_\tau^2 \mathcal{E}(r, \zeta, \tau) \quad (2.1-64)$$

By substituting Eqs.(2.1-61), (2.1-62) and (2.1-63) in Eq.(2.1-59) we get:

$$\begin{aligned} & \left(\nabla_\perp^2 + \partial_\zeta^2 - 2ik_0' \partial_\tau \partial_\zeta + k_0'^2 \partial_\tau^2 + 2ik_0 \partial_\zeta - 2k_0 k_0'^2 \partial_\tau - k_0^2 \right) \mathcal{E} \\ & + (K^2 + D) \mathcal{E} = -\mu_0 \left[\omega_0^2 T^2 P_{nl}^{env} + i\omega_0 T J^{env} \right] \end{aligned} \quad (2.1-65)$$

Some simplifications can be made once we group together the terms that make us K and K^2 as follows:

$$\left(\nabla_\perp^2 + \partial_\zeta^2 - 2k_0' \partial_\tau \partial_\zeta + 2ik_0 \partial_\zeta \right) \mathcal{E} + \left(k_0'^2 \partial_\tau^2 - 2ik_0 k_0'^2 \partial_\tau - k_0^2 \right) \mathcal{E} + (K^2 + D) \mathcal{E} = -\mu_0 \left[\omega_0^2 T^2 P_{nl}^{env} + i\omega_0 T J^{env} \right]$$

which can be written as:

$$\left(\nabla_\perp^2 + \partial_\zeta^2 + 2i \partial_\zeta (ik_0' \partial_\tau + k_0) \right) \mathcal{E} + (k_0' \partial_\tau - ik_0)^2 \mathcal{E} + (K^2 + D) \mathcal{E} = -\mu_0 \left[\omega_0^2 T^2 P_{nl}^{env} + i\omega_0 T J^{env} \right] \quad (2.1-66)$$

Multiplying $K = k_0 + ik_0' \partial t$ with i we get:

$$iK = ik_0 - k_0' \partial \tau \Rightarrow (k_0' \partial \tau - ik_0) = -iK \quad (2.1-67)$$

By substituting Eq.(2.1-63) in Eq.(2.1-66) we get:

$$\left(\nabla_\perp^2 + \partial_\zeta^2 + 2iK \partial_\zeta \right) \mathcal{E} - K^2 \mathcal{E} + (K^2 + D) \mathcal{E} = -\mu_0 \left[\omega_0^2 T^2 P_{nl}^{env} + i\omega_0 T J^{env} \right] \quad (2.1-68)$$

which is giving us:

$$\left(\nabla_\perp^2 + \partial_\zeta^2 - 2iK \partial_\zeta \right) \mathcal{E} + D \mathcal{E} = -\mu_0 \left[\omega_0^2 T^2 P_{nl}^{env} + i\omega_0 T J^{env} \right] \quad (2.1-69)$$

Here we make the slowly varying envelope approximation along the propagation direction [13], [14], [12], [69]. By this we assume that:

$$\partial_{\zeta}^2 \ll k_0 \partial_{\zeta} \quad (2.1-70)$$

This way we can neglect the contribution of ∂_{ζ}^2 , and finally write the evolution equation along the propagation direction ζ for the envelope:

$$2iK\partial_{\zeta}\mathcal{E} + \nabla_{\perp}^2\mathcal{E} + D\mathcal{E} = -\mu_0 \left[\omega_0^2 T^2 P_{nl}^{env} + i\omega_0 T J^{env} \right] \quad (2.1-71)$$

We can define

$$2ik_0 N_{Kerr} = -\mu_0 \omega_0^2 P_{nl}^{env} \quad (2.1-72)$$

$$2ik_0 (TN_{NLL} + N_{plasma}) = -\mu_0 i\omega_0 T J^{env} \quad (2.1-73)$$

Finally we rewrite the evolution equation in a more straight forward way:

$$\boxed{K \frac{\partial \mathcal{E}}{\partial \zeta} = \frac{i}{2} \left[\nabla_{\perp}^2 \mathcal{E} + D\mathcal{E} \right] + k_0 \left[T^2 N_{Kerr} + TN_{NLL} + N_{plasma} \right]} \quad (2.1-74)$$

Where the terms N_{Kerr} , N_{NLL} and N_{plasma} are source terms that account for the optical Kerr effect, nonlinear losses due to multiphoton absorption, and plasma related effects (absorption and defocusing). Since N_{Kerr} , N_{NLL} and N_{plasma} are related to the pulse envelope, we must calculate them accordingly.

Step#6: Calculation of the nonlinear terms

First we calculate N_{Kerr} . The nonlinear polarization due to the optical Kerr effect for the frequency ω was calculated as a function of the envelope in the first chapter in section 1.3.1.1:

$$P_{nl}^{env} = \frac{3}{4} \epsilon_0 \chi^{(3)} \mathcal{E}^3 \quad (2.1-75)$$

Eq.(2.1-75) can be written as a function of the nonlinear refractive index $n_2 = \frac{3}{4\varepsilon_0 n_0^2 c} \chi^{(3)}$ as:

$$P_{nl}^{env} = c\varepsilon_0^2 n_0^2 n_2 \mathcal{E}^3 \quad (2.1-76)$$

By substituting Eq.(2.1-76) in Eq.(2.1-72) we can calculate the Kerr term in Eq.(2.1-74) as a function of the central wavenumber k_0 :

$$N_{Kerr} = ik_0 n_2 I \mathcal{E} \quad (2.1-77)$$

$I \equiv \frac{\varepsilon_0 n_0 c}{2} |\mathcal{E}|^2$ is the intensity of the laser pulse, as it was defined in the first chapter.

Next we will calculate the term N_{NLL} . The nonlinear losses due to optical field ionization are associated with the dissipative current \vec{J} given by:

$$\vec{J} \cdot \vec{E} = \sum_x \rho_x W_x^{MPI} U_{i,x} \quad (2.1-78)$$

Where ρ_x , W_x^{MPI} and $U_{i,x}$ are the atom density, ionization rate $W_x^{MPI} = \sigma_{x,K} \cdot I^K$, and ionization potential of the species x in the medium. For a single species of order K we get:

$$W_{MPI} = \sigma_K \cdot I^K \quad (2.1-79)$$

and

$$\vec{J} \cdot \vec{E} = K \hbar \omega_0 \sigma_K (\rho_{at} - \rho) \mathcal{E}^{2K} = \beta_K \left[1 - \frac{\rho}{\rho_{at}} \right] \mathcal{E}^{2K} \quad (2.1-80)$$

The quantity $(\rho_{at} - \rho)$ corresponds to the population of non-ionized atoms that can still contribute electrons through MPI.

The term N_{NLL} in Eq.(2.1-73) associated with the dissipative current of Eq.(2.1-80) is calculated as follows:

$$J^{env} = J^{env} \mathcal{E} \cdot \mathcal{E}^{-1} = \beta_K \mathcal{E}^{2K} \cdot \left[1 - \frac{\rho}{\rho_{at}} \right] \mathcal{E} = \beta_K \left[1 - \frac{\rho}{\rho_{at}} \right] \mathcal{E}^{2K-1} \mathcal{E} = \beta_K \mathcal{E}^{2K-2} \left[1 - \frac{\rho}{\rho_{at}} \right] \mathcal{E} \quad (2.1-81)$$

And thus the nonlinear losses due to OFI are given by Eq.(2.1-82) [69], [10]:

$$N_{NLL} = -\frac{\beta_K}{2} \left[1 - \frac{\rho}{\rho_{at}} \right] |\mathcal{E}|^{2K-2} \mathcal{E} \quad (2.1-82)$$

β_K and σ_K are the multiphoton absorption and multiphoton ionization coefficients of the material for order K, that were already defined previously.

Finally will calculate the last term of Eq. (2.1-74), N_{plasma} . Following the Drude model the electron plasma is treated as a fluid with coefficient for inverse Bremsstrahlung

$$\sigma \equiv \frac{e^2 \tau_c}{\varepsilon_0 m_e c n_0 (1 + \omega^2 \tau_c^2)} \quad [118].$$

The evolution of the electron density of the plasma is given as a

function of the position vector \vec{r} :

$$m_e \frac{\partial^2 r}{\partial t^2} + \frac{m_e}{\tau_c} \frac{\partial r}{\partial t} = eE \quad (2.1-83)$$

The velocity of the free electrons is by definition:

$$v_e = \frac{\partial r}{\partial t} \quad (2.1-84)$$

Now we can re-write Eq.(2.1-83) as a first order ODE of the electron velocity:

$$m_e \frac{\partial v_e}{\partial t} + \frac{m_e}{\tau_c} v_e = eE \quad (2.1-85)$$

The current density is defined by:

$$J = e\rho v_e \quad (2.1-86)$$

We now multiply Eq.(2.1-83) with the term $e\rho$ and by substitution of Eq.(2.1-86) we get:

$$\begin{aligned} e\rho m_e \frac{\partial v_e}{\partial t} + e\rho \frac{m_e}{\tau_c} v_e &= e^2 \rho E \\ \Rightarrow m_e \frac{\partial J}{\partial t} + m_e \frac{J}{\tau_c} &= e^2 \rho E \\ \Rightarrow \frac{\partial J}{\partial t} &= \frac{e^2}{m_e} \rho E - \frac{J}{\tau_c} \end{aligned} \quad (2.1-87)$$

Eq.(2.1-87) can be solved in the frequency domain, giving us the current density:

$$\hat{J} = \frac{\tau_c (1 + i\omega\tau_c) e^2}{(1 + \omega^2\tau_c^2) m_e} \hat{\rho} \hat{E} \quad (2.1-88)$$

The absorption of the laser pulse from the plasma is given by:

$$\frac{1}{2} \text{Re}[J \cdot E] = \frac{\tau_c e^2}{2(1 + \omega^2\tau_c^2) m_e} \rho |E|^2 \quad (2.1-89)$$

We can write Eq.(2.1-89) using the pulse intensity $I \equiv \frac{\epsilon_0 n_0 c}{2} |\mathcal{E}|^2$ and coefficient for inverse

Bremsstrahlung $\sigma \equiv \frac{e^2 \tau_c}{\epsilon_0 m_e c n_0 (1 + \omega^2 \tau_c^2)}$ in the form:

$$\frac{1}{2}\text{Re}[J \cdot E] = \sigma I \rho \quad (2.1-90)$$

Using Eq.(2.1-88) we can now express the contribution of the electron plasma as a function of the generated plasma density and the coefficients σ , and τ_C :

$$N_{Plasma} = -\frac{\sigma}{2}(1+i\omega\tau_C)\rho\mathcal{E} \quad (2.1-91)$$

The real and imaginary parts of Eq.(2.1-91) correspond to plasma absorption and plasma defocusing respectively.

A simplified version of the model (2.1-1) where only the second order dispersion is taken into account is the following:

$$\boxed{\frac{\partial \mathcal{E}}{\partial z} = \frac{i}{2k_0} T^{-1} \nabla_{\perp}^2 \mathcal{E} + i \frac{k_0''}{2} \frac{\partial^2 \mathcal{E}}{\partial t^2} + ik_0 n_2 T |\mathcal{E}|^2 \mathcal{E} + \frac{\beta_K}{2} \left[1 - \frac{\rho}{\rho_{at}} \right] |\mathcal{E}|^{2K-2} \mathcal{E} - \frac{\sigma}{2} T^{-1} (1+i\omega_0 \tau_C) \rho \mathcal{E}} \quad (2.1-92)$$

This slightly simplified form of the propagation equation is much easier to interpret, since the evolution of the envelope along z ($\partial \mathcal{E} / dz$) is now isolated on the LHS. As already explained, each term on the RHS is corresponding to a physical effect, namely: diffraction, second order dispersion, Kerr, MPA, and Plasma absorption and defocusing. The way Eq.(2.1-92) is written makes it easy to distinguish between phase (imaginary) and amplitude terms (real) acting on electric field envelope. In most media dispersive effects can be accurately approximated by

second order dispersion $k_0'' = \left. \frac{\partial^2 k}{\partial \omega^2} \right|_{\omega=\omega_0}$ only, and the use of Eq.(2.1-92) is recommended.

2.2 Numerical implementations of the propagation equation

2.2.1 Numerical implementation of diffraction

2.2.1.1 Cylindrical symmetry scheme

Our desire is to simulate the nonlinear propagation of a laser pulse in a transparent material. As we already showed by using the electric field envelope the propagation can be described by an extended nonlinear Schrödinger equation (Eq.(2.1-74)), which takes into account diffraction, dispersion, the optical Kerr effect, multiphoton absorption, and plasma related effects as plasma defocusing and absorption. In order to numerically solve Eq.(2.1-74) we need to transform it into a matrix form, which can then be solved with the help of a numerical scheme on a computer.

The very basic effect that governs the propagation of (almost) all waves is diffraction. So we will start to model this simplest case first. Diffraction is described by the paraxial wave equation for the envelope of the electric field, which was also derived in the first chapter:

$$\frac{\partial \mathcal{E}}{\partial z} = \frac{i}{2k_0} \nabla_{\perp}^2 \mathcal{E} \quad (2.2-1)$$

Eq.(2.2-1) can be easily derived from Eq.(2.1-74) if dispersion and nonlinearities are neglected. Eq.(2.2-1) describes the evolution of the electric field envelope along the “z” direction due to diffraction only. Since ∇_{\perp}^2 is the transverse Laplacian operator (spatial partial derivatives only), there is no temporal evolution in Eq.(2.2-1). The transverse variables can be expressed in the Cartesian (x, y) or the cylindrical coordinate system (r, φ). The Laplacian operator is defined for both of the coordinate systems as follows:

$$\text{Cartesian:} \quad \nabla^2 f = \frac{\partial^2}{\partial x^2} f + \frac{\partial^2}{\partial y^2} f + \frac{\partial^2}{\partial z^2} f$$

$$\xrightarrow{\text{transverse}} \nabla_{\perp}^2 f = \frac{\partial^2}{\partial x^2} f + \frac{\partial^2}{\partial y^2} f \quad (2.2-2)$$

$$\text{Cylindrical : } \nabla^2 f = \frac{1}{r} \frac{\partial}{\partial r} \left(r \frac{\partial}{\partial r} f \right) + \frac{1}{r^2} \frac{\partial^2 f}{\partial \varphi^2} + \frac{\partial^2 f}{\partial z^2}$$

$$\xrightarrow{\text{transverse}} \nabla_{\perp}^2 f = \frac{1}{r} \frac{\partial}{\partial r} \left(r \frac{\partial}{\partial r} f \right)$$

$$\Rightarrow \nabla_{\perp}^2 f = \frac{1}{r} \left(\frac{\partial r}{\partial r} \frac{\partial}{\partial r} f + r \frac{\partial}{\partial r} \left(\frac{\partial}{\partial r} f \right) \right)$$

$$\Rightarrow \nabla_{\perp}^2 f = \frac{\partial^2}{\partial r^2} f + \frac{1}{r} \frac{\partial}{\partial r} f \quad (2.2-3)$$

Note that the symbol Δ is completely equivalent to ∇^2 , and is widely used in the literature. In this work both of the notation styles will be used. The “Greek Delta” (Δ) that stands for a small variation of a variable, i.e. Δz : small variation in the z direction, will also be used and is not to be confused with the Laplacian operator.

The diffraction of a light pulse in a transparent medium is an “initial value problem” (the alternative is a boundary value problem like in the case of Laplace’s equation), and is defined by the “parabolic” partial differential Eq.(2.2-1). Because of the above, the stability of the algorithm that will be used to solve Eq.(2.2-1) is of primary concern and in most cases a tradeoff between stability and accuracy is necessary. We will use the Crank – Nicolson algorithm to solve Eq.(2.2-1), which will be analyzed in detail later on. In any case, all physical problems that are solved numerical must be discretized first, since computers only recognize discrete values and points.

Because of discretization there is a limit in the accuracy of the result. This limit is defined in the very beginning with the resolution at which the physical space is discretized. In addition, in every calculation (addition, subtraction, multiplication, etc) an additional numerical error is induced by the “finite arithmetic” of the binary computer language. The continuous addition of errors could result in a numerical explosion of the error that will cover the interesting part of the solution. However in a numerically stable algorithm these errors will converge to 0, which makes the use of such algorithms a necessity. Lastly the accuracy is also reduced by the approximations used in the modeling of the physical phenomenon. This however is not a numerical problem and cannot be cured by technical solutions.

In order to discretize Eq.(2.2-1), first we need to define the numerical grid and the notation used in the numerical scheme. First we will assume radial symmetry in the transverse dimension. This assumption is valid for any radial symmetric beam diffracting in homogeneous media, which is enough for now. A more detailed discussion on the use of cylindrical symmetric and full X-Y simulation will follow at a later stage. Let's start by using a uniform grid in the radial axis r , with N_{\perp} equally spaced points by Δr , and a maximum box size of r_{\max} . The same goes for the propagation direction, where N equally spaced points by Δz are used to discretize propagation from $z = 0$ up to $z = z_{\max}$. So we can define the spatial numerical grid as:

$$\text{Grid} : \left\{ \begin{array}{l} r_j = j\Delta r, \quad j = 1, \dots, N_{\perp} \quad \text{where: } N_{\perp} = \frac{r_{\max}}{\Delta r} \\ z_n = n\Delta z, \quad n = 1, \dots, N \quad \text{where: } N = \frac{z_{\max}}{\Delta z} \end{array} \right\} \quad (2.2-4)$$

The graphical representation of the numerical grid described in Eq.(2.2-4) is shown in Fig 2-1.

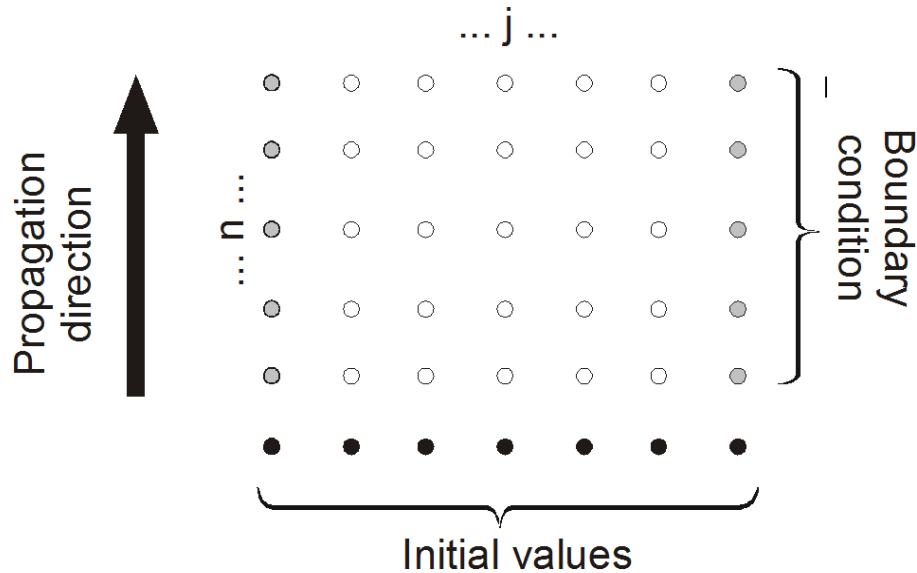


Fig 2-1 Graphical representation of a computational grid used in initial value problems.

Also let $E_j^n = \mathcal{E}(r_j, z_n)$ denote the discretized field envelope at the (j, n) point of the numerical grid. The detailed representation of the $N \times N_\perp$ numerical grid can be seen below:

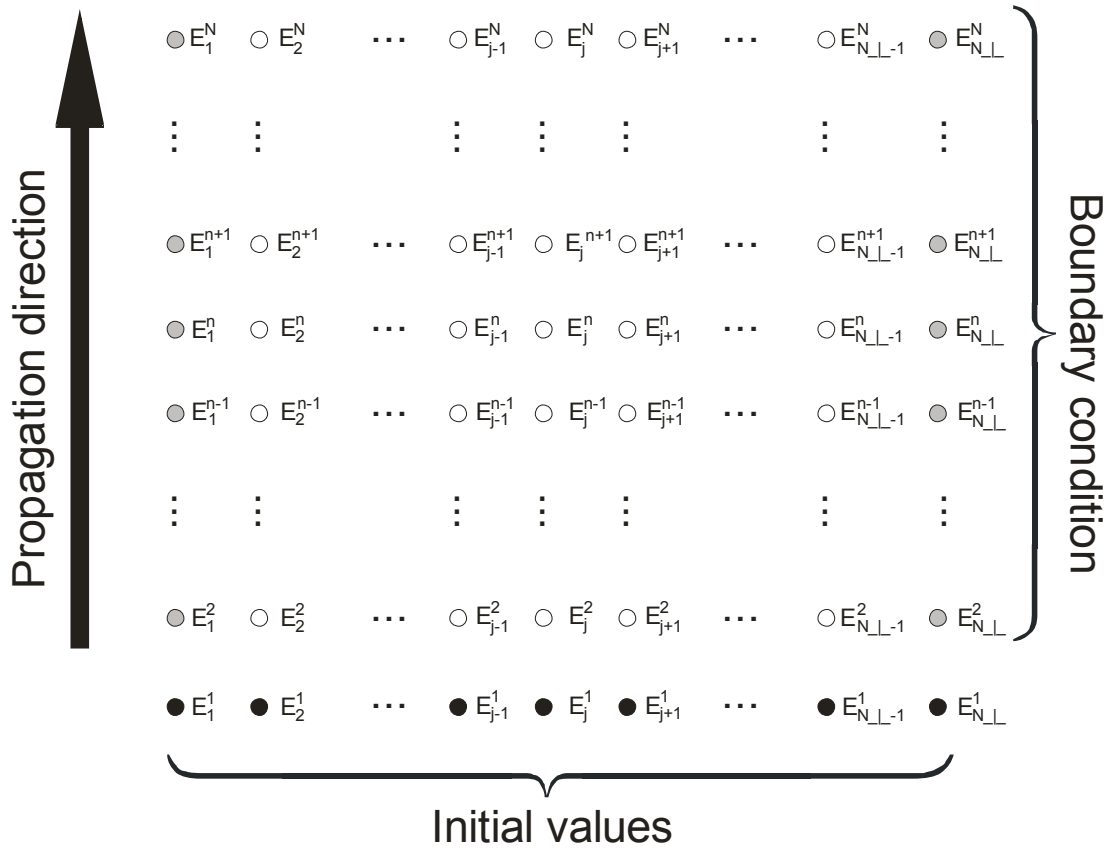


Fig 2-2 Detailed graphical representation of the numerical grid $N \times N_\perp$ used for discretizing the electric field envelope.

We will now use finite differencing methods to discretize the partial derivatives of Eq.(2.2-1). For the term $\frac{\partial \mathcal{E}}{\partial z}$ on the LHS, we will use the “Forward Differencing Method” (FDM) applied in the z direction [119]:

$$\boxed{\text{Forward Differencing in } z} \quad \frac{\partial \mathcal{E}}{\partial z} = \frac{E_j^{n+1} - E_j^n}{\Delta z} + O(\Delta z) \quad (2.2-5)$$

Here the “Big O” notation is used to give us an estimation about the growth rate of the error. In our case the error is of the order of Δz , which is relative small and just a small perturbation compared to $\frac{E_j^{n+1} - E_j^n}{\Delta z}$. For the term: $\frac{i}{2k_0} \nabla_{\perp}^2$ we have to discretize the transverse Laplacian in the cylindrical coordinate system. Using Eq.(2.2-3) we write:

$$\nabla_{\perp}^2 \mathcal{E} = \frac{\partial^2}{\partial r^2} \mathcal{E} + \frac{1}{r} \frac{\partial}{\partial r} \mathcal{E} \quad (2.2-6)$$

Now we must apply a finite differencing method to both of the partial derivatives. We will use the “Central Differencing Method” (CDM) applied in the r direction [119]:

$$\boxed{\text{Central Differencing in } r} \quad \frac{\partial}{\partial r} \mathcal{E} = \frac{E_{j+1}^n - E_{j-1}^n}{2\Delta r} \quad (2.2-7)$$

$$\boxed{\text{Central Differencing in } r} \quad \frac{\partial^2}{\partial r^2} \mathcal{E} = \frac{E_{j+1}^n - 2E_j^n + E_{j-1}^n}{(\Delta r)^2} \quad (2.2-8)$$

Also note that with Eqs.(2.2-4) we have defined that:

$$r = r_j = j\Delta r \quad (2.2-9)$$

By substitution of (2.2-7), (2.2-8) and (2.2-4) in Eq.(2.2-6) we get the discrete transverse Laplacian $\nabla_{j\perp}^2$:

$$\begin{aligned} \nabla_{\perp}^2 \mathcal{E} &= \nabla_{j\perp}^2 E_j^n = \frac{E_{j+1}^n - 2E_j^n + E_{j-1}^n}{(\Delta r)^2} + \frac{1}{j\Delta r} \frac{E_{j+1}^n - E_{j-1}^n}{2\Delta r} + O(\Delta r)^2 \\ \Rightarrow \nabla_{j\perp}^2 E_j^n &\approx \frac{E_{j+1}^n - 2E_j^n + E_{j-1}^n}{(\Delta r)^2} + \frac{1}{2j} \frac{E_{j+1}^n - E_{j-1}^n}{(\Delta r)^2} \quad (2.8) \quad (2.2-10) \end{aligned}$$

After some rearranging we get:

$$\begin{aligned}\nabla_{j\perp}^2 E_j^n &= \frac{1}{(\Delta r)^2} E_{j+1}^n - \frac{2}{(\Delta r)^2} E_j^n + \frac{1}{(\Delta r)^2} E_{j-1}^n + \frac{1}{2j} \frac{1}{(\Delta r)^2} E_{j+1}^n - \frac{1}{2j} \frac{1}{(\Delta r)^2} E_{j-1}^n \\ \nabla_{j\perp}^2 E_j^n &= \frac{1}{(\Delta r)^2} \left[\left(1 - \frac{1}{2j}\right) E_{j-1}^n - 2E_j^n + \left(1 + \frac{1}{2j}\right) E_{j+1}^n \right]\end{aligned}\quad (2.2-11)$$

And if we define the following:

$$u_j = \left(1 - \frac{1}{2j}\right) \quad (2.2-12)$$

$$v_j = \left(1 + \frac{1}{2j}\right) \quad (2.2-13)$$

$$\Delta'_j E_j^n = (u_j E_{j-1}^n - 2E_j^n + v_j E_{j+1}^n) \quad (2.2-14)$$

where the operator

$$\Delta'_j = (\Delta r)^2 \nabla_{j\perp}^2 \quad (2.2-15)$$

in Eq.(2.2-14) is the normalized discrete transverse Laplacian operator for cylindrical coordinates.

We can now write Eq.(2.2-11) by using Eqs.(2.2-12), (2.2-13), (2.2-14) as:

$$\nabla_{j\perp}^2 E_j^n = \frac{1}{(\Delta r)^2} \Delta'_j E_j^n \quad (2.2-16)$$

If we take a closer look at Eq.(2.2-14) we notice that the operator Δ'_j is actually a tridiagonal matrix which acts on the vector E_j^n as shown below:

$$\Delta'_j E_j^n = (u_j E_{j-1}^n - 2E_j^n + v_j E_{j+1}^n) = \begin{bmatrix} -2 & v_0 & 0 & 0 & 0 & 0 & 0 \\ u_1 & -2 & v_1 & 0 & 0 & 0 & 0 \\ 0 & \ddots & \ddots & \ddots & 0 & 0 & 0 \\ 0 & 0 & u_j & -2 & v_j & 0 & 0 \\ 0 & 0 & 0 & \ddots & \ddots & \ddots & 0 \\ 0 & 0 & 0 & 0 & u_{N_\perp-1} & -2 & v_{N_\perp-1} \\ 0 & 0 & 0 & 0 & 0 & u_{N_\perp} & -2 \end{bmatrix} \begin{bmatrix} E_0^n \\ E_1^n \\ \vdots \\ E_j^n \\ \vdots \\ E_{N_\perp-1}^n \\ E_{N_\perp}^n \end{bmatrix} \quad (2.2-17)$$

Eq. (2.2-17) is a $(N_\perp + 1) \times (N_\perp + 1)$ tridiagonal system. A tridiagonal system is defined by a tridiagonal matrix, which is a square matrix with nonzero elements only on the diagonal and slots horizontally or vertically adjacent to the diagonal (i.e., along the subdiagonal and superdiagonal). Tridiagonal matrix systems are easily solvable with optimized matrix algorithms [119], which in addition of being very accurate are also much faster than algorithms that solve full matrix systems. For reference a tridiagonal matrix systems requires $O(n)$ operations while a full matrix system requires $O(n)^3$. It is evident that a full matrix system becomes very expensive numerically for large grids. In addition we can use the tridiagonal property of the system to save memory and decrease computation time by using the integrated “sparse matrix function” which converts a full matrix to sparse form by squeezing out any zero elements. Generally, smart numerical implementations always result in faster and more accurate codes.

In the system (2.2-17), notice that the first line of the matrix (element v_0) is not completely defined from the finite differencing method. This does not pose a problem since in the final reformed matrix system, which will be calculated from Δ'_j with the use of a numerical scheme, the first and last lines will be replaced so that the boundary conditions are satisfied (see below).

At this point we have discretized Eq.(2.2-1) by using the finite differencing method for the partial derivatives, and finally obtaining Eq.(2.2-5) and (2.2-17). We now have to use a numerical scheme to solve Eq.(2.2-1). For this we will use the Crank – Nicolson (C-N) method, which is a second order accurate and implicit in z . In addition it is also unconditionally

numerically stable, and because of that a very good choice to implement in a numerical code. The C-N method is schematically shown below:

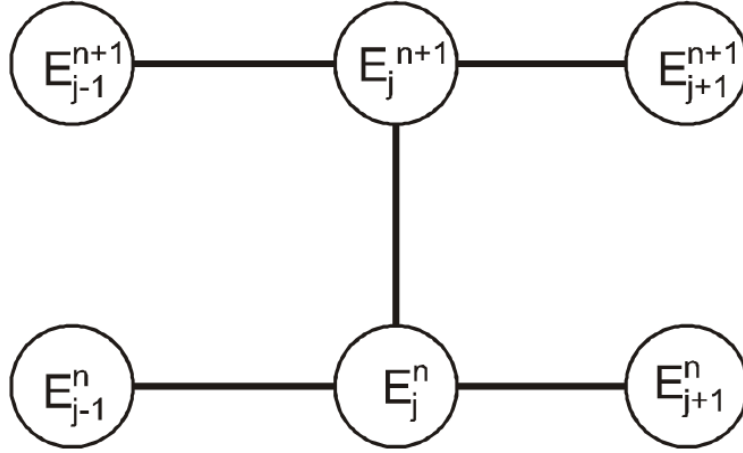


Fig 2-3 Schematic representation of the Crank – Nicolson numerical method.

The Crank – Nicolson method is actually the average of both the explicit centered differencing methods at point n (also called forward Euler) and the implicit centered differencing methods at n+1 (also called backward Euler).

$$\frac{E_j^{n+1} - E_j^n}{\Delta z} = \frac{1}{2} \left(\frac{i}{2k_0} \frac{1}{(\Delta r)^2} \Delta'_j E_j^{n+1} \right) + \frac{1}{2} \left(\frac{i}{2k_0} \frac{1}{(\Delta r)^2} \Delta'_j E_j^n \right) \quad (2.2-18)$$

The Crank – Nicolson scheme for Eq.(2.2-1) reads:

$$\begin{aligned} \frac{\partial \mathcal{E}}{\partial z} = \frac{i}{2k_0} \nabla_{\perp}^2 \mathcal{E} &\xrightarrow[\text{Crank-Nicolson}]{\text{finite differencing}} \frac{E_j^{n+1} - E_j^n}{\Delta z} = \frac{i}{2k_0} \frac{1}{2} \left[\frac{1}{(\Delta r)^2} \Delta'_j E_j^{n+1} + \frac{1}{(\Delta r)^2} \Delta'_j E_j^n \right] \\ &\Rightarrow \frac{E_j^{n+1} - E_j^n}{\Delta z} = \frac{i}{2k_0} \frac{1}{2} \frac{1}{(\Delta r)^2} \left[\Delta'_j E_j^{n+1} + \Delta'_j E_j^n \right] \Rightarrow \end{aligned}$$

$$E_j^{n+1} - E_j^n = \frac{i\Delta z}{4k_0(\Delta r)^2} [\Delta'_j E_j^{n+1} + \Delta'_j E_j^n] \quad (2.2-19)$$

which for

$$\delta = \frac{\Delta z}{2k_0(\Delta r)^2} \quad (2.2-20)$$

can be written as:

$$E_j^{n+1} - E_j^n = \frac{i\delta}{2} [\Delta'_j E_j^{n+1} + \Delta'_j E_j^n] \quad (2.2-21)$$

We now want to propagate the envelope of the field one step in the z direction, which means we want to calculate E_j^{n+1} for all j (radial coordinate). We solve Eq.(2.2-21) in a way to isolate E_j^{n+1} :

$$\begin{aligned} E_j^{n+1} - E_j^n &= \frac{i\delta}{2} [\Delta'_j E_j^{n+1} + \Delta'_j E_j^n] \\ \Rightarrow E_j^{n+1} - E_j^n &= \frac{i\delta}{2} \Delta'_j E_j^{n+1} + \frac{i\delta}{2} \Delta'_j E_j^n \\ \Rightarrow E_j^{n+1} - \frac{i\delta}{2} \Delta'_j E_j^{n+1} &= \frac{i\delta}{2} \Delta'_j E_j^n + E_j^n \\ \Rightarrow \left(1 - \frac{i\delta}{2} \Delta'_j\right) E_j^{n+1} &= \left(1 + \frac{i\delta}{2} \Delta'_j\right) E_j^n \\ E_j^{n+1} &= \left(1 - \frac{i\delta}{2} \Delta'_j\right)^{-1} \left(1 + \frac{i\delta}{2} \Delta'_j\right) E_j^n \end{aligned} \quad (2.2-22)$$

Keep in mind that Eq.(2.2-22) is still a matrix system, therefore $\left(1 - \frac{i\delta}{2} \Delta'_j\right)^{-1}$ and $\left(1 + \frac{i\delta}{2} \Delta'_j\right)$ are $(N_\perp + 1) \times (N_\perp + 1)$ complex matrices, that are calculated from Δ'_j . Let's call these two matrices $L_- = 1 - \frac{i\delta}{2} \Delta'_j$ and $L_+ = 1 + \frac{i\delta}{2} \Delta'_j$. Note here that in order to calculate Eq.(2.2-22) the

calculation of the inverse matrix of L_- cannot be avoided. L_-^{-1} is the inverse matrix of L_- , which satisfies the relation $L_-^{-1}L_- = L_-L_-^{-1} = I$ exclusively. Also remember that Δ_j' was tridiagonal, and since multiplication preserves this property, the resulting matrix $L = L_-^{-1}L_+$ will also be tridiagonal.

At this point we will apply the boundary conditions to L_+, L_- . Both Dirichlet and Neumann boundary conditions will be used, resulting in a mixed type of boundary condition:

$$\text{Neumann : } \left. \frac{\partial E^{env}}{\partial z} \right|_{r=0} = 0 \quad (2.2-23)$$

This means that at the beginning of the spatial numerical box the partial derivative of the field envelope in respect to z is zero.

$$\text{Dirichlet : } E^{env} \Big|_{r=r_{\max}} = 0 \quad (2.2-24)$$

The meaning of the Dirichlet boundary condition is that we assume that at the end of the spatial numerical box there is no radiation present. In order to satisfy the above condition we must choose a sufficiently large spatial box so that the beam is well contained inside it, and is not truncated in any way by the box. This is easily accomplished at the beginning of the simulation at $z_0 = 0$. But the possibility exists that as the simulation goes on, that due to reshaping of the beam under the effect of diffraction, the beam will become wide enough, reaching this way the boundary and cause numerical problems. To counter this effect, boundary layers are added near the edge of the numerical boxes, which act as suppressors before the radiation can reach the last grid point where the Dirichlet boundary condition is applied. In any case, the result of a simulation run must be checked for boundary problems, boundary reflections, and other numerical problems that may occur. More details about the usage of boundary layers will be given later, after the full spatio-temporal numerical grid is introduced.

In order to apply the mixed boundary conditions from Eqs.(2.2-23) and (2.2-24) to the tridiagonal matrix system we must modify the L_+, L_- matrices. That is achieved by replacing all the elements of the first and last lines of L_+ by zeroes:

$$L_{+(1,j)} = L_{+(N_\perp,j)} = (0 \quad \dots \quad 0) \quad (2.2-25)$$

Also we must replace the first line of L_- with:

$$L_{-(1,j)} = (1 \quad -1 \quad 0 \quad \dots \quad 0) \quad (2.2-26)$$

and the last line with of L_- with:

$$L_{-(N_\perp,j)} = (1 \quad 0 \quad \dots \quad 0) \quad (2.2-27)$$

So finally in full matrix form, L_+ and L_- are written as:

$$L_+ = \begin{bmatrix} 0 & 0 & 0 & 0 & 0 & 0 & 0 \\ \frac{i\delta}{2}u_1 & 1-i\delta & \frac{i\delta}{2}v_1 & 0 & 0 & 0 & 0 \\ 0 & \ddots & \ddots & \ddots & 0 & 0 & 0 \\ 0 & 0 & \frac{i\delta}{2}u_j & 1-i\delta & \frac{i\delta}{2}v_j & 0 & 0 \\ 0 & 0 & 0 & \ddots & \ddots & \ddots & 0 \\ 0 & 0 & 0 & 0 & \frac{i\delta}{2}u_{N_\perp-1} & 1-i\delta & \frac{i\delta}{2}v_{N_\perp-1} \\ 0 & 0 & 0 & 0 & 0 & 0 & 0 \end{bmatrix} \quad (2.2-28)$$

$$L_- = \begin{bmatrix} 1 & -1 & 0 & 0 & 0 & 0 & 0 \\ -\frac{i\delta}{2}u_1 & 1+i\delta & -\frac{i\delta}{2}v_1 & 0 & 0 & 0 & 0 \\ 0 & \ddots & \ddots & \ddots & 0 & 0 & 0 \\ 0 & 0 & -\frac{i\delta}{2}u_j & 1+i\delta & -\frac{i\delta}{2}v_j & 0 & 0 \\ 0 & 0 & 0 & \ddots & \ddots & \ddots & 0 \\ 0 & 0 & 0 & 0 & -\frac{i\delta}{2}u_{N_\perp-1} & 1+i\delta & -\frac{i\delta}{2}v_{N_\perp-1} \\ 0 & 0 & 0 & 0 & 0 & 0 & 1 \end{bmatrix} \quad (2.2-29)$$

Now we can finally calculate the inverse matrix of L_- in order to propagate the envelope one step in the z direction using the described Crank – Nicolson scheme:

$$E_j^{n+1} = L_-^{-1} L_+ E_j^n \quad (2.2-30)$$

If we define the matrix L as:

$$L = L_-^{-1} L_+ \quad (2.2-31)$$

we get:

$$E_j^{n+1} = L E_j^n \quad (2.2-32)$$

Note here that because L is non-singular, it always is invertible, so the linear system (2.2-32) has always a solution.

The way the described numerical scheme is implemented into a computer code is relatively simple after the derivation of Eq.(2.2-32) has been performed. The matrix that applies the Crank – Nicolson method (L) is only calculated once, even before the propagation starts. It is stored (in sparse matrix form) and is used to propagate all transverse points of the field envelope one step in the z direction. This will effectively advance the field E_j^n to E_j^{n+1} , for all r_j . Then the same procedure is repeated using the output of the previous cycle as input to propagate to the

next step. This will advance the field E_j^{n+1} to E_j^{n+2} , again for all r_j . This procedure eventually stops after the desired z – point is reached. The starting values for the field envelope must of course be defined in advance, so that E_j^2 can be calculated from E_j^1 .

In order to get a result in the end of the simulation, we must use some diagnostics to plot the physical values we are interested in. In this simple case of two dimensional (2D) paraxial diffraction, we mostly care about the evolution of the beam waist and peak intensity along the propagation. In order to plot these values, additional matrices must be used to periodically store them and finally plot them in an easy to read way. The diagnostics are therefore necessary components in any computer code. Often diagnostics can grow into very complicated structures that require a lot of memory and computation time.

Now we will describe a computer code that uses Eq.(2.2-32) to solve Eq.(2.2-1). The way we will do this is by using pseudo-code, a standard way to describe computer programs in a symbolic way:

1. Code initialization
 - Clearing all variables

2. Definition of initial data
 - Physical
 - i. Laser parameters (λ , waist, starting intensity, etc)
 - ii. Material parameters and physical constants (refractive index, etc)
 - Numerical
 - i. Transverse grid (box size, resolution, from Eq.(2.2-4))
 - ii. Propagation grid (box size, resolution, from Eq.(2.2-4))
 - iii. Boundary layers (from Eq.(2.2-23) and Eq.(2.2-24))
 - iv. Initialization of all matrices used in the code

3. Calculation of matrix L
 - Calculation of L_+ using boundary conditions (from Eq.(2.2-28))
 - Calculation of L_- using boundary conditions (from Eq.(2.2-29))
 - Calculation of L_-^{-1}
 - Calculation of $L = L_-^{-1}L_+$ (from Eq.(2.2-31))

4. Starting Electric Field Envelope calculation E_j^1 for all points in $r_j = j\Delta r$
 - Beam shape definition (Gaussian, Super – Gaussian, etc)
5. Propagation of the envelope E_j^n one step in z

Start loop z (N steps)

Start loop r (N_\perp steps)

- Calculation of E_j^{n+1} from E_j^n using $E_j^{n+1} = LE_j^n$, for each point in r. From Eq.(2.2-32).

End loop r

- Diagnostics along z

End loop z

6. Plotting of results from diagnostics

A simple numerical code, written in Matlab, can be found in the electronic file `code_linear_RZ.m`, which implements the above mentioned numerical scheme in cylindrical symmetry.

2.2.1.2 Implementation for Cartesian coordinates

In case we choose to use the Cartesian coordinate system things are even simpler. Remember that from Eq.(2.2-2) and Eq.(2.2-3), the transverse Laplacian operators can be written as:

$$\text{Cartesian: } \nabla_{\perp}^2 f = \frac{\partial^2}{\partial x^2} f + \frac{\partial^2}{\partial y^2} f$$

$$\text{Cylindrical: } \nabla_{\perp}^2 f = \frac{\partial^2}{\partial r^2} f + \frac{1}{r} \frac{\partial}{\partial r} f$$

In the simplest case where we only want to use the x and z dimensions, we can drop the term $\frac{\partial^2}{\partial y^2}$ of Eq.(2.2-2). The discrete transverse Laplacian for the x – axis can be written as:

$$\nabla_{j\perp}^2 E_j^n = \frac{1}{(\Delta x)^2} \Delta'_j E_j^n = \frac{1}{(\Delta x)^2} [E_{j-1}^n - 2E_j^n + E_{j+1}^n] \quad (2.2-33)$$

which is written in matrix form as:

$$\Delta'_j E_j^n = (E_{j-1}^n - 2E_j^n + E_{j+1}^n) = \begin{bmatrix} -2 & 1 & 0 & 0 & 0 & 0 & 0 \\ 1 & -2 & 1 & 0 & 0 & 0 & 0 \\ 0 & \ddots & \ddots & \ddots & 0 & 0 & 0 \\ 0 & 0 & 1 & -2 & 1 & 0 & 0 \\ 0 & 0 & 0 & \ddots & \ddots & \ddots & 0 \\ 0 & 0 & 0 & 0 & 1 & -2 & 1 \\ 0 & 0 & 0 & 0 & 0 & 1 & -2 \end{bmatrix} \begin{bmatrix} E_1^n \\ E_2^n \\ \vdots \\ E_j^n \\ \vdots \\ E_{N_{\perp}-1}^n \\ E_{N_{\perp}}^n \end{bmatrix} \quad (2.2-34)$$

This simplification originates from the term $\frac{1}{r} \frac{\partial}{\partial r}$ that is not present in the Cartesian case, because of $u_j = v_j = 1$, and Δr is equivalent to Δx . Following the same steps as in the cylindrical case we can now write the L_+, L_- matrices for Cartesian coordinates:

$$L_+ = \begin{bmatrix} 0 & 0 & 0 & 0 & 0 & 0 & 0 \\ \frac{i\delta}{2} & 1-i\delta & \frac{i\delta}{2} & 0 & 0 & 0 & 0 \\ 0 & \ddots & \ddots & \ddots & 0 & 0 & 0 \\ 0 & 0 & \frac{i\delta}{2} & 1-i\delta & \frac{i\delta}{2} & 0 & 0 \\ 0 & 0 & 0 & \ddots & \ddots & \ddots & 0 \\ 0 & 0 & 0 & 0 & \frac{i\delta}{2} & 1-i\delta & \frac{i\delta}{2} \\ 0 & 0 & 0 & 0 & 0 & 0 & 0 \end{bmatrix} \quad (2.2-35)$$

and

$$L_- = \begin{bmatrix} 1 & -1 & 0 & 0 & 0 & 0 & 0 \\ -\frac{i\delta}{2} & 1+i\delta & -\frac{i\delta}{2} & 0 & 0 & 0 & 0 \\ 0 & \ddots & \ddots & \ddots & 0 & 0 & 0 \\ 0 & 0 & -\frac{i\delta}{2} & 1+i\delta & -\frac{i\delta}{2} & 0 & 0 \\ 0 & 0 & 0 & \ddots & \ddots & \ddots & 0 \\ 0 & 0 & 0 & 0 & -\frac{i\delta}{2} & 1+i\delta & -\frac{i\delta}{2} \\ 0 & 0 & 0 & 0 & 0 & 0 & 1 \end{bmatrix} \quad (2.2-36)$$

We can clearly see that these new matrices for the XZ case are a bit simpler than for the RZ case. The main idea however is the same, and the pseudo – code described in the previous part is still valid.

A simple numerical code, written in Matlab, can be found in the electronic file **code_linear_XZ.m**, which implements the above mentioned numerical scheme in XZ geometry.

2.2.2 Addition of nonlinear effects

In this part we will extend the numerical scheme for paraxial diffraction, in order to include the basic nonlinear effects that act on the laser beam. We still are only considering spatial effects; therefore no change in the computational grid is required. We will assume cylindrical symmetry throughout this analysis. At this point the nonlinear effects that we will take into account are the instantaneous part of the optical Kerr effect and nonlinear losses to the beam due to Multi – Photon Absorption of order K. The nonlinear propagation equation for the field envelope is then written:

$$\frac{\partial \mathcal{E}}{\partial z} = \frac{i}{2k_0} \nabla_{\perp}^2 \mathcal{E} + i \frac{\omega_0 n_2}{c} |\mathcal{E}|^2 \mathcal{E} + \frac{\beta_K}{2} |\mathcal{E}|^{2K-2} \mathcal{E} \quad (2.2-37)$$

It is clear that the Crank – Nicolson method used to solve the linear part of Eq.(2.2-37) must be extended in order to include the two newly added nonlinear terms. We can describe these terms with the discrete operator N_j^n :

$$N_j^n = N(E_j^n) = k_0 \left[i \frac{\omega_0 n_2}{c} |E_j^n|^2 E_j^n + \frac{\beta_K}{2} |E_j^n|^{2K-2} E_j^n \right] \quad (2.2-38)$$

Remember that the linear part of Eq.(2.2-37) was solved in the previous section using finite differencing:

$$\frac{\partial \mathcal{E}}{\partial z} = \frac{i}{2k_0} \nabla_{\perp}^2 \mathcal{E} \xrightarrow[\text{Crank-Nicolson}]{\text{finite differencing}} \frac{E_j^{n+1} - E_j^n}{\Delta z} = \frac{i}{2k_0} \frac{1}{2} \left[\frac{1}{(\Delta r)^2} \Delta'_j E_j^{n+1} + \frac{1}{(\Delta r)^2} \Delta'_j E_j^n \right] \quad (2.2-39)$$

The new terms from Eq.(2.2-38) can be introduced using the Dufort – Frankel scheme, an explicit scheme that preserves the second order accuracy of the Crank – Nicolson scheme [69, 119]. The propagation equation with the addition of the Dufort – Frankel scheme for the nonlinear operator N_j^n of equation (2.22) reads:

$$\begin{aligned} \frac{\partial \mathcal{E}}{\partial z} &= \frac{i}{2k_0} \nabla_{\perp}^2 \mathcal{E} + i \frac{\omega_0 n_2}{c} |\mathcal{E}|^2 \mathcal{E} + \frac{\beta_K}{2} |\mathcal{E}|^{2K-2} \mathcal{E} \\ &\xrightarrow[\text{Dufort-Frankel}]{\text{finite differencing} \\ \text{Crank-Nicolson} \\ +} \frac{E_j^{n+1} - E_j^n}{\Delta z} = \frac{i}{2k_0} \frac{1}{2} \left[\frac{1}{(\Delta r)^2} \Delta'_j E_j^{n+1} + \frac{1}{(\Delta r)^2} \Delta'_j E_j^n \right] + \left[\frac{3}{2} N_j^n - \frac{1}{2} N_j^{n-1} \right] \\ &\Rightarrow E_j^{n+1} - E_j^n = \frac{i\delta}{2} [\Delta'_j E_j^{n+1} + \Delta'_j E_j^n] + \Delta z \left[\frac{3}{2} N_j^n - \frac{1}{2} N_j^{n-1} \right] \quad (2.2-40) \end{aligned}$$

Eq.(2.2-40) can be solved in respect to E_j^{n+1} so we can reach a relation that will give us E_j^{n+1} :

$$\begin{aligned} E_j^{n+1} - E_j^n &= \frac{i\delta}{2} [\Delta'_j E_j^{n+1} + \Delta'_j E_j^n] + \Delta z \left[\frac{3}{2} N_j^n - \frac{1}{2} N_j^{n-1} \right] \\ \Rightarrow E_j^{n+1} - E_j^n &= \frac{i\delta}{2} \Delta'_j E_j^{n+1} + \frac{i\delta}{2} \Delta'_j E_j^n + \Delta z \left[\frac{3}{2} N_j^n - \frac{1}{2} N_j^{n-1} \right] \\ \Rightarrow E_j^{n+1} - \frac{i\delta}{2} \Delta'_j E_j^{n+1} &= E_j^n + \frac{i\delta}{2} \Delta'_j E_j^n + \Delta z \left[\frac{3}{2} N_j^n - \frac{1}{2} N_j^{n-1} \right] \\ \Rightarrow \left(1 - \frac{i\delta}{2} \Delta'_j \right) E_j^{n+1} &= \left(1 + \frac{i\delta}{2} \Delta'_j \right) E_j^n + \Delta z \left[\frac{3}{2} N_j^n - \frac{1}{2} N_j^{n-1} \right] \\ \Rightarrow L_- E_j^{n+1} &= L_+ E_j^n + \Delta z \left[\frac{3}{2} N_j^n - \frac{1}{2} N_j^{n-1} \right] \end{aligned}$$

$$\Rightarrow E_j^{n+1} = L_-^{-1} \left[L_+ E_j^n + \Delta z \left[\frac{3}{2} N_j^n - \frac{1}{2} N_j^{n-1} \right] \right] \quad (2.2-41)$$

Note that $\delta, \Delta_j', L_+, L_-$, and L_-^{-1} are the same as when they were first defined for the paraxial equation of diffraction in cylindrical coordinates in previous chapter. Eq.(2.2-41) can be written in a more clear way as:

$$E_j^{n+1} = L_-^{-1} \left[L_+ E_j^n + \Delta z \left[\frac{3}{2} N(E_j^n) - \frac{1}{2} N(E_j^{n-1}) \right] \right] \quad (2.2-42)$$

We can see that we can now propagate the field one step in the z direction, using the already calculated values at position (n) and (n-1). This demands two initial conditions instead of one.

However the most important difference in the implementation of Eq.(2.2-42) is that we cannot calculate the matrix $L = L_-^{-1} L_+$ before the propagation loop, store it, and keep using it for every position in z. Here, we can only calculate L_+ and L_-^{-1} in advance, since at each step in z the matrices N_j^n and N_j^{n-1} are different and must be recalculated. This is expected to happen in the nonlinear regime where the reshaping of the beam depends on the local intensity. It is therefore also expected that nonlinear problems have higher computational demands than linear ones.

The stability of the scheme is related to the term N, which describes the perturbations that the nonlinear effects induce onto diffraction. This means that the unconditional stability of the Crank – Nicolson scheme is not preserved completely. In the nonlinear regime described by Eq.(2.2-42), the propagation must be done “slow” enough in order to have numerical convergence, which literally means that for a given transverse grid we need a sufficiently small Δz . Since Δz is a numerical constant, we can make Eq.(2.2-42) more compact by defining

$$N_j^n = N'(E_j^n) = \Delta z \cdot N(E_j^n) = k_0 \Delta z \left[i \frac{\omega_0 n_2}{c} |E_j^n|^2 E_j^n + \frac{\beta_K}{2} |E_j^n|^{2K-2} E_j^n \right] \quad (2.2-43)$$

So we can write Eq.(2.2-42) as:

$$E_j^{n+1} = L_-^{-1} \left[L_+ E_j^n + \frac{3}{2} N_j^n - \frac{1}{2} N_j^{n-1} \right] \quad (2.2-44)$$

We can again write the pseudo-code describing the implementation of the numerical scheme of Eq.(2.2-44):

1. Code initialization
 - Clearing all variables

2. Definition of initial data
 - Physical
 - i. Laser parameters (λ , waist, starting intensity, etc)
 - ii. Material parameters and physical constants (refractive index, etc)
 - Numerical
 - iii. Transverse grid (box size, resolution, from Eq.(2.2-4))
 - iv. Propagation grid ((box size, resolution, from Eq.(2.2-4))
 - v. Boundary layers (from Eq.(2.2-23) and Eq.(2.2-24))
 - vi. Initialization of all matrices used in the code

3. Calculation of non – changing matrices
 - Calculation of L_+ using boundary conditions (from Eq.(2.2-28))
 - Calculation of L_- using boundary conditions (from Eq.(2.2-29))
 - Calculation of L_-^{-1}

4. Starting Electric Field Envelope calculation E_j^1 for all points in $r_j = j\Delta r$
 - Beam shape (Gaussian, Super – Gaussian, etc)

5. Propagation of the envelope E_j^n one step in z

Start loop z (N steps)

Start loop r (N_\perp steps)

- Calculation of $N_{j,l}^n$ from Eq.(2.2-43)
- Calculation of E_j^{n+1} from E_j^n , N_j^n and N_j^{n-1} , using

$$E_j^{n+1} = L_-^{-1} \left[L_+ E_j^n + \frac{3}{2} N_j^n - \frac{1}{2} N_j^{n-1} \right]$$
 for each point in r. From Eq.(2.2-44).

End loop r

- Storing of N_j^n in place of N_j^{n-1} in order to be used for the next z-step
- Diagnostics along z

End loop z

6. Plotting of results from diagnostics

Note that up to stage #4, the only difference from the linear case is that we do not calculate and store the matrix L in step #3. Both L_+ and L_- are identical with the linear case. In step #5, each time a new N_j^n is calculated, and must be stored in order to be used as N_j^{n-1} in the next z-step. N_j^{n-2} , as well as all older values of N_j are not needed, so at each z-step the freshly calculated N_j^n overwrites N_j^{n-1} after the calculation of E_j^{n+1} . This way memory is spared, and only one N matrix is stored between subjacent z-steps.

A simple numerical code, written in Matlab, can be found in the electronic file **code_nonlinear_RZ.m**, which implements the above mentioned numerical scheme in cylindrical symmetry.

2.2.3 Addition of time and temporal effects

In this part we will extend the numerical scheme by adding the temporal coordinate. By adding time to the numerical scheme we will be able to describe linear and nonlinear temporal effects in the temporal domain. Of course we must now define a laser pulse rather than only a beam, and discretize it on a new temporal grid. The main effects that will be added are Dispersion, Self – Phase Modulation, Space – time focusing and self – steepening, as well as plasma related effects like absorption (real part) and defocusing (imaginary part).

Every time an additional dimension is added in the propagation equation, a new numerical grid must also be defined in order to discretize it properly. This means that the numerical scheme must perform additional loops for the new dimension, and thereby increase the computation time of the program significantly.

Just to get a feeling of this, let's suppose that a 2D scheme (for example XZ) has a numerical grid that consists of 300 points in the transverse direction and 1000 points in the z direction. If for each z-step M operations are needed, then the whole propagation will need $1000 \times M$ operations to finish. If we extend the scheme for one additional spatial dimension Y with a grid of another 300 points, then the number of operations for each z – step will increase to M^2 , and the whole propagation will need $1000 \times M^2$ operations. Note that the number of operations is directly related to computation time. If for example the 2D scheme described above would need 5 hours in order to finish, then the 3D scheme using the same grids, will need 90 hours. For each additional dimension the computation time will increase in similar fashion, making full 4D (x, y, z, t) numerical simulations extremely demanding on computational resources. In reality the use of specific algorithms that work fast for a high number of dimensions (like the Fast Fourier Transform for 2D) are helping in decreasing the computation time. Nonetheless the higher dimension codes are generally slow and use lower resolutions to compensate.

First we have to extend the spatial grid we used previously by adding the temporal coordinate. The discretized temporal coordinate reads:

$$t_l = t_0 + l\Delta t \quad (2.2-45)$$

The temporal grid (2.2-45) corresponds to a spectral grid:

$$\omega_l = \omega_0 + l\Delta\omega \quad (2.2-46)$$

As derived in section 2.1.1 the propagation equation for the electric field envelope including dispersion with operator D and self-steepening with operator T, is defined by Eqs.(2.1-1), (2.1-2), (2.1-3), (2.1-4). We can rewrite Eq.(2.1-1) in the spectral domain as:

$$\hat{K} \frac{\partial \hat{\mathcal{E}}}{\partial z} = \frac{i}{2} \left[\nabla_{\perp}^2 \hat{\mathcal{E}} + \hat{D} \hat{\mathcal{E}} \right] + k_0 \left[\hat{T}^2 \hat{N}_{Kerr}(\mathcal{E}) + \hat{T} \hat{N}_{NLL}(\mathcal{E}) + \hat{N}_{Plasma}(\mathcal{E}, \rho) \right] \quad (2.2-47)$$

We define the discretized operators of Eq.(2.2-47) as a function of the discrete frequency ω_l as $\hat{K}_l = \hat{K}(\omega_l)$, $\hat{T}_l = \hat{T}(\omega_l)$, and $\hat{D}_l = \hat{D}(\omega_l)$.

The numerical scheme used to solve Eq.(2.2-47) [69] is defined with the equations:

$$\hat{E}_{j,l}^{n+1} - \hat{E}_{j,l}^n = i \frac{\delta_l}{2} \left(\Delta'_j \hat{E}_{j,l}^{n+1} + \Delta'_j \hat{E}_{j,l}^n \right) + i \frac{d_l}{2} \left(\hat{E}_{j,l}^{n+1} + \hat{E}_{j,l}^n \right) + \frac{3}{2} \hat{N}'_{j,l} - \frac{1}{2} \hat{N}'_{j,l} \quad (2.2-48)$$

where:

$$\delta_l = \frac{\delta}{\hat{K}_l} = \frac{\Delta z}{2(\Delta r)^2 \hat{K}_l} \quad (2.2-49)$$

$$d_l = \frac{\Delta z \hat{D}_l}{2 \hat{K}_l} \quad (2.2-50)$$

The nonlinear term is written as:

$$\hat{N}'_{j,l} = \Delta z \cdot \hat{N}(E_{j,l}^n, \rho_{j,l}^n) = \frac{k_0 \Delta z}{\hat{K}_l} \left[\hat{T}_l^2 \hat{N}_{Kerr}(E_{j,l}^n) + \hat{T}_l \hat{N}_{NLL}(E_{j,l}^n) + \hat{N}_{Plasma}(E_{j,l}^n, \rho_{j,l}^n) \right] \quad (2.2-51)$$

while $\Delta'_j = (\Delta r)^2 \nabla_{j\perp}^2$ remains as it was defined in Eq.(2.2-15)

Taking similar actions as in the derivation of Eq.(2.2-41) we can find the value of the at point n+1 starting from point n:

$$\hat{E}_{j,l}^{n+1} = L_{-,l}^{-1} \left[L_{+,l} \hat{E}_{j,l}^n + \frac{3}{2} \hat{N}_{j,l}'^n - \frac{1}{2} \hat{N}_{j,l}'^{n-1} \right] \quad (2.2-52)$$

The matrices $L_{-,l}$ and $L_{+,l}$ are defined by:

$$L_{+,l} = 1 + \frac{\delta_l}{2} \Delta_j' + i \frac{d_l}{2} \quad (2.2-53)$$

$$L_{-,l} = 1 - \frac{\delta_l}{2} \Delta_j' - i \frac{d_l}{2} \quad (2.2-54)$$

Which are written in full matrix form as:

$$L_{+,l} = \begin{bmatrix} 0 & 0 & 0 & 0 & 0 \\ \ddots & \ddots & \ddots & 0 & 0 \\ 0 & \left(\frac{\delta_l}{2} u_j + i \frac{d_l}{2} \right) & \left(1 - \delta_l + i \frac{d_l}{2} \right) & \left(\frac{\delta_l}{2} v_j + i \frac{d_l}{2} \right) & 0 \\ 0 & 0 & \ddots & \ddots & \ddots \\ 0 & 0 & 0 & 0 & 0 \end{bmatrix} \quad (2.2-55)$$

$$L_{-,l} = \begin{bmatrix} 0 & 0 & 0 & 0 & 0 \\ \ddots & \ddots & \ddots & 0 & 0 \\ 0 & -\left(\frac{\delta_l}{2} u_j + i \frac{d_l}{2} \right) & \left(1 + \delta_l - i \frac{d_l}{2} \right) & -\left(\frac{\delta_l}{2} v_j + i \frac{d_l}{2} \right) & 0 \\ 0 & 0 & \ddots & \ddots & \ddots \\ 0 & 0 & 0 & 0 & 0 \end{bmatrix} \quad (2.2-56)$$

As we can see the introduction of the temporal dimension has modified the L matrices by an additional frequency term. However $L_{+,l}$ and $L_{-,l}$ still operate on the transverse vectors $\hat{E}_{j,l}^n$,

which are now defined for each frequency component ω_l . This means that the previously used Crank – Nicolson and Dufort Frankel schemes are still applicable, since the propagation from point (n) to point (n+1) is done for each frequency component separately ($\hat{E}_{j,l}^n \rightarrow \hat{E}_{j,l}^{n+1}$). This means that in the numerical code a new frequency loop must be introduced, which will apply the C-N scheme for all discrete frequencies ω_l . Since Eq.(2.2-52) is written in the frequency domain, two Fourier transformations (one to go the frequency domain and one to back to the time domain) are also necessary to complete the calculation ($E_{j,l}^n \rightarrow \hat{E}_{j,l}^n \rightarrow E_{j,l}^n$).

For the calculation of the electron density of the plasma, the plasma evolution equation (2.1-7) must be solved N_{\perp} times.

The pseudo-code describing the implementation of the numerical scheme of Eq.(2.2-52):

1. Code initialization
 - Clearing all variables
2. Definition of initial data
 - Physical
 - i. Laser parameters (λ , waist, starting intensity, pulse duration, spectral phase, Chirp, etc)
 - ii. Material parameters and physical constants (refractive index, dispersion relation, etc)
 - Numerical
 - iii. Transverse grid (box size, resolution, from Eq.(2.2-4))
 - iv. Propagation grid (box size, resolution, from Eq.(2.2-4))
 - v. Temporal and frequency grid (box size, resolution, from Eqs.(2.2-45), (2.2-46))
 - vi. Boundary layers (from Eq.(2.2-23) and Eq.(2.2-24))
 - vii. Initialization of all matrices used in the code
3. Calculation of non – changing matrices
 - Calculation of $L_{+,l}$ using boundary conditions (from Eq.(2.2-53))
 - Calculation of $L_{-,l}$ using boundary conditions (from Eq.(2.2-54))
 - Calculation of $L_{-,l}^{-1}$

4. Starting Electric Field Envelope calculation $E_{j,l}^1$ for all points in $r_j = j\Delta r$ and $t_l = t_0 + l\Delta t$
 - Pulse shape (Gaussian, Super – Gaussian, etc)

5. Propagation of the envelope $E_{j,l}^n$ one step in z, and calculation of ρ :

Start loop z (N steps)

Start loop r (N_\perp steps)

- Calculation of electron density ρ from Eq.(2.1-7):

$$\frac{\partial \rho}{\partial t} = \sigma_K |\mathcal{E}|^{2K} (\rho_{at} - \rho) + \frac{\sigma}{U_i} \rho |\mathcal{E}|^2 - a_{rec} \rho^2$$
, by solving N_\perp ordinary differential equations (odes) for the whole temporal box.

- Calculation of $N_{j,l}^n$ for all time steps (loop)

- Fourier transform of $E_{j,l}^n$, $N_{j,l}^n$ and $N_{j,l}^{n-1}$ in order to be able to use Eq.(2.2-52) which is in the frequency domain.

Start loop ω (l steps)

Calculation of $\hat{E}_{j,l}^{n+1}$ from $\hat{E}_{j,l}^n$, $\hat{N}_{j,l}^n$ and $\hat{N}_{j,l}^{n-1}$, using Eq.(2.2-

52): $\hat{E}_{j,l}^{n+1} = L_{-,l}^{-1} \left[L_{+,l} \hat{E}_{j,l}^n + \frac{3}{2} \hat{N}_{j,l}^n - \frac{1}{2} \hat{N}_{j,l}^{n-1} \right]$ for a point r_j and a

frequency component ω_l .

End loop ω

- Inverse Fourier transform to get back to the time domain:

$$IFT\{\hat{E}_{j,l}^{n+1}\} \rightarrow E_{j,l}^{n+1}$$

End loop r

- Storing of $\hat{N}_{j,l}^n$ in place of $\hat{N}_{j,l}^{n-1}$ in order to be used for the next z-step
- Diagnostics along z

End loop z

6. Plotting of results from diagnostics

2.2.4 "Frozen time" scheme (XYZ)

In cases where the spatial reshaping of filaments is studied in two spatial dimensions (XYZ), temporal effects can be safely neglected entirely in order to reduce computation time. Thus the envelope evolution equation of the envelope $\mathcal{E}(x, y, z)$ is now rewritten in three spatial dimensions (XYZ) in the form:

$$\frac{\partial \mathcal{E}}{\partial z} = \frac{i}{2k_0} \nabla_{\perp}^2 \mathcal{E} + i \frac{\omega_0}{c} n_2 |\mathcal{E}|^2 \mathcal{E} + \frac{\beta_K}{2} \left[1 - \frac{\rho}{\rho_{at}} \right] |\mathcal{E}|^{2K-2} \mathcal{E} - i \frac{\omega_0}{n_0 c} \cdot \frac{\rho}{2\rho_c} \mathcal{E} \quad (2.2-57)$$

Note that Eq.(2.2-57) does not take into account dispersion, self-steepening, and SPM .

The plasma density in the last term of Eq.(2.2-57) must still be calculated by Eq.(2.1-7), which takes into account the temporal intensity profile of the pulse. However, since temporal effects are neglected, we assume that the pulse shape remains undistorted, or "frozen", along propagation. This way the plasma density can be calculated by solving multiple ODEs (in the form of Eq.(2.1-7)) on a temporal grid (like the one described by Eq.(2.2-45)), which is quite inexpensive in term of computation time. The real gain in computation time is coming from the

removal of the temporal dimension from the propagation equation, where most of the calculations take place (2 Fourier transforms and the solution of the propagation equation for each frequency component separately).

This simplification of the numerical model is mostly valid in cases where the main focus of the simulations revolves around the study of spatial dynamics. In addition dispersion must be relatively weak compared to the other effects, which is the case in most gases or even liquids and condensed materials for long pulse durations. The validity of the "frozen time" scheme for any given numerical experiment must be carefully evaluated by the use of the characteristic lengths (Table 1) of each physical mechanism. The characteristic lengths can give a good estimation about the significance of each physical effect, and if or not it can be safely neglected.

2.2.5 Uniform and non-uniform grids

Up to this point three different computational grids have been introduced, one for each dimension. These are the transverse and propagation grids of Eq.(2.2-4) and the temporal grid of Eq.(2.2-45). In all three cases the spacing between neighboring grid points is constant along the whole grid. These types of numerical grids are called uniform, and are ideal for the mapping of physical space in the modeling of processes that do not exhibit great variation. A good example of such a physical process is dispersion in the temporal dimension. However in the case of filamentation phenomena, the use of uniform grids for the mapping of space is not recommended.

Let's assume for simplicity that a cylindrical symmetric uniform grid in the transverse dimension is used to model a pulse in the single filamentation regime. The initial laser beam will shrink down to a much smaller core, and will propagate along z with only small variation in size. In order to properly describe the physical effects in the filament core where the intensity is high, a minimum resolution is required. This resolution however is maintained over the rest of numerical box, where the intensity is much lower and the required numerical resolution is

smaller. Thus the use of a uniform grid in the modeling of filaments results in a wasteful increase of computation time and memory, which should always be avoided.

A solution to this problem is to use non-uniform grids. A non-uniform grid has an uneven distribution of points, in order to provide high resolution when it is need and low resolution everywhere else. This way a physical phenomenon can be model accurately without the use of excess grid points. In the case of filamentation, a good non-uniform grid would have a higher resolution at the center and lower resolution in the periphery. A schematic representation of such a non-uniform grid is shown in Fig 2-4.

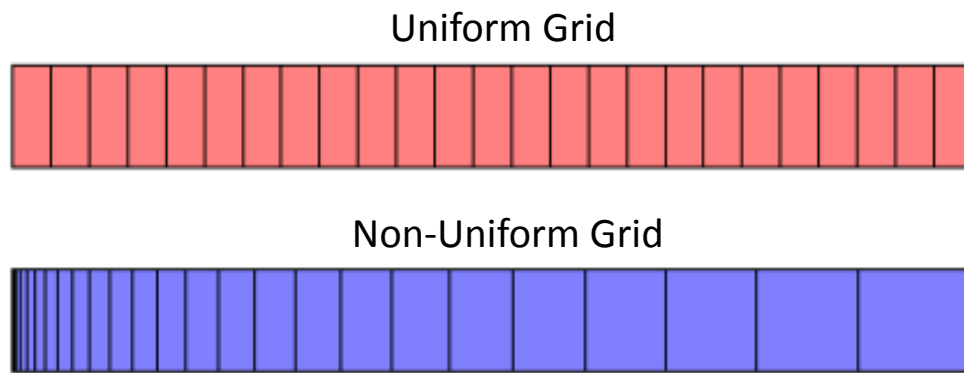


Fig 2-4 Schematic representation of a uniform computational grid (first line), and a non-uniform computational grid (second line).

The numerical implementation of a non-uniform grid is done with the help of a mapping function between the physical space r and computational space R .

$$r = f(R) \tag{2.2-58}$$

Of course the numerical scheme must now be expressed in the terms of Eq.(2.2-58), which mean that the transverse variable r and all partial derivatives of it must be rewritten as bellow [69]:

$$\frac{\partial}{\partial r} = \frac{1}{f'(R)} \frac{\partial}{\partial R} \tag{2.2-59}$$

$$\frac{\partial^2}{\partial r^2} = \frac{1}{f'^2} \left(\frac{\partial^2}{\partial R^2} - \frac{f''}{f'} \frac{\partial^2}{\partial R^2} \right) \quad (2.2-60)$$

The transverse Laplacian of Eq.(2.2-3) will be rewritten as:

$$\begin{aligned} \nabla_{\perp}^2 &= \frac{\partial^2}{\partial r^2} + \frac{1}{r} \frac{\partial}{\partial r} = \frac{1}{f'^2} \left(\frac{\partial^2}{\partial R^2} - \frac{f''}{f'} \frac{\partial^2}{\partial R^2} \right) + \frac{1}{r} \frac{1}{f'(R)} \frac{\partial}{\partial R} \\ &\Rightarrow \nabla_{\perp}^2 = F(R) \frac{\partial^2}{\partial R^2} + G(R) \frac{\partial}{\partial R} \end{aligned} \quad (2.2-61)$$

where:

$$F(R) = \frac{1}{f'^2} \quad (2.2-62)$$

$$G(R) = \left(\frac{1}{f \cdot f'} - \frac{f''}{f'^3} \right) \quad (2.2-63)$$

In order to use the same numerical schemes as described in sections 2.2.1 - 2.2.3 it is needed to discretize the computational space using again a uniform grid:

$$R_j = j\Delta R \quad (2.2-64)$$

Note that we still map the physical space with a non-uniform grid expressed by the function f .

Now we can rewrite the matrices Δ'_j , L_+ , and L_- using the discrete versions of $F_j = F(R_j)$ and

$$G_j = G(R_j):$$

$$u_j = F_j - G_j \quad (2.2-65)$$

$$v_j = F_j + G_j \quad (2.2-66)$$

And

$$\Delta'_j = \begin{bmatrix} -2 & v_0 & 0 & 0 & 0 & 0 & 0 \\ u_1 & -2F_1 & v_1 & 0 & 0 & 0 & 0 \\ 0 & \ddots & \ddots & \ddots & 0 & 0 & 0 \\ 0 & 0 & u_j & -2F_j & v_j & 0 & 0 \\ 0 & 0 & 0 & \ddots & \ddots & \ddots & 0 \\ 0 & 0 & 0 & 0 & u_{N_\perp-1} & -2F_{N_\perp-1} & v_{N_\perp-1} \\ 0 & 0 & 0 & 0 & 0 & u_{N_\perp} & -2F_{N_\perp} \end{bmatrix} \quad (2.2-67)$$

Using Eq.(2.2-65)-(2.2-67), the same numerical schemes can be applied for any given mapping function f .

2.2.6 Boundary conditions

In simulations, light that reaches the boundary of the numerical box will be back-reflected towards the center. This back-reflection is a numerical artifact and can lead to huge numerical problems if left unattended. Moreover numerical back-reflections can be easily misinterpreted as actual physical phenomena, which can lead to results that are in fact nothing more than numerical errors.

The use of extremely large numerical boxes can be used to delay the occurrence or reflections; however it is extremely costly in terms of computation time. The correct way to avoid numerical back-reflection is with the use of appropriate boundary layers which will cause light to disappear when it reaches the edge of the numerical box. A simple way to implement this approach is with the addition of a boundary layer, through an absorption function that is applied to the envelope.

Another other type of boundary condition that can be used to avoid back-reflections is known as "perfectly matched layers" in the literature [120], which reduces the reflection coefficient to zero close to the box edge.

In general both of the above boundary condition can be applied, and a sufficient number of steps in the z -direction must be used in order to have good results.

2.2.7 Checking for numerical errors

The end result of any numerical experiment must always be checked for numerical errors. These errors are not always easily recognizable, especially in the study of complex phenomena taking place in laser filaments. However a simulation result that is free of numerical errors will not change much when the resolution or the size of the numerical box is increased. Therefore once an interesting result is obtained, both resolution and box size should be increased by a factor of 2 or 3, in order to check for any discrepancies. The most efficient way to this, is by increasing the resolution of each dimension (r , t , z) separately while keeping the box size constant. In a similar way, the increase of the box size should be done with a simultaneous increase of grid points so that the overall resolution remains the same.

For diffraction, which is the basis of the whole model, the accuracy of the numerical scheme is proportional to $\frac{\Delta z}{(\Delta r)^2}$. The smaller $\frac{\Delta z}{(\Delta r)^2}$, the better the accuracy of the simulation. This means that the accuracy of the numerical scheme can be improved either by decreasing Δz or by increasing Δr . Decreasing Δz is in most cases a good approach; however it can result in a large accumulation of errors if the too many points are used. The second way to increase accuracy is to increase Δr , which means fewer points in the transverse direction. Of course Δr must be sufficiently small to properly describe the filament structures, which are quite small at the core. In practice a tradeoff between numerical accuracy $\frac{\Delta z}{(\Delta r)^2}$ and proper discretization of the transverse dimension is used. In case where the temporal dimension is also taken into account, the accuracy of the numerical scheme is also dependent on $\frac{\Delta z}{(\Delta t)^2}$, which should in the same fashion kept as small as possible. When performing numerical simulations, once a good numerical accuracy has been reached, it should be kept constant when resolution is increased in any dimension. This means that a decrease of Δr by a factor of X (for example to better resolve tiny features at the core of a filament) should be accompanied by an decrease of Δz by a factor of X^2 , so that the accuracy of the numerical scheme is kept constant.

2.3 Typical simulation results

In this section typical simulation results will be presented. The numerical scheme used in this section is assuming cylindrical symmetry, and the propagation medium is air at atmospheric pressure.

2.3.1 Linear diffraction

The basis of any spatial wave propagation code is the effect of diffraction. The laser pulse used will have a Gaussian spatial shape with beam waist $500 \mu\text{m}$ at $1/e^2$ radius at a wavelength $\lambda = 800 \text{ nm}$. The starting peak intensity is 1 W/cm^2 . The spatial spreading of the beam can be seen in Fig 2-5.

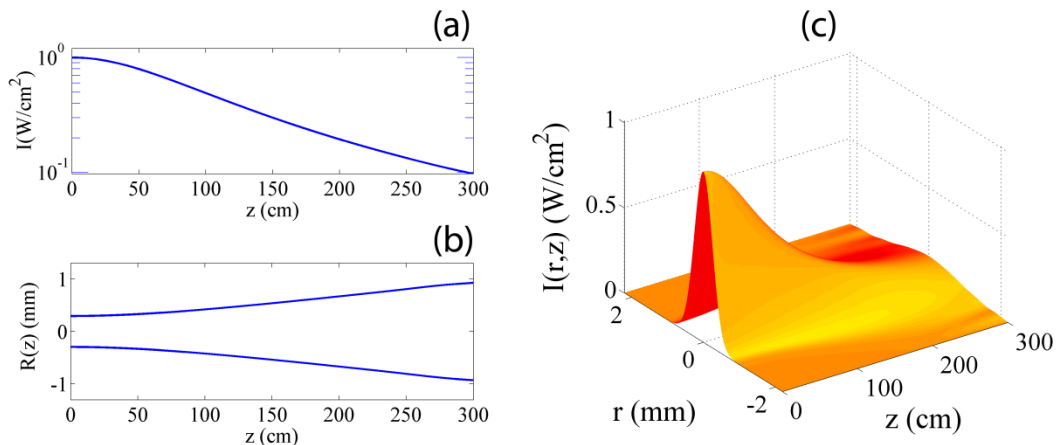


Fig 2-5 Diffraction of a collimated Gaussian beam in air. (a) Peak intensity along propagation distance. (b) Beam waist at FWHM along propagation distance. (c) 3D radial intensity distribution along z .

The numerical parameters used to generate the results shown in Fig 2-5 are the following: For the transverse dimension: $r_{\text{max}} = 2.2 \text{ mm}$ and $N_{\perp} = 251$ points, which corresponds to $\Delta r = 8.7 \mu\text{m}$. For the longitudinal dimension: $z_{\text{max}} = 3 \text{ m}$ and $N = 1000$ points, which

corresponds to $\Delta z = 3 \text{ mm}$. A typical computer needs a few seconds to numerical solve the problem over the whole propagation distance.

A second example of a Gaussian beam with a larger beam waist of 2 mm at $1/e^2$ radius and an initial curvature of $f = 150 \text{ cm}$ is shown in Fig 2-6.

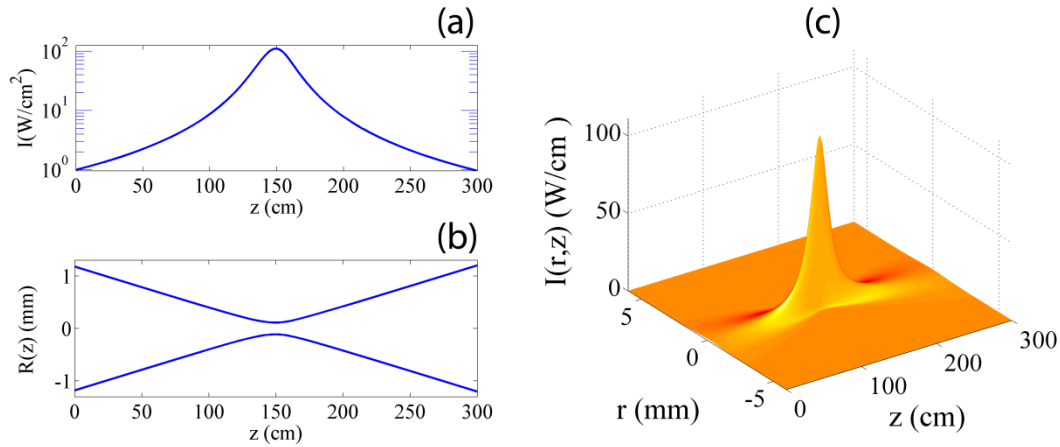


Fig 2-6 Diffraction of a focused Gaussian beam in air. (a) Peak intensity along propagation distance. (b) Beam waist at FWHM along propagation distance. (c) 3D radial intensity distribution along z .

2.3.2 Addition of time and dispersion

The first physical effect that will be added is dispersion. This demands the addition of the temporal dimensions and the definition of temporal grid as described in section 2.2.3. In order to be able to observe dispersion properly, the pulse duration is chosen to be as short as $t_p = 10 \text{ fs}$, which will result in a broad spectrum centered around $\lambda_0 = 800 \text{ nm}$, shown in Fig 2-7.

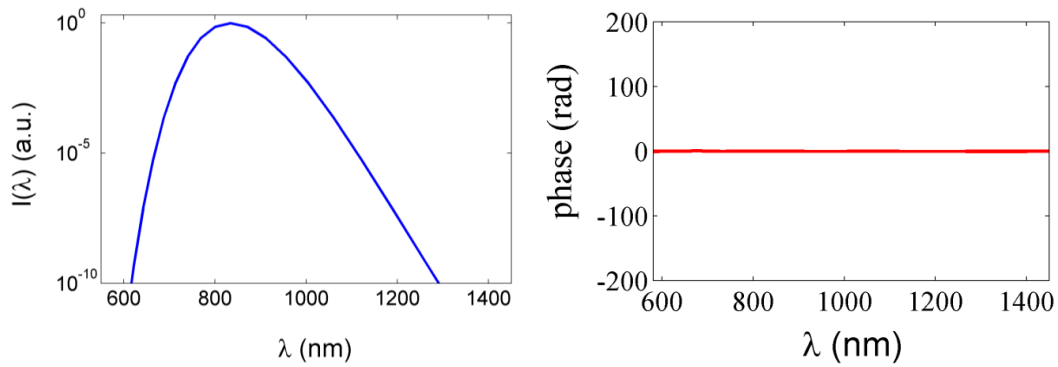


Fig 2-7 Fourier limited spectrum (left) and spectral phase (right) of a 10 fs laser pulse at 800 nm.

In order to isolate the effect of dispersion, the beam is considered collimated with a waist of 5 mm at $1/e^2$ radius, which is large enough in order to neglect diffraction over the propagation distance of 3 m. The dispersion of air is modeled in this case by using the second order dispersive coefficient only; with $k'' = 0.2 \text{ fs}^2 / \text{cm}$. As we can see in Fig 2-8 the initial 10 fs pulse is evenly spreading out as it propagates over 3 m in air. Since diffraction is effectively negligible, the observed intensity drop is solely due to dispersion.

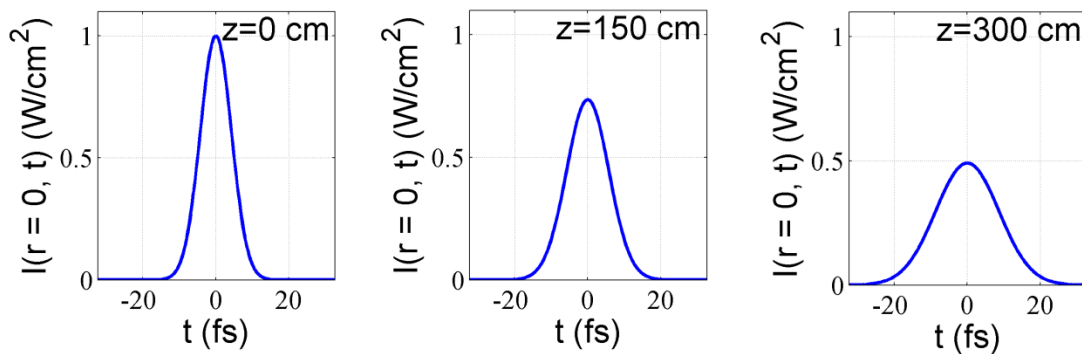


Fig 2-8 Pulse duration at $r=0$ of a 10 fs pulse (first column) after propagation of 150 cm (second column) and 300 cm (third column) in air.

In general both diffraction and dispersion are spreading the beam in space and time. The combined action of both diffraction and dispersion can be seen in Fig 2-9, where the intensity cross-sections of a wavepacket at various positions along z are plotted in the XY plane. In this case the beam has a waist of $500 \mu\text{m}$ at $1/e^2$ radius and 10 fs pulse duration, which makes both diffraction and dispersion observable over the 3 m long propagation in air.

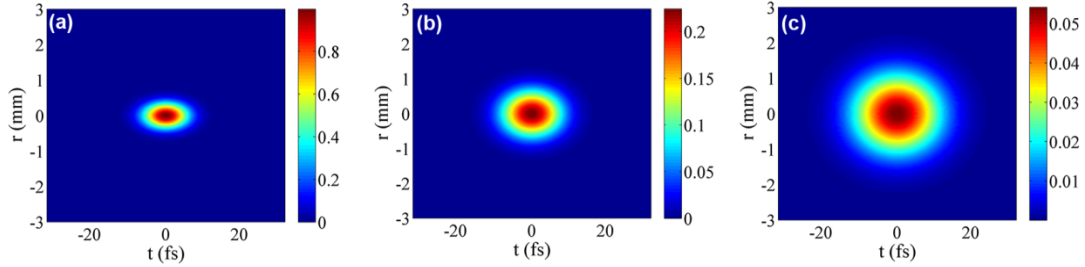


Fig 2-9 Spatio-temporal (r - t) intensity cross-section of a Gaussian wavepacket undergoing diffraction and dispersion in air. (a) $z = 0$ cm, (b) $z = 150$ cm, and (c) $z = 300$ cm. Initial pulse duration and beam waist is 10 fs and $500 \mu\text{m}$ respectively.

2.3.3 Addition of the optical Kerr effect

Next the optical Kerr will be added to the simulation. The power of the wavepacket has to be increased above the critical value in order to overcome diffraction. For air the nonlinear refractive index is $n_2 = 3.2 \times 10^{-19} \text{ cm}^2 / \text{W}$ which gives a critical value from self-focusing $P_{cr} \approx 3.2 \text{ GW}$. The addition of the Kerr effect has both spatial and temporal implications, in the form of spatial self-focusing and temporal self-phase modulation (SPM) and spectral broadening.

The collimated 800 nm laser pulse used has a Gaussian spatio-temporal intensity distribution with $w_0 = 500 \mu\text{m}$ and $t_p = 35 \text{ fs}$. The specific wavelength and pulse duration corresponds to the output of the Ti-Sapphire laser in the laboratory, and will be used extensively throughout this thesis. The starting peak intensity is $I_0 = 2 \times 10^{12} \text{ W} / \text{cm}^2$ which corresponds to roughly $2.5 P_{cr}$. Dispersion and diffraction are accounted for as in the previous example.

In Fig 2-10 we can see the peak intensity and beam waist along z . The beam starts to self-focus and collapses after ~ 46 cm of propagation. At the point of collapse intensity becomes extremely high and the beam shrinks so much that it cannot be properly modeled with the current resolution. This extreme behavior will result in an explosion of numerical errors and the "crash" of the code. This outcome is expected since MPA, which is the main mechanism responsible for the arrest of the collapse is not modeled here.

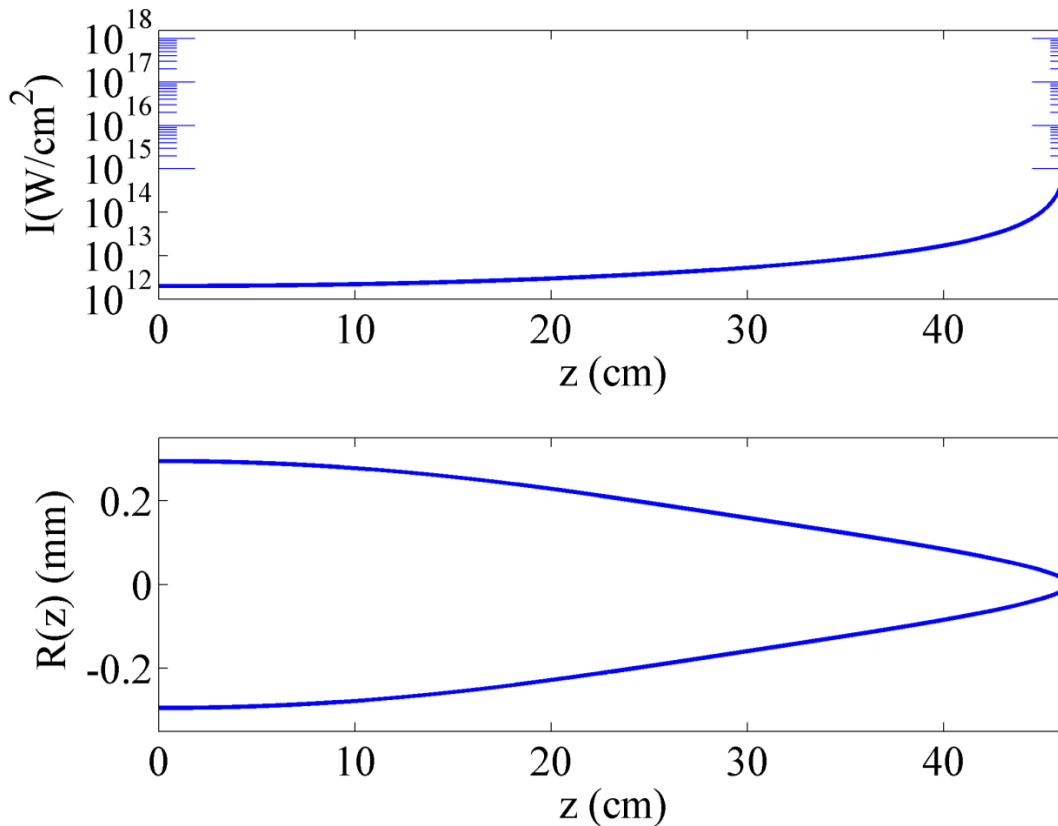


Fig 2-10 Peak intensity (first line) and beam waist at FWHM (second line) of 2.5 Pcr laser pulse propagating in air under the effects of diffraction, dispersion and the optical Kerr effect. The pulse collapses after 46.35 cm of propagation in the absence of any saturating mechanisms.

Temporally the pulse experience self-compression and spectral broadening due to the self-phase modulations (SPM). This can be seen in Fig 2-11 where the pulse profiles and corresponding spectra are depicted at various propagation distances. As we can see in the first line, the pulse intensity is increased and the duration is decreasing as is approaches the collapse

point. The new frequencies generated by SPM are covering a large part of the spectral window from 650 nm up to 1000 nm, resulting in a spectrum that is over 3 times broader at the exit.

The temporal reshaping stops at the point of collapse where the numerical code crashes. However, once the filament is formed and all physical effects are taken into account, the temporal reshaping of the pulse will increase dramatically.

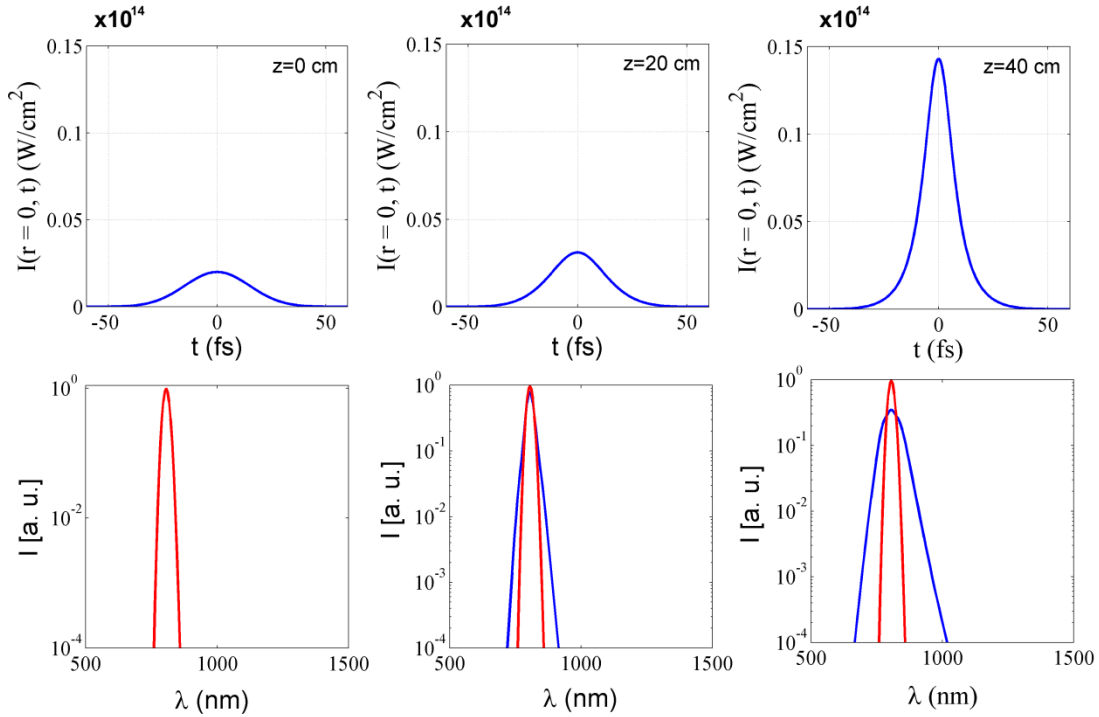


Fig 2-11 Pulse profiles (first line) and corresponding spectra (second line) of a 35 fs 2.5 Pcr laser pulse propagating in air under the effects of diffraction, dispersion and the optical Kerr effect. In the second line, the initial spectra is depicted with red, while the blue line corresponds to the spectral content at the given position in z.

2.3.4 Addition of saturating mechanisms

In order to propagate further we need to introduce the main physical mechanisms responsible for the arrest of the collapse, namely optical field ionization (OFI), and plasma defocusing. In air MPA is of the order of $K = 8$ photons, if we consider oxygen as the main molecule contributing electrons. This approximation is valid since oxygen has a lower electron gap $U_i = 12.06 \text{ eV}$ in contrast to the electron gap of Nitrogen which is $U_i = 15.576 \text{ eV}$. In case of only oxygen, the coefficient for MPA and MPI are $\beta_8 = 4 \times 10^{-95} \text{ cm}^{13} / W^7$ and $\sigma_8 = 4 \times 10^{-96} \text{ s}^{-1} \text{ cm}^{16} / W^8$. The density of neutral oxygen molecules in air is $\rho_{nt} = 5 \times 10^{18} \text{ cm}^{-3}$.

Using the same wavepacket as previously, we can now observe how MPA is arresting the collapse in Fig 2-12. As we can see a filament is created at around $z = 45 \text{ cm}$ and extends up to $z = 105 \text{ cm}$. In Fig 2-12(a) we can see that the intensity reaches values around $3 \times 10^{13} \text{ W} / \text{cm}^2$ (blue continuous line) which leads to the generation of plasma with an electron density above $3 \times 10^{16} \text{ cm}^{-3}$ (green dashed line). The beam waist, shown in Fig 2-12(b), shrinks down to a diameter of about $100 \text{ }\mu\text{m}$, and remains almost constant as long as the filament is maintained. In Fig 2-12(c) we can see the radial intensity distribution along z , zoomed close to the core of the filament.

As we can see, after about 60 cm of propagation (from 45 cm up to 105 cm) the filament starts to break up, and the linear effects of diffraction and dispersion dominate.

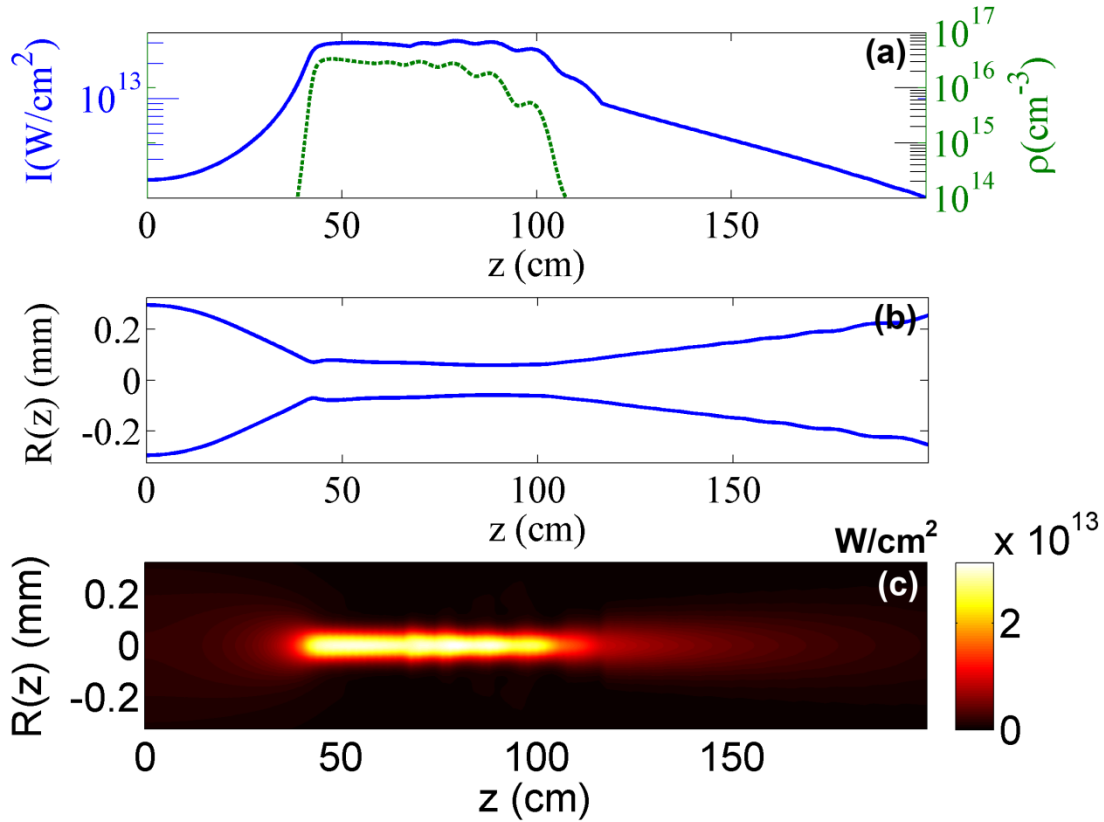


Fig 2-12 Nonlinear propagation of a 2.5 Pcr laser pulse in air. The physical effects that are taken into account are diffraction, dispersion, Kerr, OFI and plasma defocusing. (a) Peak intensity (blue continues line) and plasma density (green dashed line) as a function of propagation distance. (b) Beam waist at FWHM as a function of propagation distance. (c) Radial intensity distribution vs. propagation distance.

Fig 2-13 shows the temporal dynamics that take place inside the filament. As we can see the initial Gaussian pulse (shown of Fig 2-13(a)) is undergoing pulse splitting under the combined action of linear and nonlinear effects. The evolution of the intensity profile along z can be seen in Fig 2-13(c) for the center of the beam ($r = 0$).

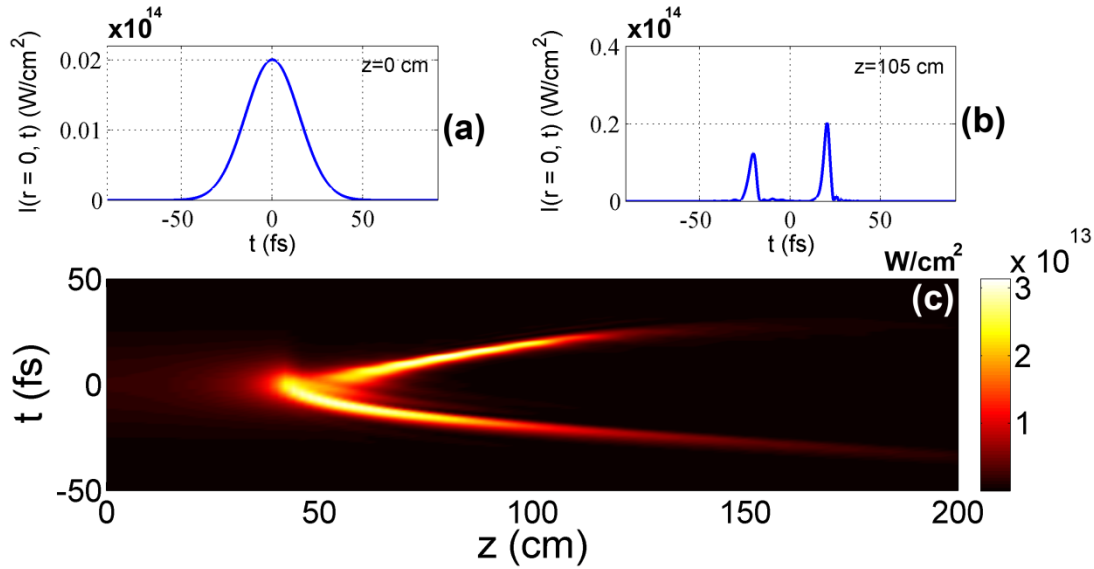


Fig 2-13 Temporal evolution of a 35 fs Gaussian laser pulse, undergoing pulse splitting. (a) Initial pulse profile. (b) Pulse profile at the end of the filament. (c) Pulse profile as a function of propagation distance.

The nonlinear propagation of the pulse will lead to spectral broadening due to Kerr and plasma related SPM. Fig 2-14 shows the spectrum of the pulse at the end of the filament ($z = 105$ cm). As we can clearly see the spectrum at this point, represented with the blue line, is spanning from the near UV up to the near IR, and is much broader than at the start (red line). Note that the abrupt cut off at 1600 nm is not a physical effect but the absorbing boundary condition of the spectral box which forces the field to vanish.

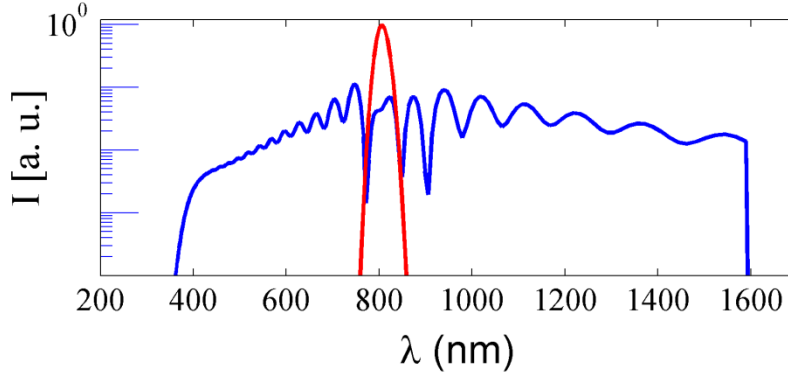


Fig 2-14 Spectral broadening of a 35 fs 800 nm pulse carrying 2.5 Pcr in air. The red line is the spectrum at the start of the propagation. The blue line corresponds to the spectrum at the end of the filament at $z = 105$ cm.

2.3.5 Addition of self-steepening

As already mentioned, self-steepening is the formation of a steep edge in the trailing part of the pulse profile. In numerical simulations this physical effect can be arbitrarily switched on or off by substituting the space-time coupling term T in Eq.(2.1-1) with $T = 1 + i\omega_0^{-1} \frac{\partial}{\partial t}$, or $T = 1$ respectively. Other nonlinear effects like avalanche ionization, plasma absorption, and electron recombination are less important, since they have very little effect on femtosecond pulses. However for longer pulses, as in the picosecond timescale, they must also be taken into account.

In Fig 2-15 we can see the effect of self-steepening on the pulse shape and spectrum of the previously used laser pulse. The oscillations in the intensity profile of the pulse are not numerical artifacts, but the manifestation of optical shock formation. The tendency to form a steep edge in the trailing part of the pulse should in principle result in a bluer spectrum, since the term $\frac{\partial I(t)}{\partial t}$ of Eq.(1.3-33) will decrease. As we can see the second line of Fig 2-15, self-steepening will

indeed force strong blue shift in spectrum, since even the spectral region beyond 350 nm is covered. This was not the case in Fig 2-14 where self-steeping was not accounted for.

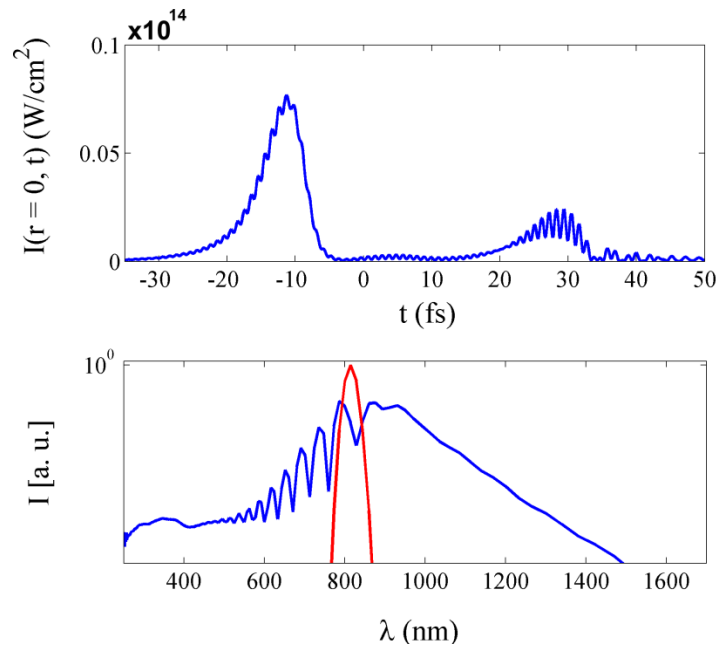


Fig 2-15 Pulse profile (first line) and spectrum (second line) of a 35 fs 800 nm pulse carrying 2.5 Pcr undergoing filamentation in air, taking into account self-steeping. The red line is the spectrum at the start of the propagation. The blue line corresponds to the spectrum at the end of the filament at $z = 105$ cm.

3. Filamentation tailoring with photonic lattices

3.1 Classical approaches

Filamentation tailoring denotes the selective optimization of specific filament attributes. Its importance is fundamental in view of the numerous applications of filaments that are promising but remained compromised up to now by the poor control over the filamentation process. For instance, it has recently been shown that the THz emission from 2-color filaments strongly depends on the uniformity of the plasma string and its length [87]. In another example one could consider the use of long filaments at intensities just below ionization for the generation of higher harmonics and attosecond pulses.

Yet, as filamentation results from the competition between self-action effects, its attributes are not easily controllable, while the control is further hindered by the high intensities in filaments (exceeding 10^{13} W/cm² in air) that exclude optical elements from being introduced in their path. Thus, the majority of efforts, up to date, were limited to the control of the spatial and temporal characteristics of the initial laser pulses [10]. Examples of these approaches include the use of amplitude and phase masks or the introduction of aberrations on the initial beam wavefront [53, 115]. More recently impulsive alignment of molecular gases has been shown to also strongly affect the propagation of laser pulses [121].

3.2 Radial symmetric lattice in air

To find more efficient ways to control filamentation one must go back to the principles of nonlinear propagation. The propagation of intense pulses under fairly constant intensity and beam waist has also been observed in solitons, where the intensities are much lower than those observed in filaments. In this case, self-focusing induced by the optical Kerr effect is balanced by diffraction or other linear propagation phenomena. Since the intensity never reaches values

where multiphoton absorption is important, these pulses propagate practically without losses. However, it is known that in two spatial dimensions the soliton solutions supported by the nonlinear Schrödinger equation are unstable [23] leading to diffraction or wave collapse of the initial beam. Nevertheless, it was shown that in the presence of a periodic waveguide lattice, light has the tendency to be localized in the high-index areas leading to the formation of discrete solitons [122, 123]. Interestingly, in two-dimensional setting such soliton solutions can be stabilized by the presence of a periodic lattice [124-126]. Experimentally, two-dimensional lattice solitons were observed [127] using an optical induction technique [128]. It was already demonstrated that the attributes of solitons can be tailored by using discrete waveguide arrays (see [129] and references therein). In the presence of a periodic potential, self-focusing balances the linear diffraction induced by the waveguide array. Furthermore, the soliton attributes such as the peak intensity and width are controlled by the waveguide array parameters and the total input power.

Inspired by the waveguide arrays and optically induced lattices used to control the attributes of solitons, we investigate the use of lattices to control the features of intense femtosecond laser filaments. In this way, we demonstrate a propagation regime of intense lattice solitons bridging the field of spatial solitons with that of filamentation. By tuning the parameters of the lattice, we can tailor the filaments' uniformity, peak intensity, plasma density, beam width and total length. This tunability is not the result of a linear guiding effect but of an enforced balance between the nonlinear propagation effects and the linear diffraction induced by the lattice.

To start with, we consider a discrete waveguide array structure, similar to that used in [126] to control the attributes of solitons. A proper choice of the array parameters allows for a control of the FWHM and the peak intensity of a propagating soliton. Application of this idea to the dynamic propagation of optical pulses during filamentation in gases, without introducing optical materials in their paths, can be realized by using, for instance, plasma photonic lattices that can survive high intensities. Plasma is an ideal candidate for generating a waveguide array structure by interference of intense light beams [130, 131], since it withstands damage in contrast with classical optical elements, while the refractive index of the medium can be easily perturbed with changes as large as $\Delta n \sim 10^{-3}$. Another possibility is to use positive or negative Δn lattices exploiting the molecular alignment of air molecules (or other gases) [121]. In the latter case the

laser intensities needed are lower than the ones needed for ionization and one can use pulse trains to further enhance the alignment [132] and consequently the strength of the lattice.

The numerical model that is used in the simulations resolves the nonlinear Schrödinger type equation (Eq.(2.1-92)) , which is extended by an additional term taking into account the photonic lattice:

$$\frac{\partial \mathcal{E}}{\partial z} = \frac{i}{2k_0} T^{-1} \Delta_{\perp} \mathcal{E} - i \frac{k''}{2} \frac{\partial^2 \mathcal{E}}{\partial t^2} + N(\mathcal{E}^2, \rho) \cdot \mathcal{E} + i k_0 T^{-1} \Delta n(x, y) \cdot \mathcal{E} \quad (3.2-1)$$

Eq.(3.2-1) describes the evolution of the slowly varying envelope $\mathcal{E}(x, y, z, t)$ of the electric field $E = \text{Re}[\mathcal{E} \exp(ik_0 z - i\omega_0 t)]$ of a laser pulse that propagates in the z direction in a transparent

Kerr medium. $k_0 = k(\omega_0) = \frac{n_0 \omega_0}{c}$ and ω_0 are the central wavenumber and frequency of the carrier wave, respectively, n_0 is the linear refractive index of the medium and c is the speed of light in vacuum. The model takes into account diffraction, group velocity dispersion with coefficient $k'' = \left. \frac{\partial^2 k}{\partial \omega^2} \right|_{\omega_0}$, and various nonlinear effects $N(E^2, \rho)$, as also described in Eq.(2.1-92)

In particular we can write:

$$N(\mathcal{E}^2, \rho) = iT \frac{\omega_0}{c} n_2 |\mathcal{E}|^2 - T^{-1} \frac{\sigma}{2} (1 + i\omega_0 \tau_c) \rho - \frac{\beta_K}{2} |\mathcal{E}|^{2K-2} \left[1 - \frac{\rho}{\rho_{at}} \right] \quad (3.2-2)$$

where $T = \left(1 + \frac{i}{\omega_0} \frac{\partial}{\partial t} \right)$ is an operator that corresponds to the space-time focusing and self-steepening of the laser pulse. The first term of Eq.(3.2-2) accounts for the Kerr nonlinearity with coefficient $3.2 \times 10^{-19} \text{ cm}^2 / W$, leading to a critical power for self-focusing $P_{cr} = 3 \text{ GW}$ [17, 18]. The second term accounts for plasma absorption and plasma defocusing, $\sigma = 5.5 \times 10^{-20} \text{ cm}^2$ is the cross section for inverse Bremsstrahlung, and $\tau_c = 350 \text{ fs}$ is the collision time in air. Finally the last term in Eq.(3.2-2) accounts for multiphoton absorption, where

$\beta_K = K\hbar\omega_0\rho_{at}\sigma_K = 4\times 10^{-95} \text{ cm}^{13}\text{W}^7$, and $\sigma_K = 3.4\times 10^{-96} \text{ cm}^{16}/\text{W}^8/\text{s}$ are the multi-photon ionization coefficients for $K = \left\langle \frac{U_i}{\hbar\omega_0} + 1 \right\rangle = 8$ photons in air [10, 133, 134].

Eq.(3.2-1) is coupled with the evolution equation for the electron density in the form of Eq.(3.2-3), which describes plasma generation as a result of the laser pulse interaction with the medium:

$$\frac{\partial \rho}{\partial t} = \sigma_K |\mathcal{E}|^{2K} (\rho_{nt} - \rho) + \frac{\sigma}{U_i} \rho |\mathcal{E}|^2 \quad (3.2-3)$$

Eq.(3.2-3) takes into account multiphoton ionization with rate $W_{MPI} = \sigma_K I^K$, as well as avalanche ionization where ρ_{nt} is the density of neutral atoms.

Before moving to the filamentation regime we confirmed the existence of soliton solutions for a lattice consisting of an array of equally spaced negative Δn rods using a simplified form of Eq.(3.2-1) (keeping only the diffraction, the Kerr, and the linear potential terms). We look for soliton solutions to a simplified form of Eq.(3.2-1), with a lattice consisting of an array of equally spaced negative Δn rods (see inset of Fig 3-1(a)). Eq.(3.2-1) can be written in normalized coordinates $\zeta = z/z_0$, $\xi = x/w_0$, $\eta = y/w_0$, $\psi = E/A$. In particular, we set $z_0 = w_0^2 k_0$, $A^2 = 1/(k_0 n_2 z_0)$ and keep only the diffraction, the Kerr, and the linear potential terms leading to

$$i\psi_\zeta + \frac{1}{2}(\psi_{\xi\xi} + \psi_{\eta\eta}) + V(\xi, \eta)\psi + |\psi|^2 \psi = 0 \quad (3.2-4)$$

In Eq.(3.2-4) the potential contrast is related to the index contrast by $V_0 = (\Lambda k_0)^2 \Delta n_0$, where Λ is the lattice period. In our numerical simulations, each rod is modeled by an eighth order super-Gaussian (mimicking a realistic experimental plasma profile in air), the distance between neighboring waveguides is unity, the diameter of each waveguide is 0.75, whereas $V_0 = 20$.

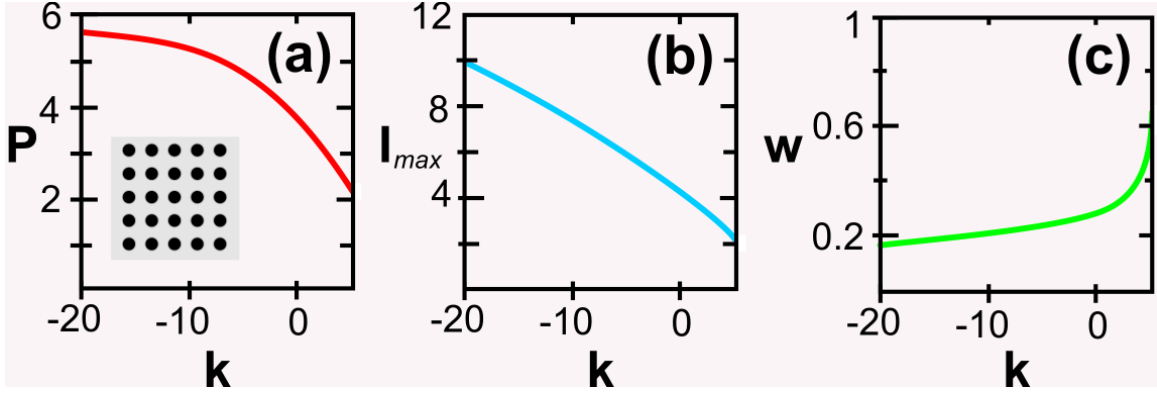


Fig 3-1 A family of two-dimensional lattice solitons. (a) Total power P , (inset: graphic representation of the rectangular lattice, black represents lower refractive index), (b) maximum intensity I_{max} , and (c) beam width are shown as a function of the propagation constant k (all values are given in normalized units).

In this type of lattice, light has the tendency to become localized in the high index areas between the low-index leaky-waveguides. Although the potential maxima are not isolated, this lattice supports stable lattice solitons of the form $\psi = u(\xi, \eta) \exp(ik\zeta)$. We are interested in soliton solutions with eigenvalues in the semi-infinite gap of the spectrum. The properties of this family of stationary solutions are shown in Fig 3-1. In particular, the total power $P = \iint |\psi(\xi, \eta)|^2 d\xi d\eta$, the maximum intensity I_{max} , and the soliton width w , defined as the averaged value $w = \sqrt{\langle \bar{r}^2 \rangle} = \left(\iint \bar{r}^2 |\psi|^2 d\xi d\eta / P \right)^{1/2}$ are presented as a function of the propagation constant k . The solitons shown in Fig 3-1 exhibit both lower and upper power thresholds. The upper power threshold is independent of the lattice type and is equal to the critical power of the NLS equation without a lattice $P_{max} = P_{cr} \approx \pi \cdot 1.86225 \approx 5.85043$ (norm. units). On the other hand, the lower power threshold P_{min} depends on the parameters of the lattice.

We are now interested in the transition from lattice solitons to the regime of single filamentation with power close to P_{cr} . We therefore consider the cylindrically symmetric version of Eq.(3.2-1) which describes well the single filamentation regime and a cylindrically symmetric waveguide array structure for which stable lattice solitons exist as in the case of square lattices,

as it was shown previously. The isolated negative index plasma strings are thus transformed into plasma cylinders and the structure resembles now to a multilayered waveguide. The refractive index of this structure reads:

$$n_{cyl}(x, y, z) = n_o + \Delta n_o \sum_{m=0}^4 f\left(\sqrt{x^2 + y^2} - \left(m + \frac{1}{2}\right)\Lambda\right) \quad (3.2-5)$$

where $f(r)$ is the function describing a generic refractive index distribution, in our case a super-Gaussian of order p : $f(r) = \text{Exp}\left[-(r/w)^{2p}\right]$, w is the typical width of the distribution $f(r)$ and with order $p = 8$, Λ is the period of the structures, n_o is the bulk refractive index and Δn_o is the refractive index modulation amplitude. For the simulations that will be shown in the following, unless stated otherwise, $w = 100 \mu\text{m}$, $\Lambda = 350 \mu\text{m}$ and $\Delta n_o = -3.3 \times 10^{-7}$ corresponding to electron densities of $\rho_{plasma} \cong 1.14 \times 10^{15} \text{cm}^{-3}$. The graphical representation of the lattice can be seen in Fig 3-2.

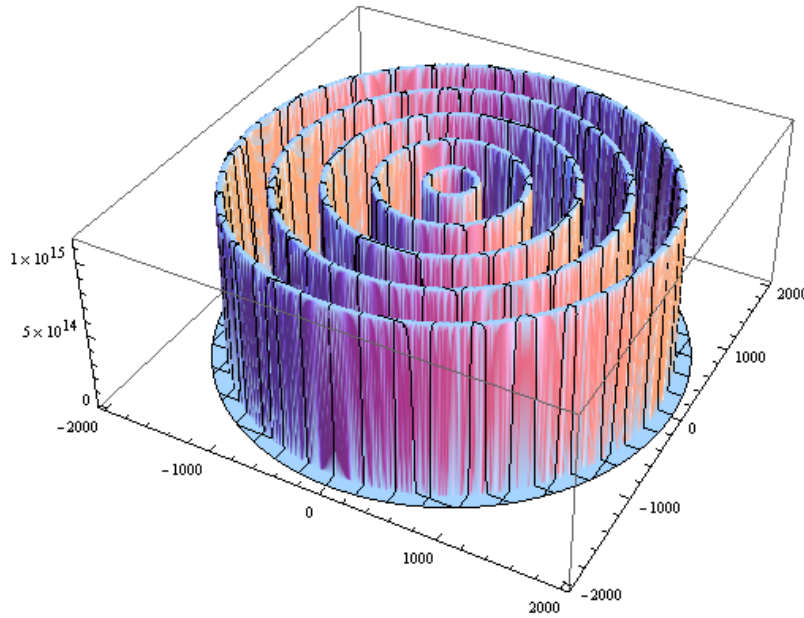


Fig 3-2 3D graphical representation of the electron density distribution used for the lattice realization in the transverse plane.

The input laser pulse is 35 fs long, with a Gaussian spatio-temporal profile, a central wavelength at 800 nm, and a beam waist of 500 μm ($1/e^2$ radius), with no initial wavefront curvature. Simulations were performed for propagation in air at atmospheric pressure, while the input power is either $10^{-6} P_{cr}$ for the linear regime or $1.25 P_{cr}$ for the nonlinear regime.

Fig 3-3 depicts simulation results that show the effect of the lattice on the propagation of pulses in both the linear and nonlinear regimes. Fig 3-3(a) shows the propagation of the pulse in the linear regime ($10^{-6} P_{cr}$) without the presence of the lattice, which corresponds to diffraction of the beam over 3 m of propagation. As the power is increased to $1.25 P_{cr}$ the beam self-focuses and reshapes into a typical filament in air, which extends from 125 cm to 150 cm as shown in Fig 3-3(b). In this case, the peak intensity in the nonlinear focus reaches $3 \times 10^{13} \text{ W/cm}^2$, while the beam waist shrinks down to $\sim 100 \mu\text{m}$. At this intensity, multiphoton ionization is not negligible and the plasma density reaches 10^{16} cm^{-3} . Fig 3-3(c-d) show the effect of the lattice on the propagation of the pulse. In the linear regime (Fig 3-3(c)), the beam is coupled in the lattice but the energy gradually spreads out during propagation as a result of diffraction. When the power is increased the behavior is strikingly different. As shown in Fig 3-3(d) a quasi-stationary soliton-like filament is formed with nearly constant intensity of $5 \times 10^{12} \text{ W/cm}^2$ over 1.8 m of propagation. The peak intensity is about 1 order of magnitude lower than that obtained in the typical filament shown in Fig 3-3(b), i.e. not significant enough to generate through multiphoton ionization a plasma that could affect propagation. This result clearly demonstrates filamentation tailoring while the balance of the nonlinear propagation effects of the high power beam with the linear propagation effects induced by the lattice reveals a new regime bridging solitonic and filamentary propagation. This propagation regime is not the result of a linear guiding effect. As shown in Fig 3-3(c), where only linear effects are present, the coupling between the concentric waveguide structures leads to the spreading of the energy towards the outer waveguides. On the other hand, practically all the energy is maintained in the central waveguide when the input intensity is high, thus the nonlinear propagation effects balance the linear diffraction properties of the lattice. In addition, the results of simulations made with a lattice comprising only the central plasma ring are close to the case without lattice and significantly differs from the propagation in the full lattice.

The ability of the waveguide structure to affect filamentation properties is clearly visualized in Fig 3-4 which shows the evolution of the filament width as a function of the

propagation distance. Without lattice (Fig 3-4(a)), the filament width remains fairly constant, around $100\ \mu\text{m}$, for about 25 cm. Fig 3-4(b) depicts the width of the filament tailored by the lattice. The effect of the waveguide structure on the beam waist of the propagating pulse is striking. The lattice leads to an almost constant beam waist of $\sim 270\ \mu\text{m}$ for a propagation distance of 180 cm. In this case, the beam width actually depends on the lattice period, allowing control over its size and consequently its peak intensity.

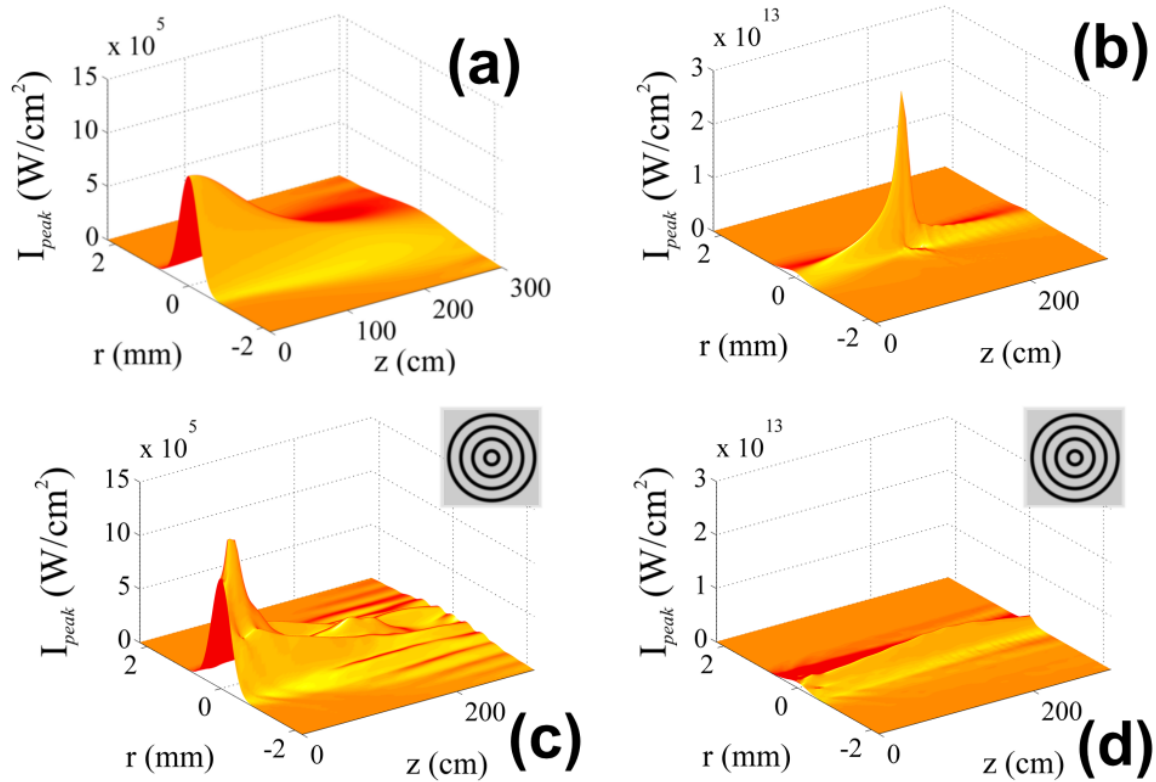


Fig 3-3 Peak Intensity $I_{peak}(r, z)$ for various propagation regimes. The first row (a), (b) refers to propagation in air without the presence of a lattice while the second row (c), (d) refers to the propagation in the presence of a cylindrical lattice. The left column (a), (c) refers to the linear propagation regime $P_{in} = 10^{-6} P_{cr}$ while the right column refers to the nonlinear propagation regime $P_{in} = 1.25 P_{cr}$. (Lattice parameters $\Lambda = 350\ \mu\text{m}$, $w = 100\ \mu\text{m}$, $\Delta n_o = -3.3 \cdot 10^{-7}$) (insets: graphic representation of the cylindrical lattice, black represents lower refractive index)

A systematic study of the effect of lattice parameters (period and modulation) on the propagation of the filament is shown in Fig 3-3(c) and Fig 3-3(d). Fig 3-3(c) depicts the peak intensity as a function of the propagation distance for various depths Δn_o of the effective

refractive index modulation, for a constant period of $\Lambda = 350 \mu\text{m}$. The modulation depth Δn_o is varied from 0 (curve (i)), corresponding to the absence of lattice, to -5.0×10^{-7} (curve (v)). As the modulation becomes deeper the peak intensity drops and its distribution is widened and shifted towards longer propagation distances. Furthermore, these curves show that the balance between nonlinear effects and diffraction by the lattice is quite sensitive to the modulation depth Δn_o . Curve iv in Fig 3-4(c) with $\Delta n_o = -3.3 \times 10^{-7}$ presents the optimum value for this balance. For weaker modulation depths, [curves i, ii, and iii in Fig 3-4(c)], the peak intensity is still high, and nonlinear effects (mainly the optical Kerr effect) dominate. By further strengthening the modulation amplitude, [curve v in Fig 3-4(c)], the peak intensity monotonically decreases due to the prevailing linear effect of the waveguide structure over nonlinear effects.

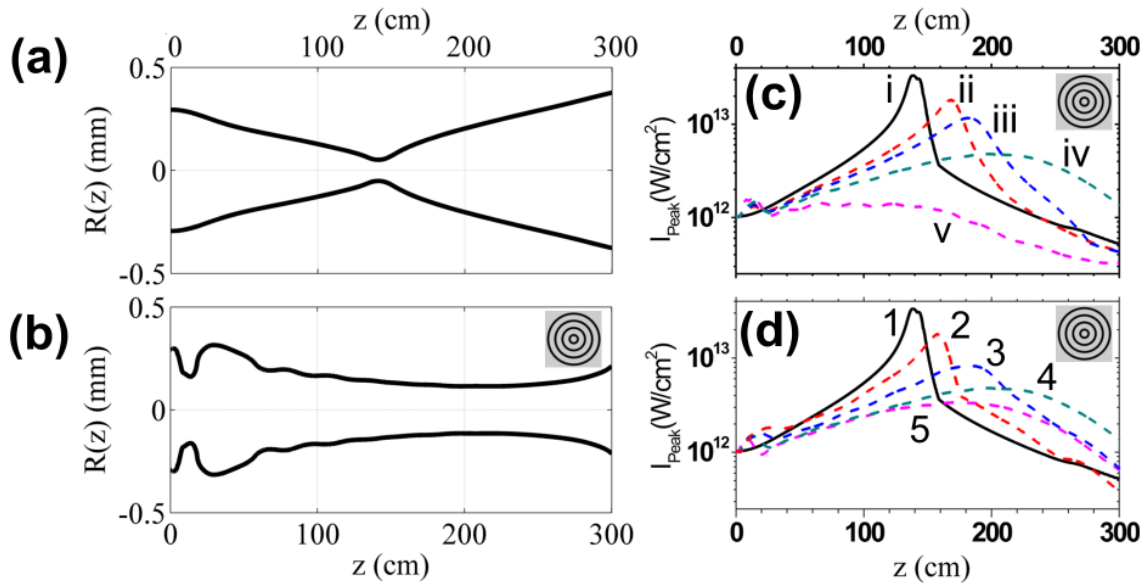


Fig 3-4 (a-b) Beam waist as a function of the propagation distance z . (a) without lattice (b) with lattice. (c-d) Peak Intensity I_{peak} as a function of the propagation distance z for: (c) various lattice strengths (Δn_o) (i) 0, (ii) -2×10^{-7} , (iii) -2.5×10^{-7} , (iv) -3.3×10^{-7} , (v) -5.0×10^{-7} . and (d) various lattice periodicities (Λ) (1) ∞ , (2) $450 \mu\text{m}$, (3) $400 \mu\text{m}$, (4) $350 \mu\text{m}$, (5) $300 \mu\text{m}$. (insets: graphic representation of the cylindrical lattice, black represents lower refractive index)

Another important parameter of the lattice that affects the propagation attributes is its period Λ . Fig 3-4(d) depicts the peak intensity as a function of the propagation distance for various lattice periods, for a constant modulation depth $\Delta n_o = -3.3 \times 10^{-7}$. The period Λ is varied

from infinity [curve (1)], corresponding to the absence of lattice, down to $300 \mu\text{m}$ [curve (5)]. The behavior is similar to that obtained for a variation of the modulation depth. As the lattice period gets smaller, the peak intensity drops and its distribution is widened and shifted towards longer propagation distances. As shown by these curves the regime where nonlinear propagation effects and the linear contribution of the lattice are balanced is also sensitive to the period Λ . Curve 4 in Fig 3-4(d), for which $\Lambda = 350 \mu\text{m}$ presents the optimum value for this balance.

To get a better understanding on the homogeneity of the tailored filament it is best to compare the radial fluence distribution with and without lattice vs z , as it is shown in Fig 3-5. As we can see in Fig 3-5(a), the filament in the absence of the lattice is exhibiting an intense focal spot, typical in the nonlinear regime. In comparison, the fluence of the tailored filament shown in Fig 3-5(b) is much more homogeneous.

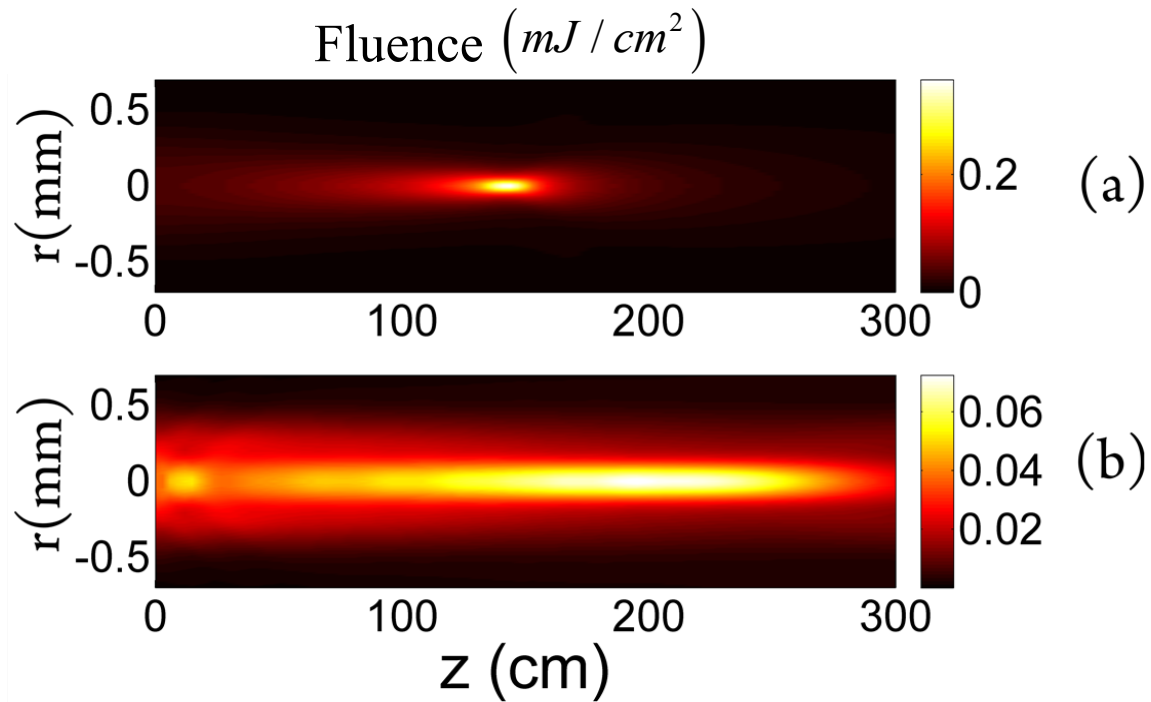


Fig 3-5 Radial fluence distribution along z . (a) Without lattice. (b) With optimal lattice.

In conclusion, we have presented a robust way to tailor the attributes of intense femtosecond laser filaments in transparent media by the use of lattices. By tuning the parameters of the lattice, we enforce the formation of a new kind of filaments that can also be described as

intense lattice solitons, with regulated attributes like their peak intensity, plasma density, beam waist, length and uniformity. We have shown that this filamentation tailoring is not a linear guiding effect but a result of the balance between the nonlinear propagation effects and the linear diffraction induced by the lattice. In contrast to typical filaments, where self-action effects dominate and prohibit control over the filamentation attributes, we manage to gain control by introducing a lattice and appropriately tuning its period and modulation depth. Our approach opens up the way for extensive control of the filament attributes in the spatial and temporal domain, with a big potential impact to various applications utilizing filaments, such as THz generation or attosecond pulse generation, among many others.

3.3 Soliton to filament transition and superposition

It is of particular interest to exploit the transition between lattice solitons and lattice filaments. Fig 3-7 shows simulations of Eq.(3.2-1) when the input pulse keeps the same temporal profile as previously and the input beam corresponds to a lattice soliton, for cylindrical (Fig 3-7(a)) or rectangular lattices (Fig 3-7(b)).

However before exploring the most complex case with all physical effects taken into account, it is better to make a small step first. When all other effects in Eq.(3.2-1) are ignored except diffraction and the optical Kerr effect, pulsed cylindrical lattice solitons remain quasi stationary over extremely long propagation distances. However even without dispersion and non-Kerr nonlinearities, the fact the wavepacket has a Gaussian pulse shape leads to perturbations of the perfectly stationary soliton solution. This happens because the soliton beam shape is calculated based on a given intensity value, the peak intensity in this case. However when we move away from the central time slice, the beam shape does not correspond anymore to the exact soliton solution (for the given lattice) and light is slowly diffracting. This can be seen in Fig 3-6 where the spatiotemporal intensity profiles of a pulsed version of the soliton solution for the radial lattice setup are shown at three different positions along z . We can clearly see that after 16.8 m of propagation, light is diffracting close to the tails of the pulse and redirected to the second ring waveguide. After 26.6 m the pulse has clearly split in time, since the leading and

trailing parts of the pulse cannot support solitonic propagation due the low intensity. Close to the center time-slice the pulse is propagation quasi-stationary with a slightly lower peak intensity. As we can see the propagation of solitons is extremely sensitive, since even the transition from a continuous wave spatial soliton to its pulsed version results in observable perturbations in the propagation regime.

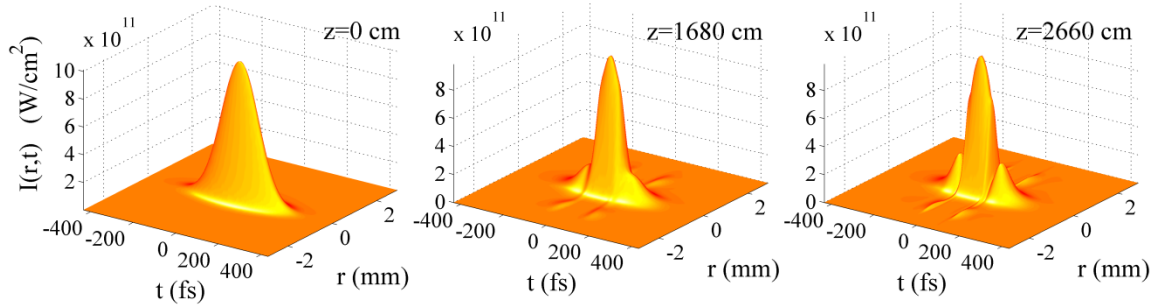


Fig 3-6 Spatiotemporal intensity distribution at different positions in z of the pulsed version (200 fs at FWHM) of soliton solution for the radial lattice setup.

When GVD and higher order nonlinearities (multiphoton ionization, plasma defocusing, optical shock) are also taken into account as in the filamentation dynamics, the propagation distance of lattice solitons dramatically reduces (5 m in the example of Fig 3-7(a)). In general, as the maximum intensity of the input lattice soliton increases and its beam width decreases, high-order effects become more important, leading to faster reshaping of the lattice soliton into a standard filament. Without the presence of the lattice, a pulsed lattice soliton is rapidly self-focused and a filament is formed reaching intensities as high as $3 \times 10^{13} \text{ W/cm}^2$ (“*normal filament*” in Fig 3-7(a)). The lattice regulates the pulse propagation, as is clearly shown in Fig 3-7(a). The propagation distance of the lattice filaments and that of the lattice soliton (with all effects included) are in the same order of magnitude. More generally, our simulations show that the features of lattice filaments closely follow those of lattice solitons. Furthermore, filamentation tailoring by means of lattices is feasible with various types of lattices beyond the cylindrical lattices discussed above. For instance, results using rectangular lattices, obtained from (3+1)D simulations with “frozen” time (pulse duration fixed), are shown in Fig 3-7(b) and

demonstrate tailoring properties of filaments in a similar way to the cylindrical ones. A more detailed presentation of the square lattice geometry will be given later on.

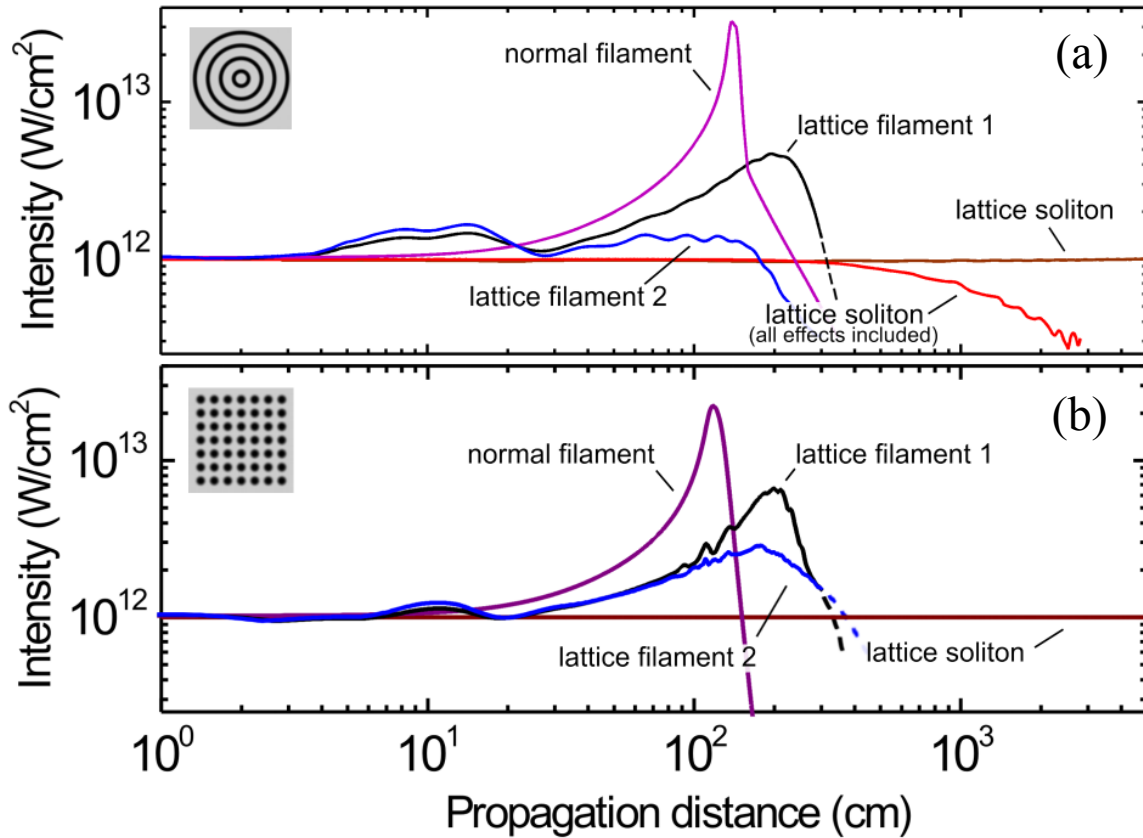


Fig 3-7 Peak intensity as a function of propagation distance reveals the transition dynamics between lattice solitons and lattice filaments. (a) 2D+1 (cylindrically symmetric) simulations. (b) 3+1D (frozen time) simulations using a rectangular plasma lattice. (a) and (b): *Lattice soliton*: pulsed version of the cylindrical lattice soliton solution (taking into account only diffraction and Kerr effect). *Lattice soliton (all effects included)*: including GVD, multiphoton ionization and plasma defocusing. *Normal filament*: typical filament in air from a Gaussian spatio-temporal pulse. *Lattice filament 1,2*: tailored lattice filaments for two different cases of lattice strength (Δn). (insets: graphical representation of the lattices used, black represents lower refractive index)

Finally, it is worth noting that the same approach of filamentation tailoring using lattices in gases can be used as well for filaments in transparent solids. In this case the lattice can be either

transient (like plasma lattices) or permanently written in the bulk in the form of an array of waveguides (see section 3.7), which can be easily fabricated (see for instance [135])

To summarize this section, we have presented a robust way to tailor the attributes of intense femtosecond laser filaments in transparent media by the use of lattices. By tuning the parameters of the lattice, the formation of a new kind of filaments is enforced that can also be described as intense lattice solitons, with regulated attributes like their peak intensity, plasma density, beam waist, length and uniformity. It is shown that this filamentation tailoring is not a linear guiding effect but a result of the balance between the nonlinear propagation effects and the linear diffraction induced by the lattice. In contrast to typical filaments, where self-action effects dominate and prohibit control over the filamentation attributes, we manage to gain control by introducing a lattice and appropriately tuning its period and modulation depth.

3.4 Temporal solitons and nonlinear light bullets

One of the major goals in the study of nonlinear wave interactions in optics is the generation of pulses that propagate in the form of localized wavepackets in all the transverse dimensions of space, as well as in time i.e., nondiffracting and non-dispersing [136]. Localization is typically achieved by nonlinearity that competes with the natural spreading of the wave in space or time. (N+1) dimensional solitons have N localized dimensions and the 1 refers to the propagation dimension. Numerous observations of (1+1)D solitons were made in Kerr media with refractive index change $\Delta n = n_2 I$ that vary linearly with the wave intensity. (N+1)D solitons in Kerr media with $N > 2$ are however unstable. The prototypical model for (3+1)D solitons, the light bullet proposed by Silberberg in 1990, triggered intense experimental and theoretical activity in the field so as to generate spatio-temporal solitons [137]. Even though the field has greatly advanced in the last 20 years, up to date a true (3+1)D soliton has never been reported [136].

3.4.1 Previous works in the literature

The simplest case is the (1+1)D temporal soliton inside a single mode optical fiber. The existence of this soliton was first predicted in 1973 [138], and observed later in 1980 [139]. The basic principle tells us that by choosing an appropriate wavelength inside the anomalous dispersion regime of an optical fiber, the nonlinear phase shift due to the Kerr effect can be perfectly matched by the dispersion inside the glass core. As a result, a stationary wave in time is created that can propagate inside the fiber over many kilometers. Additional research that followed has led to commercial soliton based fiber-optic telecommunication systems [140, 141]. (1+1)D spatial solitons were observed in 1990 [142] by launching a beam in a planar waveguide, effectively limiting diffraction to only one dimension. In analogy to temporal solitons, diffraction must be perfectly matched by the Kerr induced self-focusing in order to create a stationary beam in one spatial dimension. (2+1)D spatial solitons on the other hand are unstable in homogeneous Kerr media since they suffer from modulation instability. The reason is that self-focusing leads only to stronger self-focusing, and without a saturating mechanism even small xy fluctuations will lead to beam collapse. One type of saturating mechanism was provided by the photorefractive effect in electro-optic materials, and in 1993 the first (2+1)D spatial soliton was observed [117, 143]. Another type of saturating mechanism was created through the parametric interaction between multiple beams in $\chi^{(2)}$ media. In this case the cascading effect between multiple $\chi^{(2)}$ processes creates a tunable effective $\chi^{(3)}$ which acts as a saturating nonlinearity. The first (2+1)D solitons using this technique were generated in 1996 [144] and great progress has been made since [145]. One of the main drawbacks of both of the above techniques is that the use of high intensity pulses is prohibited due to the low damage threshold of both photorefractive and $\chi^{(2)}$ materials.

The generation of full (3+1)D spatiotemporal solitons is the most difficult task, since a balance in all 4 dimensions must be reached, utilizing numerous linear and nonlinear effects. It was predicted [137] that in anomalous dispersion homogeneous Kerr media, collapse can be arrested by diffraction and anomalous dispersion which oppose self-focusing and self-compression, creating this way a light-bullet. But since 2 spatial dimensions are needed, this approach is unstable due to modulation instabilities. In reality the collapse is arrested by

multiphoton ionization and stimulated Raman scattering, and since these are dissipative processes a light bullet cannot be sustained due to high nonlinear losses. Many lossless mechanisms have been proposed for the stabilization of the above process. The effect of higher order dispersion [146], competing higher order nonlinearities [147], materials with symmetric nonlocal nonlinear response [148], optical lattices [149] and nonlocal media [150] are all good candidates for the stabilization and the arrest of collapse. But until now no configuration has been found that supports stable light bullets. In one of the latest works [151] it is shown that the propagation of light inside optical tandems, i.e. radially periodic rings with different dispersive and nonlinear properties, can lead to the creation of stable light bullets.

The use of an artificial saturable Kerr nonlinearity in order to avoid pulse collapse limits these approaches strictly to theoretical study. In the majority of setups used so far, anomalous dispersion materials is needed to counterbalance temporal collapse, which is a limiting factor in experimental applications. In the most extreme cases the propagation regime of the soliton or bullet-like structure is taking place in the weak nonlinear regime, since modulation instabilities and nonlinear losses have devastating effect on the bullet-stability. In addition higher order effects like multi-photon absorption, optical field ionization, pulse self-steepening and plasma defocusing are rarely taken into account. Different types of spatiotemporal localized structures such as X-waves [66], Bessel-Airy linear bullets [152] and Airy-Airy-Airy nonlinear light bullets [153] have been experimentally observed, whereas three dimensional vortices have been predicted. The main limiting factors in the experimental realization of light bullets are the anomalous dispersion and the slow time response of nonlinear media that mathematically support stable bullets.

The availability of intense ultra-short light bullets in normally dispersive media would however offer ultimate control over a high power wavepacket, which could be used in various materials and have applications in fields like THz generation [87], telecommunications, optical metrology and sensing, long range femtosecond filamentation [154] and attosecond pulse generation [10, 78].

In the next section we will exploit the filament dynamics in the presence of the lattice described in section 3.2 in both the spatial and the temporal domain. We find from numerical simulations that it is possible to generate spatiotemporal structures supporting intense laser propagation in normally dispersive air at a wavelength of 800 nm and remaining almost invariant

(in space, time and maximum intensity) for over 90 cm in a lattice. We call these structures intense dynamic bullets (IDB) to distinguish them from perfectly stationary light bullets or solitons. The lattice is essential in the formation of the IDB. The role of each physical mechanism in the formation of the IDB is also analyzed.

3.4.2 Intense dynamic bullets in a periodic lattice

The lattice consists of concentric rings that describe a perturbation of the refractive index. These perturbations can be realized using different approaches for various transparent media. For example plasma can be used in the case of gases. One dimensional plasma lattices have recently been generated in air by interference of intense IR light beams for periodicities ranging from 500 nm [130] to 100 μm [131] and electron densities higher than 10^{18} cm^{-3} . The generation of cylindrically symmetric lattices is demanding but feasible since their Fourier transform is simply a sum of zero order Bessel functions. Note that the effect of such lattices on intense pulse propagation has not been explored yet. Thus, in principle, illumination of an amplitude mask allows the generation of intense concentric rings in the Rayleigh range of a long Fourier transforming lens. Furthermore, one could consider the use of positive or negative Δn lattices exploiting the molecular alignment of air molecules (or other gases). In the latter case the laser intensities needed are even lower than the ones needed for ionization and one can use pulse trains to further enhance the alignment [132] and consequently the strength of the lattice. Finally, in the case of filamentation in transparent solids, like glasses, one can use permanently written lattices in the bulk of the glass [155].

In our case, the cylindrically symmetric refractive index modulation is identical to the one used in section 3.2, and can be written as $n_{\text{cyl}}(r) = n_0 + \Delta n$, for $\Delta n = \Delta n_0 \sum_{m=0}^5 f(r - r_m)$.

Where $f(r) = \exp\left[-(r/w)^{2p}\right]$ is the function describing the refractive index distribution of each ring, in our case a super-Gaussian of order $p = 8$ with width $w = 100 \mu\text{m}$. The position of each ring is defined by $r_m = [m + 1/2]\Lambda$. The period of the lattice is $\Lambda = 350 \mu\text{m}$ and the refractive index modulation is $\Delta n_0 = -3 \times 10^{-7}$. Assuming that plasma is used to generate such a

modulation, this corresponds to a moderate plasma density of $\sim 10^{15} \text{ cm}^{-3}$. The laser pulse used in the simulations has a Gaussian spatiotemporal profile with duration of 35 fs at FWHM and 500 μm beam width ($1/e^2$ radius). The 150 μJ pulse is launched in the center cylinder of the refractive index modulation as it is shown in Fig 3-8.

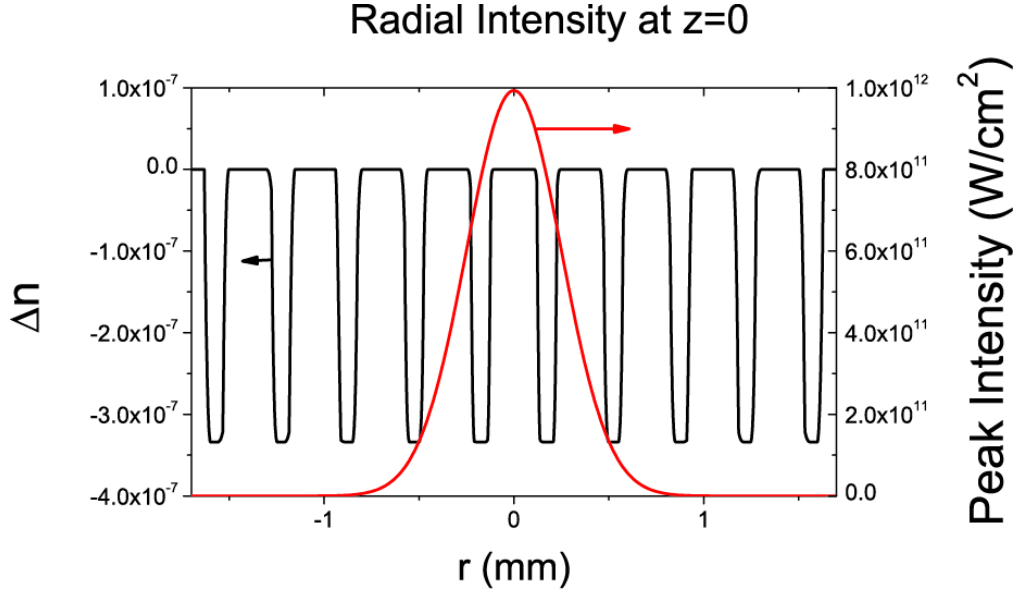


Fig 3-8 Input radial intensity distribution superimposed on the lattice potential.

The model relies on a nonlinear propagation equation along the z direction for the frequency components $\hat{\mathcal{E}}(r, z, \omega)$ of the envelope $\hat{\mathcal{E}}(r, z, t)$ of the laser pulse coupled with an evolution equation for the electron density $\rho(r, z, t)$ generated by the intense pulse [10]. The model used in section 3.2 can be written in the frequency domain as follows:

$$\frac{\partial \hat{\mathcal{E}}}{\partial z} = i \left[\frac{\Delta_{\perp}}{2K_{\omega}} + D(\omega) + k_0 \Delta n \right] \hat{\mathcal{E}} + i \frac{\omega}{2c} \frac{\hat{P}_{NL}}{\epsilon_0} \quad (3.4-1)$$

$$\frac{\hat{P}_{NL}}{\epsilon_0} = 2n_0 n_2 \overline{|\mathcal{E}|^2} \mathcal{E} - \frac{\omega_0^2}{\omega^2} \frac{\overline{\rho}}{\rho_C} \mathcal{E} - \frac{c\beta_K}{\omega} \overline{|\mathcal{E}|^{2K-2}} \mathcal{E} \quad (3.4-2)$$

$$\frac{\partial \rho}{\partial t} = \sigma_K |\mathcal{E}|^{2K} \rho_{nt} \quad (3.4-3)$$

The first term on the right hand side of Eq.(3.4-1) describes diffraction and space-time focusing through the operator $K_\omega \equiv k_0 + k_0' \cdot \delta\omega$, $\delta\omega \equiv (\omega - \omega_0)$, $k_0 = k(\omega_0)$.

$k(\omega) \equiv \sum_m k_0^{(m)} (\delta\omega)^m / m!$ denotes the dispersion relation in air and $k_0^{(n)} = \left. \frac{\partial^n k}{\partial \omega^n} \right|_{\omega_0}$ denote the

dispersive coefficients corresponding to the frequency ω_0 of the carrier wave. Dispersion and the effect of the lattice are described by $D(\omega) \equiv k(\omega) - K(\omega)$ and Δn , respectively. The

nonlinear polarization \hat{P}_{NL} in Eq.(3.4-2) accounts for the optical Kerr effect, plasma defocusing, and multiphoton absorption (MPA), first calculated in the temporal domain and transformed into spectral components of \hat{P}_{NL} . Pulse self-steepening is given by the explicit frequency dependence

$\omega \equiv \omega_0 + \delta\omega$ in Eq.(3.4-1). In some simulations discussed below and referred to as "Shock term off", its effect was switched off by setting $\omega = \omega_0$ in the explicit frequency dependence of the

nonlinear polarization in Eqs.(3.4-1) and (3.4-2). The gas filling the gap of the lattice is air with nonlinear index $n_2 = 3.2 \times 10^{-16} \text{ W/cm}^2$, multiphoton ionization and absorption cross sections

$\sigma_K = 3.4 \times 10^{-96} \text{ s}^{-1} \text{ cm}^{16} \text{ W}^{-8}$ and $\beta_K = K \hbar \omega_0 \rho_{nt} \sigma_K$ for $K = 8$ photons. The density of neutral oxygen molecules is $\rho_{nt} = 0.5 \times 10^{19} \text{ cm}^{-3}$ and the critical plasma density is $\rho_C \approx 1.7 \times 10^{21} \text{ cm}^{-3}$.

From Marburger's formula $P_{cr} = \frac{3.77 \lambda^2}{8 \pi n_0 n_2}$, the critical power for collapse of a Gaussian

beam is $P_{cr} \sim 3 \text{ GW}$. In the following we consider pulses with peak power of $1.25 P_{cr}$ and we stress that the critical power is only used as a reference indicating that a beam with the same input power would collapse in a pure Kerr medium. Due to the weak dispersion in air ($k'' \sim 0.2 \text{ fs}^2 / \text{cm}$), self-focusing prevails for input powers only a few percent above P_{cr} [156].

Fig 3-9 (**Video_IDB.mov**) depicts the spatiotemporal reshaping of the laser pulse as it propagates in air without (top row) or with (bottom row) the lattice. In the case of standard filamentation in air, the intense pulse initially shrinks both in space and time due to the Kerr nonlinearity. At the nonlinear focus ($z \sim 130 \text{ cm}$), the pulse becomes sufficiently intense to

generate an underdense plasma which defocuses the pulse trailing part while nonlinear effects including the Kerr effect and multiphoton absorption compete to sustain propagation of the leading part in the form of a filament ($130 \text{ cm} < z < 150 \text{ cm}$). Beyond the filamentation stage $z > 150 \text{ cm}$, the pulse finally widens due to diffraction and dispersion. Such behavior is typical for pulses undergoing filamentation and is accompanied by high nonlinear losses [10].

Propagation of the same intense pulse inside the lattice is significantly different: during the initial self-focusing stage, the beam does not shrink as much as it does without the lattice. After the initial self-focusing stage, the spatiotemporal dynamics reach a quasi-equilibrium. The intensity profile of the resulting IDB remains almost stationary in both space and time for about 1 m, *i.e.* a factor of 5 larger than the filamentation distance in air for the same input pulse. The IDB finally starts to spread out slowly at $z \sim 240 \text{ cm}$. The peak intensity for the two regimes as a function of the propagation distance is shown in Fig 3-11.

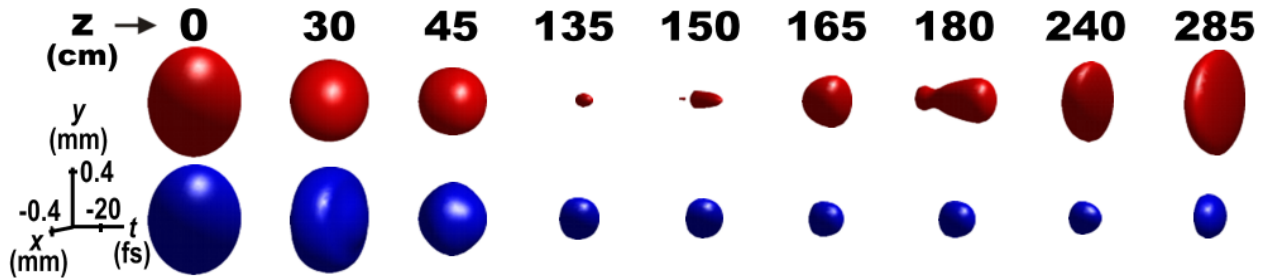


Fig 3-9 3D iso-surface plots of the intensity distributions for the cases of a standard filamentation (red iso-surfaces, first row) and the IDB formation inside the periodic lattice (blue iso-surfaces, second row), for various propagation distances (Video_IDB.mov). Isovalue is set to half of the peak intensity at each z position.

In Fig 3-10 we can see the energy that is contained in various sized cylinders for the normal filament and the IDB along propagation distance. The radius of the cylinder is varied from $100 \mu\text{m}$ (blue line) up to the whole numerical box at 2.2 mm (purple line). As we can clearly see radial energy distribution is much more homogeneous in the case of the IDB, especially for small cylinders. We can see in Fig 3-10(b) that the energy contained in the cylinder with $100 \mu\text{m}$ radius is slowly but constantly increasing (with exception of the small transitional stage at the first 25 cm) up in the first 2 m of propagation. The energy is starting to spread out after $z \sim 240 \text{ cm}$, which corresponds to the point where the IDB breaks down. On the other hand, the standard filament is showing a strong energy concentration at the same radius.

This increase however only lasts a few centimeters before rapidly decreasing due to beam spreading and nonlinear losses (Fig 3-10(a)).

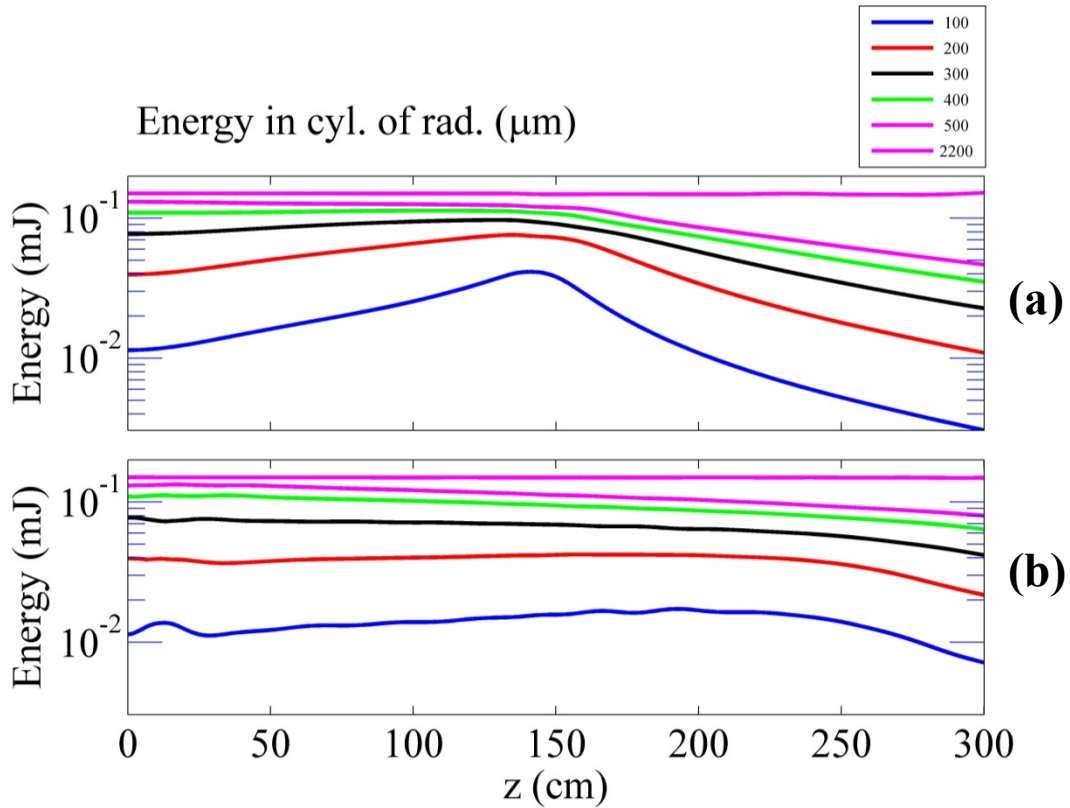


Fig 3-10 Energy contained in different cylinders (from 100 μm up to 2.2 mm radius) for (a) the normal filament and (b) the IDB, versus propagation distance.

In order to investigate the interplay between different physical mechanisms responsible for the IDB formation, we performed numerical experiments by switching off each of the relevant effects, at $z = 150$ cm, where the IDB is already formed. Namely, we considered the effects of dispersion, self-steepening (shock-terms) and the periodic potential. Fig 3-11(b) shows the radially averaged pulse duration over a 100 μm radius which corresponds to the central cylinder of the lattice. The duration of the IDB remains nearly constant to about 15 fs over 90 cm (continuous curve). When group velocity dispersion (GVD) is switched off at $z = 150$ cm, the IDB with peak power above P_{cr} undergoes self-compression due to the competition between self-steepening and nonlinearity (Kerr focusing and plasma defocusing). This leads to a

continuous decrease of the pulse duration [dash-dotted curve in Fig 3-11(b)] that ultimately becomes shorter than the single cycle limit (not shown here) and results from a well identified singularity of the standard filamentation model in the absence of GVD [157]. The periodic lattice modifies the effective diffraction of the beam and plays a crucial role in its stabilization since the pulse duration increases (dotted curve in Fig 3-11(b)) if the lattice is replaced by air. In this case, the beam survives until $z = 170$ cm but then rapidly disperses. Finally the dashed curve depicts the pulse duration if the shock-term is switched off at $z = 150$ cm. The comparison of the dashed and continuous curves shows that the shock-term is essentially limiting dispersion since the pulse broadens in its absence.

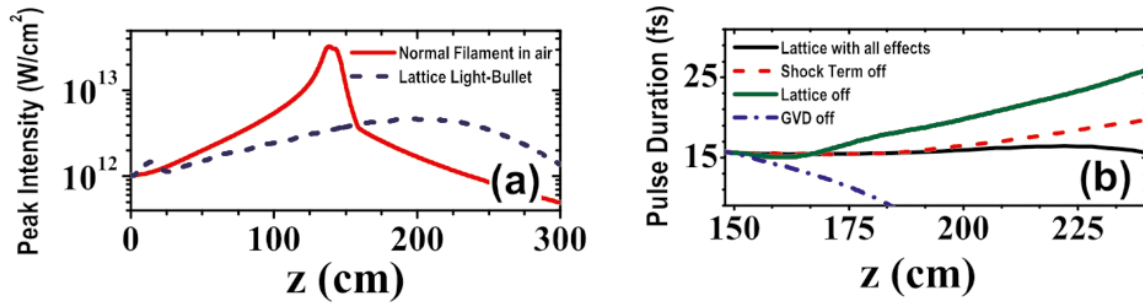


Fig 3-11 (a) Peak intensity vs z for a standard filament in air (continuous line) and the IDB (dashed line). (b) Pulse duration (Radially averaged over $100 \mu\text{m}$) of the IDB vs propagation distance z when all effects are accounted for (continuous curve) or when a specific effect is switched off at $z = 150$ cm: dotted curve: the lattice is removed; dashed curve: self-steepening is switched off; dash-dotted curve: GVD is switched off.

From these numerical experiments, we identified the physical effects that dynamically balance each other to generate an IDB via nonlinear propagation in the periodic potential. Fig 3-12 shows the evolution of typical lengths characterizing these effects, namely the Kerr effect

$$L_{Kerr} = (k_0 n_2 I^2)^{-1}, \quad \text{diffraction } L_{Diff} = k_0 R^2 / 2, \quad \text{Dispersion } L_{GVD} = T^2 / (2 \cdot k''), \quad \text{MPA}$$

$$L_{MPA} = 1 / (2 \beta_K I^{K-1}), \quad \text{self-steepening } L_{Shock} = cT / (n_2 I) \quad \text{and the effect of the lattice}$$

$$L_{Lat} = (k_0 \Delta n)^{-1}. \quad \text{In these expressions, the peak intensity of the pulse } I \text{ varies as a function of}$$

propagation distance, as well as the filament width R and the shortest pulse duration t_p supported by the pulse spectrum. For standard filamentation (Fig 3-12(a)), the main prevailing effect is

MPA as indicated by the shortest lengths of all effects over the whole filamentation distance $130 < z < 150$ cm. The Kerr and self-steepening effects need centimetric lengths to play a role while diffraction and dispersion need about 10 cm. Thus the filament lives for about $20 \times L_{MPA}$ or equivalently one L_{Diff} or L_{GVD} . For the IDB (Fig 3-12(b)), the intensity is stabilized by the lattice at a lower level than that reached in the filament, thus the Kerr effect prevails with a typical length in the range 10-15 cm over the whole propagation distance $150 < z < 240$ cm. Two independent equilibriums take place in the spatial and temporal dimensions: For the spatial equilibrium, diffraction and the lattice effect with lengths in the range 30-40 cm both compete with the Kerr effect as $1/L_{Kerr} \sim 1/L_{Diff} + 1/L_{Lat}$. For the equilibrium of the pulse profile, self-steepening and dispersion compete with self-phase modulation induced by the Kerr effect as $1/L_{Kerr} \sim 1/L_{Shock} + 1/L_{GVD}$. These two separate equilibriums maintain the peak intensity below ionization threshold for a propagation distance of about $10 \times L_{Kerr}$ or $2 \times L_{GVD}$, which is a factor of at least 5 larger than the filamentation length for the same input pulse.

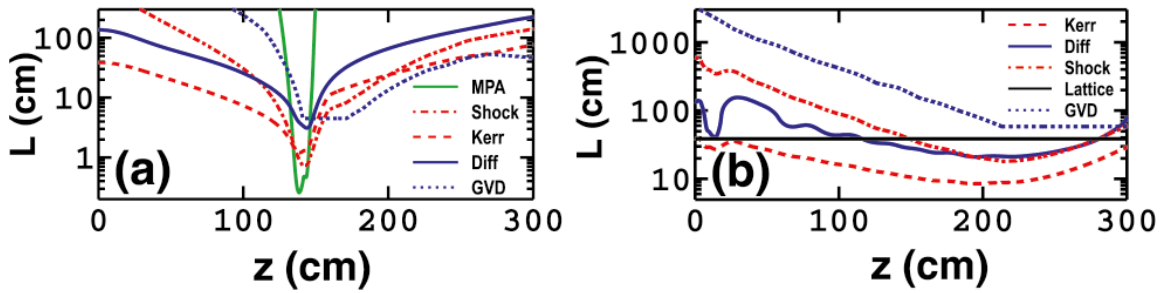


Fig 3-12 The smallest lengths characterize the most important physical effects in competition along the propagation axis. (a) Case of a standard filament. (b) Case of an IDB in a periodic lattice.

3.4.3 The effect of random noise

Up until now only perfect noise-less Gaussian pulses have been used in the numerical simulations. However real femtosecond laser sources always contain some amount of noise in the beam in and pulse shapes. This random noise, originating from the laser cavity, is the main reason multi-filament structures form in the high power regime.

In order to test the durability of the IDB shown in Fig 3-9, the simulations of both normal filament and IDB were repeated with the addition of random noise in the input beam profiles, imitating this way a real laser source in the laboratory. The results can be seen in Fig 3-13, where the 3D isosurfaces of the normal filament and the IDB can be seen at different positions in z . As we can clearly see the IDB (second line) is not as stable as in the ideal noise-free case. In the first 30 cm of propagation the wavepacket is showing signs of stability loss, which however are smoothed out at $z = 135$ cm. As in the ideal case the IDB is propagating relatively unchanged up to $z = 240$ cm, which shows that the IDB is quite resistant to the added noise. However when the IDB starts to break-up after $z = 240$ cm, it does so in much more abrupt fashion compared to noise-less case. As we can in the last frame of Fig 3-13, at $z = 285$ cm, the IDB can barely be recognized with the chosen iso-value.

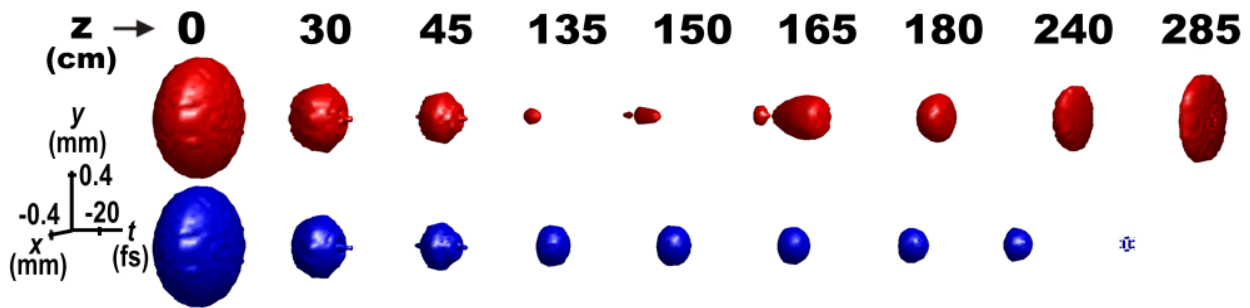


Fig 3-13 Same as Fig 3-9 with the addition of random noise.

For the standard filament case with noise, shown in red in the first line of Fig 3-13, the propagation is not much different than in the ideal case (first line in Fig 3-9). Since the power is not high enough to support multiple filamentation, no modulation instability is observed and the spatiotemporal reshaping is very similar with the noise-less case.

To summarize sections 3.4.2 and 3.4.3, we have shown numerically that filamentation of intense pulses in a radial symmetric periodic potential leads to the generation of intense dynamic bullets. Their intensity is above $10^{12} \text{ W} / \text{cm}^2$ and their power is above P_{cr} while they exhibit a quasi-stationary spatiotemporal profile for long propagation distances as a result of the competition of linear and nonlinear effects. In the spatial domain the Kerr self-focusing is mainly balanced by the combined action of the effective lattice diffraction whereas in the temporal

domain self-steepening and normal dispersion compete with self-phase modulation. Since the lattice parameters are in a feasible regime for experimental realization (refractive index changes in the order of 10^{-7} and periodicity of $350 \mu\text{m}$), these intense dynamic bullets can be realized in transparent media using permanent or transient refractive index modification induced by high power commercial fs laser sources. In addition the IDBs proved to be resistant to numerically added random noise in the starting intensity profile of the pulse.

3.5 Increasing the power of tailored filaments using cylindrical lattices

Up to this point we have seen that by using a cylindrical symmetric lattice consisting out of concentric rings, the propagation of intense laser pulses can be controlled both spatially and temporally. Although the pulse power is above the critical value ($1.25 P_{cr}$), the increase of power is the next logical step.

For all the following numerical experiments in this section (3.5 - 0) the initial laser pulse is similar to the one used in the previous sections ($\lambda = 800 \text{ nm}$, 35 fs). The main difference lies in the fact that the input power is doubled to $2.5 P_{cr}$. However, since filamentation tailoring is based on the equilibrium between lattice diffraction and self-focusing, the starting peak intensity of the beam is very important. Because of this, the beam waist is increased to $707 \mu\text{m}$, which corresponds to a factor of $\sqrt{2}$ so that the starting peak intensity is kept at the same value as in sections 3.2 and 3.4.2. Following the same reasoning, the lattice period has to be appropriately increased by the same factor, to $\Lambda = 495 \mu\text{m}$. This way a similar result should be obtained if the refractive index modulation depth and ring thickness is kept close to the values used in the previous numerical experiments ($\rho_0 = 1.14 \times 10^{15} \text{ cm}^{-3} \Rightarrow \Delta n_0 = -3.3 \times 10^{-7}$, $w = 100 \mu\text{m}$).

However this goal is not so easily reached since the dynamic spatiotemporal equilibrium proves to be quite sensitive an increase in input power. In simulations it proved impossible to obtain any type of IDB for higher power by just tuning the lattice characteristics (period Λ , waveguide thickness w and refractive index depth Δn_0). As we can see in Fig 3-14(b), this is because the center part of the beam (inside the first ring), has enough power to generate a

filament on its own, effectively neglecting the regulating effect of the lattice entirely. When Δn_0 is doubled (shown in Fig 3-14(c)) and the lattice strength is increased, the filament is completely contained in the center waveguide, which is effectively the opposite of our goal. This wave guiding effect is only getting stronger as the lattice strength is increased further, as can be seen in Fig 3-14(d) where the Δn_0 is increased by a factor of 5. For comparison the $2.5 P_{cr}$ standard filament (without lattice) is depicted in Fig 3-14(a).

An intuitive approach is the addition of a diffracting element inside the center ring, in order to suppress the on-axis filament formation. Such elements can be a diverging lens, an additional on-axis super-Gaussian anti-waveguide, or even a miniature lattice of much smaller scale. In any case the diffractive element must be impervious to the high intensity of the laser pulse, thus as before an electron plasma will be used to simulate it. Aside from the addition of a diffracting element, in all three cases the main lattice will remain unchanged. Results of these approaches will be analyzed in the next sections (0 - 0).

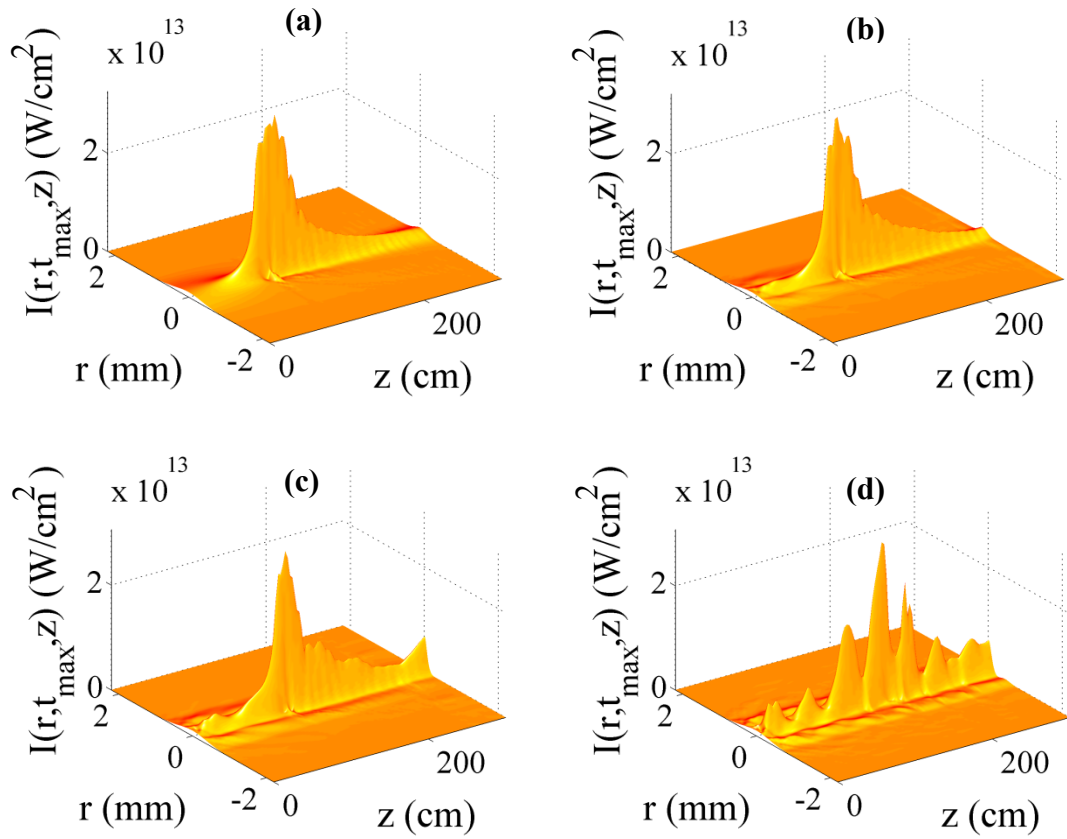


Fig 3-14 Radial peak intensity along propagation distance for a 2.5 Pcr filament (a) without lattice, and inside the radial plasma lattice with maximum plasma density of (b) $\rho = \rho_0 = 1.14 \times 10^{15} \text{ cm}^{-3}$ ($\Delta n_0 = -3.3 \times 10^{-7}$), (c) $\rho = 2 \times \rho_0$, and (d) $\rho = 5 \times \rho_0$.

3.5.1 Addition of a diverging lens to the cylindrical lattice

The first approach explored will be the addition of a diverging plasma lens inside the center ring. The refractive index distribution of the lens is chosen to be Gaussian, which ideal since the input beam shape of the laser also Gaussian.

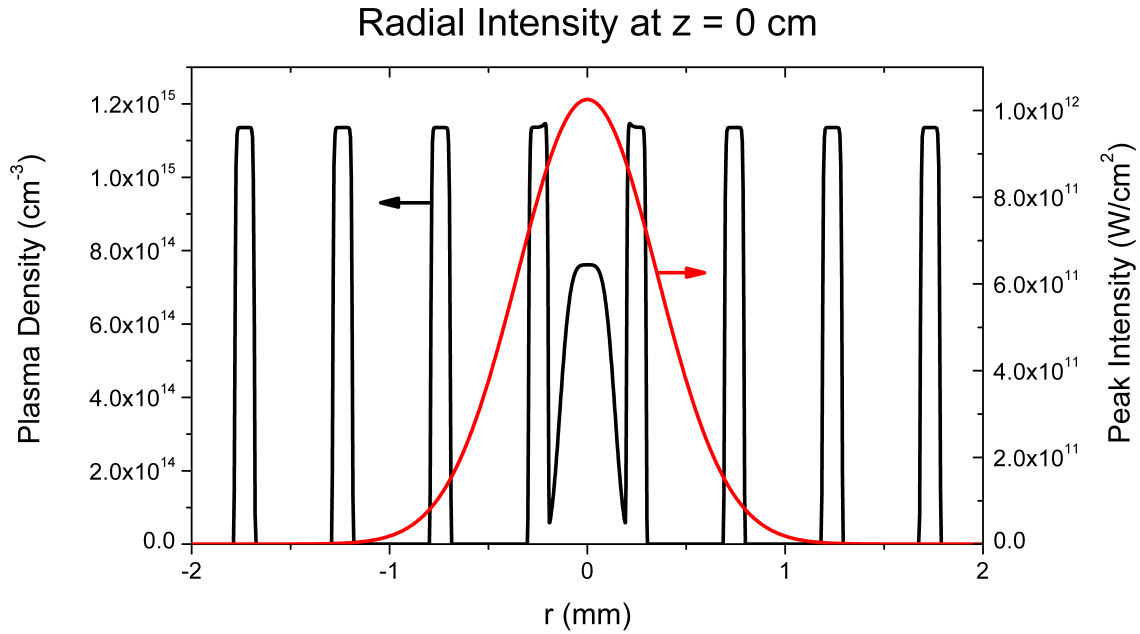


Fig 3-15 (black line) Lattice and diverging lens. (red line) Gaussian beam profile superimposed on the radial lattice. The maximum electron density of the rings of the main lattice is

$\rho = \rho_0 = 1.14 \times 10^{15} \text{ cm}^{-3} \left(\Delta n_0 = -3.3 \times 10^{-7} \right)$, while the maximum density of the central plasma

lens is $\rho = 0.67 \times \rho_0$.

Since the refractive index modulation of plasma is negative, the lens must have a convex shape in order to diverge light off-axis. The plasma lens has a diameter of 300 μm at FWHM with a maximum plasma density which is 67% of the plasma density of the main lattice ($\rho = 7.64 \times 10^{14} \text{ cm}^{-3}$), which was found to be the optimum value. The input beam and lattice with the added diverging lens are shown in Fig 3-15.

The result of the simulation can be seen in Fig 3-16, where the radial intensity along z is shown over 6 m of propagation. As we can see the addition of the diverging lens is able to suppress the filament creation and regulate the peak intensity at values under the ionization threshold. The maximum intensity value reached is $\sim 2 \times 10^{12} \text{ W/cm}^2$, which is varying slightly over 2 m. After 5 m of propagation the beam breaks up and diffraction dominates.

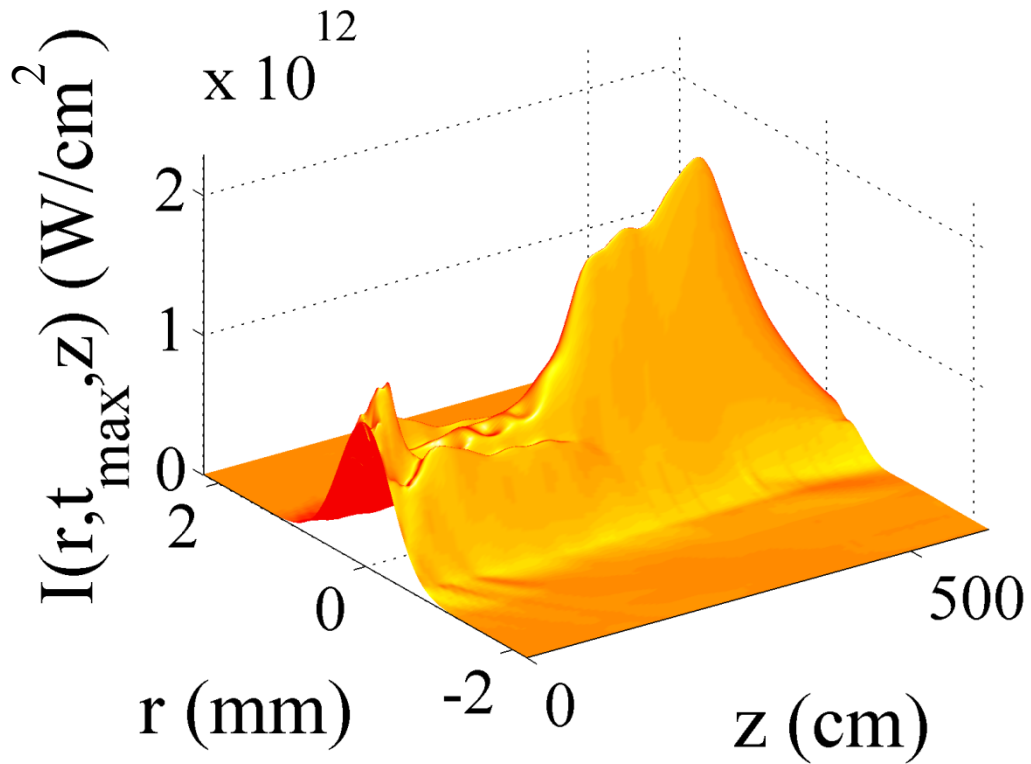


Fig 3-16 Radial intensity along propagation of the $2.5 P_{cr}$ tailored filament, inside the radial lattice with the addition of the on-axis diverging plasma lens.

3.5.2 Addition of an anti-waveguide to the cylindrical lattice

The second approach is the addition of an on-axis anti-waveguide in order to prevent the filament formation. For this setup a standard super-Gaussian index modulations was used. The super-Gaussian function is of 8th order like the lattice itself, and the maximum index depth is $3 \times \Delta n_0$ which corresponds to an electron density of $\rho = 3.42 \times 10^{15} \text{ cm}^{-3}$.

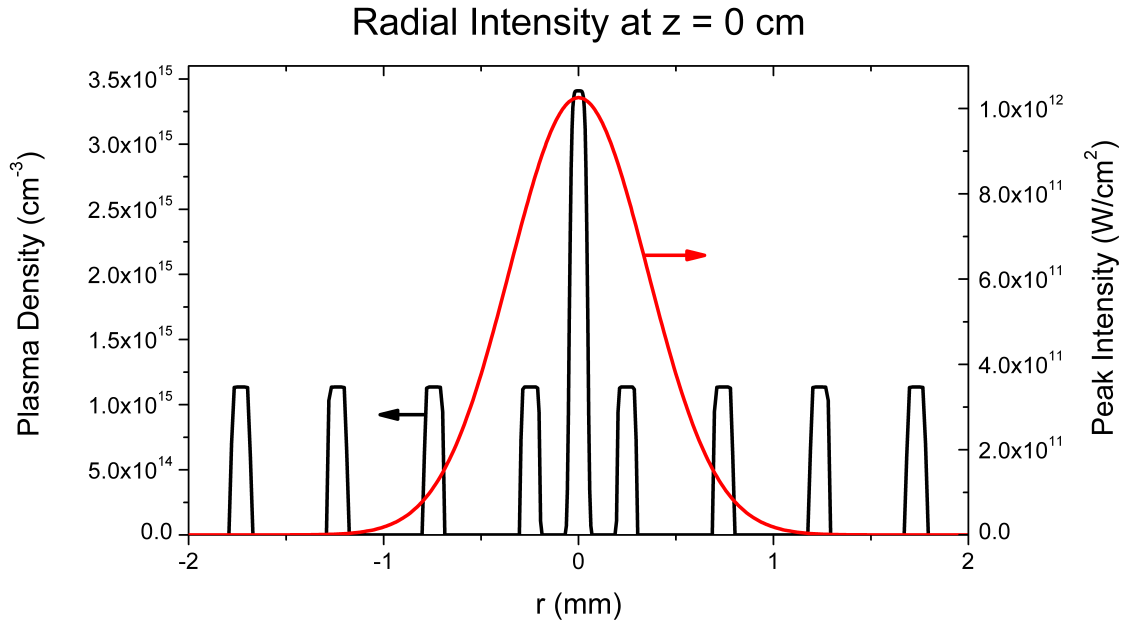


Fig 3-17 (black line) Lattice and central anti-waveguide. (red line) Gaussian beam profile superimposed on the radial lattice. The maximum electron density of the rings of the main lattice is $\rho = \rho_0 = 1.14 \times 10^{15} \text{ cm}^{-3}$ ($\Delta n_0 = -3.3 \times 10^{-7}$), while the density of the central anti-waveguide is $\rho = 3 \times \rho_0$.

Unfortunately the addition of the on-axis anti-waveguide cannot tailor the $2.5 P_{cr}$ filament, but only delay its formation. This can be seen in Fig 3-18(a)-(c) where the radial intensity distribution of the filament along z is plotted, for three anti-waveguides strengths. In Fig 3-18(a) the anti-waveguide has the same refractive index depth with the rest of the lattice, but as we see an intense focus is still forming and intensity reaches values as high as $\sim 3 \times 10^{13} \text{ W/cm}^2$. In Fig 3-18(b) and (c) the plasma density of the anti-waveguide is increased

by a factor of three and five respectively. However this increase of strength is only able to delay the formation of the filament, rather than tailor it.

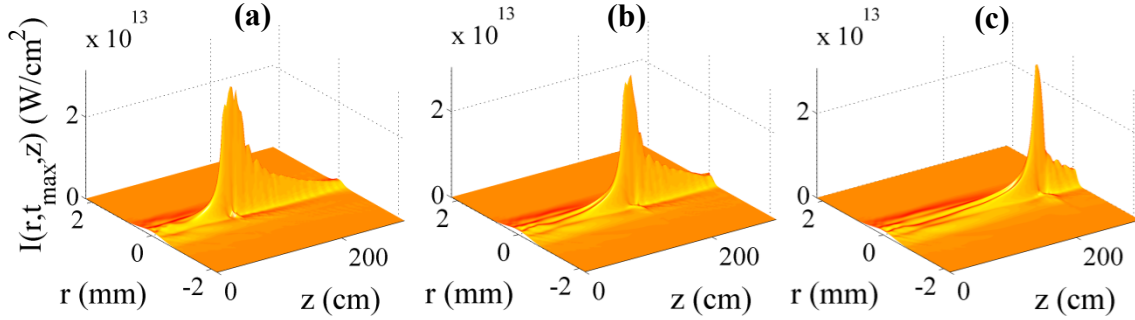


Fig 3-18 Radial intensity along propagation of the $2.5 P_{cr}$ tailored filament, inside the radial lattice with the addition of the on-axis super-Gaussian anti-waveguide. The electron density of the ring is $\rho = \rho_0 = 1.14 \times 10^{15} \text{ cm}^{-3}$ ($\Delta n_0 = -3.3 \times 10^{-7}$), while the density of the central anti-waveguide is (a) $\rho = \rho_0$, (b) $\rho = 3 \times \rho_0$, and (c) $\rho = 5 \times \rho_0$.

The delay of the onset of the filament formation is due to the change of the optical path length at the center of the beam. The optical path length is defined by

$$OPL = n \times L \quad (3.5-1)$$

where n is the total refractive index of the medium and L the physical length. The reduction of n by a factor of Δn_0 (Fig 3-18 (a)), $2 \times \Delta n_0$ (Fig 3-18 (b)), and $5 \times \Delta n_0$ (Fig 3-18 (c)) will force the beam to propagate additional distance in the space to cover the same overall optical path. In short the filament forms always after propagating a given OPL, when n is reduced due to the on-axis anti-waveguide then physical distance the L is increased to compensate.

3.5.3 Addition of a miniature lattice to the cylindrical lattice

The third approach consists of the addition of a miniature cylindrical plasma lattice inside the central waveguide. Although the experimental realization of such a lattice is a formidable task, the theoretical study can be done relatively easily.

The miniature plasma lattice is placed inside the central part of the main lattice, opposing the effect of self-focusing. The miniature lattice has a period of 50 μm and the plasma rings have 10 μm thicknesses at FWHM with an 8th order super-Gaussian profile. For this geometry the miniature lattice consist out of 5 concentric rings. The maximum plasma density and corresponding refractive index modulation was varied in the multiple simulations so that optimal value could be obtained at $\rho \approx 3 \times \rho_0$. In Fig 3-19 we can see the plasma lattice with the added miniature lattice, and the superimposed input beam profile.

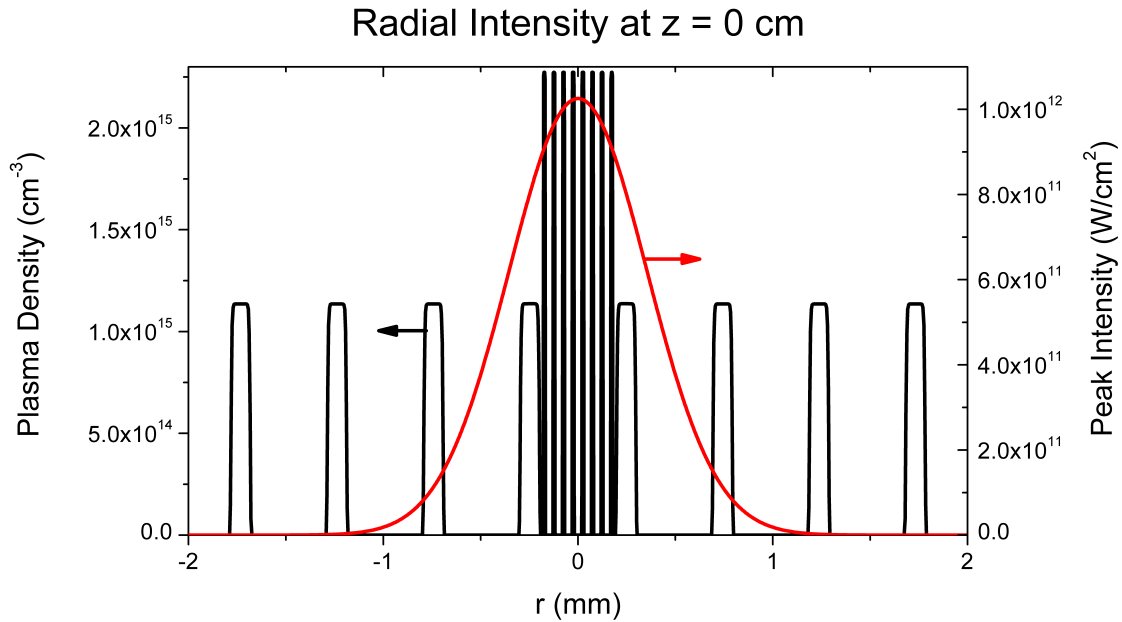


Fig 3-19 (black line) Lattice and miniature lattice. (red line) Gaussian beam profile superimposed on the radial lattice. The maximum electron density of the rings of the main lattice is $\rho = \rho_0 = 1.14 \times 10^{15} \text{ cm}^{-3}$ ($\Delta n_0 = -3.3 \times 10^{-7}$), while the density of the miniature lattice is in this case $\rho = 3 \times \rho_0$.

The impact of this new complex lattice on the propagation of the beam can be seen in Fig 3-20, where the radial intensity along propagation distance is plotted in logarithmic scale. As we can see it is possible to limit the peak intensity and beam waist of the filament over the 8 m of propagation shown in Fig 3-20. The peak intensity keeps an almost constant value of $\sim 2-3 \times 10^{12} \text{ W/cm}^2$ from 2 m up to 5 m of propagation, well under the ionization threshold. After 5 m of propagation the beam starts to break up abruptly, in a similar way as in the case of the diverging lens shown in section 3.5.1.

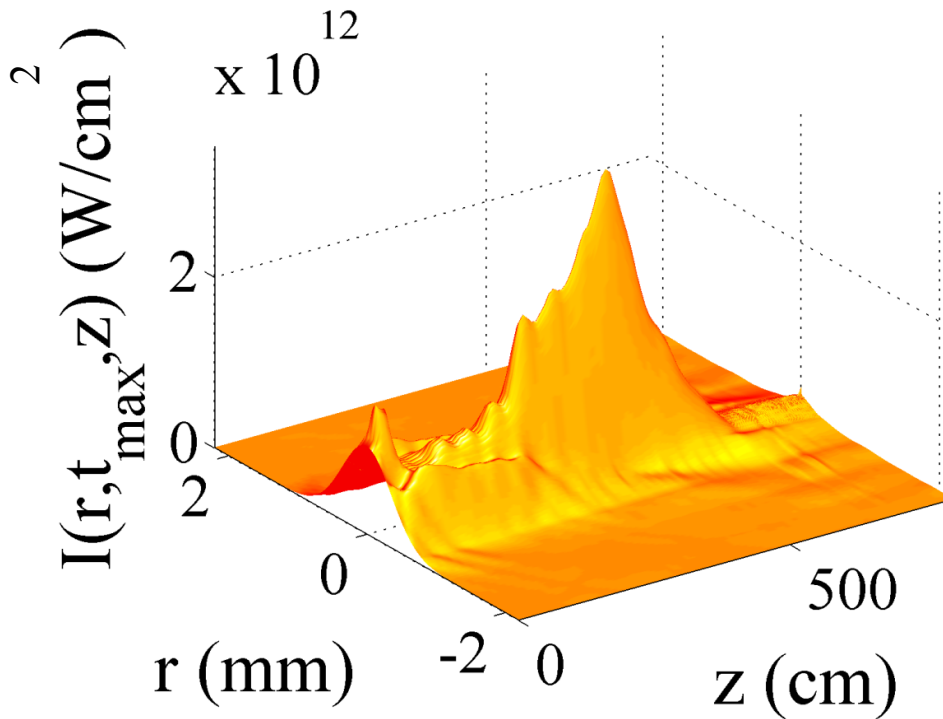


Fig 3-20 Radial intensity along propagation of the $2.5 P_{cr}$ tailored filament, inside the radial lattice with the addition of the miniature plasma lattice inside the central cylinder.

From the result in the previous three sections we can conclude that the tailoring of higher power single filaments is theoretically possible. However in order to reach higher powers, the lattice has to be modified by the addition of a diffraction element in the center waveguide preventing the formation of an on-axis filament. Numerical simulations showed that the diffracting element can be either a diverging lens or a miniature lattice.

3.6 Square lattices in the single filamentation regime

In this section, the tailoring of filaments with the use of square lattices will be investigated in numerous transparent nonlinear materials. Since square lattices are widely used in the literature to study soliton dynamics, the following results are bridging the regimes of high power filaments and low power solitons. First a simple and clear example will be shown on how to tailor a single filament using a square lattice. Next the importance of various factors like: the waveguide shape, focusing geometry and lattice size will be studied in fused silica and BK7 glass, water.

All numerical experiments in this section are performed with the "frozen time" scheme. The refractive index modulation is now simulated as a phase mask, rather than a pre-existing electron plasma, which has effectively no difference in the "frozen time" numerical scheme used in the XYZ geometry.

3.6.1 Filamentation tailoring in air with square lattices

For this first demonstration of filamentation tailoring with square lattices, the lattice characteristics are chosen close to the before mentioned cylindrical cases. The square lattice used has consists of a multiple rods each with a 8th order super-Gaussian refractive index distribution, placed at the points of a square grid. A schematic representation of such a square lattice can be seen in Fig 3-21.

The 800 nm laser pulse has a Gaussian spatiotemporal profile, with 35 fs duration and a beam waist of 500 μm at $1/e^2$ radius. The power contained in the initial wavepacket is $1.25 P_{cr}$, which makes the starting pulse identical to the one used in sections 3.2 and 3.4.2. The physical parameters for air that are used in this section are identical to the ones used in the previous sections.

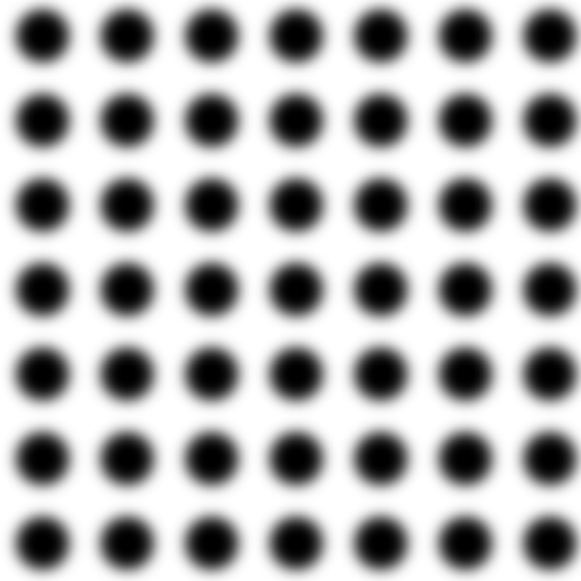


Fig 3-21 Graphical representation of a square lattice.

In Fig 3-32 we can see the effect of the square lattice on the beam waist and peak intensity of the filament. The optimum lattice parameters were found to be $\Delta n_0 = -7 \times 10^{-7}$, $\Lambda = 300 \mu m$ and $w = 100 \mu m$. As we can see in Fig 3-22(a) and (b) the square lattice regulates the beam waist, and prevents the nonlinear focus formation in a much similar way it was observed in the cylindrical case. The control over the beam intensity is obtained again by tuning of the diffractive strength of the lattice through the index depth Δn_0 and period Λ . This can be clearly seen in Fig 3-22(c) and (d) where the peak intensity of the tailored filament can be increased or decreased through a slight modification of the Δn_0 and Λ .

The results essentially show that for propagation in air at input power slightly over the critical value, both cylindrical symmetric and square lattices are able to tailor the filament in a similar way. In both cases the peak intensity and beam waist can be controlled by slightly tuning the lattice parameters.

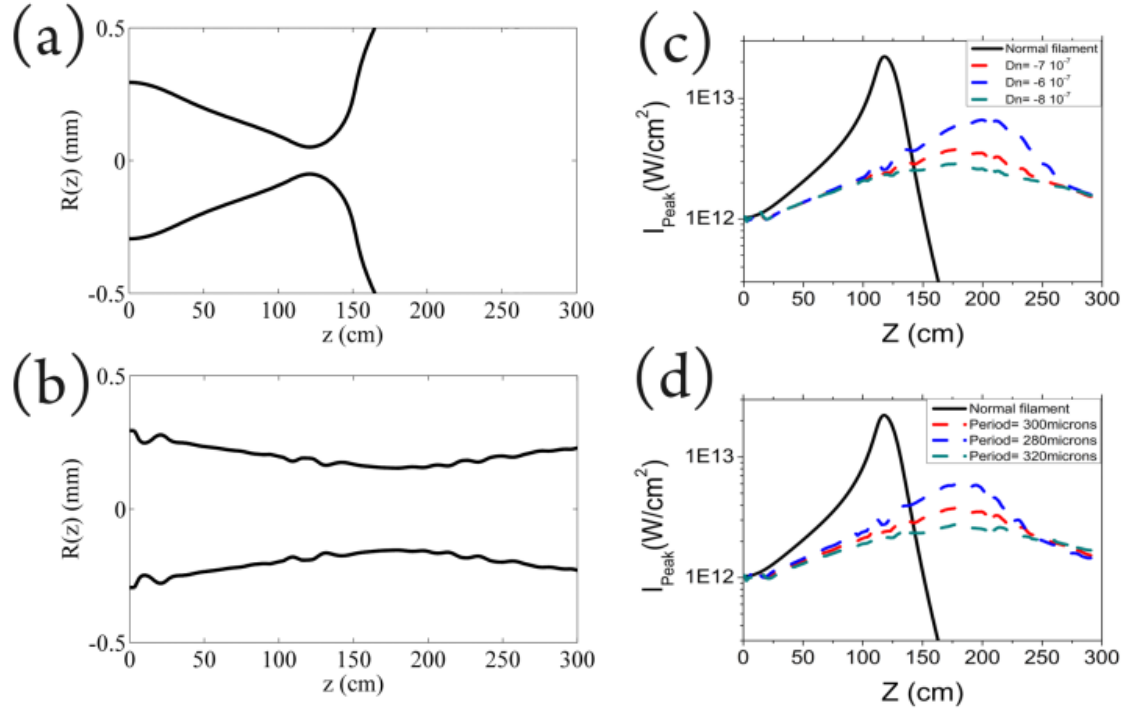


Fig 3-22 (a-b) Beam waist as a function of the propagation distance z . (a) without lattice (b) with square lattice. (c-d) Peak Intensity I_{peak} as a function of the propagation distance z for: (c) various lattice strengths Δn_o : (black line) 0, (blue line) -6×10^{-7} , (red line) -7×10^{-7} , (green line) -8×10^{-7} . (d) For various lattice periodicities Λ : (black line) ∞ , (blue line) $320 \mu m$, (red line) $300 \mu m$, (green line) $280 \mu m$.

In the next sections, the use of square lattices is explored in nonlinear media exhibiting stronger nonlinearity like fused silica, water and BK7 glass.

3.6.2 Filamentation in fused silica

In this section the use of square lattices inside the bulk of fused silica glass will be explored. Since fused silica is a condensed medium it has a much stronger nonlinear response than air. On the other hand it has a higher refractive index and is also much more dispersive. The latter is effectively neglected in the simulation, since the "frozen time" scheme is used.

We will start by simulation a standard filament inside the bulk of fused silica glass without any lattice present. The material parameters for fused silica used in the simulation are $n_2 = 3.2 \times 10^{-16} \text{ cm}^2 / W$ associated with a critical power for self-focusing of $P_{cr} \approx 2.3 MW$ [158] at the laser wavelength of 800 nm [12, 159]. The linear refractive index is $n_0 = 1.453$ at the given wavelength. The coefficients for MPI and MPA are $\sigma_5 = 1.3 \times 10^{-55} \text{ s}^{-1} \text{ cm}^{10} / W^5$ and $\beta_K = K \hbar \omega_0 \sigma_K \rho_{nt}$ using $U_i = 7.8 \text{ eV}$, $K = 5$ photons and $\rho_{nt} = 2.1 \times 10^{22} \text{ cm}^{-3}$ atoms [160, 161]. The cross-section for inverse Bremsstrahlung is $\sigma = 2.78 \times 10^{-18} \text{ cm}^2$ [158, 162]. The dispersive coefficient is $k'' = 360 \text{ fs}^2 / \text{cm}$, and can safely be neglected for simulations of a few centimeters. Avalanche ionization and electron recombination ($\tau = 150 \text{ fs}$) are neglected since they are on a much larger time scale than the pulse duration (35 fs).

Fig 3-23 shows the peak intensity, electron density and beam waist at FWHM vs propagation distance of a standard $2.5 P_{cr}$ filament in fused silica. The initial collimated wavepacket has 35 fs duration, with a central wavelength of 800 nm, and a beam waist of 40 μm at $1/e^2$ radius. As we can see the peak intensity reaches very high values, over $5 \times 10^{12} \text{ W} / \text{cm}^2$, which is enough to generate an electron plasma with a density above $2.5 \times 10^{16} \text{ electrons} / \text{cm}^3$. The slightly lower intensities reached in fused silica when compared to air are due to the fact that MPA and MPI, which are the main limiting nonlinear effects, are much stronger here. The material parameters of fused silica result in a different equilibrium between linear and nonlinear effects, and the generation of much narrower filament. As we can see in Fig 3-23(b) the filament diameter shrinks down to $\sim 7 \mu\text{m}$, while the length of the nonlinear focus is roughly 1 mm. These values are much smaller than the ones observed in air, where the typical filament diameter is about 100 μm and the length of the nonlinear focus is typical in the order of 10-30 cm for the same input power.

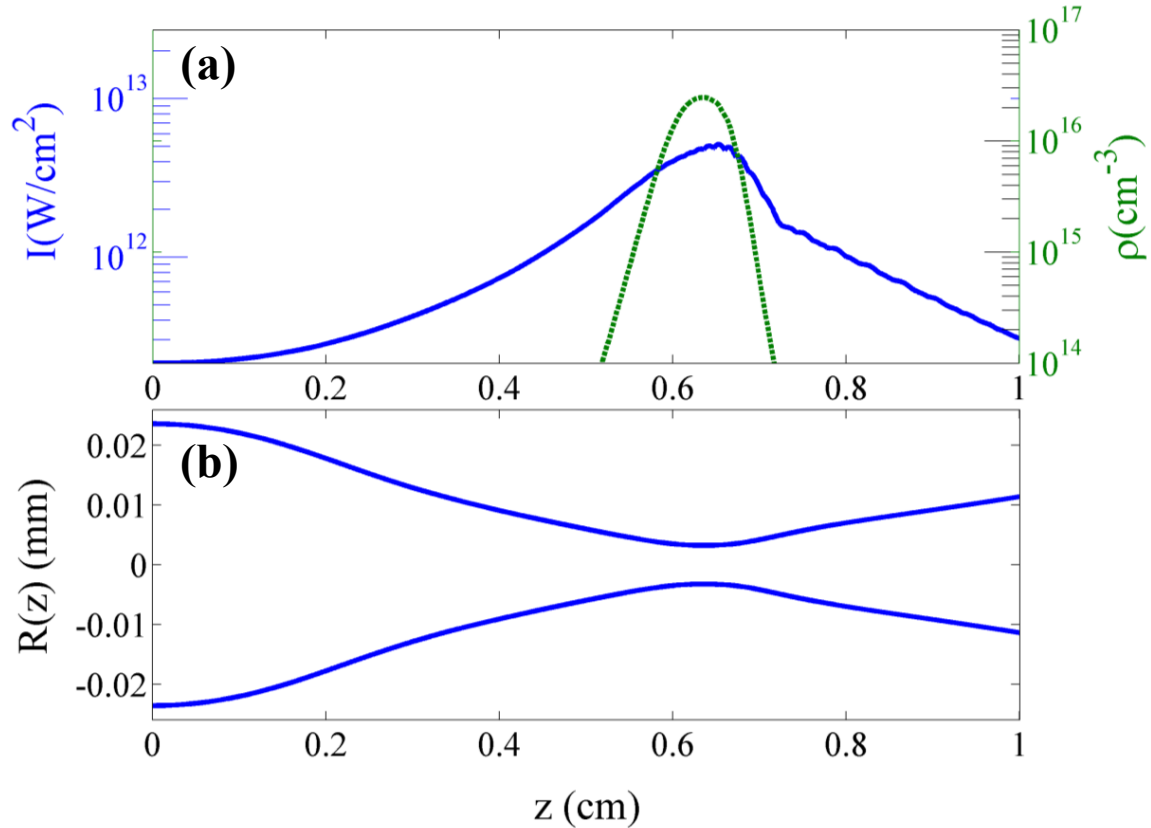


Fig 3-23 A standard $2.5 P_{cr}$ filament in fused silica glass. (a) Peak intensity and electron density vs propagation distance. (b) Beam waist at FWHM vs propagation distance.

In the next two sections we will explore the effects of square lattices on the filaments in fused silica glass.

3.6.2.1 Single-waveguide excitation in fused silica

Before exploring filamentation tailoring is useful to demonstrate the most basic phenomenon observed in square lattices, discrete diffraction. Discrete diffraction is extensively used in the literature mainly to test the fabrication quality of a lattice after construction and also to study soliton dynamics [163, 164]. Discrete diffraction is effectively observed by the illumination of single waveguide with a low power beam. The beam will gradually spread out by

moving from one waveguide to the next, as it was recently reported in [164]. The next step is to increase input power in order to observe localization at the center waveguides.

As we can see in Fig 3-24, discrete diffraction and localization at high input power are both observed when a narrow beam excites a single waveguide of the square lattice in fused silica glass. In this case the input beam has a beam waist is $w_0 = 3\mu m$ which is slightly smaller than the waveguide diameter and an input power of $10^{-6} P_{cr}$ and $1.25 P_{cr}$ for the linear and nonlinear case respectively. The lattice used in Fig 3-24 has 31×31 Gaussian waveguides with period $\Lambda = 14\mu m$ and waveguide diameter $w = 4\mu m$. The refractive index potential is $\Delta n_0 = +10^{-3}$.

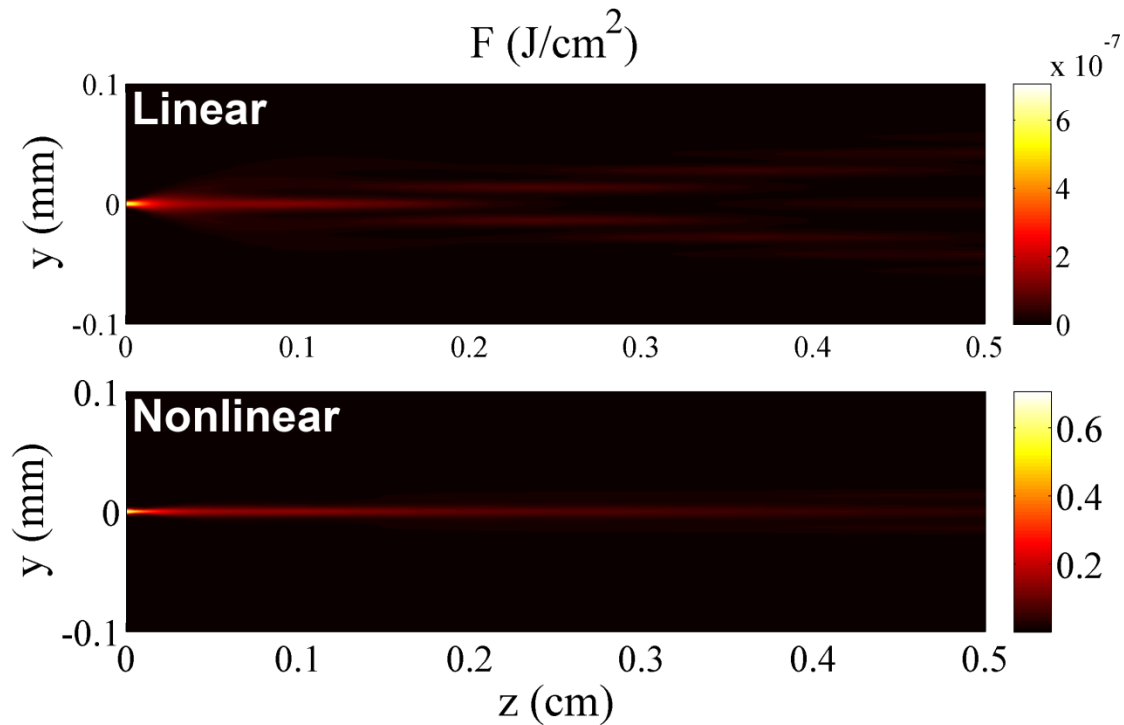


Fig 3-24 Cross sectional fluence along propagation distance. Observation of (first line) discrete linear diffraction and (second line) localization in the nonlinear regime in a 31×31 lattice in fused silica glass.

3.6.2.2 Multi-waveguide excitation in fused silica

The single waveguide excitation regime is very limiting concerning filamentation tailoring, due to the constraints it applies on the initial beam waist and total input power. This is because in the single-waveguide excitation regime the beam waist must be smaller or equal to the waveguide diameter, which effectively limits the total power the beam can carry. In the nonlinear regime, the increase of input power will increase the starting peak intensity to values over the ionization threshold and the filament will be formed before the lattice could have any effect on it. Since the techniques for writing lattices in fused silica produce waveguides of rather small diameter ($\sim 10 \mu\text{m}$) [158], the input power in the single waveguide excitation regime is limited to a few P_{cr} .

In this section the use of square lattices for the tailoring of filaments in fused silica will be explored in the multi-waveguide excitation regime. For this numerical experiment we will use a square lattice close to the one of the previous section with $\Delta n_0 = +10^{-3}$ and $w = 4 \mu\text{m}$, with a varying periodicity from $10 - 30 \mu\text{m}$. The input beam carries 2.5 critical powers and has a beam waist of $100 \mu\text{m}$ at $1/e^2$ radius. The pulse duration is 35 fs and the central wavelength 800 nm. In order to save computation time the beam has an initial curvature of 5 cm, and in the absence of the periodic lattice generates a standard filament with the nonlinear focus at $z = 2.5$ cm. As we can see in Fig 3-25, where the starting beam intensity is superimposed to the lattice potential, multiple waveguides are illuminated.

By varying the period of the lattice it possible to control the peak intensity and beam waist of the $2.5 P_{cr}$ filament inside the lattice. This can be seen in Fig 3-26, where the maximum reached intensity and the minimum beam waist at FWHM are plotted as a function of the lattice period. As can see by for the given lattice strength a very good control over peak intensity and beam waist is achieved for a wide variety of periods. The maximum intensity of the tailored filament can be varied from $4 \times 10^{11} \text{ W} / \text{cm}^2$ to

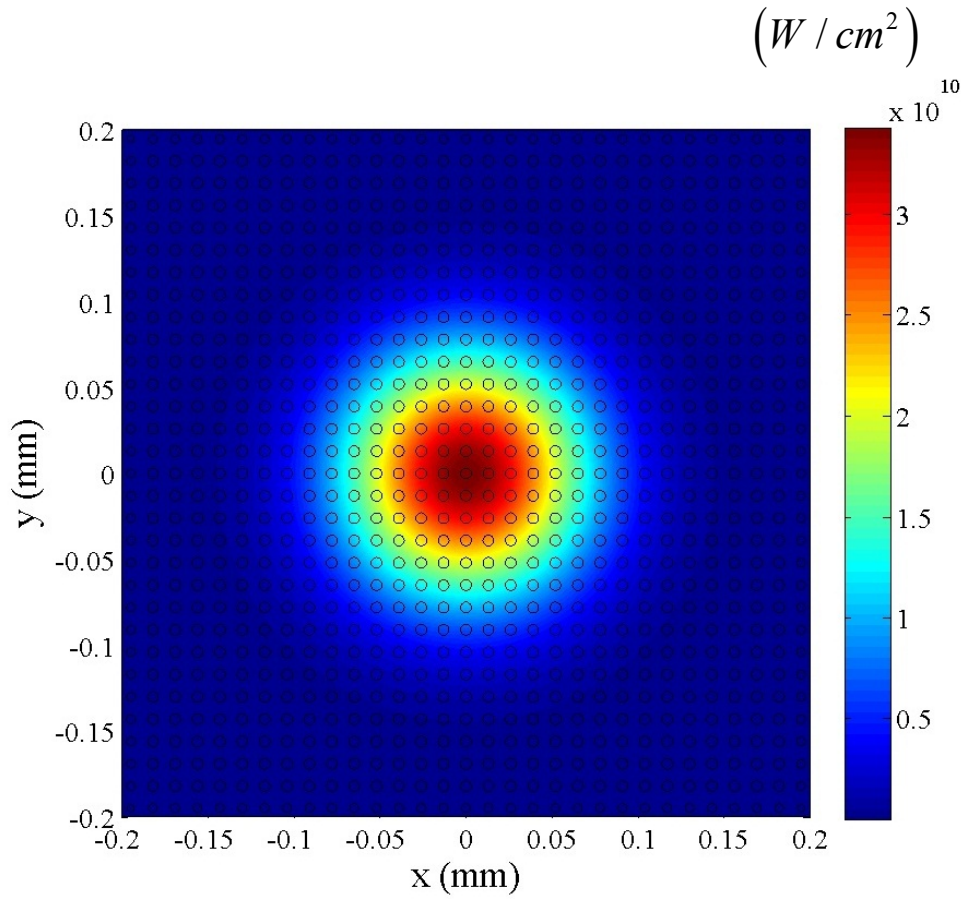


Fig 3-25 Peak intensity of the input beam superimposed with square lattice potential in fused silica.

The period, index depth and waveguide diameter of the lattice is

$$\Lambda = 20\mu m, \Delta n_0 = +10^{-3}, w = 4\mu m \text{ respectively.}$$

$1.5 \times 10^{12} W/cm^2$ as is shown in the blue line in the first row of Fig 3-26. Note that the maximum intensity reached by the filament in the absence of the lattice is about $\sim 5 \times 10^{12} W/cm^2$, represented by the red line. An interesting observation is that the maximum intensity is not monotonically varying with the increase of the periodicity of the lattice. The intensity is increasing as a function of Λ up to $\Lambda = 16 \mu m$. Further increase of Λ is causing the filament to slowly become less intense. The minimum beam diameter is varying from $18 \mu m$ to $8 \mu m$ as Λ is increased (blue line in the second row of Fig 3-26). The minimum beam waist of the same filament in the absence of the lattice is about $\sim 5.5 \mu m$ (red line in the second row of Fig

3-26). Since the beam waist is linked with peak intensity of the beam, for periods larger than 16 μm the beam waist is starting to increase.

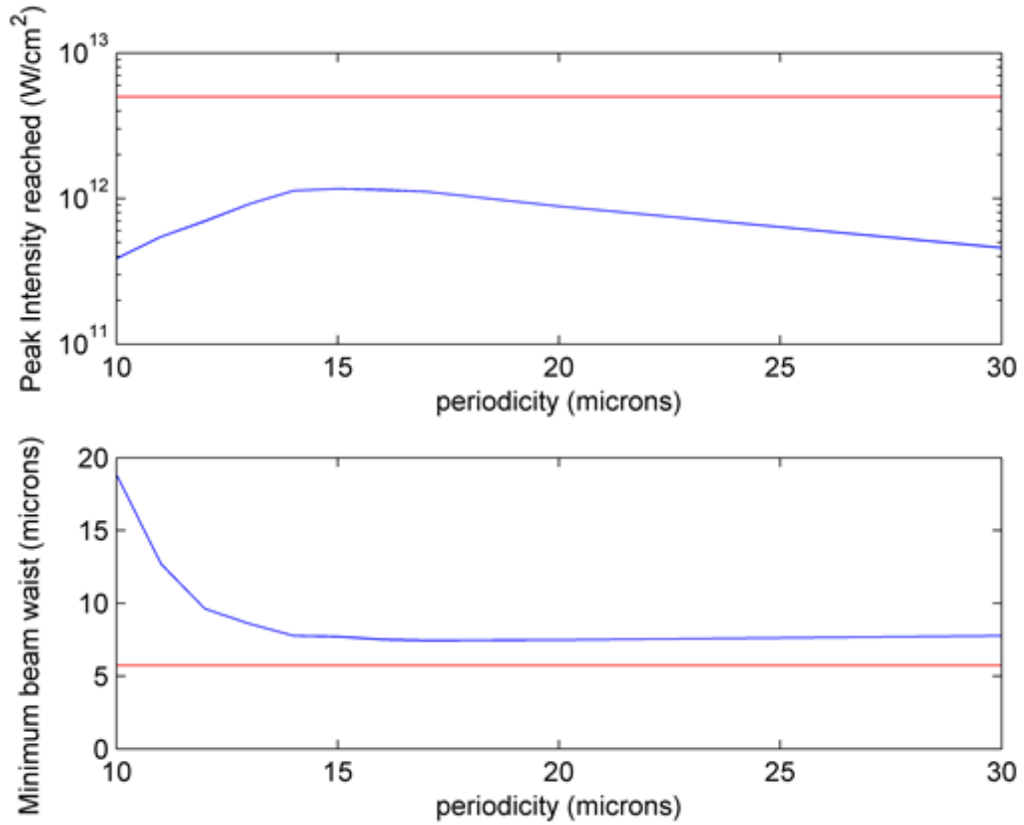


Fig 3-26 (Blue line): Tuning of the maximum intensity (first row) and minimum beam waist (second row) of the $2.5 P_{cr}$ filament by the variation of the lattice period. The period of the square lattice is varied from 10 μm up to 30 μm , while the rest of the lattice parameters are kept constant ($\Delta n_0 = +10^{-3}$, $w = 4 \mu\text{m}$). Red line represents the maximum intensity and minimum beam waist of the filament without lattice.

3.6.3 Filamentation in water

In this section the tailoring of filaments in water using square lattices will be explored. In addition, the importance of the lattice size, lattice starting position and initial beam curvature will be presented in the following sections.

Simulations in water use the following material parameters: nonlinear refractive index is $n_2 = 1.6 \times 10^{-16} \text{ cm}^2 / \text{W}$, which corresponds to a critical value for self-focusing of $P_{cr} = 4MW$ [19, 20], for $K = 5$ photons. The MPI and MPA coefficients are $\sigma_K = 1 \times 10^{-54} \text{ s}^{-1} \text{ cm}^{10} / \text{W}^5$ and $\beta_K = 8.3 \times 10^{-50} \text{ cm}^7 / \text{W}^4$ [20, 165] respectively. The density of neutral molecules is $\rho_n = 6.6 \times 10^{22} \text{ cm}^{-3}$ [166], and the linear refractive index is $n_0 = 1.33$.

Again we will start this section by simulating a standard filament in water without any lattice present. The numerical scheme that will be used will be again the "frozen time" scheme, as in all 2D lattice cases. The input beam used has a beam waist of $40 \mu\text{m}$ at $1/e^2$ radius with a Gaussian spatiotemporal profile with 35 fs duration and an 800 nm central wavelength. The beam carries 2 critical powers and has a flat spatial phase.

We can see the peak intensity, electron density and beam waist of the filament in water in Fig 3-27. The peak intensity reaches values as high as $5 \times 10^{12} \text{ W} / \text{cm}^2$, and is generating an electron plasma with a maximum density of $4.6 \times 10^{16} \text{ cm}^{-3}$. The beam waist is as small as $8.7 \mu\text{m}$ on the nonlinear focus, which is about 2 mm long in z . As we can see filamentation in water is very similar to filamentation in condensed media, since most physical parameters, like the nonlinear refractive index, ionization potential, MPI and MPA coefficients, have similar values. It is thus expected that the tailoring of filaments with periodic lattices will work in the same fashion.

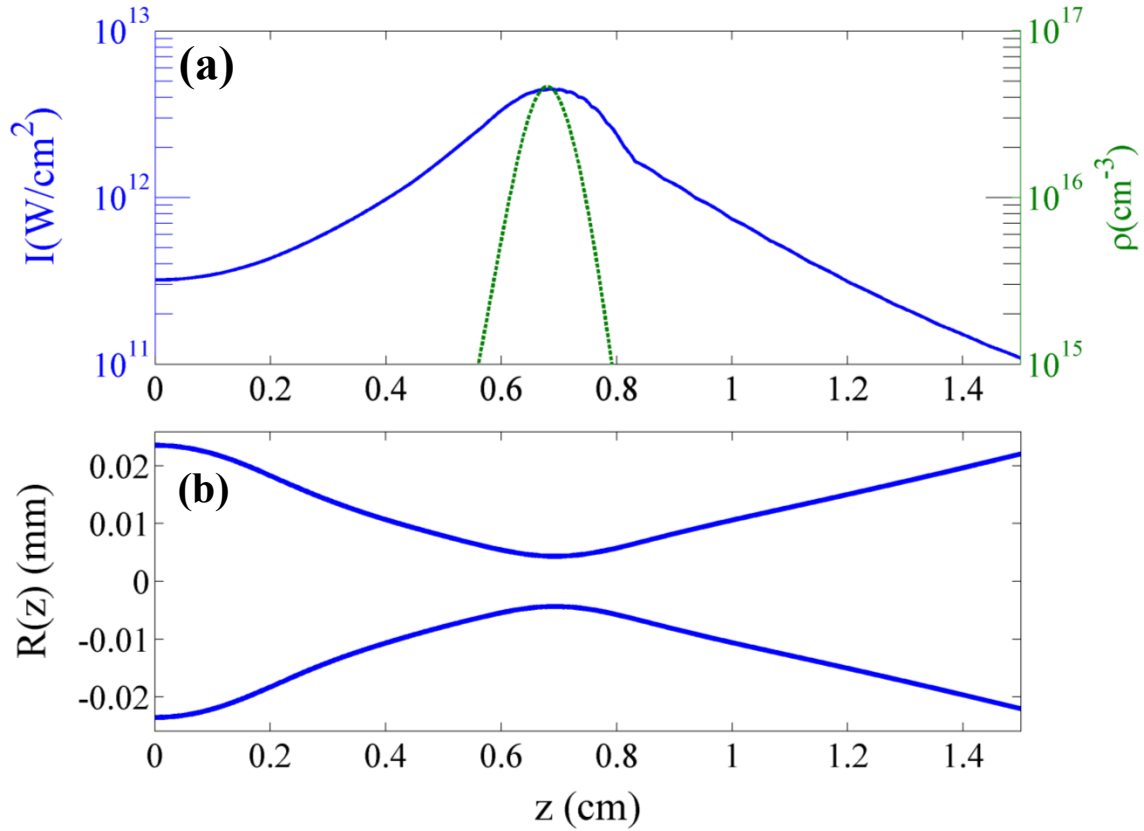


Fig 3-27 A standard $2P_{cr}$ filament in fused water. (a) Peak intensity and electron density vs propagation distance. (b) Beam waist at FWHM vs propagation distance.

The square periodic lattice used here consist of negative Δn anti-waveguides, since in water the writing of permanent positive Δn waveguides is impossible. This could experimentally be realized by multiple plasma strings generated by individual laser filaments in a water tank. The lattice used has a period of $\Lambda = 15 \mu\text{m}$ with a maximum index depth $\Delta n_0 = -4 \times 10^{-4}$. Each waveguide has a super-Gaussian refractive index profile of order 5, with a diameter of $w = 5 \mu\text{m}$. These values are in agreement with the plasma strings generated by laser filaments in water at the given wavelength. In Fig 3-28 we can see the initial beam profile superimposed to the lattice potential.

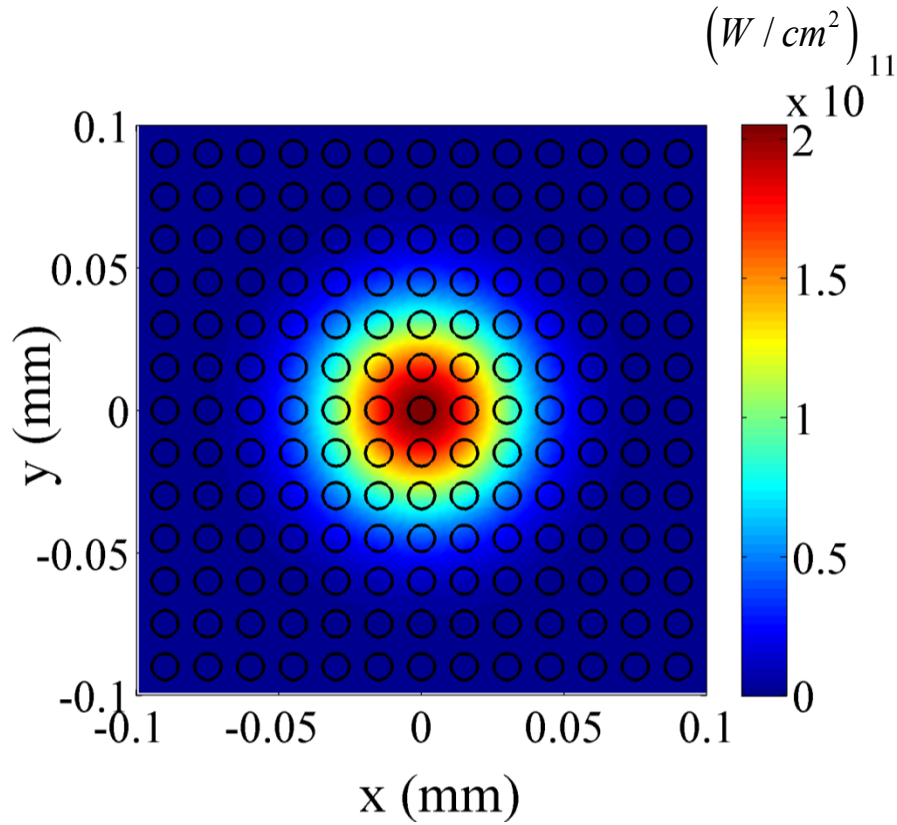


Fig 3-28 Cross section of the peak intensity of the input beam superimposed with square lattice potential in water. The period, index depth and waveguide diameter of the lattice is $\Lambda = 15\mu m$, $\Delta n_0 = -4 \times 10^{-4}$, and $w = 5\mu m$ respectively.

In Fig 3-29 we can see the radial intensity distribution of the tailored filament in water along propagation distance. Again as in the previous cases (air and fused silica glass) we can clearly see that the lattice is regulating the propagation by limiting the intensity and beam waist. The spiky structures that are observed on the intensity profile in Fig 3-29 are not numerical artifacts, but are manifested due to the strong lattice potential which is in a dynamic equilibrium with the optical Kerr effect. These radial intensity oscillations are not observed if the lattice potential is lower, as in the case of air in section 3.6.1 where $\Delta n_0 \sim 10^{-7}$. Note that similar oscillations were also observed in filamentation tailoring in fused silica (data not shown), where that lattice potential was strong.

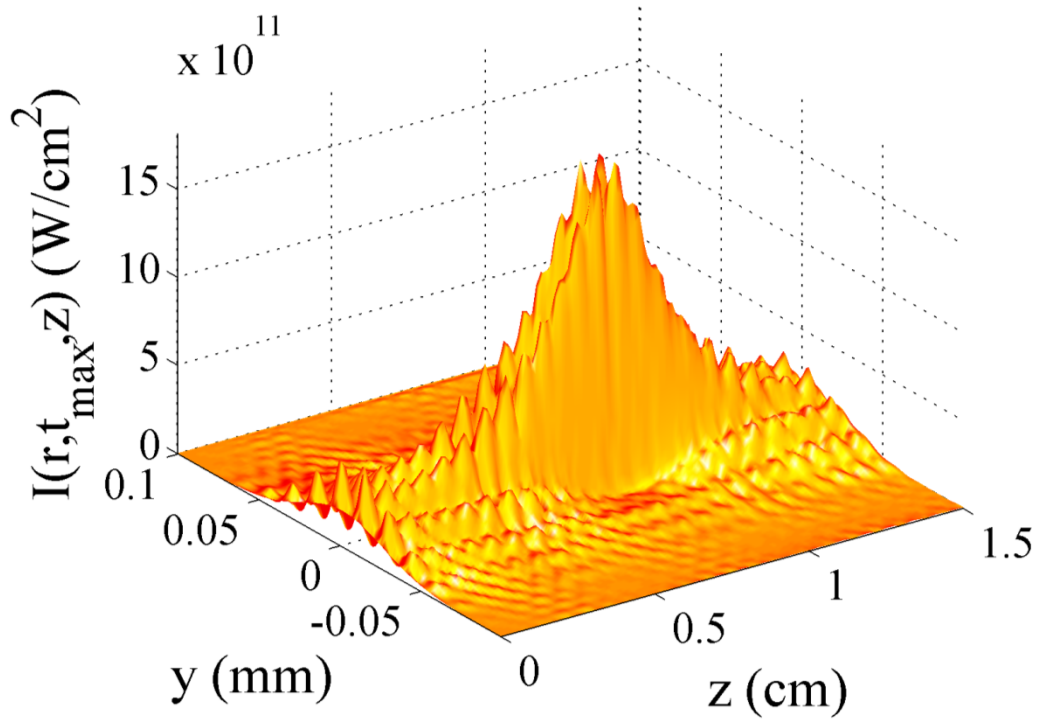


Fig 3-29 Cross sectional intensity distribution along propagation distance of the $2P_{cr}$ tailored filament inside the square lattice in water.

3.6.4 Dependence on setup parameters

Since filamentation tailoring with square lattices in water is one of the most delicate cases explored this far, it will be used to study the effect that various setup parameters have on the tailored filament.

3.6.4.1 The importance of initial beam curvature

In most simulations the initial beam has a flat spatial phase, i.e. it is collimated. In these cases the focus that is observed is enforced by the optical Kerr effect and its shape and position depends on the input beam power and size. In the physically limited laboratory however the use of focused beams is often a necessity. In this section the importance of focusing geometry will be determined when a square lattice in water is used to tailor the filaments.

In order to investigate the importance of initial beam curvature, the collimated pulse of the previous section will be used. Instead of an infinite beam curvature (collimated beam), four different focusing setups will be used, with $f = 30$ cm, 10 cm, 5 cm, and 1 cm. The result of those simulations can be seen in Fig 3-30, where the radial intensity distribution along propagation distance is depicted for the four focusing geometries. As we can see the beam behavior is not changing drastically from the collimated case, even if the linear focus is at $z = 5$ cm. However when $f = 1$ cm, the focusing becomes too strong and the focus is significantly affected.

This behavior is to some degree also observed in standard filaments where the main effect controlling the focus is self-focusing. In the presence of a photonic lattice, where the focus is a result of both self-focusing and lattice diffraction, the importance of initial beam curvature is further diminished. As we can see, the initial curvature becomes effectively important only when the linear focus is very close to the position of the nonlinear focus inside the lattice. This observation is very important for laboratory experiments paired with numerical simulations, since in these cases the experimental setup can be difficult to simulate or vice versa.

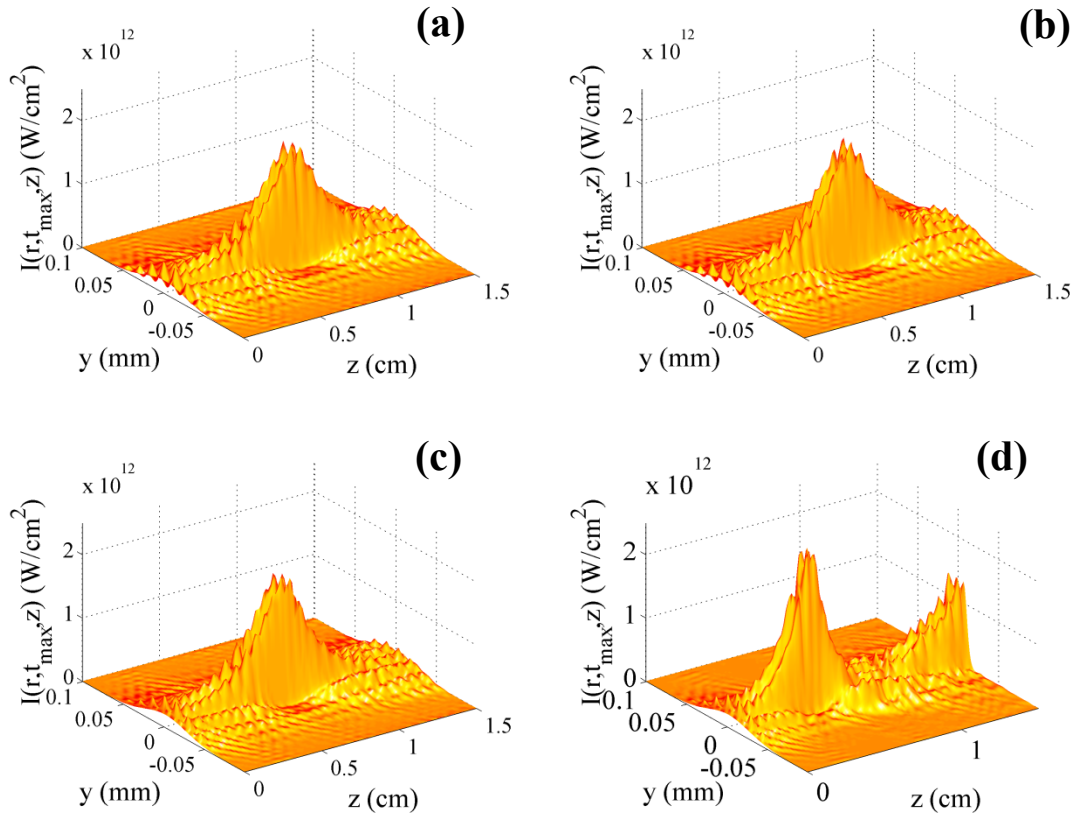


Fig 3-30 Cross sectional intensity distribution along propagation distance of the $2P_{cr}$ tailored filament inside the square lattice in water, for four different input beam curvatures. (a) $f = 30$ cm, (b) $f = 10$ cm, (c) $f = 5$ cm, and (d) $f = 1$ cm.

3.6.4.2 The importance of lattice size

Up until now we have used periodic lattices that always cover the whole numerical box. This way all parts of the beam will "feel" the effect of the lattice even after a possible spreading along propagation. This approach can lead to large number of waveguides contained in a lattice, as for example in section 3.6.2.2 a 31×31 lattice was used in fused silica which counts 961 individual waveguides. The large number of waveguides can be slightly problematic for numerical simulations, since a larger numerical box and higher enough resolution might be required. In addition the use of non-uniform grids may result in poor waveguide discretization at the box edges. However in a laboratory experiment, where each waveguides has to be separately

written in the bulk of the glass, large lattices are very difficult to manufacture. In the case of a plasma lattice (negative Δn) in a gas or liquid, the experimental realization of a large number of waveguides is even more difficult, since multiple plasma channels need to be generated simultaneously. Therefore the importance of the lattice size on the filamentation tailoring process must be investigated, which will be done in this section.

For this purpose the tailored filament of section 3.6.3 (2 Pcr filament in water, collimated input beam) will be used. The lattice size will be changed from 9x9 to 7x7, to 5x5, and 3x3 as depicted in Fig 3-31. Note that any change in lattice size is leaving the periodicity and waveguide profile unaltered ($\Lambda = 15\mu m$, $\Delta n_0 = -4 \times 10^{-4}$, and $w = 5\mu m$), and only the number of waveguides contained in the lattice is modified.

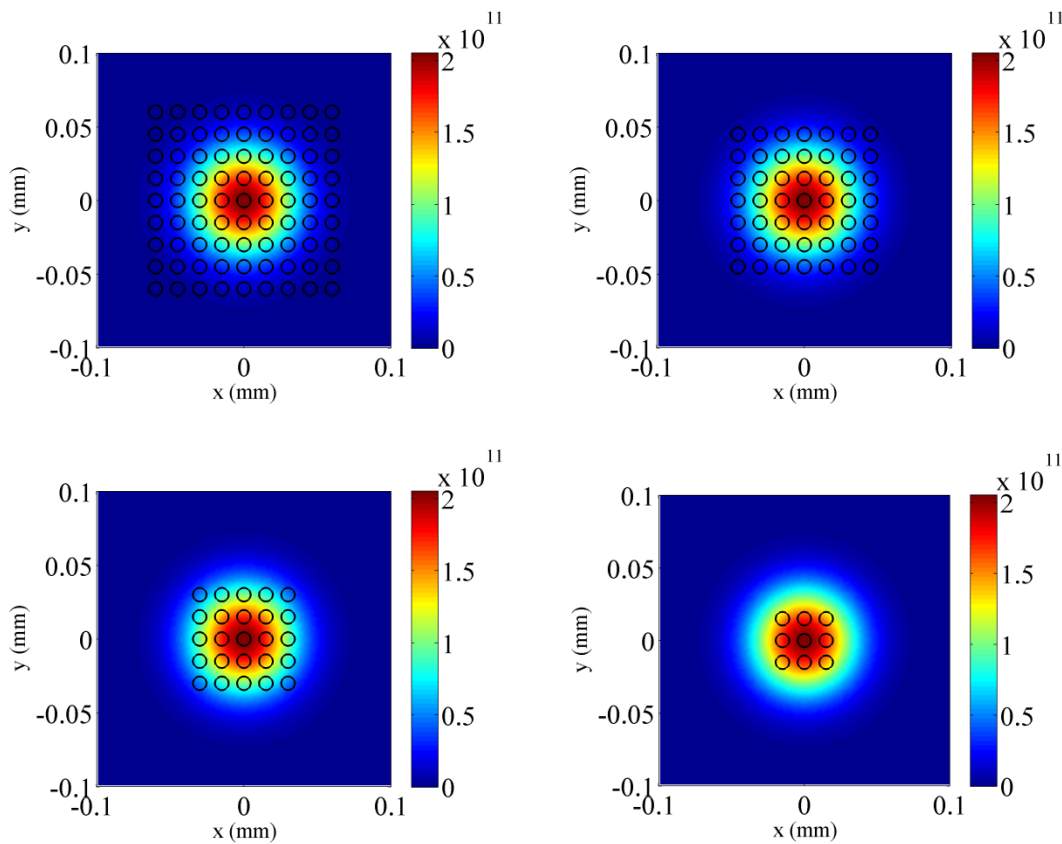


Fig 3-31 Cross section of peak intensity of the input beam superimposed with the four square lattices in water. (a) 9x9, (b) 7x7, (c) 5x5, and (d) 3x3.

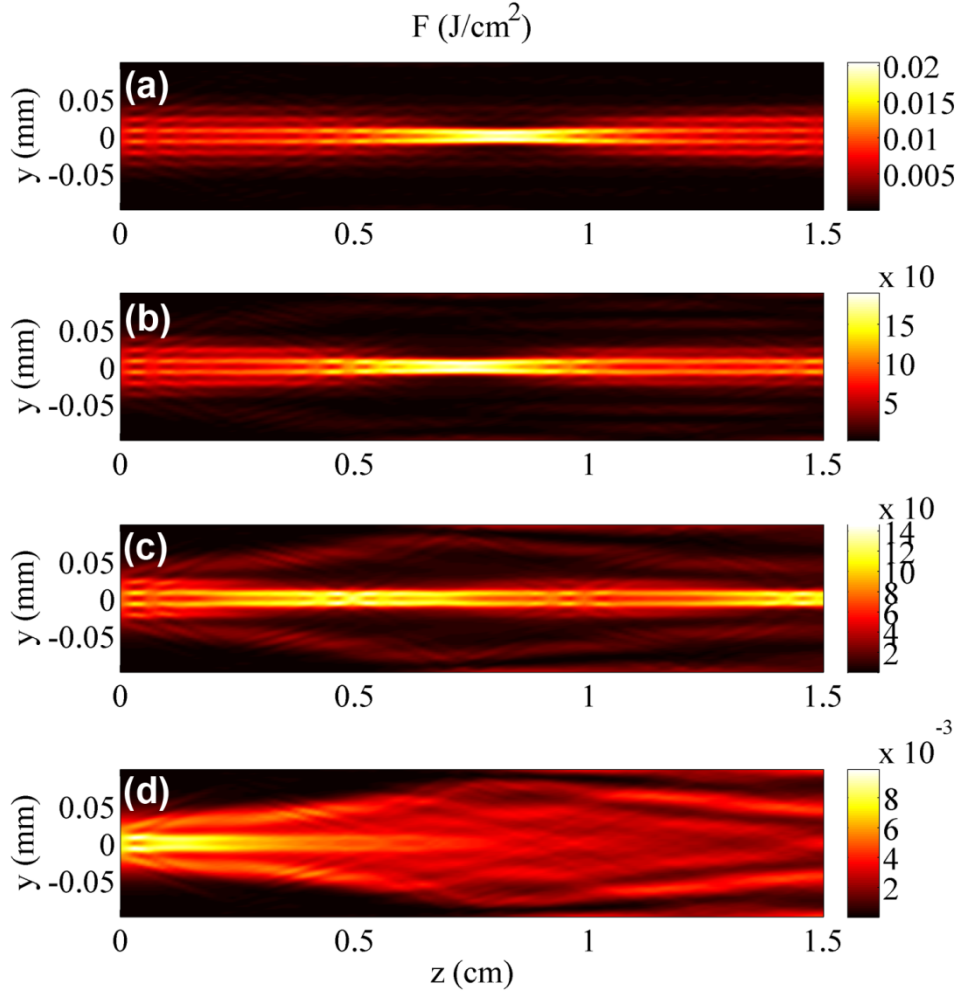


Fig 3-32 Cross sectional fluence distribution along propagation distance of the $2P_{cr}$ tailored filament inside the square lattice in water, for four different lattice sizes. (a) 9x9, (b) 7x7, (c) 5x5, and (d) 3x3.

Fig 3-32 shows the radial fluence distribution along propagation distance of the $2P_{cr}$ filament for the four different lattice sizes. The tailored filament inside the 9x9 lattice depicted in Fig 3-32(a) is essential identical to the one obtained in section 3.6.3 (lattice covering the whole box). As the lattice size is decreased the edges will diffract light outwards. This can clearly be seen in Fig 3-32(b) and (c) where the strong diffraction at the edge of the lattice is causing light to rapidly spread out. However even at this point, the intense part of the beam that is inside the lattice is still evolving similar to the full lattice case. In other words, the tailoring process is

mainly a local effect. This observation can be very useful in future laboratory experiments, since it shows that it is possible to tailor a filament with the use of a 25 waveguide lattice. Further decrease of the lattice size results in the complete loss of the filamentation process, which can be seen in Fig 3-32(d).

The next two sections are combining numerical simulation with laboratory experiments in BK7 glass and water.

3.7 Permanent elliptical waveguide lattice in BK7 glass

As demonstrated in the previous sections by means of numerical simulations the techniques for stabilizing spatial solitons via the use of photonic lattices [122, 123, 126, 129, 167] extend advantageously to filamentation control. We showed that the temporal dynamics of a self-induced filament (SF) is quenched by sending the laser pulse in a lattice of reduced refractive index generated by plasma in air. Diffraction due to the lattice modifies the competition between linear and nonlinear effects that occur in a SF. It prevents high intensities to be reached, thereby limiting nonlinear losses, by regularizing the energy flux from the periphery to the core of the filament. A nonlinear structure called intense lattice filament (LF), or tailored filament, forms over a short propagation distance in the lattice, with attributes that can be effectively tailored by adjusting the lattice properties (modulation depth and period).

In this section, we extend this idea to lattices in solid media by combining numerical simulations with laboratory experiments. We present the first experimental realization of LFs and show that the LF properties can indeed be tailored. We demonstrate that a LF can be refilled in energy by interaction with a filament, opening the way to remote replenishment of filaments.

For our experiments, we fabricated photonic lattices in BK7 glass using the femtosecond laser writing technique [168, 169]. Our lattice consists of 8 periodically arranged waveguides 24

mm long, spaced by $25\ \mu\text{m}$ with an elliptical cross section ($5 \times 25\ \mu\text{m}$), see Fig 3-33 and inset in Fig 3-34(c). The refractive index modification is negative and is estimated to be $\Delta n \sim -10^{-4}$.

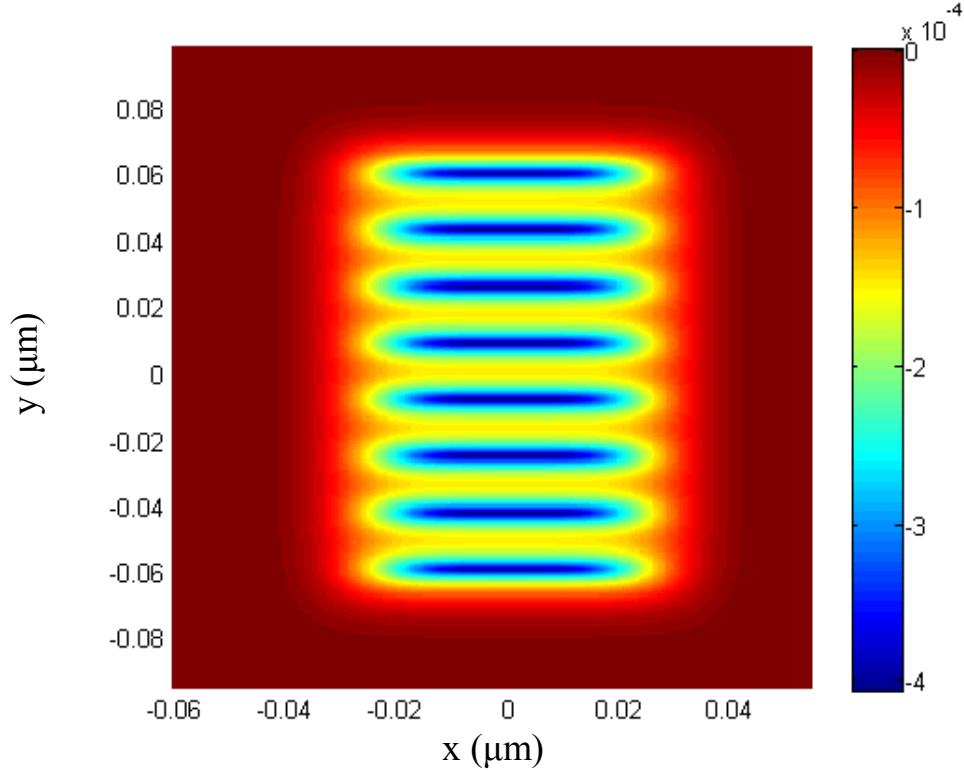


Fig 3-33 Elliptical waveguide lattice in BK7 glass, used in the simulations.

The input laser pulse is a Gaussian beam centered at 800 nm with a beam waist of $80\ \mu\text{m}$ and a pulse duration of 35 fs. The input power is $0.6\ \mu\text{J}$ corresponding to $5P_{cr}$ (where $P_{cr} = 3.7\ \text{MW}$ in BK7 [10]). An initial curvature corresponding to the effect of a 30 cm focal length lens is added to take into account the focusing. The model for the lattice reproduces the experimental lattice, and particularly the elliptical cross section as can be seen in Fig 3-33.

Due to the high intensity of the filament, its propagation is accompanied by a nonlinear fluorescence emission [170]. This emission is laterally (yz plane in Fig 3-34) imaged on a linear CCD camera, using a 0.11 NA microscope objective, and thus allowing the visualization of the

nonlinear propagation. Since a nonlinear law correlates the fluorescence signal to the intensity, the image contrast and the intensity ratio between SF and LF are affected [170].

Fig 3-34 depicts both numerical and experimental results showing how the photonic lattice affects the propagation of the filament. In the presence of the lattice, the peak intensity drops and the filament length extends from 2 to 7 mm giving rise to a LF.

The inherent birefringence of the induced structures, a common side effect in laser structuring of glass, is exploited to fine tune the LF attributes by rotating the input laser polarization (the optical properties of the birefringent lattice are a function of the input polarization orientation). A study of the effect of the input polarization P and period Λ on the propagation of the LF is presented in Fig 3-35. For a given period ($\Lambda = 25 \mu\text{m}$), as the input polarization is rotated, the peak intensity drops, its distribution becomes more homogeneous and the propagation length is extended. The optimal configuration, in terms of length and uniformity, is achieved for $P = 60^\circ$ (Fig 3-35 (b)). Then, by further rotating the polarization, the beam is still elongated but is less uniform with an intense peak at 4 mm (Fig 3-35 (d)). Similarly, at a given polarization state ($P = 60^\circ$), when the lattice period is increased to $35 \mu\text{m}$ (Fig 3-35 (c)), the propagation length remains relatively long but a peak emerges at 5.5 mm affecting the LF uniformity.

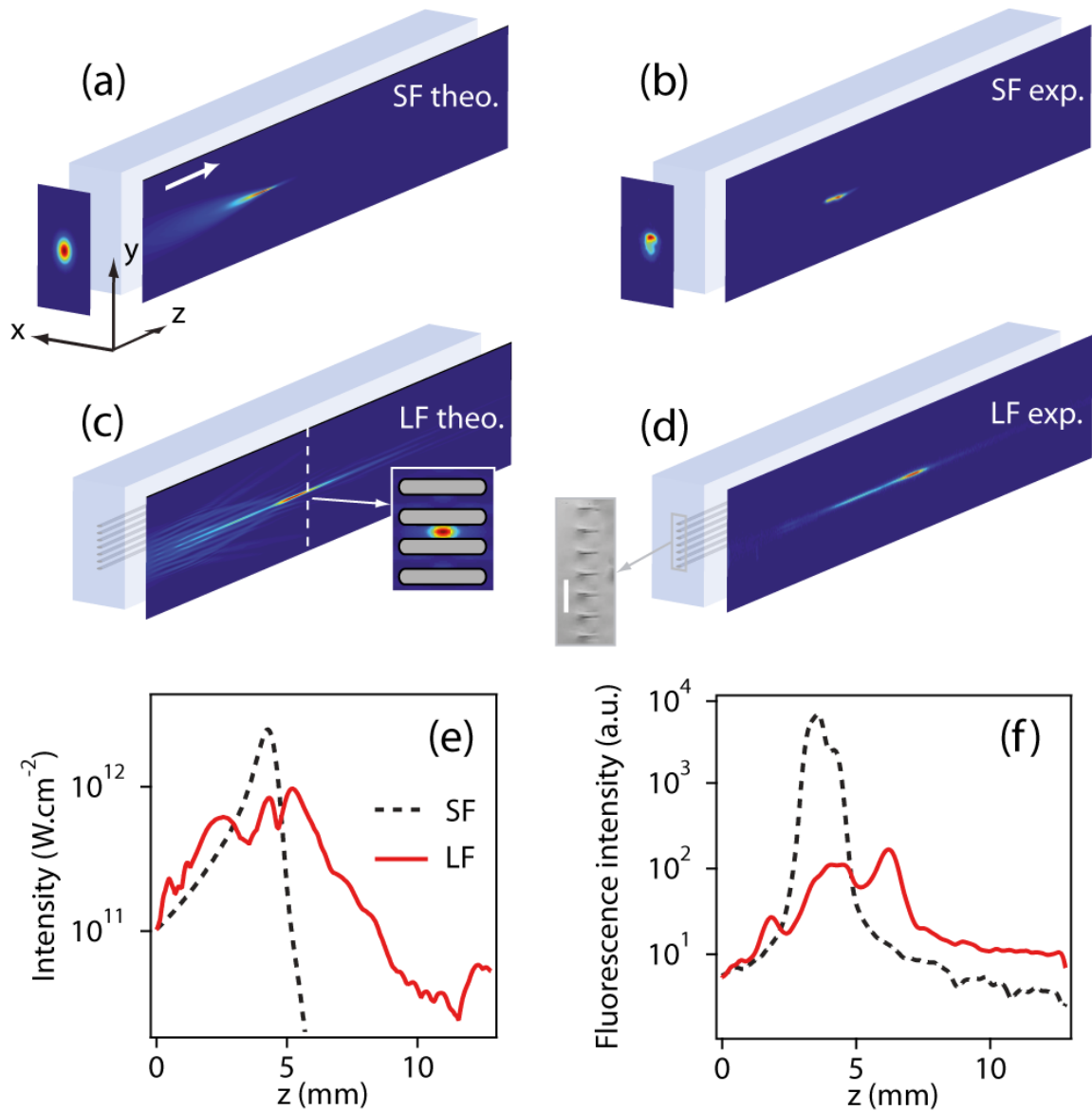


Fig 3-34 (a and b). Simulated and experimental self-induced filament (SF) propagation (yz plane). (c and d) Simulated and experimental lattice filament (LF) propagation. The input is an $80\ \mu\text{m}$ wide Gaussian beam (xy plane). The white arrow indicates the light propagation direction. The photonic lattice parameters are: $\Delta n = -4 \times 10^{-4}$, $\Lambda = 25\ \mu\text{m}$ and $L = 24\ \text{mm}$. For the simulation, the inset shows the elliptical cross section. For the experimental visualization, the emitted fluorescence is collected by imaging the yz plane on a CCD camera. Note that the yz images size is $0.4 \times 13\ \text{mm}$. The inset shows a transverse view of the fs laser induced structures. The white line corresponds to $30\ \mu\text{m}$. (e and f) are the corresponding intensity profiles versus the propagation length.

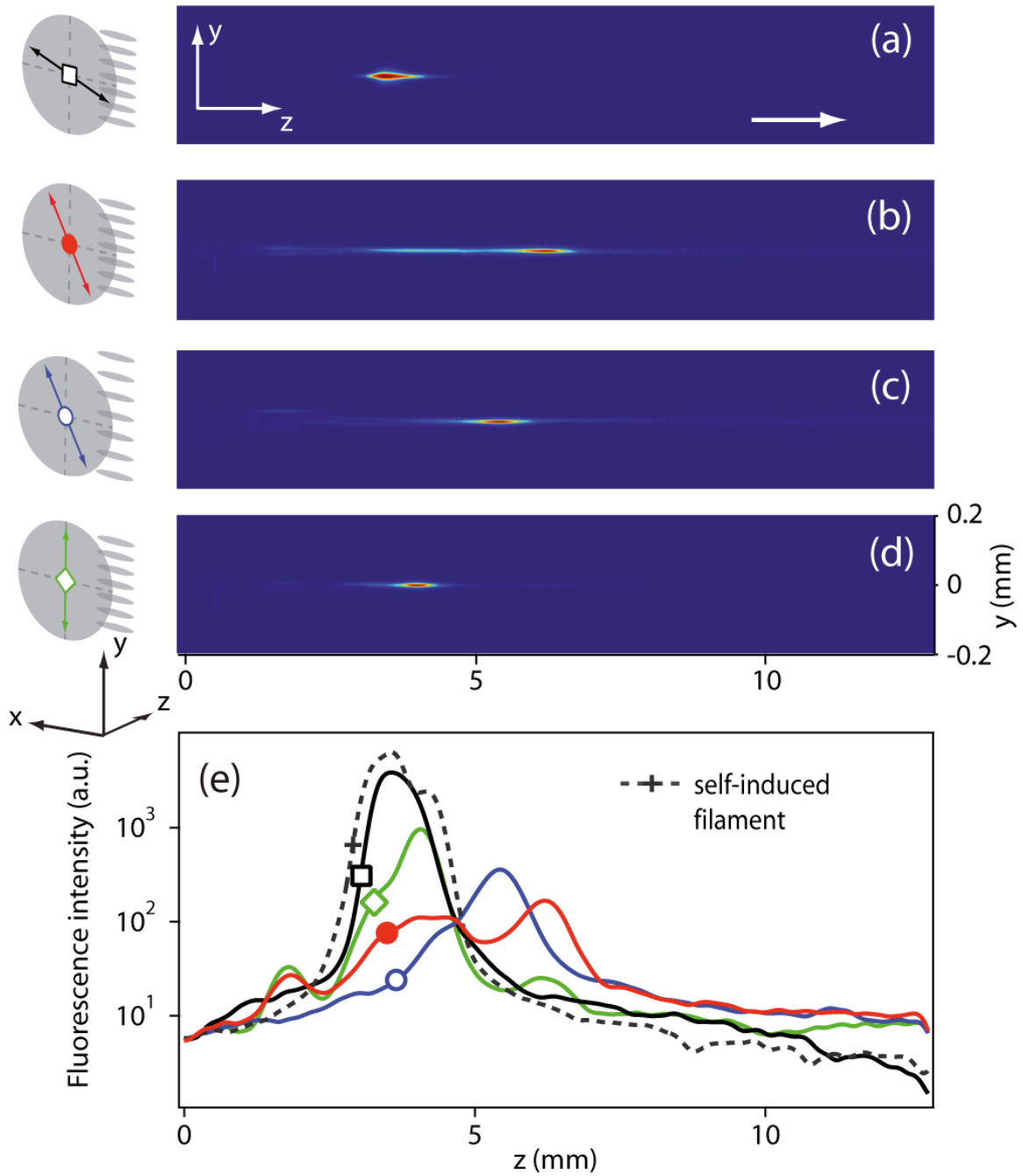


Fig 3-35 Fluorescence images for different input polarization (P) and lattice period (Λ): (a) $P = 20^\circ$, $\Lambda = 25 \mu\text{m}$; (b) $P = 60^\circ$, $\Lambda = 25 \mu\text{m}$; (c) $P = 60^\circ$, $\Lambda = 35 \mu\text{m}$ and (d) $P = 90^\circ$, $\Lambda = 25 \mu\text{m}$. (e). Corresponding longitudinal profiles (in log scale) compared to the SF profile (gray dashed line).

As depicted in Fig 3-36, the photonic lattice also affects the filament width and consequently the output power. Without lattice, the measured waist at FWHM of the SF is $5 \mu\text{m}$ (dashed line). The presence of the lattice leads to a clear widening up to $8.5 \mu\text{m}$ ($P = 60^\circ$). The total losses encountered by the pulse during the propagation, as measured by the output power, are shown in Fig 3-36(b). For input powers much smaller than P_{cr} , the intensity does not reach values where multiphoton absorption is important and the pulse propagates almost without losses (dashed line). By increasing the input power, nonlinear losses become more significant. For instance, for an input power of $5P_{cr}$, the losses can be as high as 25% for a SF. However, due to its larger width and consequently lower intensity, the LF experiences weaker nonlinear losses during the propagation (10% at $5P_{cr}$). Thus, due to their tailored properties (intensity, propagation length, uniformity and width), the formation of LFs also offers significantly lower losses, which makes them great candidates for applications such as pulse compression, etc.

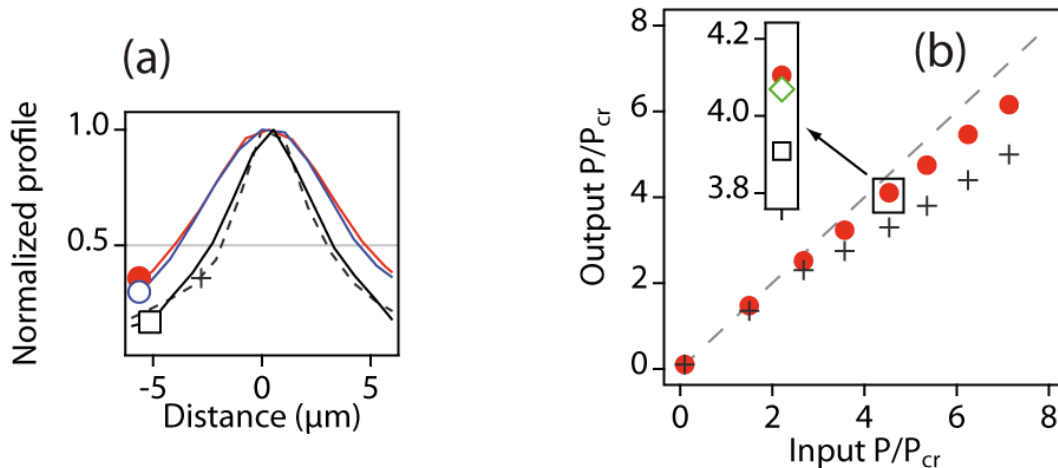


Fig 3-36 (a). Transverse profile of the LF for various configurations (P and Λ , see Fig 3-35) compared to SF (dashed curve and crosses). (b). Power measured at the output of the glass sample for different input power for the LF (filled circles) and the SF (crosses). The gray dashed line represents the linear propagation regime (i.e. no losses). The inset shows the output power for $5P_{cr}$ input power in various configurations. The drop of the peak intensity and the increase of the propagation length are associated to a widening of the filament, and consequently a more significant output power.

In the following, the nonlinear nature of the lattice filaments is clearly demonstrated during their interaction. We explore the interaction between filaments in lattices and offer additional means of tailoring the LF attributes. We used the experimental setup presented in Fig 3-37(a) to separate two filaments both spatially and temporally. We study first the interaction between two LFs. As qualitative reference we show in Fig 3-37(b) the fluorescence images of two SFs (labeled SF1 and SF2) separated by 50 μm (along the y axis, green arrow) that are either overlapped in time (i.e. zero time delay, $\tau = 0$) or not ($\tau \neq 0$).

We clearly observe no interaction between the two SFs even when they are overlapped in time as expected for a separation distance that is larger than the typical interaction length of SFs [171]. Fig 3-37(c) shows the same experiment for two beams LFs (labeled LF1 and LF2) (with $P = 60^\circ$, $\Lambda = 35 \mu\text{m}$, same as Fig 3-35(c)) that are also spatially separated by 50 μm . When the LFs are not overlapped in time the image is equivalent to the addition of two independent LFs as expected if no interaction takes place. However, the situation is strikingly different when the two LFs are at zero time delay. Interaction is now clear. Indeed, due to their wider transverse distribution, compared to the SFs, there is coupling between the two LFs leading to an energy exchange. The total energy (integrated intensity) of the LF1 is shown in Fig 3-37(d) and compared to the evolution of the total energy of the LF2. While the energy of LF1 increases by about 25%, the energy of LF2 drops by a similar quantity. A careful view of Fig 3-37(b) shows that the maximum intensity of the 2 LFs is slightly different. The energy transfer occurs between the 2 LFs from the stronger to the less intense filament, LF2 and LF1 respectively. As plotted in Fig 3-37(e) ($\tau = 0$ case) the energy transfer leads to a more intense LF. This behavior is also encountered during the interaction of solitons and filaments. Nonlinear interaction through the energy reservoir that sustains these structures leads to an energy exchange.

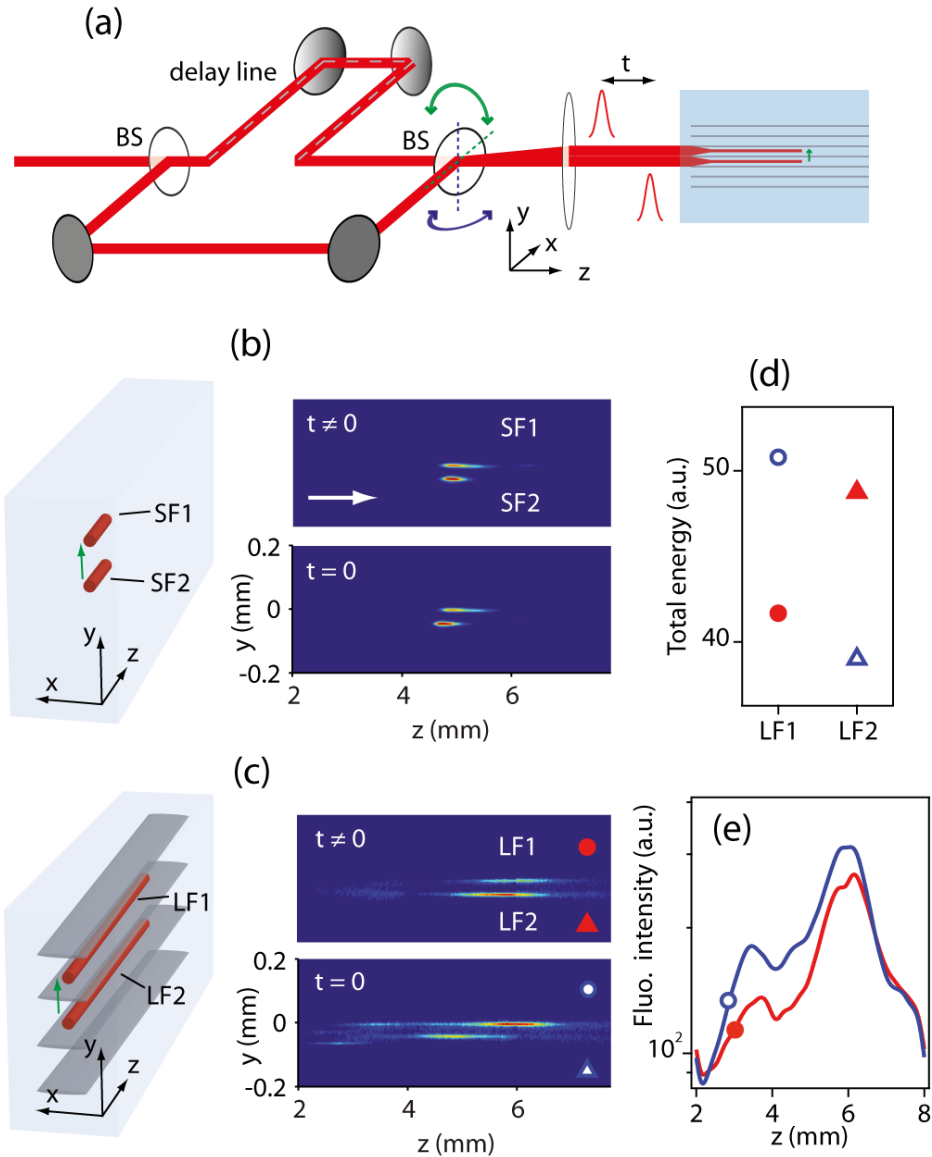


Fig 3-37 (a) Experimental setup. A delay line is used to separate in time the two pulses. One of the beam splitter (BS) is slightly rotated either around the x (green arrows) or the y axis (blue arrows) to spatially separate the two filaments. (b) Two SFs (SF1 and SF2) spaced by 50 μm (green arrow) overlapped in time ($\tau = 0$, bottom) and not ($\tau \neq 0$, top). (c) Same as (b) for two LFs (LF1 and LF2). The top and the bottom filaments are labeled 1 and 2 respectively. The widening of the LF waist increases the coupling and leads to the 2 LFs to interact. (d) Total energy (integrated fluorescence intensity) of the LF1 (circles) and the LF2 (triangles) at both $\tau = 0$ (opened symbols) and $\tau \neq 0$ (filled symbols) cases. An energy transfer occurs from LF2 to LF1. (e) Longitudinal profiles of the LF1 for $\tau = 0$ (opened blue circle) and $\tau \neq 0$ (filled red circle) cases.

Next we investigated the interaction between a SF and a LF. The spacing between the two input beams is reduced to $20\ \mu\text{m}$ in the y direction. As sketched in Fig 3-38(a) and (b), one beam is slightly shifted along the x axis (blue arrow) to spatially place it out of the photonic lattice. Again as a qualitative reference, we show in Fig 3-38(a) the interaction of two SFs (SF1 and SF2), separated by $20\ \mu\text{m}$. In this case, the SFs are close enough to strongly interact when they are overlapped in time, and merge to form an intense filament with its focus shifted towards the laser source. This configuration leads to an unstable propagation. On the other hand, Fig 3-38(b) shows that when the two pulses are not temporally overlapped the LF propagation is not affected by the presence of the SF. However, when they are at $\tau = 0$ (bottom image), the intensity of the LF is increased, a clear indication of energy transfer from the SF to the LF. The wider spatial profile of LFs enables them to interact with other nonlinear optical waves like SF in favor of their energy.

To better visualize this effect we show in Fig 3-38(c) the propagation of the LF for longer propagation distances (from 6 to 13 mm). The corresponding transverse profiles measured at a propagation distance $L = 10$ mm are plotted in Fig 3-38(d). The dashed line represents the profile of a single LF (without the SF). At this distance, the LF is spatially broadened. In the presence of a SF at $\tau \neq 0$ (filled circle), the widened profile simply corresponds to the addition of two contributions: the single LF signal (centered at position 2, dashed curve) and the intense SF trace (centered at the position 1, not shown). We observe that when the two filaments are at $\tau = 0$ (open circle), the LF is drastically affected by the presence of the SF. The propagation length of the LF is enhanced up to 11 mm leading to the sharp peak centered at the position 2. The increased background corresponds to the SF signal. It is worth noting that this behavior is not observed when a single LF propagates with twice the initial power (i.e. $10P_{cr}$). In that case, though the amplitude is twice more intense, the distribution is similar to the initial LF. These results suggest that the SF acts as an energy reservoir for the LF, allowing a significant increase of its propagation length.

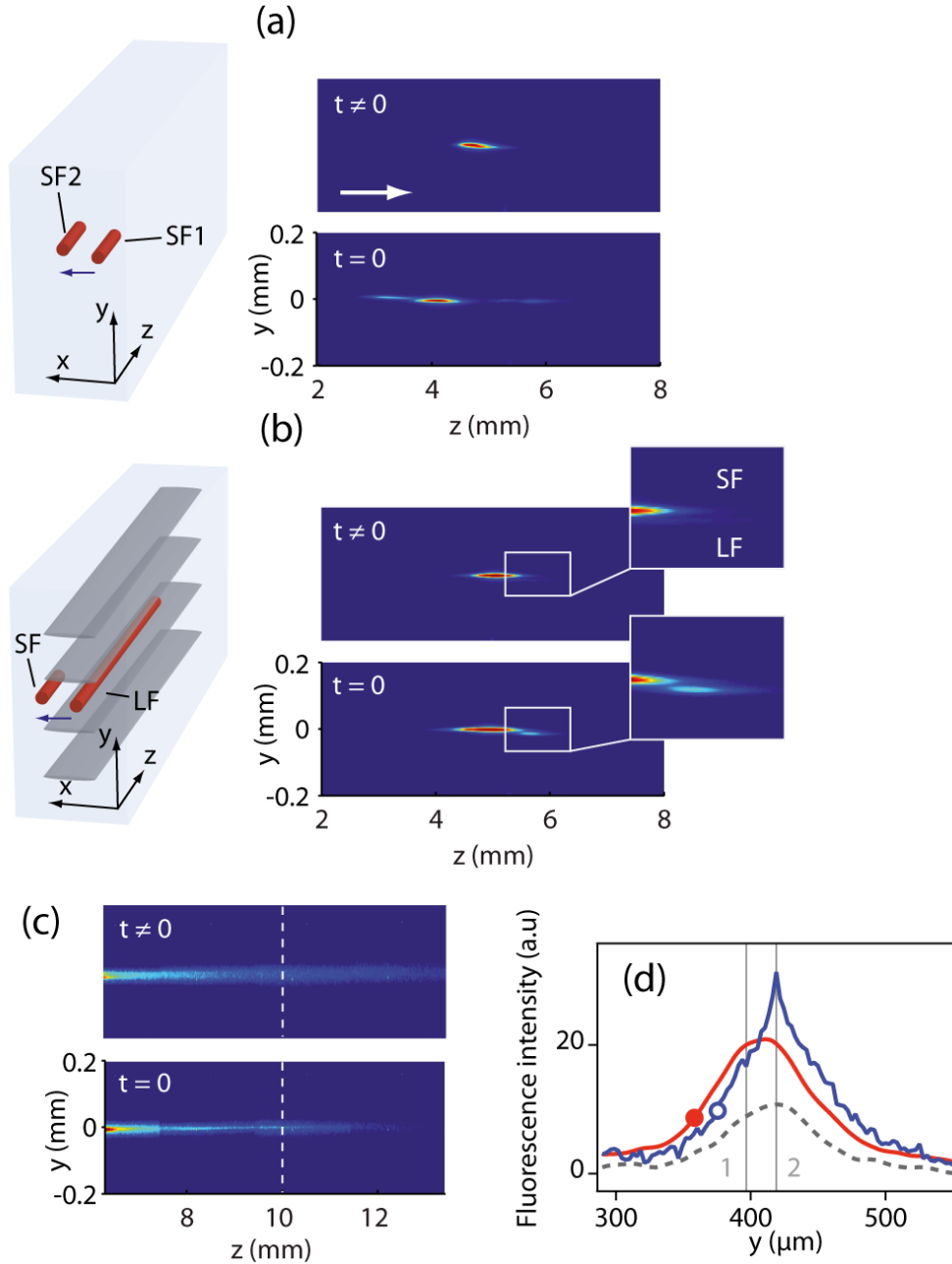


Fig 3-38 (a) Two SFs (SF1 and SF2) spaced by $20\ \mu\text{m}$ (blue arrow) overlapped in time ($\tau = 0$, bottom) and not ($\tau \neq 0$, top). (b) One SF and one LF at $\tau = 0$ (bottom) and $\tau \neq 0$ (top). The SF is obtained by slightly shifting the top beam (blue arrow) to be out of the photonic lattice. (c) Same as (b) for longer propagation length (from 6.5 to 13 mm). (d) Transversal profile at $z = 10\ \text{mm}$ (white line of c) of a single LF (dashed gray curve), of both the SF and LF at $\tau \neq 0$ (filled red circle) and of both the SF and LF at $\tau = 0$ (open blue circle). The 2 gray lines represent the position of the SF (1) and the LF (2).

To summarize, we have shown the first experimental evidence of photonic lattice filaments in solid media, i.e. new type of filaments with some attributes belonging to solitons and others to self-induced filaments. Self-action effects, which dominate self-induced filamentation and exclude any remote control over the filament attributes, have been regulated by appropriately selecting the lattice properties. Likewise, the inherent birefringence of the lattice fabricated in glass has been exploited to fine tune the lattice filament attributes by rotating the input polarization. We have also shown that, through a nonlinear interaction process, a second filament can be used as a virtual optical element to further tailor a lattice filament in respect to its intensity, uniformity and propagation length. Since our results open up the way for all optical control of the propagation of intense ultrafast wavepackets, our approach is expected to have a significant impact not only on the technologies utilizing laser filaments but also on numerous photonic applications.

The results shown in this section are the first experimental evidence of the filamentation tailoring with use of a lattice with positive Δn . The experimental demonstration of filamentation tailoring using a negative index plasma lattice will be demonstrated in the next section.

3.8 Filamentation tailoring in Bessel-like plasma lattices in water

In this section we provide another direct experimental evidence of effective control of the filament properties using a periodic lattice in water. The lattice is a transient plasma lattice generated by two co-propagating non-diffracting intense Bessel beams. The complex intensity pattern induced by the interference of the two Bessel beams correspondingly leads through multiphoton ionization to a local quasi-2D periodic plasma lattice. With numerical simulations we confirm that the observed tunability is not a result of linear guiding but of an enforced balance between the nonlinear propagation effects and linear diffraction from the refractive index modulation induced by the plasma lattice.

The schematic of the experimental setup is shown in Fig 3-39(a). The output of a Ti:Sapphire amplified laser system (35 fs pulses with energies up to 30 mJ, central wavelength 800 nm, 50 Hz repetition rate, linearly polarized) was split into two arms, the pump and the probe

(BS1). The pump pulses (up to 1 mJ) were used for the generation of the plasma lattice. Using a half-waveplate their polarization was rotated by 90° and then their spatial phase was modulated by a reflective type phase-only spatial light modulator (SLM, Hamamatsu LCOS). The phase modulated pump beam was then transmitted through the beamsplitter (BS2) and was collinearly recombined with the delayed probe beam. The two beams were directed into a variable length tank filled with distilled, de-ionized water. The probe beam used to generate the filament was independently focused inside the water tank, using a +200 mm focal-length lens. The relative timing between pump and probe was adjusted by using an optical delay line.

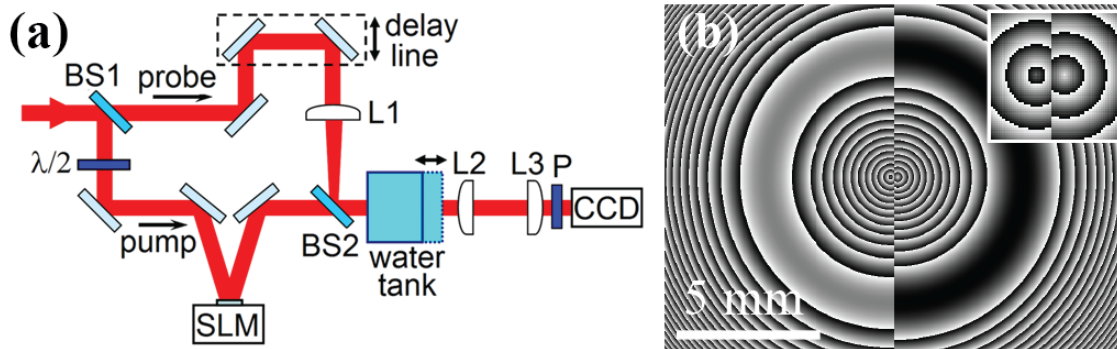


Fig 3-39 (a) Schematic of the experimental setup: BS1, BS2, beam-splitters; L1, L2, L3, lenses; P, polarizer; SLM, spatial light modulator. (b) Gray-scale image of the phase mask (white denotes 2π phase and black 0). A zoomed view of the central part of the mask is shown in the inset.

The position of the imaging part of the setup, comprised of a two-lens telescope (L2, L3) with magnification of 5.7 and a charge-coupled device (CCD) camera, was used to capture the pump and probe intensity distributions in water on the exit window of the water tank.. Since the polarizations between pump and probe are crossed, their intensities could be recorded independently using an analyzer placed in front of the CCD.

Let us now explain in more detail the way we create the desired lattice of refractive index modulation in water. It is important that the lattice length be sufficiently long, much longer than the normal filament [172]. Therefore, to create such long transient structures we used non-diffracting Bessel beams [173] which can be realized with good approximation by focusing Gaussian beams with a conical lens, or an axicon [174]. By combining two parallel, co-

propagating Bessel beams that are π phase shifted in respect to each other, we succeeded to generate a quasi-periodic modulation of the intensity and thus of the corresponding refractive index. In our experiment, each Bessel beam was generated by using a combination of radially symmetric linear and quadratic phase corresponding to an axicon combined with a spherical lens, which is necessary for their spatial separation and the extension of the Bessel zone. In our case, the required phase is given by $\varphi(r) = -(2\pi/\lambda)[\tan(\gamma) \cdot r + r^2/2f]$, where r is the radius, λ is the wavelength, γ is the Bessel cone angle, and f is the focal length of the lens. The phase mask used is shown in Fig 3-39(b). The left- and right- π phase shifted halves of the image correspond to the wrapped (modulo 2π) phase of a Bessel beam of cone angle 0.25° , combined with a negative lens ($f = -700$ mm). The centers of the two distributions are separated by $250 \mu\text{m}$ as can be seen from the inset in Fig 3-39(b).

The resulting simulated intensity distribution that is created at a propagation distance of 100 cm from the SLM is depicted in Fig 3-40(a), while Fig 3-40(b) shows the experimentally recorded intensity of the pump beam at the same distance. There is a fairly good qualitative agreement between simulation and experiment, while the most important aspect is that the intensity profile remains practically invariant along the propagation axis. As clearly shown in Fig 3-40(c), the mean period changes by less than 1.5% within 15 mm of propagation. The high intensity of the pump beam leads to electron excitation and plasma formation that in turn perturbs the refractive index [165, 175]. In this way the intensity and plasma distribution act as a template for the generation of an elongated transient refractive index modulation. Due to the multiphoton nature of the process the refractive index distribution is proportional to a power of the intensity distribution $\Delta n \propto I^K$ ($K=5$ for water at 800 nm).

In the experiment, the probe pulse energy was set at $\sim 2 \mu\text{J}$, slightly above the experimental threshold for filamentation, and the created light filament was launched parallel and exactly in-between the central pump intensity fringes as shown by a yellow spot in Fig 3-40(d). The red solid and black dashed curves in this figure represent the intensity profiles, along the x -direction, of the filament and the pump beams, respectively. For comparison, in the linear regime the measured waist of the probe beam was $40 \mu\text{m}$. Clearly, in such an arrangement at an appropriately adjusted pump-probe delay, the reduced refractive index due to the plasma generated by the pump effectively results in the formation of a $\sim 75 \mu\text{m}$ -wide slab type (quasi-2D) lattice for the probe beam propagation.

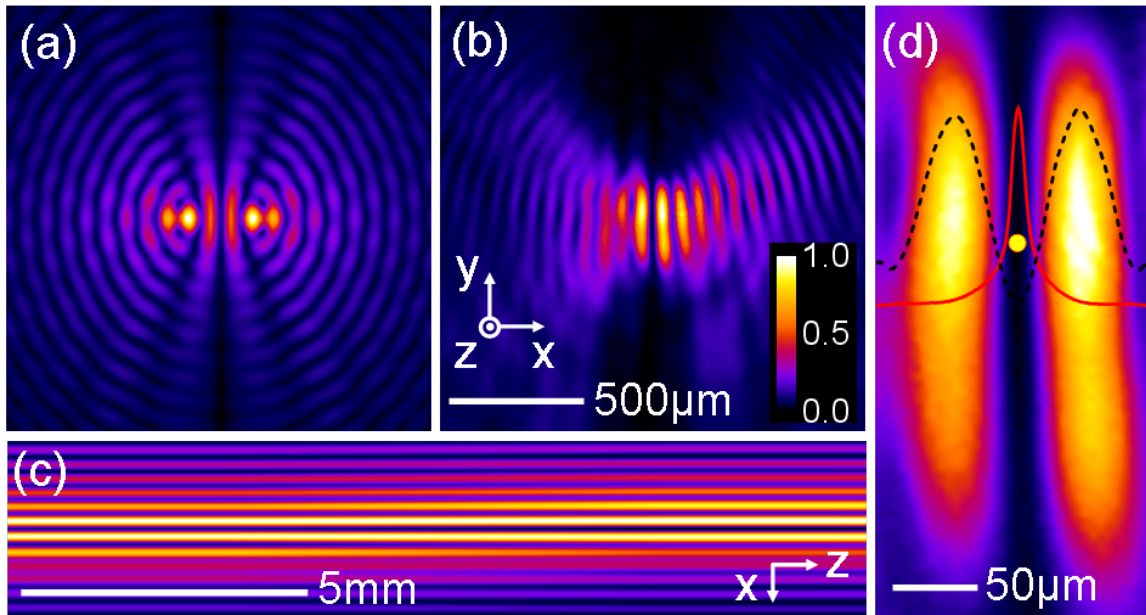


Fig 3-40 The simulated (a) and measured (b) double-Bessel intensity distribution of the pump beam. (c) xz -plane cut of the pump intensity. (d) Magnified image of the two brightest pump fringes with a yellow spot indicating the launching position of the filament.

The laser system compressor was tuned to compensate for the normal group-velocity dispersion of water and optics upstream to obtain the shortest pulses, and hence the highest pump intensities, at a propagation distance of 7 cm in water. The position of L1 was also adjusted to initiate the probe beam filamentation at the same z -position.

The xz -cuts of the recorded filament intensity in the absence of the lattice (top) and with the lattice at 80 fs relative delay (bottom) between pump and probe are shown in Fig 3-41(a). These filament profiles were obtained by stitching the respective filament intensity distributions captured at various z -planes over 6.6 mm of propagation with a 0.2 mm step (in each step the length of the variable water cell is increased).

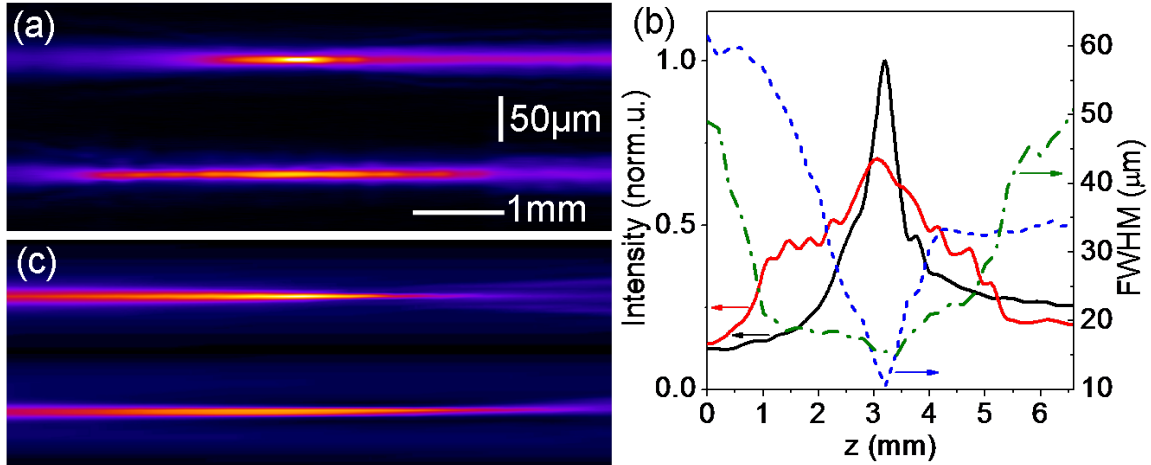


Fig 3-41 (a) Experimental xz -plane intensity distribution of the filament without lattice (top), and in the presence (bottom) of the plasma lattice. (b) The 1D filament intensity without (black solid) and with lattice (red solid). Blue dashed and green dash-dotted curves are the respective FWHM of the filament. (c) The simulated intensity of the filament without (top) and in the presence (bottom) of the lattice.

Note that the action of the lattice drastically changes the filamentary propagation, resulting in filament elongation and peak intensity depression, similarly to the prediction of numerical simulations in section 3.2 [172]. Our measurements indicate that at the relative delay of 80 fs, this refractive index modulation is due to the presence of the pump excited plasma. To better visualize the differences between these two filamentation regimes, in Fig 3-41(b) we plot the respective filament peak intensities and beam widths (FWHM). As can be seen, the propagation inside the plasma structure generated by the pump results in a ~ 4 times elongation of the filament length (FWHM) while its peak intensity is decreased by $\sim 40\%$. Moreover, a nearly constant filament waist of $\sim 20 \mu\text{m}$ is sustained over more than 3 mm of propagation, which is in striking contrast with the typical filament behavior whose minimum waist of $10 \mu\text{m}$ is doubled within less than half a millimeter. This result is a clear demonstration of filamentation tailoring where the competition of nonlinear effects with the linear diffraction induced by the lattice results in a new regime of filamentary propagation.

To confirm that the observed changes in the filament propagation are not just the result of linear wave guiding inside the plasma-induced positive index slab waveguide, numerical simulations were conducted using the three-dimensional (3D: 3 spatial coordinates with frozen

time) propagation code. The refractive index changes due to the free-electron plasma generated in the trail of the pump pulse were modeled based on a five-photon ionization process in water at 800 nm wavelength and the Drude model for plasma defocusing and absorption [175] using the pump intensity distribution of Fig 3-40(a). The peak power of the probe pulse was set to P_{cr} where $P_{cr} = 3.8MW$ is the critical power for self-focusing in water ($n_2 = 1.9 \times 10^{-16} W / cm^2$ at 800 nm). The simulated xz-plane intensity profiles of the probe filament are shown in Fig 3-41(c) where the upper and the lower images represent propagation without and with the lattice, respectively. In excellent agreement with the experiment, similar changes in the filament attributes - its elongation, greater uniformity, and peak intensity depression - are clearly identified. In the linear regime the coupling of the probe beam into the neighboring waveguides of the lattice leads to the spreading of energy toward the outer waveguides, thus confirming that the observed changes in the filamentary propagation in the high-intensity regime are not the result of linear guiding (data not shown).

To summarize this section, it is experimentally demonstrated that femtosecond laser filamentation can be tailored by using periodic lattices of refractive index inside a water tank. The major filament attributes, such as its length, uniformity, peak intensity and diameter were effectively controlled. Numerical simulations confirm that the observed changes in the filamentary propagation are not the result of a linear guiding but of an enforced balance between the nonlinear propagation effects and linear diffraction caused by the refractive index modulation of the lattice. The results suggest that more sophisticated structures both transient (e.g. laser generated plasma, molecular alignment [176]) and permanent (e.g. laser written waveguides in solids as was shown in section 3.7) can open the way for extensive and effective control of the filamentation process.

3.9 Multi filamentation control with 2D lattices in fused silica

Up until now filamentation tailoring with photonic lattices have been limited to the single filamentation regime. In this section the effect of 2D lattices on the propagation of Gaussian wavepackets in the multi-filamentation regime will be numerically investigated.

3.9.1 Bravais lattices

Due to symmetry reasons, there exist exactly five basic lattice cell geometries (Bravais lattices) in periodic crystalline structures in two dimensions. These are: square, rhombic, rectangular, parallelogramic (or oblique) and hexagonal. They are shown in Fig 3-42. The first case, the square lattice, has already been extensively studied in sections 3.6 in multiple materials. The remaining 4 types of lattice geometries have been extensively studied in the field of spatial solitons in the literature (see [136] and referenced therein). The use of them in filamentation tailoring in the multi-filament regime will be investigated here.

Each of the five lattices shown in Fig 3-42 is defined by three parameters, the distance a_1 and a_2 from one point to his two first neighbors and the angle φ formed by the two vectors \vec{a}_1 and \vec{a}_2 . A schematic representation of a 2D rectangular lattice can be seen in Fig 3-43, showing a_1 , a_2 , and φ .

All five lattices shown in Fig 3-42 can be generated by using different values for the parameters a_1 , a_2 , and φ using the following rules:

- **Square lattice:** $|a_1| = |a_2|$, $\varphi = 90^\circ$
- **Rectangular lattice:** $|a_1| \neq |a_2|$, $\varphi = 90^\circ$
- **Rhombic lattice:** $|a_1| = |a_2|$, $\varphi \neq 90^\circ$
- **Parallelogramic lattice:** $|a_1| \neq |a_2|$, $\varphi \neq 90^\circ$
- **Hexagonal lattice:** $|a_1| = |a_2|$, $\varphi = 120^\circ$

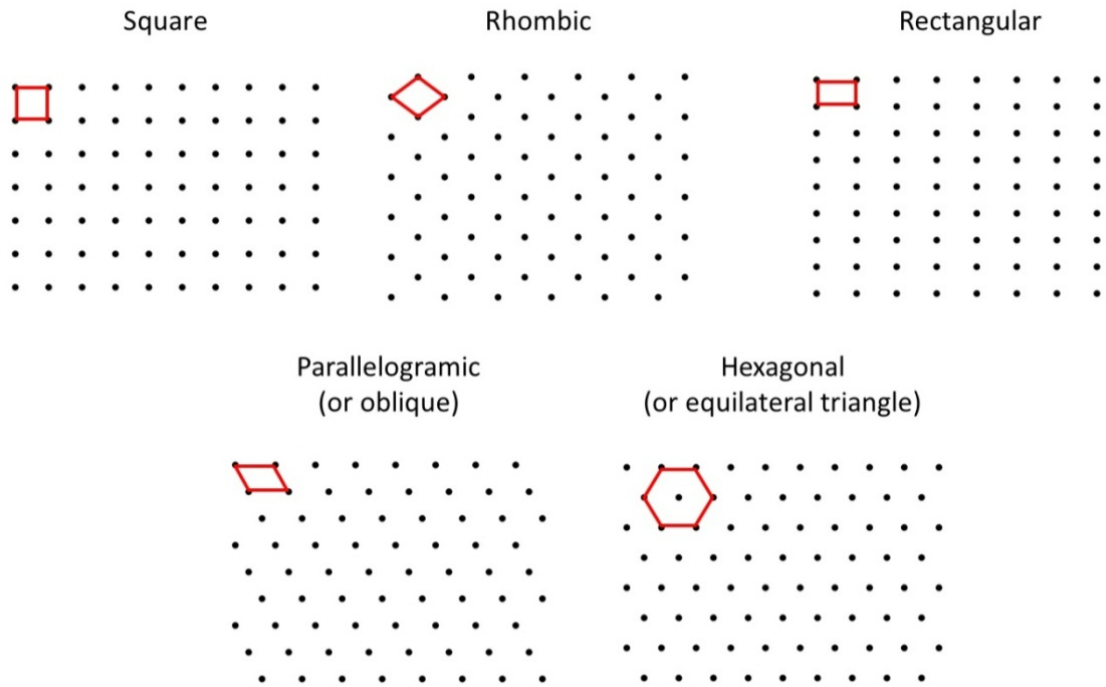


Fig 3-42 Schematic representation of the five basic two dimensional lattice geometries. Square, rhombic, rectangular, parallelogramic, and hexagonal.

Where the vectors \vec{a}_1, \vec{a}_2 and the angle φ are shown in Fig 3-43

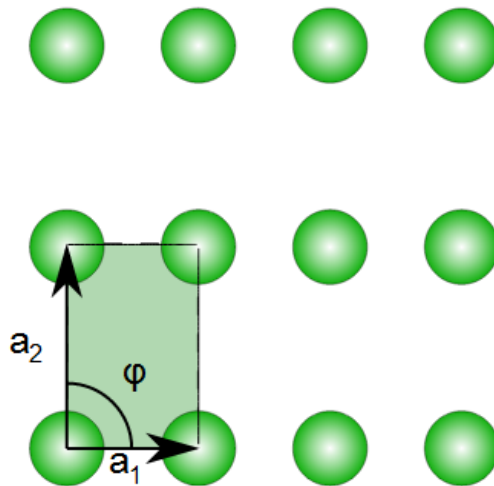


Fig 3-43 Schematic representation of a 2D rectangular lattice, with parameters $(\vec{a}_1, \vec{a}_2, \varphi)$.

To investigate the effect of the five 2D lattices depicted in Fig 3-42 we modeled each of them as in a similar way as the square lattice used in section 3.6. Each waveguide has a 2D super-Gaussian refractive index distribution of order $K = 5$ which corresponds to the multiphoton ionization order of fused silica in which the propagation is taking place. The diameter of each waveguide is $10 \mu\text{m}$ at FWHM with a maximum refractive index modulation of $+10^{-4}$. The spacing a_1 , and a_2 was varied from $25 \mu\text{m}$ to $75 \mu\text{m}$ for each of the five lattice geometries. In the cases of rhombic and parallelogramic lattices where $a_1 \neq a_2$, we used $a_1 = a_2 \pm 10 \mu\text{m}$. The input laser pulse used is a $10 P_{cr}$, 35 fs Gaussian laser pulse with $100 \mu\text{m}$ beam waist at $1/e^2$ radius. The propagation length is set to 3 cm which is enough to observe spatial dynamics within the bulk of fused silica glass. Since only spatial dynamics are studied here, for convenience the "frozen time" scheme is used in the simulations.

The best results for all five cases are depicted in Fig 3-44, where the radial fluence distribution is plotted along z . Note that in all cases the first priority is to lower the peak intensity of the tailored filament, so that MPA losses are limited. Then the fine tuning of the lattice can give spatial control over the intensity distribution of the beam. As we can see in Fig 3-44, any one of the five lattices can effectively tailor the $10 P_{cr}$ filament to some degree. For the right parameters $(\bar{a}_1, \bar{a}_2, \varphi)$ the spatial energy distribution is reformed into a multi-peak structure which propagates over 3.2 cm inside the bulk of fused silica glass. In contrast to the tailoring of single filaments, in the multi-filamentation regime, multiple filaments are now spatially controlled using the lattice lattice geometry. The small spatial oscillations along z are expected since the lattice-filament interaction is a dynamic equilibrium between the optical Kerr effect and lattice diffraction.

Further study of filamentation tailoring with the use of 2D Bravais lattices is out the scope of this thesis.

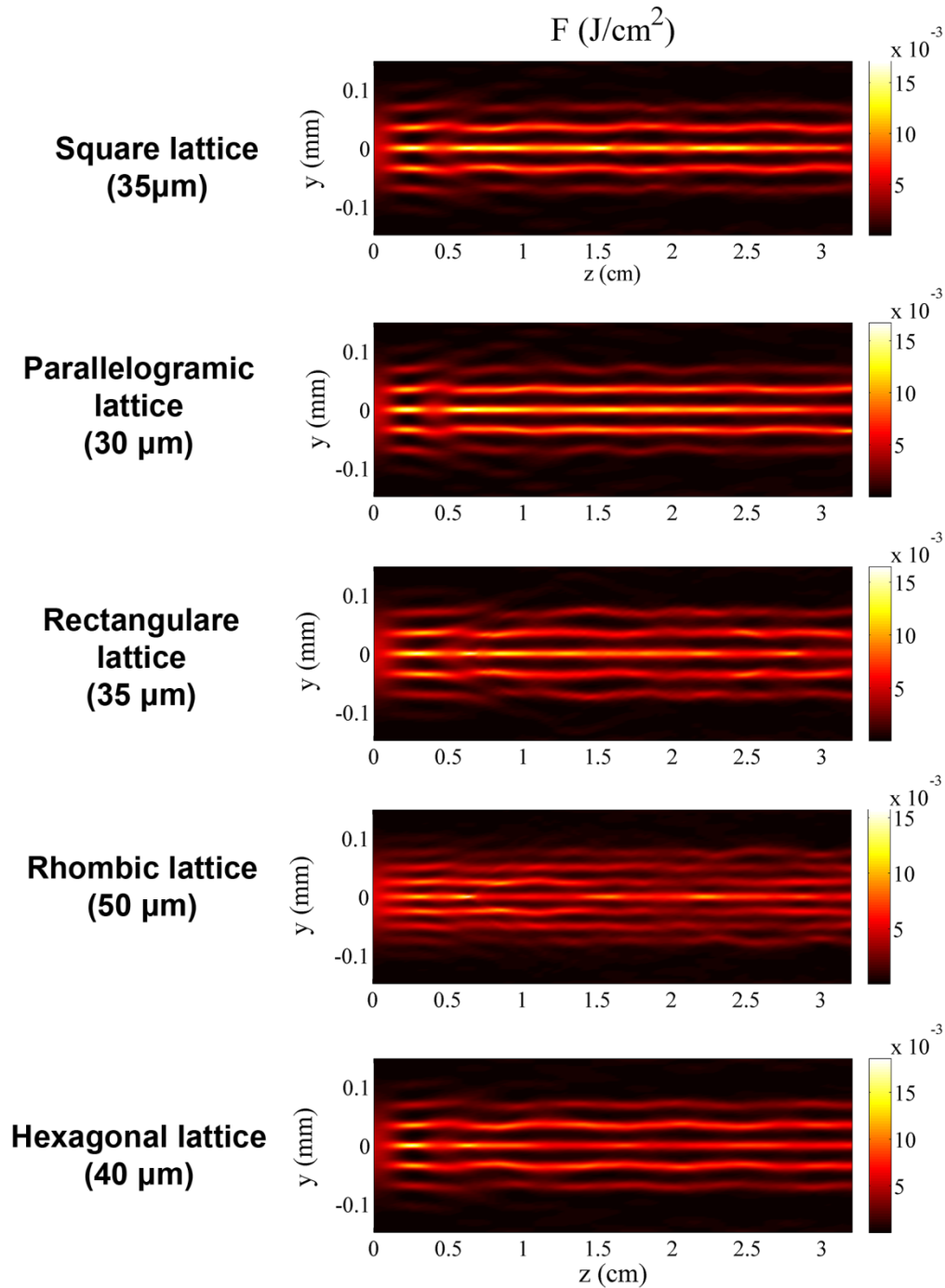


Fig 3-44 Filamentation tailoring in the multi-filament regime with use of 2D Bravais lattices. Each line shows the best result for the given lattice geometry. Plotted is the cross sectional intensity distribution vs z. First line: square lattice with 35 μm spacing. Second line: Parallelogramic lattice with 30 μm and 40 μm spacing, $\phi = 60$. Third line: Rectangular lattice with 35 μm and 45 μm spacing. Fourth line: Rhombic lattice with 50 μm and 60 μm spacing, $\phi = 30$. Last line: Hexagonal lattice with 40 μm spacing.

3.9.2 Discrete cylindrical lattices

Another, more intuitive lattice geometry is the discrete version of the cylindrical lattice used in section 3.2. In this case each ring is approximated by a number of rods, similar to the plasma strings generated by individual filaments (negative Δn) or permanently written waveguides (positive or negative Δn) as the ones in section 0. Since each successive ring has a bigger radius, the number of rods contained in each ring must be increased (doubled in this case), each time we move to an outer ring. Such a type of lattice is depicted in Fig 3-45, where the first layer has 5 rods, organized in a standard pentagon. Each waveguide has super-Gaussian refractive index distributions of order 5, like in the previously shown 2D Bravais lattices. The maximum refractive index modulation is $\Delta n_0 = +10^{-4}$.

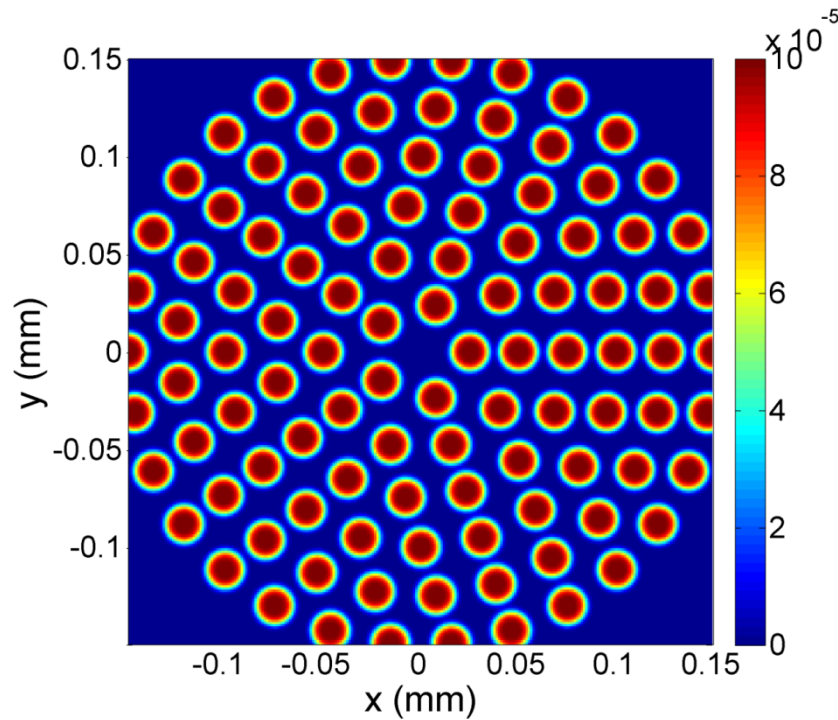


Fig 3-45 XY cross section. Refractive index modulation of the discrete cylindrical pentagonal lattice. Each waveguide has a super-Gaussian distribution of order 5 and a diameter of $10\ \mu\text{m}$ at FWHM. The spacing between each ring of waveguides is $25\ \mu\text{m}$ and the modulation depth $\Delta n = 10^{-4}$.

The input pulse has a Gaussian spatio-temporal intensity distribution with the central wavelength at 800 nm and pulse duration of 35 fs at FWHM. The beam is collimated with a 100 μm waist at $1/e^2$ radius, and is launched inside the lattice exciting multiple waveguides as seen in Fig 3-46. The material parameters for fused silica that were used in the simulations are identical with the ones used in section 3.6.2. Again the "frozen time" numerical scheme was used, since we are only interested in the spatial dynamics of the propagation.

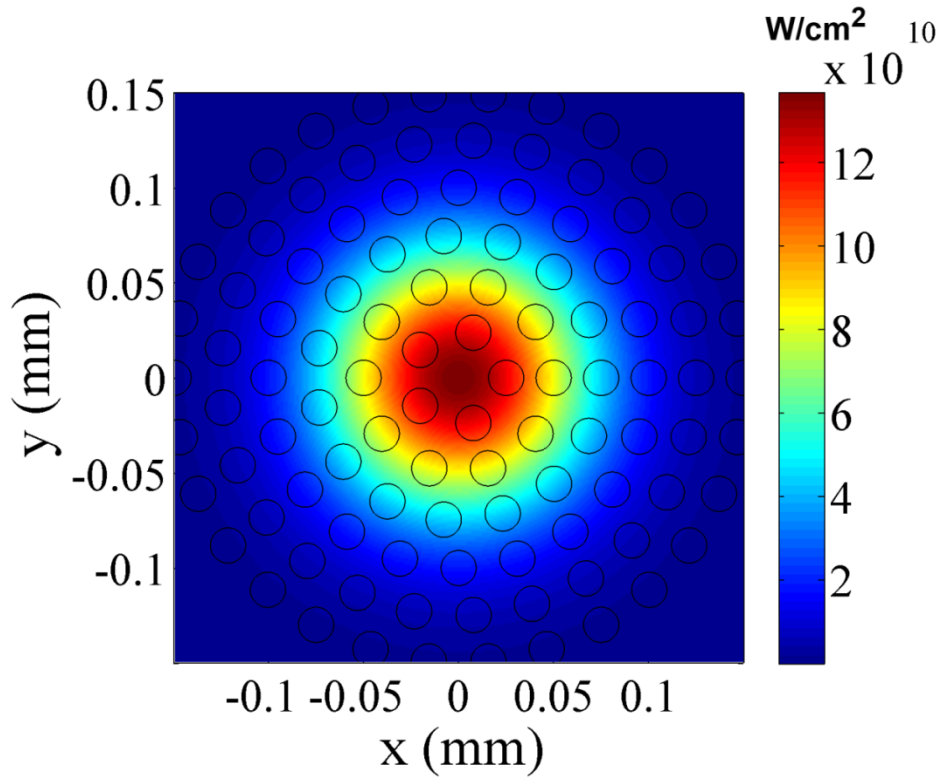


Fig 3-46 XY cross section. Gaussian beam launched in the pentagonal lattice of Fig 3-45.

Fig 3-47 shows the tailored filament attributes inside the lattice depicted in Fig 3-45. In Fig 3-47(a) we can see the peak intensity (blue continuous line) and corresponding electron density (green dashed line) along propagation distance. As we can see, the intensity is limited under $4 \times 10^{12} \text{ W/cm}^2$ while the plasma remains relatively low (about $\sim 2 \times 10^{15} \text{ cm}^{-3}$). In Fig 3-47(b) we can see the radial fluence distribution of the beam along propagation. We can clearly

see that the beam is reorganized in a pentagonal pattern at $z = 1.5$ cm and propagates as 5 distinct "beamlets" up to $z = 3.2$ cm. Interestingly, the point where the reshaping process completes coincides with the point of maximum intensity and plasma density. This indicates that the equilibrium is reached gradually, since once the threshold intensity value ($\sim 4 \times 10^{12} \text{ W/cm}^2$) is reached the reshaping process stops and the beam shape stabilizes. Before this point, the system seems to be oscillating around the most stable state, as the peak intensity is oscillating over one order of magnitude along z .

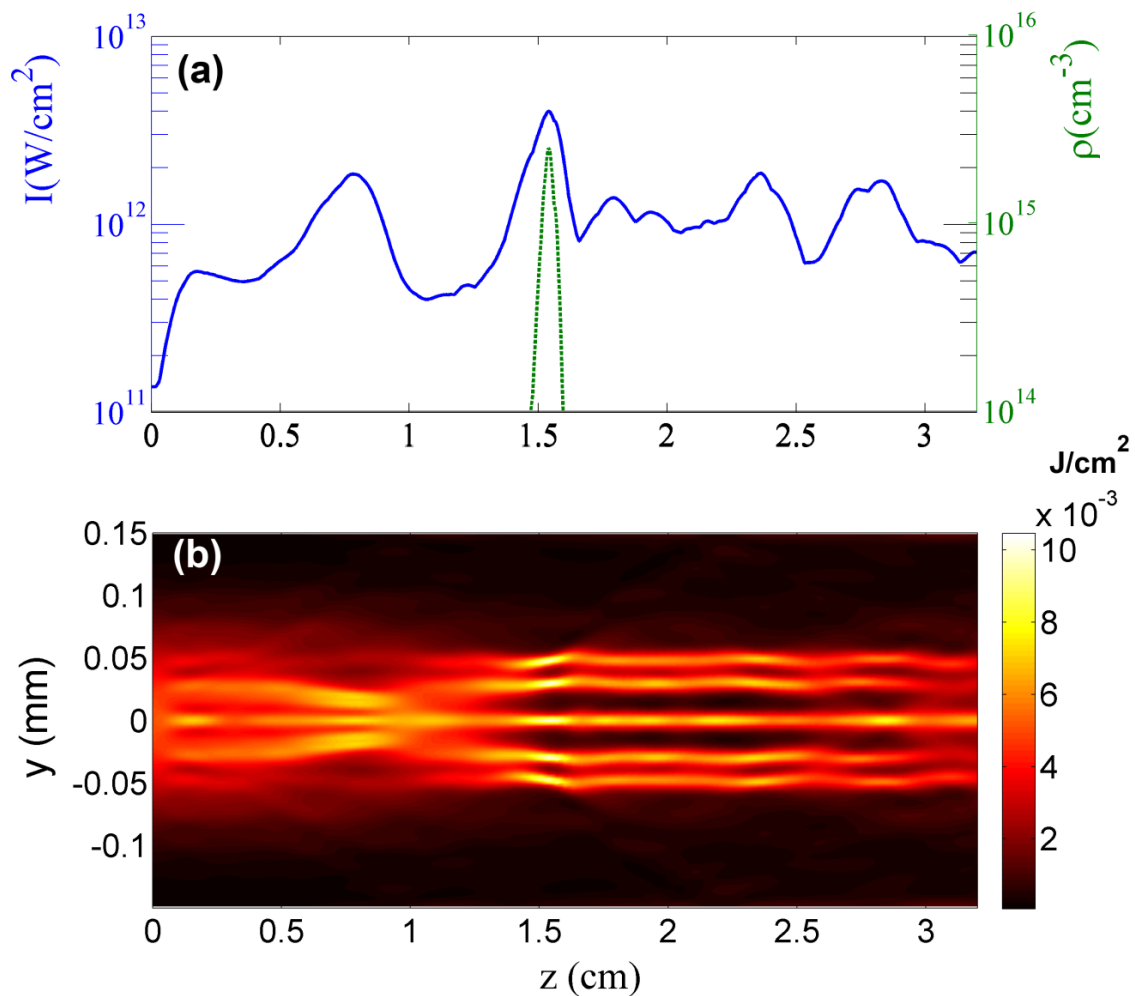


Fig 3-47 (a) Peak intensity and electron density along propagation, and (b) Cross sectional fluence distribution, of the $10 P_{cr}$ laser pulse propagating in fused silica glass along z .

Note that in the case of the discrete cylindrical pentagonal lattice, the reshaping process is much slower than it was for the 5 Bravais lattices in section 3.9.1. Here, 1.5 cm of propagation inside the lattice are necessary in order to obtain a stable distribution, while in all cases of section 3.9.1 the required distance is shorter than 0.25 cm. This observation gives us an additional control factor of the propagation of high power beams, since the spatial energy localization can be delayed in z by over 1 cm by choosing the appropriate lattice geometry.

If we take a closer look on the spatial intensity cross-sections at various positions along z , an interesting observation can be made. As we can see in Fig 3-48 at $z = 0.64$ cm, the beam is initially self-focusing and 5 intense spots are formed in the center ring, which coincide with the 5 lattice waveguides. After this point the lattice induced diffraction is overcoming the optical Kerr effect and the beam starts spreading out, which can be seen at $z = 1.12$ cm. At $z = \sim 1.6$ cm, the spatial equilibrium between Kerr and diffraction is obtained, and the waveguides of the second ring are excited. As we can see not all waveguides are illuminated equally. Half of the waveguides of the second ring are much brighter than the rest. This distribution of bright spots seems to be rotating as the beam propagates along z ($z = 20.8$ cm, $z = 2.4$ cm, and $z = 2.88$ cm), as shown in Fig 3-48. Note that the positions at which the cross-sections are chosen are not equally spaced in z , which means that the speed of the rotation is not constant. This is expected since, as in all tailored filaments shown before, the propagation is governed by the dynamic equilibrium between self-focusing and lattice diffraction. The stationary behavior observed in solitons cannot be seen in pulses carrying above 1 critical power.

The most important limiting factor to the tailoring process of filaments using periodic lattices is the fact that the lattice itself is mandatory for the whole process. This means that tailored filament can only exist inside the lattice potential. Any change in the lattice parameters after the equilibrium has been obtained will have destructive consequences on the tailored filament. This can be seen in Fig 3-49, where the radial fluence distribution of the tailored filament is shown, but this time the lattice stops at $z = 2$ cm. As we can clearly see the spatial beam distribution quickly disperses, since the equilibrium is lost.

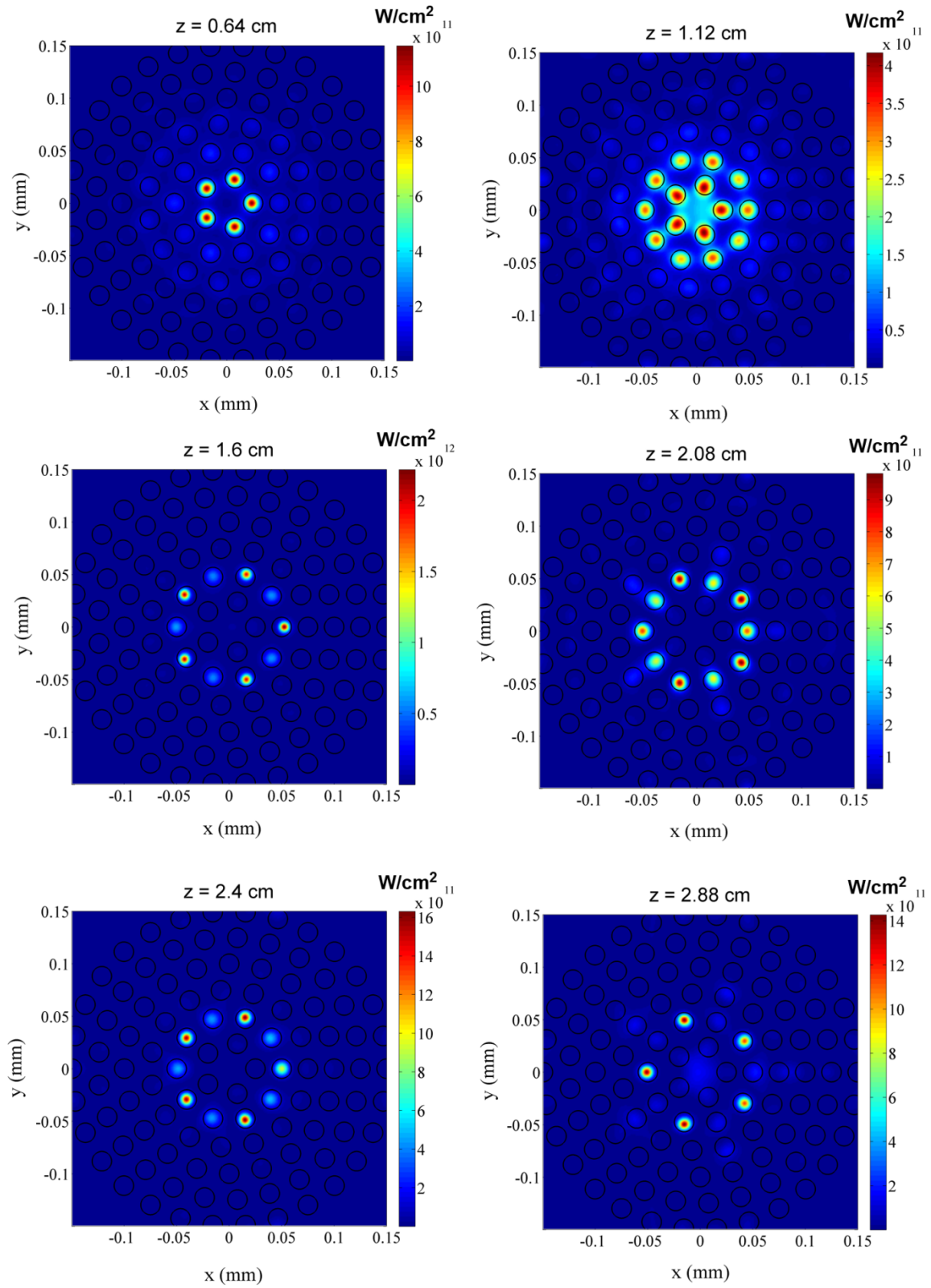


Fig 3-48 Discrete cylindrical pentagonal lattice. Intensity cross-sections at various position along z.

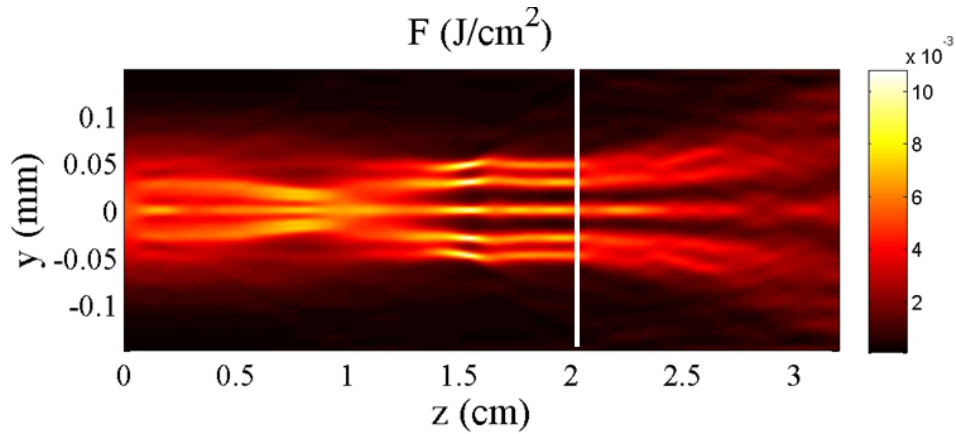


Fig 3-49 Cross sectional fluence distribution, of the $10 P_{cr}$ laser pulse propagating inside the cylindrical symmetric lattice in fused silica glass along z . Lattice stops at $z = 2$ cm.

For practical applications it would be useful to be able to extract the tailored filament at the edge of glass sample. However this proves to be extremely difficult. As we already seen in Fig 3-49, the beamlets diffract rapidly once the equilibrium is perturbed. By changing the medium from glass to air is even more severe. This can be clearly seen in Fig 3-50, where the tailored filament shown in Fig 3-47(b) is propagating an addition 1 cm in air. As we can see right after the silica block ends (white line) the beamlets are diffracting rapidly.

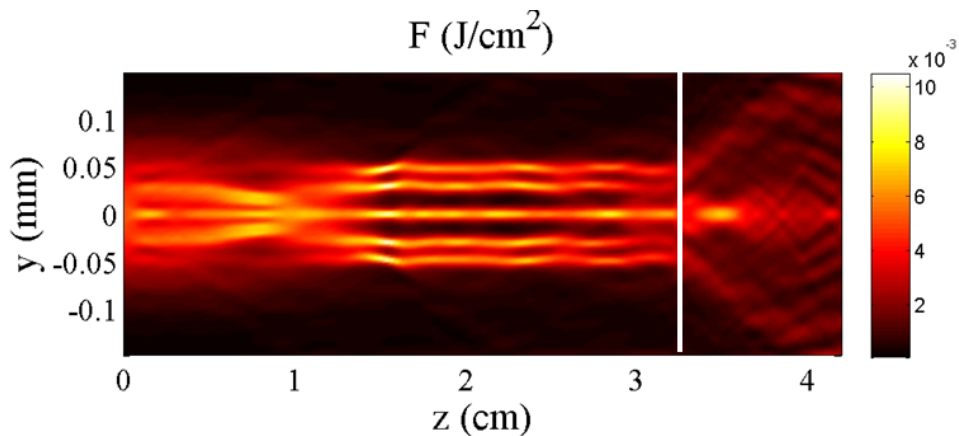


Fig 3-50 Cross sectional fluence distribution, of the $10 P_{cr}$ laser pulse propagating inside the cylindrical symmetric lattice in fused silica glass along z . Silica block stops at $z = 3.2$ cm, while the beam propagates an additional 1 cm in air.

4. Filamentation tailoring with non-diffracting beams

The linear wave equation supports various stationary solutions, which are called non-diffracting waves. A non-diffracting wave is essentially maintaining its spatial intensity distribution as it propagates in space. Numerous different non-diffracting solutions have been discovered in the literature in multiple dimensions, like the Airy beams, Bessel beams, and Mathieu beams [177]. The main limitation of non-diffracting waves is that they have infinite size and energy, and thus can only exist in theory. However the finite versions of them do exhibit non-diffracting properties over a limited distance in space.

The importance of non-diffracting waves in optics is essential, since their non-diffracting properties can prove useful for both experimental and practical applications. In this section non-diffracting beams will be used in order to tailor light filaments in air, water and fused silica glass.

4.1 Finite energy Bessel beams

Bessel beams are the simplest type of conical waves. Conical waves owe their name to the fact that their energy flux is on the surface of a cone. In addition they are stationary, *i.e.* nondiffracting, stationary solutions to the wave equation. The main linear characteristic of optical Bessel beams is the ability to propagate without diffracting in space, maintaining a constant intensity profile.

Bessel beams in particular, can be viewed as the superposition of infinite plane waves whose wave-vector lies on a cone or as a superposition of two Hankel beams [178]. As the conical wave propagates, due to interference effects, an intense central core, surrounded by lower intensity rings is formed along the propagation direction. The intensity distribution of a Bessel beam is analytically described by the Bessel function of the first kind J_a [179] by:

$$J_a(x) = \sum_{m=0}^{\infty} \frac{(-1)^m}{m! \Gamma(m+a+1)} \left(\frac{1}{2}x\right)^{2m+1} \quad (4.1-1)$$

where Γ is the gamma function of ordinal in mathematics, an extension of the factorial function to real and complex numbers, with its argument shifted down by 1:

$$\Gamma(n) = (n-1)! \quad (4.1-2)$$

The Bessel function was first defined by the Daniel Bernoulli and Friedrich Bessel, as the solution of Bessel's differential equation:

$$x^2 \frac{\partial^2 y}{\partial x^2} + x \frac{\partial y}{\partial x} + (x^2 - a^2)y = 0 \quad (4.1-3)$$

The central part of the 2D Bessel function can be seen in Fig 4-1.

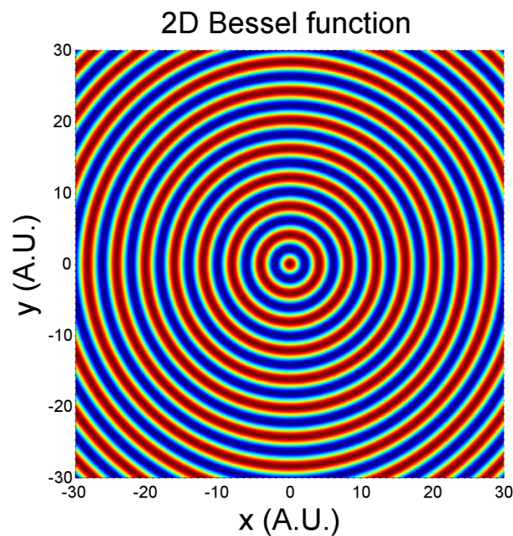


Fig 4-1 Graphical representation of a 2D Bessel function.

Ideal theoretical optical Bessel beam are infinite in size, carrying infinite energy, therefore not experimentally feasible. In the laboratory frame, Bessel beams have finite size and energy; however they retain their nondiffracting properties of the ideal Bessel beam over a small distance in space, called the Bessel zone.

4.1.1 Generation with an axicon

Bessel beams are commonly generated using axicons [174], while more complex optical systems such as holographic elements [180] and lensacons [181] can also be used offering a more flexible setup. An axicon is an optical element with one side flat and the other side conical. As the pulse propagates through the axicon and exits from the conical side, the wavefront is transformed to conical. The total length of the Bessel zone depends on the input beam diameter and the axicon's conical angle.

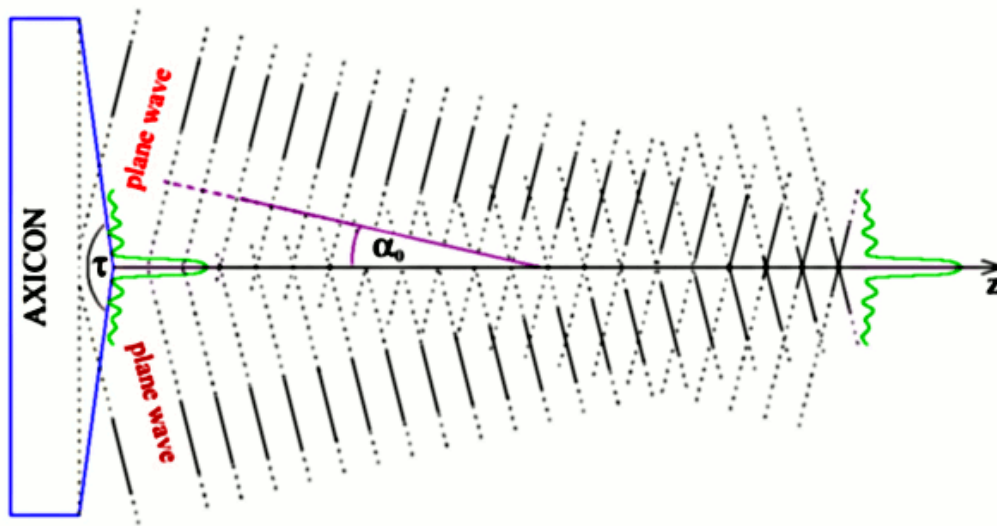


Fig 4-2 Generation of a Bessel beam using an axicon with cone angle of τ .

4.1.2 Stationary UV Bessel filaments in air

In this section the use of Bessel beams will be utilized to control the attributes of UV filaments in air.

When the input laser pulse power is low its propagation is governed by the laws of linear optics. For instance, when a laser pulse is focused by a spherical lens the longitudinal length L of the focal region, known as the Rayleigh length, is $L \propto d^2$ while the intensity $I \propto 1/d^2$, where d is

the focal spot diameter. Thus, in the linear regime any extension of the focal region is always in the expense of intensity. In contrary, when the laser pulse power exceeds the critical power for self-focusing P_{cr} [12], a number of interesting nonlinear effects take place associated with the filamentation phenomenon. This phenomenon can be qualitatively explained as a dynamical competition between linear and nonlinear effects including Kerr self-focusing, ionization defocusing, nonlinear losses and dispersion effects [10]. For typical Gaussian beams, focused by spherical lenses, filamentation extends on a region much longer than the Rayleigh length L while the intensity is maintained at very high levels ($\sim 10^{13}$ W/cm²). Although filamentation seems a perfect candidate for the generation of long regions of high intensity there are also drawbacks. As mentioned already filamentation is a dynamical process with strong spatio-temporal effects that lead to a more or less modulated on axis distribution of intensity and plasma density. This modulation can somehow be moderated when the beam propagates in a medium exhibiting strong nonlinear absorption (two or three photon absorption), or when the high intensity peak is reached by means of a sufficiently smooth growth inside the nonlinear medium (adiabatic coupling) [182, 183].

On the other hand, filamentary-like propagation is also achievable, even in the linear propagation regime, by Bessel beams. In the nonlinear regime the high intensity core of the Bessel beam will lead to the generation of free electrons through multi-photon ionization.

Filamentation dynamics in various media using pulsed Bessel beams has already been studied (see [184], and references therein). More recently, ultrafast IR (800 nm) Bessel beams have been used to generate long plasma strings in air [185, 186]. In these works the reported simulated electron density values were in the range of 10^{16} cm³. Furthermore, the plasma density was not uniform exhibiting either oscillations, due to the use of narrow beams and a blunt-tip axicon, [185] or significant variation over the propagation distance [186]. Also, it was reported [186] that by adding temporal chirp in the pulse, the plasma string position and length could be relatively extended but in the expense of peak electron density.

In this section we report on the creation of tunable in length, uniform plasma strings of high electron densities ($\sim 10^{18}$ cm⁻³) in air using UV short pulse Bessel beams. The use of UV radiation makes the ionization process very efficient and along with the optimization process achieved by the tuning of the Bessel beam angle makes it a perfect candidate for the generation of very long and uniform plasma strings in air. The string length tunability is achieved without

sacrificing the plasma uniformity, while the impact on the peak electron densities is also very small.

4.1.2.1 Experimental setup

A hybrid feedback distributed dye/KrF excimer laser, delivering 0.5 ps (or 5 ps), 248 nm pulses was used in our study. The output laser beam profile was top-hat with spatial dimensions of 50 mm x 50 mm. The central part of the laser beam was selected by means of an iris and was directed towards the optical system that transformed the beam to conical. The optical system was either a simple fused silica axicon, with base angle of $\gamma = 5^\circ$ (170° apex angle) or a system composed by the same axicon preceded by a fused silica plano-concave lens of $f = -200$ mm focal distance, placed 3 cm from the axicon, as shown in Fig 4-3(a). In the experiments both available laser pulse modes, 0.5 ps and 5 ps, were used.

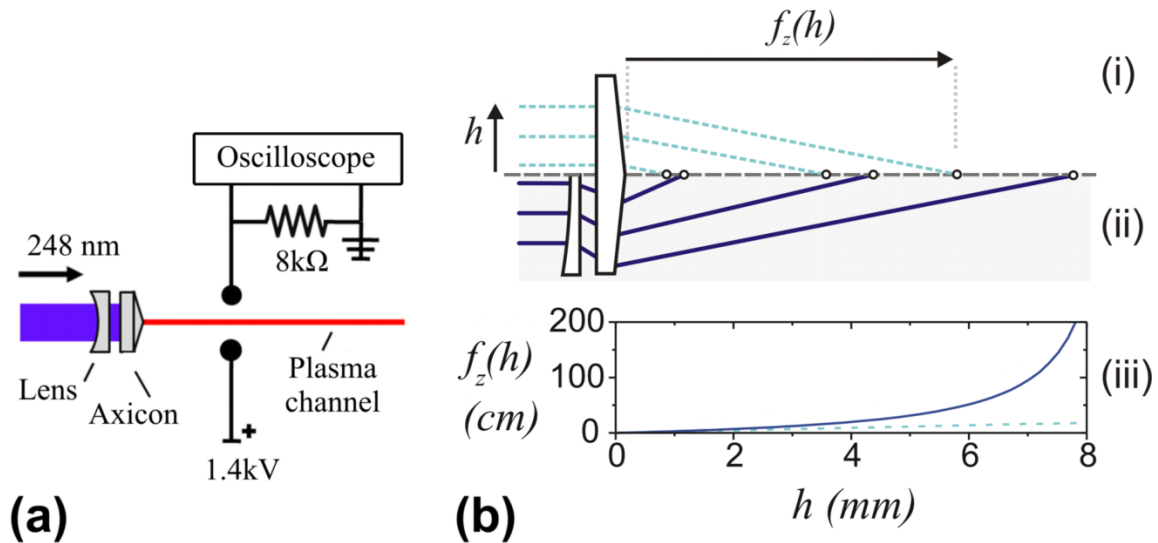


Fig 4-3 (a) Experimental setup. (b) Ray tracing for (i) an axicon, (ii) an axicon preceded by a diverging lens. (iii) Axial focusing distance $f_z(h)$ as a function of the ray height h for an $\gamma = 5^\circ$ axicon (dashed line) and a combination of this axicon with a diverging lens ($f = -200$ mm) (solid line).

An electric conductivity technique was used to characterize the generated plasma strings after the axicon [187]. The measurement system consisted of two steel electrodes (~ 1 mm

diameter) separated by 3 mm distance. A Teflon slit aperture was placed in front of the electrodes to exclude undesired ionization on the electrode's surfaces from the UV laser beam. The plasma string passed between the two electrodes while a DC high voltage (1.4 kV) was applied on them. The laser generated plasma redistributed in the presence of the applied external electric field (~ 4.7 kV/cm) and screened out [188] the external field, generating a potential drop across the electrodes that caused a current to flow through the $8\text{ k}\Omega$ probe resistance. The voltage drop across the resistance was measured using a standard oscilloscope. When this detection setup is operated in the ohmic regime (current is proportional to the applied high voltage) the measured electric signal depends linearly on the mean, over the plasma channel diameter, excited electron density $\langle N_e \rangle$. The correlation of the electric conductivity measurements to plasma density estimations was done by comparison with a precise, but more complex, holographic method [175].

As mentioned above an axicon was used to generate the Bessel beam. From a ray tracing point of view an axicon focuses all the rays that lie on a cylinder of radius h to an axial focus at a distance $f_z(h)$ from the axicon apex, as shown in Fig 4-3(b)(i). In contrast to a spherical lens the axial focus position depends linearly on the ray height h . For an axicon with small base angle the axial focus position can be written as: $f_z(h) \cong h / [(n - n_o)\gamma]$, where γ is the base angle of the axicon, n is the refractive index of the axicon and n_o is the refractive index of the surrounding medium (air). The longitudinal size of the focal region in this case is defined by the base angle of the axicon and the beam diameter. A highly efficient way to expand this region is to place a diverging lens before the axicon. The axial focusing range is expanded while the axial focus position is now a nonlinear function of the ray height h , as shown in Fig 4-3(b)(ii). In this case with a good approximation the axial focus position can be written as:

$$f_z(h) \cong \frac{h}{(n - n_o)\gamma + h/f} \quad (4.1-4)$$

where f is the focal distance of the diverging lens. It is clear that after the insertion of the diverging lens the optical system acts as an axicon with an effective base angle γ_{eff} given by:

$$\gamma_{eff} \cong \gamma + \frac{h}{f(n-n_o)} \quad (4.1-5)$$

The effective base angle is no longer constant and linearly depends on the ray height. Fig 4-3(b)(iii) shows the significant extension of the longitudinal focusing range achieved by this approach.

4.1.2.2 Experimental and simulation results

The electron density distributions of the plasma strings created when using the axicon alone are shown in Fig 4-4(a) for both pulse durations. In both cases a homogeneous plasma channel ~ 150 mm long is created. The estimated electron density values are in the range of $\sim 2.5 \cdot 10^{18} \text{ cm}^{-3}$ and 10^{17} cm^{-3} for the 0.5 ps and 5 ps pulses respectively. The difference in the peak electron densities is due to the lower pulse intensity of the longer pulses.

Although homogeneous, the plasma strings obtained in this way are relatively short in length. To obtain longer plasma strings we introduced the diverging lens as described above. The obtained plasma string electron distributions are shown in Fig 4-4(b), for the same input pulse parameters as in Fig 4-4(a). One observes a considerable increase in the length of the plasma strings, without any compromise in the plasma uniformity, accompanied by a small reduction of the peak electron density. For the shorter 0.5 ps pulses the plasma string length was extended by a factor of $\sim 10x$ with a $\sim 3.4x$ reduction of the electron density ($\sim 7.4 \times 10^{17} \text{ cm}^{-3}$). Despite this reduction, the plasma density is still 2 orders of magnitude higher than previously reported values from relative studies [15, 16]. Likewise, for the 5 ps pulses the plasma string length was increased by a factor of $\sim 5x$, accompanied with a $\sim 2x$ reduction of the electron density values ($\sim 6 \cdot 10^{16} \text{ cm}^{-3}$).

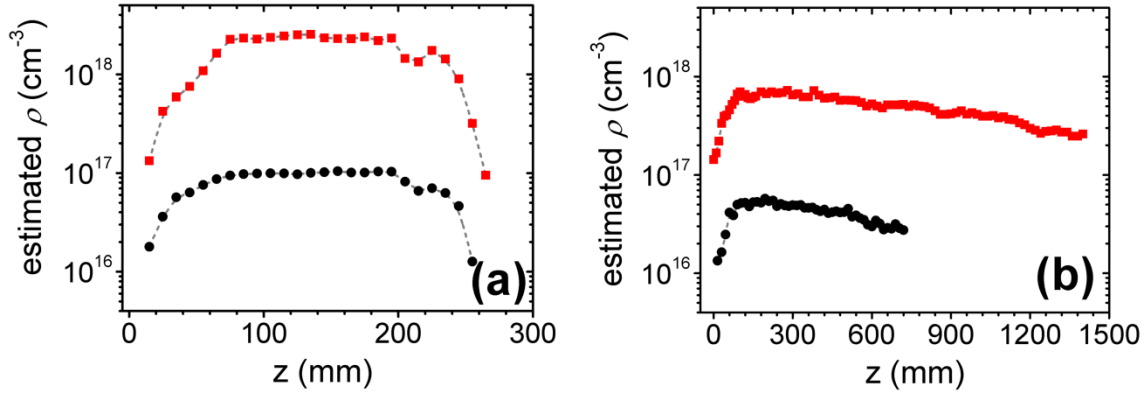


Fig 4-4 Electron density ρ versus propagation distance for 248 nm, UV Bessel beams. (squares) - 7.5 mJ, 0.5 ps, (circles) - 10.25 mJ, 5 ps. (a) axicon only (base angle $\gamma = 5^\circ$), (b) axicon with diverging lens ($f = -200$ mm)

Beyond the spatially achieved stationarity we verified that this conically driven filamentary propagation does not involve any temporal effects either. For this we monitored the UV laser pulse spectrum before and after the formation of the plasma strings. The comparative spectra are shown in Fig 4-5 for both pulse durations, showing insignificant spectral evolutions. This is a strong indication that no temporal effects, like pulse splitting, take place during the pulse propagation and plasma string formation.

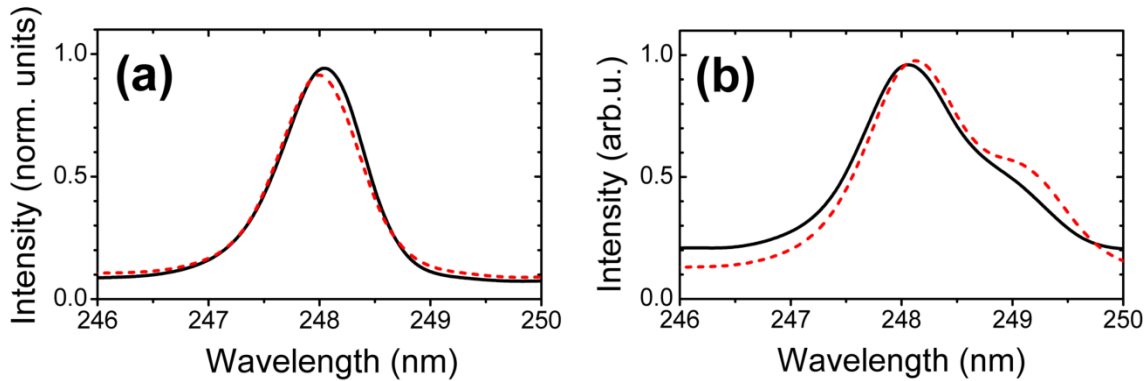


Fig 4-5 The measured spectra of the pulse before (solid curve) and after (dashed line) formation of the plasma channel; (a) for 5 ps pulse duration and (b) for 0.5 ps pulse duration.

In order to further explore this conical filamentation regime numerical simulations of the nonlinear propagation have also been performed, using a complete 3D code that solves the nonlinear Schrödinger equation (NLSE) coupled with a rate equation for the electron density evolution. The numerical model is described in detail in [8] and it takes into account diffraction, plasma defocusing, group velocity dispersion by using the full dispersion relation (Sellmeier - like) for air, and nonlinear effects such as the Kerr effect, and multi photon absorption. The electron density evolution equation takes into account multi-photon ionization, as well as avalanche ionization and trapping. The effect of the axicon is modeled by the multiplication of the input field with a phase mask, $\exp[i\varphi(h)]$ where $\varphi(h) = -2\pi h \lambda^{-1} \sin[(n-1)\gamma]$, λ is the wavelength and n , γ are respectively the refractive index and the base angle of the axicon.

Simulations were performed under the same conditions as in the experiment (0.5 ps, 248 nm, axicon base angle $\gamma=5^\circ$, diverging lens $f = -200$ mm). Furthermore, to clarify the role of nonlinear effects in the propagation we simulated two distinct cases: one for input energy of 7.5 mJ, as in our experiments, and one for very low, 7.5 nJ input energy (corresponding to a power $7 \cdot 10^{-5} P_{cr}$) with all other parameters unchanged. The results of the simulation are shown in Fig 4-6. As it is clear, the on-axis intensity for the low input energy is $\sim 10^6$ times smaller than the on-axis intensity, corresponding to the 10^6 times higher input energy, but follows the same shape as for the high input laser energy. This result confirms that the propagation is governed by the linear induced conical wavefront. The on-axis electron density, for the case of the 7.5 mJ input energy is also shown in Fig 4-6. The peak electron density value of $6.5 \cdot 10^{17} \text{ cm}^{-3}$ of the simulation agrees nicely with the measured one $7.4 \cdot 10^{17} \text{ cm}^{-3}$, while the simulated electron density is decaying faster as a function of the propagation distance. This discrepancy could be attributed to the fact that the electric conductivity technique, which is sensitive to the plasma string volume between the electrodes, results in averaged electron density values $\langle N_e \rangle$, while the simulation results refer to the peak electron densities in the center of the plasma string core. Finally, the numerical results show no temporal evolution of the filamented laser pulses, in agreement with the experimental findings.

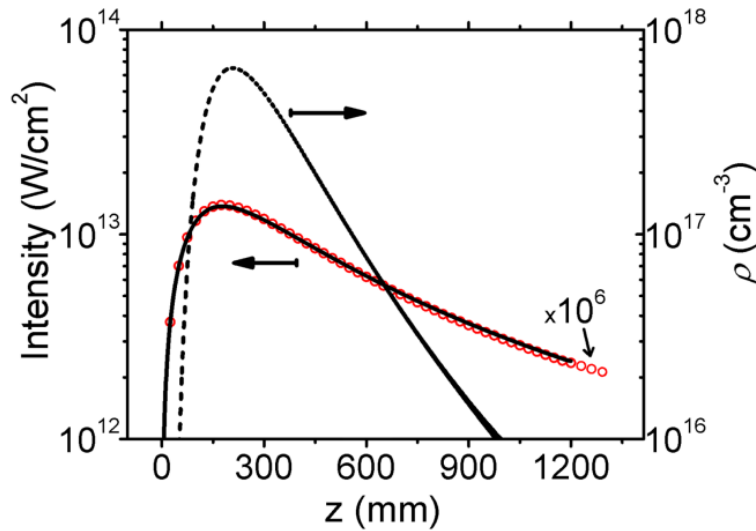


Fig 4-6 Simulated on axis intensity and electron density profiles for 7.5 mJ, 248 nm, 0.5 ps pulses illuminating an axicon (base angle $\gamma = 5^\circ$) preceded by a diverging lens ($f = -200$ mm). (solid line) – Intensity, (circles) – intensity values for 7.5 nJ pulses ($\times 10^6$), (dashed line) – on axis electron density

To summarize, we have demonstrated in this section that long, uniform and high density plasma strings can be generated in air using conically shaped UV short laser pulses. The combination of axicons with diverging lenses, actively tunes the conical angle, and results in a remarkable increase of the plasma string length with no sacrifice in the string uniformity and minimal peak electron density changes. Since the beam propagation is mainly governed by linear effects the propagation is stationary both in space and in time. These results could be scaled-up to higher input energies as the presence of strong nonlinear absorption would result to intensity clamping effects that would further flatten the intensity spatial profile, keeping the plasma density high over long propagation distances. The presented approach is an attractive candidate for numerous applications like THz pulse generation or lightning control.

4.1.3 X-waves

In this section the X-wave will be introduced, and the interaction of nonlinear X-waves with low power wavepackets will be explored.

X-waves are spatiotemporal conical wavepackets that propagate without undergoing diffraction and dispersion. They take their name from their intensity distribution in both the near field and far field which has the shape of an X centered around an intense core, as is shown in Fig 4-7. X-waves are known in the context of linear acoustics [189-194] and electromagnetic propagation [195, 196]. In optics they are found to be a stationary solution to the linear propagation equation in dispersive materials:

$$\frac{\partial \mathcal{E}}{\partial z} = \frac{i}{2k} \Delta_{\perp} \mathcal{E} - \frac{k''}{2} \frac{\partial^2 \mathcal{E}}{\partial t^2} \quad (4.1-6)$$

The first experimental measurement of the intensity distribution of an optical X-wave was done in 1997 [197], which sparked great research activity in the field of nonlinear optics since [69].

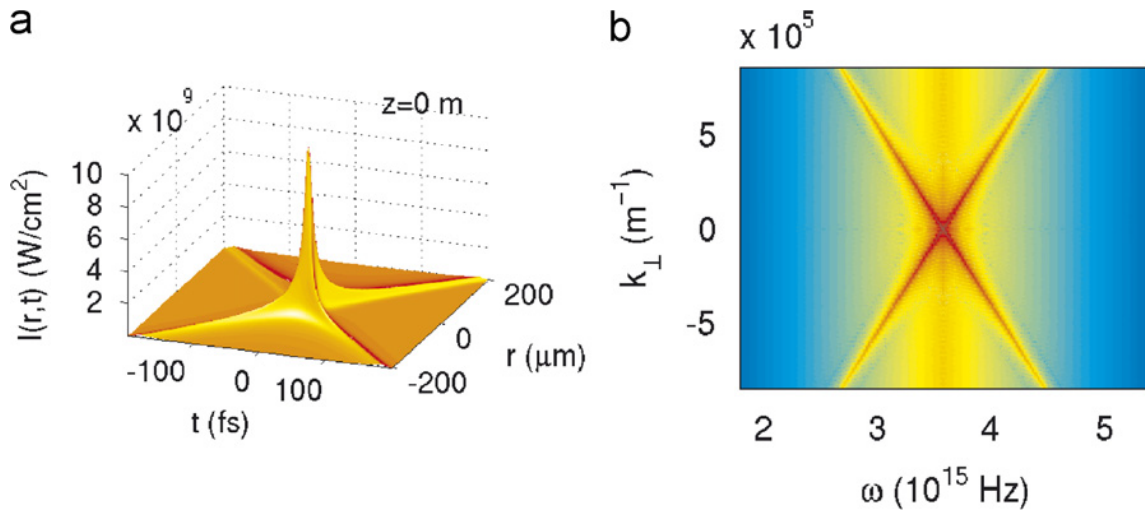


Fig 4-7 (a) Near field (r, t) profile of an X-wave. (b) Far-field (k_{\perp}, ω) of the X-wave in (a). Taken from [10].

4.1.3.1 The angular spectrum

The angular spectrum, or else (θ, λ) spectrum is the spectrum of a wavepacket as a function of propagation angle. The reason it is measured is because it is a robust way to extract the group velocity of a pulse. If we analyze the wavevector $k(\omega)$ in its longitudinal and transverse components like shown in Fig 4-8(b). The group velocity is then equal to the inverse derivative of k_z (the longitudinal wavevector) with respect to ω , but from the Pythagorean theorem we can write the relation

$$k_z = \sqrt{k^2(\omega) - k_{\perp}^2(\omega)} \quad (4.1-7)$$

$k(\omega) = \frac{\omega \cdot n(\omega)}{c}$ is given by the material dispersion relation, while the transverse component of the wavevector is directly calculated from the experimentally measured (θ, λ) spectrum from

$$k_{\perp}(\omega) = \theta \cdot k(\omega) \quad (4.1-8)$$

As we already mentioned in the first chapter, the group velocity is given by

$$v_{group} = \frac{\partial \omega}{\partial k_z} \quad (4.1-9)$$

The angular spectrum can be used to validate that a wavepacket is an X-wave or not. A wavepacket has to be both non-diffracting and non-dispersing to be an X-wave. The first can be satisfied if a non-diffracting beam, like a Bessel, is used as input. To be non-dispersing, the wavepacket has to satisfy the X-wave dispersion relation

$$k_z(\omega) = k_0 + \frac{\Omega}{v_{group}} \quad (4.1-10)$$

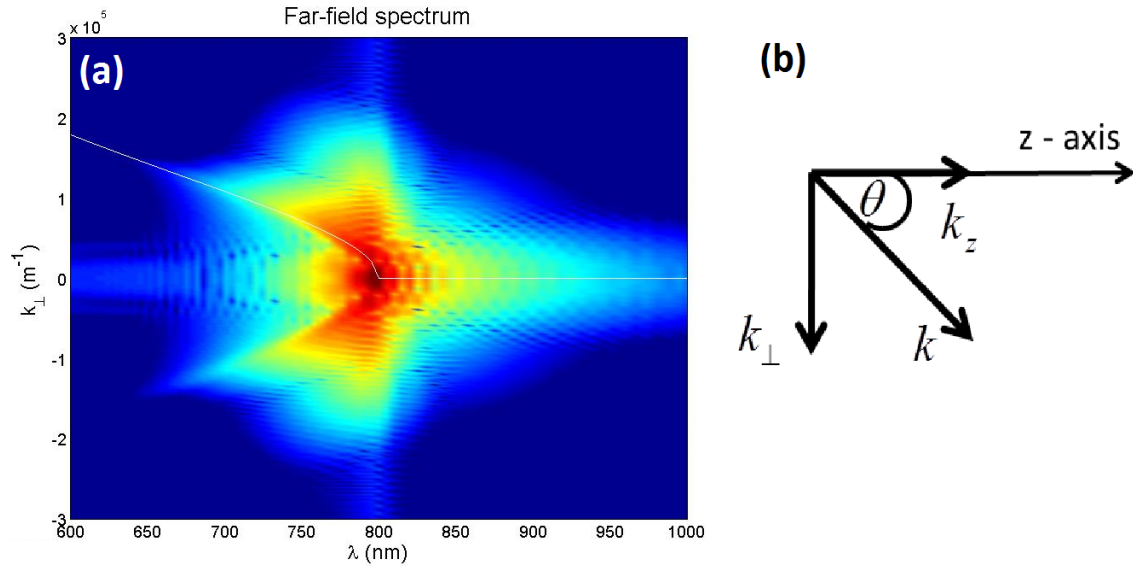


Fig 4-8 (a) Angular spectrum of a simulated $5P_{cr}$ Gaussian pulse. (b) Angular wavevector analyzed in its components.

where $\Omega = \omega - \omega_0$, $k_0 = k(\omega_0)$ and $k(\omega) = \frac{\omega \cdot n(\omega)}{c}$, using $n(\omega)$ can be given by the Sellmeier dispersion relation for the material. Add the above in Eq.(4.1-10) we can write

$$k_z(\omega) = \frac{\omega_0 \cdot n(\omega_0)}{c} + \frac{\omega - \omega_0}{v_{group}} \quad (4.1-11)$$

Note that the group velocity in Eq.(4.1-11) is a free parameter and is found by the best fit of the X-wave curve (white line in Fig 4-8) in the angular spectrum. In order to plot the X-wave curve in Fig 4-8 we need to calculate

$$k_{\perp}(\omega) = \sqrt{k^2(\omega) - k_z^2(\omega)} \quad (4.1-12)$$

for a given value of v_{group} .

As we can see by substituting $k(\omega) = \frac{\omega \cdot n(\omega)}{c}$ and the measured angular spectrum from Eq.(4.1-11) we can calculate the X-wave curve for a given group velocity from the equation:

$$k_{\perp}(\omega) = \sqrt{\left(\frac{\omega \cdot n(\omega)}{c}\right)^2 - \left(\frac{\omega_0 \cdot n(\omega_0)}{c} + \frac{\omega - \omega_0}{v_{group}}\right)^2} \quad (4.1-13)$$

The group velocity is found by the best-fit-value of the X-wave curve and the conical shape in the angular spectrum of the wavepacket, shown with the white line in Fig 4-8(a). This way the group velocity of a pulse can be measured from the angular spectrum as shown in Fig 4-8(a), where the angular spectrum of a $5P_{cr}$ Gaussian pulse is shown after undergoing spectral broadening in air. In this case the group velocity of the pulse was calculated to be $v_{group} = 2.998 \times 10^8 \text{ m/s}$.

4.1.3.2 Linear X-wave generation by cross-phase modulation in air

In this section we experimentally study in detail the effect of cross phase modulation (XPM) in the absence of energy transfer between a filament (1055 nm) and a weak probe pulse (527 nm) in conditions similar to those simulated in [198]. We observe that XPM induces on the probe a reshaping into a linear X-wave that travels at the same group velocity as the filament. As the X-wave is well spectrally isolated, we filter out the filament at the end of the sample and characterize the propagation of the X-wave alone in air, which shows remarkable nondiffracting properties. Moreover we show that, as long as the XPM-inducing pulse maintains a high intensity over a long propagation distance, a filament is not strictly necessary to induce the X-wave reshaping; to this purpose we repeat the experiment using a Bessel pulse as the driving pulse.

Experiments in the filamentation regime were carried out using 1.2 ps duration (FWHM) 1055 nm laser pulses delivered by a 10 Hz amplified Nd: glass laser. The beam was split into

two by means of a 50/50 beam splitter. On one arm the 527 nm pulse was generated by frequency doubling the fundamental pulse with a potassium diphosphate crystal beyond which a variable delay line was mounted. The green and IR pulses were then recombined with an IR high reflectivity dielectric mirror and focused with an $f = 50$ cm lens to a diameter of $100 \mu\text{m}$ onto the input facet of a 2 cm long fused silica sample. The energies of the two pulses (E_{pump}, E_{probe}) were controllable independently by first-order half-wave plates and polarizers. The absence of energy transfer from the filament to the green pulse was experimentally verified by measuring the energy of the green pulse before and after the sample with a power meter (OPHIR, Nova).

In Fig 4-9 we show the angularly resolved (θ, λ) spectrum of the 527 nm pulse measured with an imaging spectrometer (Lot-Oriel, MS260i) after the sample and recorded with a digital Nikon D70 camera.

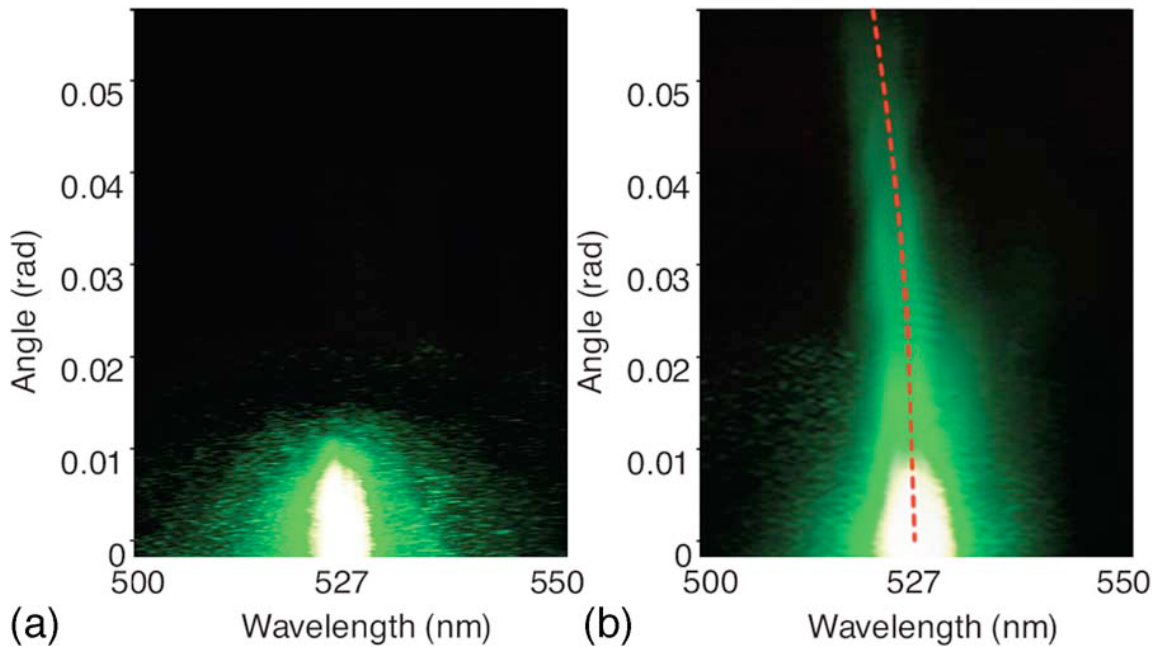


Fig 4-9 (θ, λ) Spectrum of the 527 nm probe pulse after the sample (a) when the IR pulse is locked and (b) when the IR filamenting pulse is co-propagating with the probe in the sample. XPM induces the formation of conical structures on the probe spectrum. The dashed curve is the plot of Eq.(4.1-14), describing the X-wave shape with the experimental group velocity of the X wave v_x deduced from the spectrum of the filament as described in [7].

In Fig 4-9(a) the IR pulse was blocked, and the weak green pulse was let to propagate alone inside the sample; as expected the intensity profile in the spectrum is Gaussian like. In Fig 4-9(b) the filamenting IR pulse ($E_{pump} = 20\mu J$) was spatially and temporally superimposed to the central portion of the green pulse ($E_{probe} = 0.5\mu J$). Although in the absence of any energy transfer from the filament, the green seed pulse clearly reshapes and develops conical tails, which in the angularly resolved spectrum are the well-known signature of X-wave formation [199].

To prove the genuine X-wave nature of this object, however, it is necessary to show its non-dispersive and non-diffracting propagation. To demonstrate the first, in Fig 4-9(b) we fit the spectrum using the X-wave relation that, for a given material and central wavelength, describes in the (θ, λ) spectrum the loci, where the angular dispersion is able to compensate the material dispersion. In (k_{\perp}, ω) coordinates, equivalent to (θ, λ) , this relation takes the simple form [200]:

$$k_z(\omega) = k(\omega_0) + \frac{\omega - \omega_0}{v_x} \quad (4.1-14)$$

where ω_0 is a reference central frequency and $k_{\perp}(\omega) = \sqrt{k(\omega)^2 + k_z(\omega_0)^2}$ and v_x is the group velocity of the X-wave. As can be seen in Fig 4-9(b), the curve matches very closely the experimental shape. We underline that this simple spectral intensity characterization is sufficient to prove that the pulse propagates without dispersing within the glass sample as, indeed, for a given medium; pulse spreading along the propagation direction is completely determined by the pulse dispersion relation $k_z = k_z(\omega)$. We note also that in our fit the group velocity of the X-wave is not a free parameter; indeed, it is the group velocity of the driving pulse measured experimentally using the method described in detail in [200] and yielding $v_x = 2.22 \pm 0.03 \times 10^8$ m/s. This allows us to confirm experimentally the prediction made in [198, 200] that the X wave induced by XPM travels at the same group velocity as the driving pulse.

We then verified the nondiffracting propagation of the X-reshaped green pulse. To demonstrate this we simply let the two pulses propagate out of the sample in air, where the

nonlinear refractive index is about 1000 times smaller than in silica, thus quenching the filament and all nonlinear effects. We then removed the IR light with a low-pass filter and scanned the green beam profile along its propagation in air, starting from the output facet of the sample. Our imaging system was composed by a lens and a 12-bit CCD camera (DTA iCam 400 E).

In Fig 4-10(a) the normalized intensity profile of the probe at the output facet of the sample is shown. The effect of XPM from the filament is evident, with the formation of a narrow (7.8 μm at FWHM) central peak surrounded by slowly decaying tails. We could fit its radial intensity profile with a rational function having the form $a/(br^2 + cr)$, which agrees well with the $1/r^2$ decay for large radii expected for a linear X wave [190]. In Fig 4-10(b) the measured FWHM of the beam profile along the z axis is shown. As can be seen, the central peak propagates non-diffractively, keeping its FWHM constant within the experimental error for a distance of about 5 mm, and then diffracts abruptly. This behavior at the end of the nondiffracting zone is typical of all the experimental realizations of conical waves and is due to the finite energy contained in the conical wave packet. Notably, on the same distance of 5 mm a collimated Gaussian beam with the same initial diameter would have reached a FWHM of about 120 μm .

We performed a complementary experiment using a pulsed Bessel beam (PBB) instead of the filament as the driving pulse. Here our driving pulse was a 1 mJ, 35 fs pulse positively chirped to 1 ps (to optimize pump and seed temporal overlap) at 800 nm from an amplified Ti:sapphire laser system. The probe pulse was generated by frequency doubling with β -barium borate crystal. The setup scheme was conceptually the same as the first experiment, with the addition of a 175 apex angle axicon mounted onto the IR beam line to reshape the driving pulse into a Bessel beam.

As we show in Fig 4-11(a), the probe pulse (as expected) developed X-wave tails in the (θ, λ) spectrum due to XPM. We also performed a series of numerical simulations to confirm the validity of this last experimental result. In Fig 4-11 the numerically predicted (θ, λ) spectra of the probe pulse with and without XPM reshaping are reported. As may be seen, the numerics confirm our experimental findings. We note that the driving Bessel pulse suffered no significant changes owing to self-induced nonlinear effects as verified both numerically and experimentally (data not shown); i.e., no spectral broadening was observed. These last results confirm that the XPM reshaping of the probe pulse into an X-wave is not necessarily related to filamentation of

the pump pulse. Indeed Eq.(4.1-14) is derived under the sole assumption that the scattering polarization is localized in space (allowing the probe spectrum to spread in angle) and in time (allowing the probe to spread its temporal spectrum) [68].

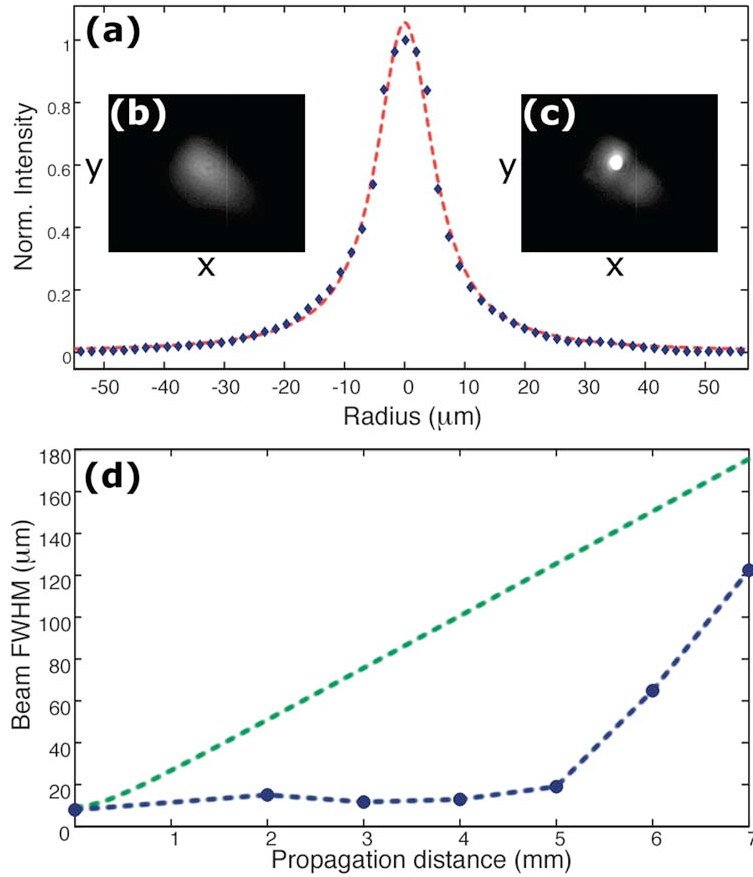


Fig 4-10 (a) Normalized intensity profile of the probe at the output of the sample in the presence of XPM. The dashed curve is the fit of the profile with a rational quadratic function. In the insets the near field of the green pulse is acquired with the CCD system (b) without XPM and (c) with XPM. Note that the probe energy was unchanged between the two measurements. (d) Probe beam FWHM along propagation after the sample (dashed curve with solid circles), nondiffracting over 5 mm. The theoretically predicted broadening for a Gaussian beam with the same FWHM is shown for comparison (dashed curve).

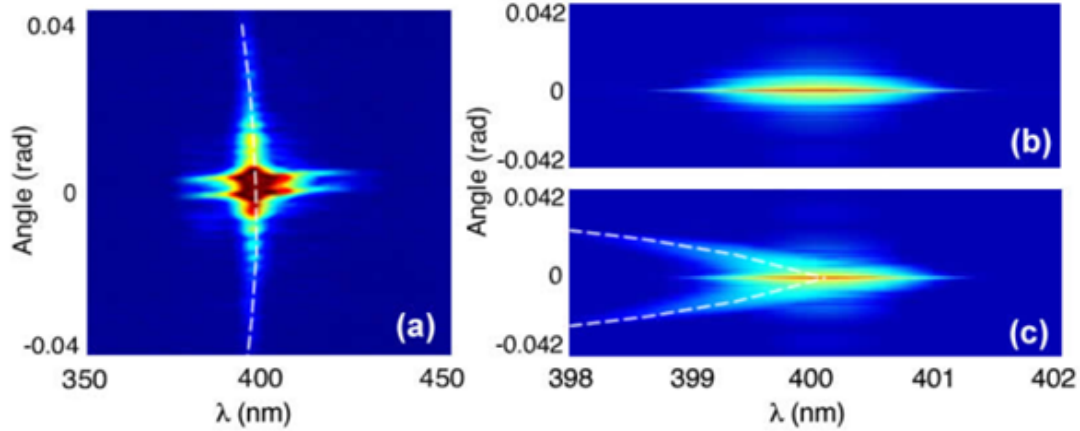


Fig 4-11 (a) Experimentally measured (θ, λ) spectrum for the probe pulse at 400 nm reshaped by XPM driven from a PBB at 800 nm. The white curve is the X-wave relation curve calculated with Eq.(4.1-14), where $v_x = 2.043 \times 10^8$ m/s is the theoretically predicted group velocity for the PBB. Numerically simulated (θ, λ) spectrum for the probe pulse (b) before interaction with the driving pulse and (c) with XPM induced by the PBB.

To summarize this section, it was shown that the spatiotemporal reshaping induced by XPM from an intense driving pulse on a weaker probe at a different wavelength in a bulk Kerr medium. It was shown that the XPM can be exploited to generate spectrally isolated linear X-waves that propagate over a finite distance with no dispersion and no diffraction. Moreover the generality of this mechanism, which holds as long as the driving pulse propagates for a distance long enough with a sufficient intensity. These results can be useful both as a tool to better understand current studies on two-color systems in the field of ultrashort nonlinear optics and to provide a feasible method to generate X-waves in the optical domain.

Next the nonlinear propagation of another type of non-diffracting beam will be investigated, the nonlinear propagation of the Airy beam.

4.2 Finite energy Airy beams

The Airy function was discovered by Berry and Balazs in 1979 [201] in the field of quantum mechanics a 1D non-spreading solution of the Schrödinger equation. They still are the only 1D solution that has been found up to this day. The Airy function is mathematically defined in integral form as:

$$Ai(x) = \frac{1}{\pi} \int_0^{\infty} \cos\left(\frac{t^3}{3} + xt\right) dt \quad (4.2-1)$$

which is the solution of the differential equation:

$$\frac{\partial^2 y}{\partial x^2} - xy = 0 \quad (4.2-2)$$

In optics, Airy beams are beams whose electric field follows the Airy function, which can be either 1D or 2D. They retain their non-spreading nature and propagate in space without changing their electric field profile. This non-spreading property is fundamental, and can be used in either in the spatial or temporal dimension, given non-diffracting and non-dispersing wavepackets respectively.

The electric field and intensity distribution of a 1D Airy beam is given by

$$\mathcal{E}(z=0, x) = \mathcal{E}_0 Ai(x/w_0) \quad (4.2-3)$$

where Ai denotes the Airy function and w_0 is a scaling factor. The electric field and intensity distribution for an Airy beam with $w_0 = 1$ can be seen in Fig 4-12. As we can see the Airy beam intensity profile exhibits multiple lobes which are decreasing in amplitude as we move further out.

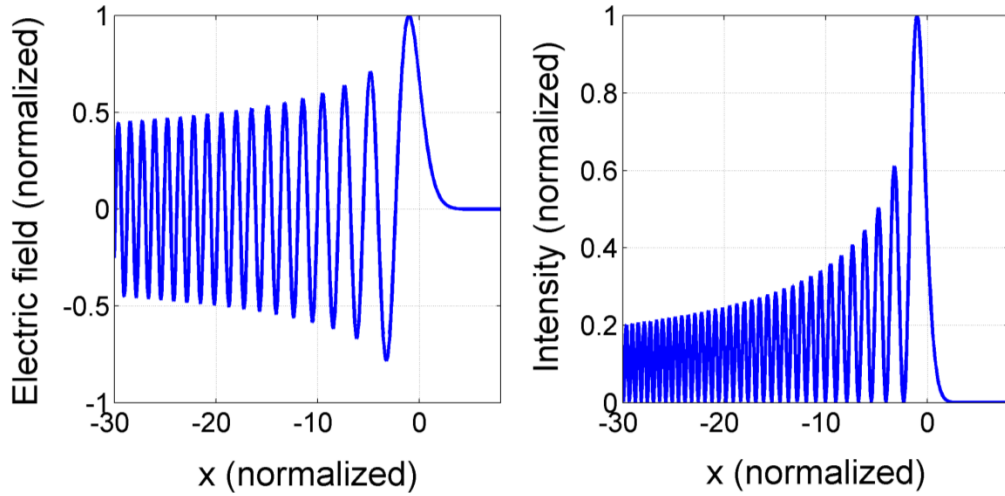


Fig 4-12 Normalized (a) electric field ϕ , and (b) intensity distribution of a 1D Airy beam.

Airy beams can also be easily extended into two spatial dimensions, as can be seen in Fig 4-13, or even 3D Airy wavepackets that have an Airy intensity distribution in X , Y and t , a was shown in [153].

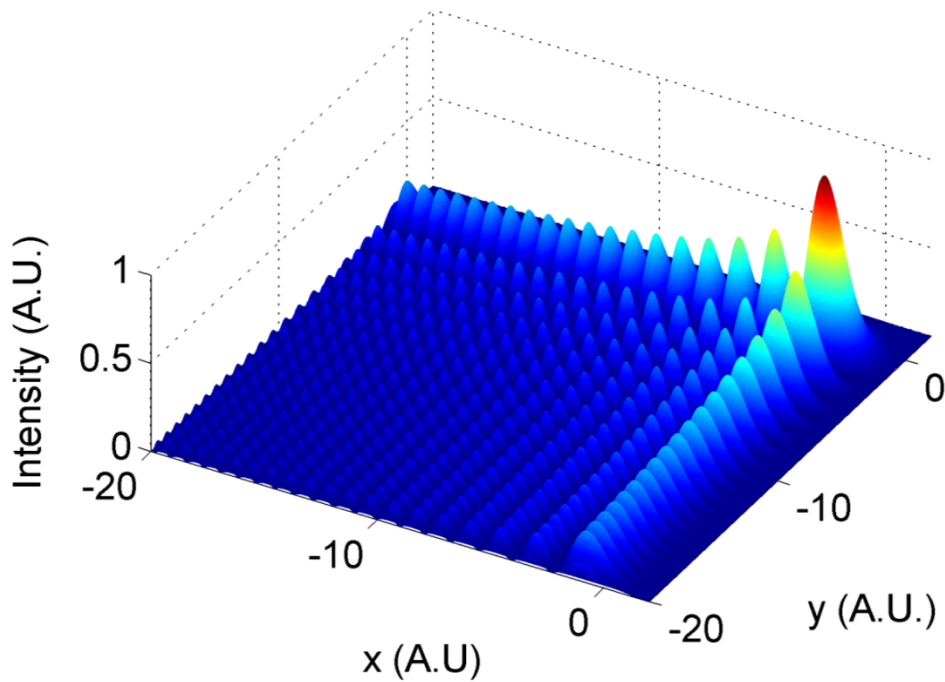


Fig 4-13 Normalized 2D Airy intensity distribution with $w_0 = 1$.

Ideal theoretical Airy beams have infinite size, and therefore carry infinite energy. In reality finite energy Airy beams (FEABs) are realized instead. The experimental techniques to generate FEABs produce beams with an Airy profile multiplied with an exponential decay factor. These techniques will be presented in detail later in section 4.2.2. The normalized electric field and intensity of a 1D finite energy Airy beam can be seen in Fig 4-14.

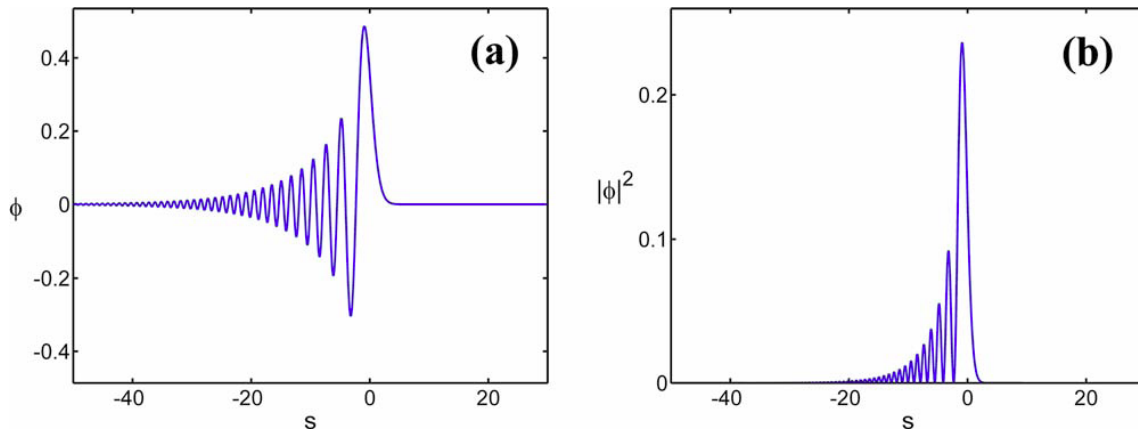


Fig 4-14 Normalized (a) electric field ϕ , and (b) intensity distribution of a 1D finite energy Airy beam. Taken from [202].

4.2.1 Airy beams in the literature

Although the discovery of optical Airy beams is very recent, they have triggered great interest in the science of optics and led to a number of publications. Airy beams with finite energy were first proposed as genuine non-spreading optical waves [202, 203]. Even though Airy beams are intrinsically one-dimensional structures [201], but several combinations were demonstrated since 2007 for realizing a two- or three-dimensional non-spreading optical wave packet by linear superposition of sub-dimensional non-spreading structures [204-206]. In 2010, Chong *et al.* generated Bessel-Airy beams consisting of a Bessel beam in the transverse plane and an Airy distribution along the longitudinal dimension [152]. Abdollahpour *et al.* generated three-dimensional (3D) Airy light bullets consisting of an Airy beam profile in each dimension [153]. Nonlinear generation techniques were also used; for example, by Ellenbogen *et al.* who

generated Airy beams at the second harmonic of a pump beam by using nonlinear three-wave mixing in nonlinear crystals [207].

In the linear regime the propagation dynamics of Airy beams has been studied extensively. The two most exotic features of Airy beams (namely, self-healing and transverse acceleration) have been investigated by Broky *et al.* [208] and Siviloglou *et al.* [209]. The dependence of Airy wave packets on wavelength, spatial coherence and dispersion have been investigated in [210, 211]. One of the interests of these structures is their potential for applications in extreme nonlinear optics. Airy beams in the nonlinear regime were discussed in Refs. [153, 212-214] from the observation of spectacular manifestations common with the nonlinear dynamics of light filaments, such as supercontinuum generation and conical emission. Lotti *et al.* recently discovered the existence of stationary nonlinear Airy beams in one transverse dimension as will also be shown in section 0 [215]. An open question concerns the properties of multidimensional Airy beams in the nonlinear regime. High-intensity Airy beams propagating in a gas or a transparent medium can be strongly affected by nonlinear effects that play a key role in the dynamics of ultrashort laser pulse propagation (i.e., the optical Kerr effect, multiphoton absorption and ionization to cite only a few [10, 216, 217]).

4.2.2 Generation techniques

The experimental generation of Airy beam is achieved by mainly two techniques, both of which induce a strong spatial cubic phase, as the one shown in Fig 4-15, on a Gaussian laser beam, followed by a Fourier transformation with the help of a converging lens. The FEAB is formed at the focal plane of the Fourier lens. The technique is based on the discovery the FEAB and a Gaussian with an added cubic spatial chirp are a Fourier pair [202, 203].

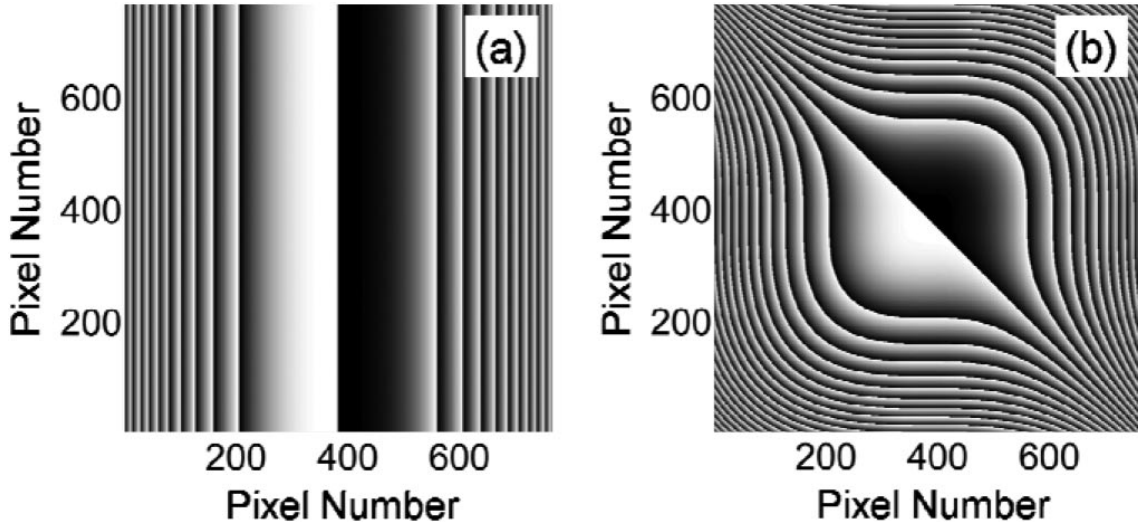


Fig 4-15 Phase masks used to generate (a) 1D and (b) 2D-Airy beams. The cubic phase is ‘wrapped’ between $[0, 2\pi]$. In the gray scale pattern, black corresponds to 0 and white to 2π radians. Taken from [203].

The first technique that was developed in [203] is using a spatial light modulator (SLM) to induce the spatial cubic phase on the driving Gaussian laser beam. The experimental setup can be seen in Fig 4-16.

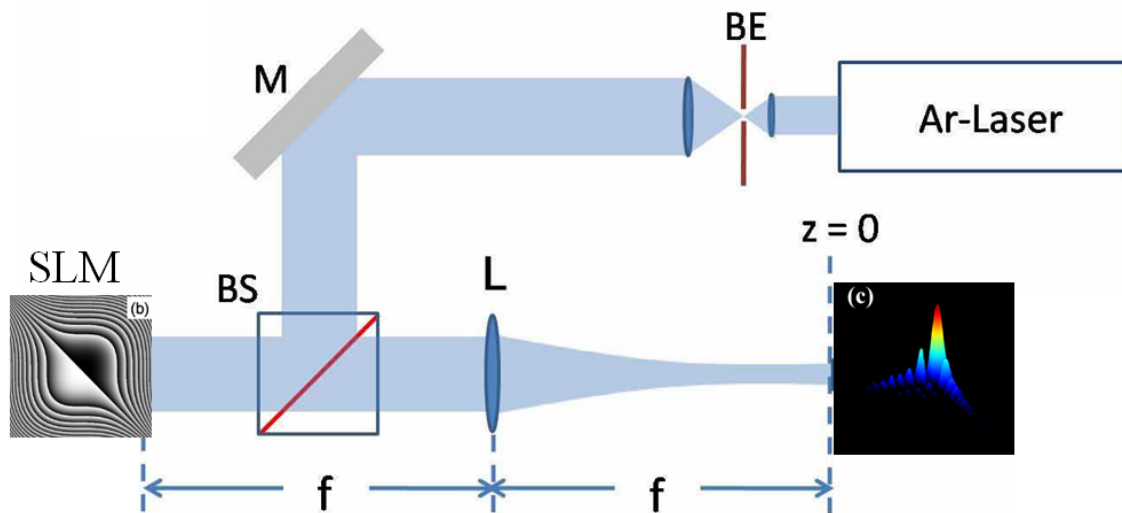


Fig 4-16 Experimental setup for the generation of a 2D FEAB. Taken from [208].

The second and more recent approach is using cylindrical lenses, utilizing aberrations in order to induce the cubic phase shift to the driving Gaussian laser beam [204]. The experimental setups for 1D and 2D can be seen in Fig 4-17(a) and (b) respectively.

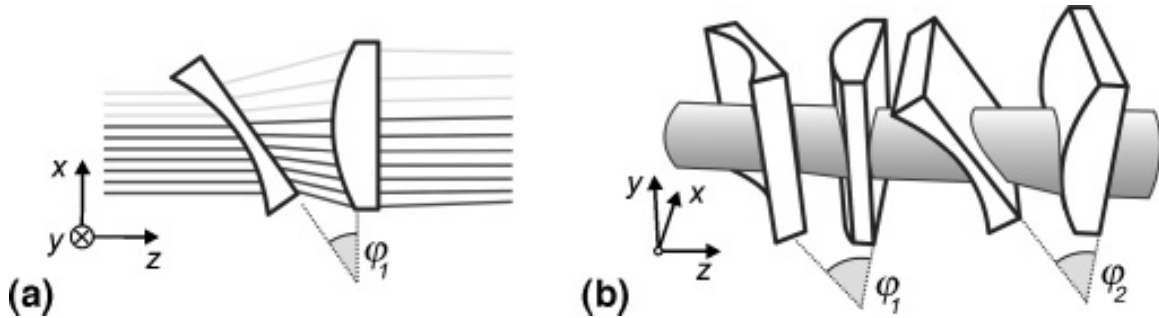


Fig 4-17 Tilted cylindrical telescope systems. (a) Configuration for the generation of 1D (along the x axis) cubic phase modulation. (b) Configuration for the generation of the 2D cubic phase modulation (along the x and y axes). Taken from [204].

In simulations the easiest way to implement Airy beams is to use the analytic function that gives the Airy beam field distribution directly. However, the experimental generation method can also be simulated, as can be seen in Fig 4-18. The drawback of this approach is of course that additional simulation time is needed to reform the Gaussian into the FEAB over a propagation distance of $f + f/2$.

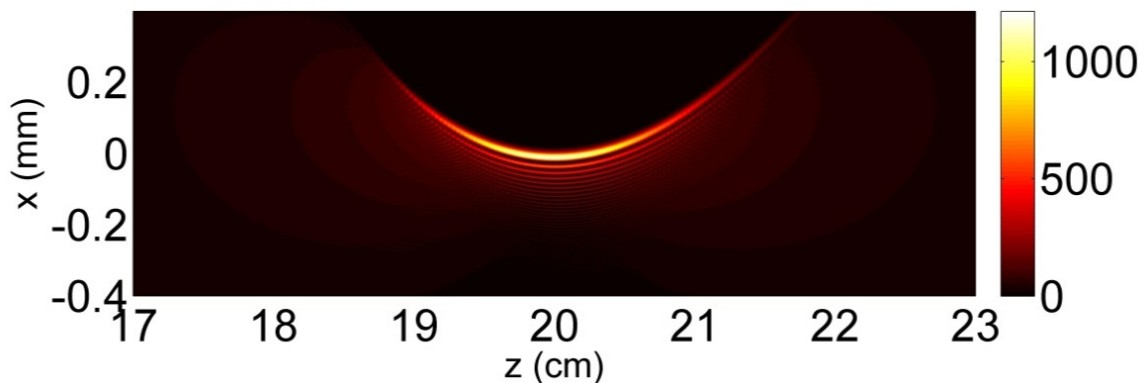


Fig 4-18 Simulated peak intensity along propagation distance of a 1D FEAB. The generation technique mimics the experimental one, using a phase mask (at $z = 0$ cm) which is applied to a Gaussian and a focusing lens $f = 10$ cm located at $z = 10$ cm. Focal plane at $z = 20$ cm.

4.2.3 The Linear Airy beam

The propagation of the finite-energy Airy beam (FEAB) introduced by Siviloglou and Christodoulides [202, 203] is governed by the paraxial equation

$$\frac{\partial \mathcal{E}}{\partial z} = \frac{i}{2k} \Delta_{\perp} \mathcal{E} \quad (4.2-4)$$

where Δ_{\perp} denotes the Laplacian in the transverse diffraction plane and k denotes the propagation constant. Eq.(4.2-4) describes the evolution of the envelope of the electric field of a quasi-monochromatic beam ($\Delta\lambda / \lambda \ll 1$) in a dispersionless medium along the propagation axis z in the linear regime (i.e., due to diffraction effects). It is directly derived from the Maxwell equations for a material without magnetization and no free charges and currents, by applying the paraxial approximation (wavelength much shorter than beam waist: $\lambda_0 \ll w_0$) and the slowly varying envelope approximation (wavelength much shorter than typical evolution distance for the beam envelope: $\lambda_0 \ll z_0$, where $z_0 = \frac{kw_0^2}{2}$ denotes the diffraction length of a beam of waist w_0) [10].

In one transverse dimension x , the propagation of the FEAB given by

$$\mathcal{E}(z=0, x) = \mathcal{E}_0 Ai(x/w_0) \exp[ax/w_0] \quad (4.2-5)$$

where Ai denotes the Airy function and w_0 denotes the width of the central lobe. Along z the 1D Airy beam is described by

$$\mathcal{E}(z, x) = \mathcal{E}_0 Ai(s - \zeta^2 + i2a\zeta) \exp[a(s - 2\zeta^2)] \exp[i\zeta(-2\zeta^2/3 + a^2 + s)] \quad (4.2-6)$$

where $s = x/w_0$ and $\zeta = z/4z_0$ are the normalized transverse coordinate and propagation distance respectively.

4.2.3.1 Transverse acceleration, self-healing and the Airy zone

The most impressive attribute of the linear Airy beam is the transverse acceleration, which causes the beam to propagate in a parabolic trajectory [209], while keeping a constant central lobe diameter. This exotic behavior is forced by a strong spacial cubic phase which is imprinted on the beam profile. This spacial chirp causes a constant energy flux from the oscillating tail of the beam towards the main lobe, effectively forcing the beam to accelerate in the transverse direction. Most importantly, spatial acceleration is maintained from the transition from the infinite size Airy to the FEAB as can be seen in Fig 4-19.

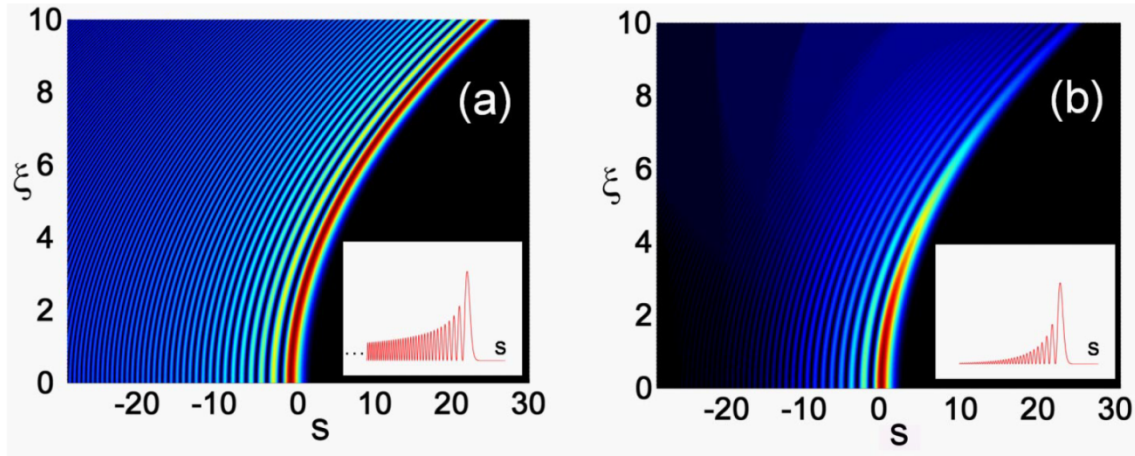


Fig 4-19 Transverse acceleration of (a) an infinite energy 1D Airy beam, and (b) a finite energy 1D Airy beam. Insets showing the initial intensity distributions. Taken from [203].

From Eq.(4.2-6), the acceleration obeys $s - \zeta^2 = s_0$ (physical units);

$$x = x_0 + \frac{z^2}{4k^2 w_0^3} \quad (4.2-7)$$

where x_0 denotes the initial position of the peak at $z = 0$. Eq.(4.2-7) shows that the Airy beam follows a parabolic trajectory $x = x_0 + z^2 / 2r_c$ with curvature radius $r_c = 2k^2 w_0^3$. The typical propagation distance for the peak of the Airy beam to translate by w_0 is $4z_0$.

However, due to the finite size and energy, FEAB will gradually spread as they propagate. More specifically, the peak intensity of a FEAB beam should vary as $\exp[-az^2 / 4z_0^2]$; which corresponds to the length over which the intensity of the FEAB is larger than half the maximum value due to finite size effects is

$$z_A = 4z_0 \sqrt{\ln(2) / a} \quad (4.2-8)$$

By analogy with the Bessel zone for Bessel beams, we will call this quantity the Airy zone. The FEAB given by Eq.(4.2-6) extends to two transverse dimensions (x, y) by a superposition of two one-dimensional (1D) FEABs: in this case, its acceleration in the $y - z$ plane is characterized by the same curvature $y = y_0 + z^2 / 2r_c$, where y_0 denotes the initial position of the peak at $z = 0$.

The acceleration of the peaks of the intensity distribution is even preserved in the temporal domain, where an pulse with an Airy distribution in time can propagate at superluminal or subluminal velocities inside the Airy zone.

In addition to transverse acceleration, Airy beams exhibit another interesting property, the ability of self-healing or self-reconstruction. This property, which is also observed in Bessel beams, was first investigated in [208] and is shown in Fig 4-20.

As we can see in Fig 4-20(a)-(c) an Airy beam is able to reconstruct itself when part of the beam is blocked. This reconstruction is fueled by the transverse energy flux from the secondary lobes of the Airy, as it shown in Fig 4-21. These results were confirmed by numerical simulations as can be seen in the second line of Fig 4-20(d)-(f).

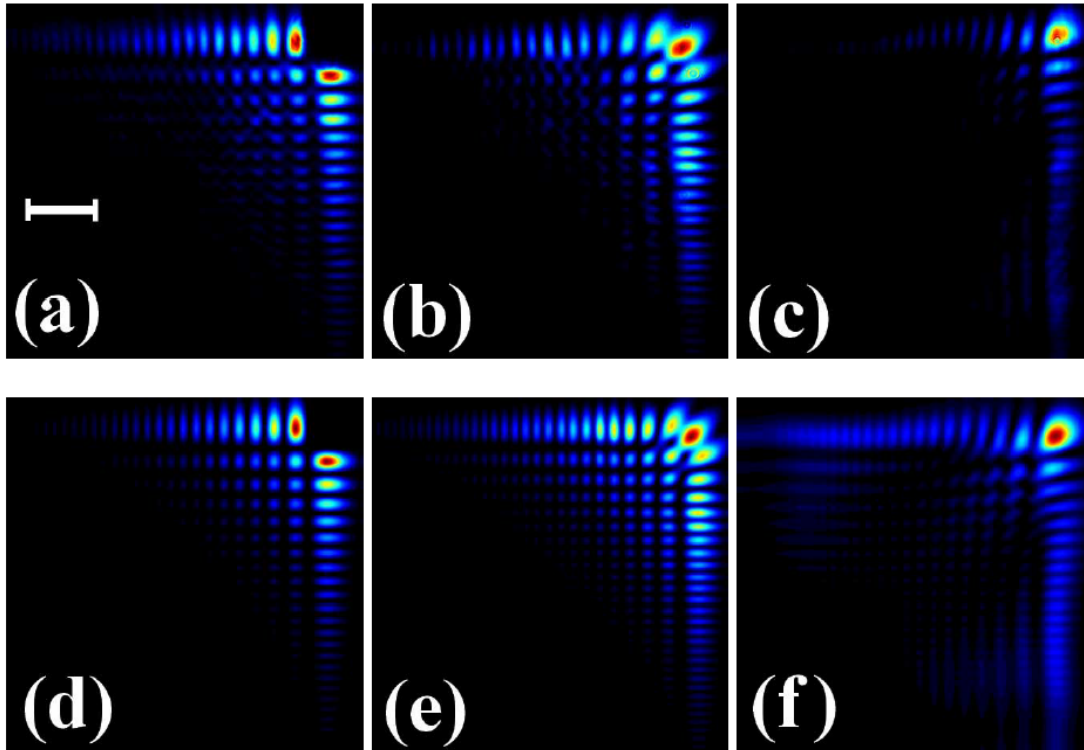


Fig 4-20 Self-healing of an Airy beam when its main lobe is blocked. Observed intensity profile at (a) the input $z = 0$, (b) $z = 11$ cm, and (c) $z = 30$ cm. The corresponding numerical simulations are shown in (d-f). Taken from [208].

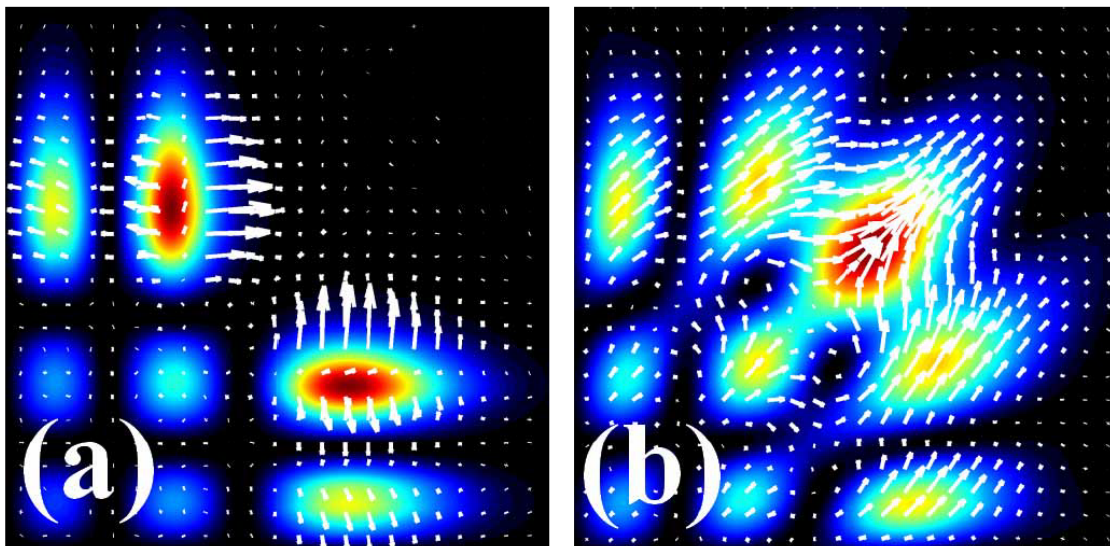


Fig 4-21 Calculated transverse power flow at (a) the position where the main lobe is removed ($z = 1$ cm) and (b) 10 cm after ($z = 11$ cm) (a). Taken from [208].

4.2.4 Nonlinear Airy beams

In this section we will investigate the propagation dynamics of intense Airy beams with particular emphasis on the competition between the features of linear Airy beam propagation (acceleration property, stationarity) and the trend of the most intense lobes of an Airy beam to behave as filaments. We identify nonlinear propagation regimes of intense Airy beams in a Kerr medium by means of numerical simulations, with special attention paid to beam transverse acceleration and stationarity. We notably answer to the following questions: Is the Airy beam profile affected by nonlinear propagation or by finite size effects? Does the trajectory and transverse acceleration of the most intense peak of an Airy beam depend on its power content?

Throughout this section we will use the "frozen time" numerical scheme for all simulations both in air and water. The material parameter for air and water are the same as the ones used in sections 3.2 and 3.6.3 respectively, also given in section 9. The propagation equation is the same as the one used in all "frozen time" cases:

$$\frac{\partial \mathcal{E}}{\partial z} = \frac{i}{2k} \Delta_{\perp} \mathcal{E} + i \frac{\omega_0}{c} n_2 |\mathcal{E}|^2 \mathcal{E} - \frac{\beta_K}{2} |\mathcal{E}|^{2K-2} \mathcal{E} - i \frac{\omega_0 \rho}{2n_0 c \rho_c} \mathcal{E} \quad (4.2-9)$$

which is coupled with electron evolution equation which considers only MPI of order K

$$\frac{\partial \rho}{\partial t} = \sigma_K |\mathcal{E}(t)|^{2K} (\rho_{nt} - \rho) \quad (4.2-10)$$

4.2.4.1 Nonlinear propagation of 2D Airy beams (x, y, z)

In this section the nonlinear propagation dynamics of FEAB will be investigated in air and water, both with numerical simulations and laboratory experiments.

4.2.4.1.1 Initial condition: Truncated Airy beam

Our simulations start from an already formed Airy beam described by

$$\mathcal{E}(z=0, x, y) = \mathcal{E}_0 Ai(x/w_0) Ai(y/w_0) T(x, y) \quad (4.2-11)$$

where T mimics the effect of a circular diaphragm which truncates the Airy beam and transforms it into a FEAB: $T(x, y) = 1$ if $r \equiv \sqrt{x^2 + y^2} < r_d$ and $T(x, y) = 0$ if $r \geq r_d$. This input condition constitutes a two-dimensional FEAB similar to Eq.(4.2-5), as if it was generated in vacuum; for example, by methods described in [203, 204] and entered in the nonlinear medium (air) from the focus. With air, this can be achieved with the setup proposed by Diels *et al.* [218]. By placing the circular diaphragm at the focal point we truncate the already formed wide Airy beam to the desired size without influencing the shape of the inner lobes. The position immediately after the circular diaphragm is the initial state for the simulation. This is analogous to linearly focusing a beam on the entrance face of a sample and investigating the subsequent nonlinear dynamics [182]. The corresponding laser pulse is assumed to be Gaussian with full width at half maximum of 35 fs and to remain undistorted (frozen time). We consider Airy beams with initial peak intensity $I_0 = 7 \times 10^{12} \text{ W/cm}^2$ and different lobe width $w_0 = 100 \mu\text{m}$, $w_0 = 200 \mu\text{m}$, and $w_0 = 300 \mu\text{m}$.

Widening the main lobe width while keeping the input intensity $I_0 = |\mathcal{E}|^2$ constant is effectively increasing the power content of the main lobe, P_A , which is evaluated as the power in the quadrant of the (x, y) plane delimited by the first zero of the Airy function:

$$P = \int_{u_0 w_0}^{+\infty} \int_{u_0 w_0}^{+\infty} |\mathcal{E}(x, y)|^2 dx dy = I_0 (w_0 \cdot f)^2 \quad (4.2-12)$$

where $f = m^{-2} \int_{u_0}^{+\infty} Ai^2(u) du = 1.71$, $u_0 = -2.34$ denotes the first zero position, and $m \sim 0.54$

denotes the maximum of the Airy function. The three chosen lobe widths correspond to powers

$P_A = 2 \text{ GW} (0.65 P_{cr})$, $P_A = 8 \text{ GW} (2.6 P_{cr})$, and $P_A = 18 \text{ GW} (5.8 P_{cr})$. The critical power for self-focusing and the ratio P/P_{cr} , where P denotes the total beam power, usually constitutes a reference for evaluating the potential of a Gaussian beam for self-focusing at powers slightly exceeding P_{cr} , or breaking up into multiple filaments at higher powers. For Airy beams, the main lobe power P_A is a much better indicator than the total power in the Airy beam for characterizing self-focusing of the main lobe since P strongly depends on the truncation size whereas P_A does not, except in extreme situations that no longer correspond to an Airy beam. Using P_A also allows us to consider P_{cr} as an estimate for the self-focusing threshold even if the main Airy lobe is not Gaussian. For the three powers considered above, P_A exceeds P_{cr} for the Airy beams with $w_0 = 200 \mu\text{m}$ and $300 \mu\text{m}$, which are thus expected to self-focus and collapse upon themselves. Higher powers are actually required in order to clearly observe self-focusing. We compare nonlinear propagation of the three intense Airy beams defined above, hereafter called Airy beams with moderate powers, with that of high power Airy beams having the same peak intensity and width but a tenfold increase of the ratio P_A/P_{cr} .

4.2.4.1.2 Propagation of intense Airy beams in the weakly nonlinear regime

Fig 4-22 shows cross sections of intense Airy beams at different propagation distances during their nonlinear propagation. For the three cases displayed in columns $w_0 = 200 \mu\text{m}$, $200 \mu\text{m}$, and $300 \mu\text{m}$, the radius of the circular diaphragm is $r_d = 4.5 \text{ mm}$. Propagation distances increase from top to bottom from $z = 0$ up to $z = 80 \text{ cm}$ with 20 cm steps. The last row of Fig 4-22 shows the beam profiles that would be obtained for a linear propagation over 80 cm of each input Airy beam with the same w_0 . The intense peak of the Airy beam accelerates transversely faster when the initial size of the central lobe is small. At a propagation distance of 80 cm , the peak of the Airy beam with $w_0 = 100 \mu\text{m}$ (first column in Fig 4-22) reached the position $x = y \sim 2.5 \text{ mm}$, whereas the peaks of the Airy beams with $w_0 = 200 \mu\text{m}$ and $w_0 = 300 \mu\text{m}$ (second and third column in Fig 4-22) show a slower transverse acceleration by a factor of 8 and 27,

respectively. It is readily seen in the third column in Fig 4-22 that the Airy beam with the largest lobe remains nearly in place but undergoes self-focusing. The effect of self-focusing on the Airy lobes is also clear from the comparison of the beam cross sections after nonlinear and linear propagation over 80 cm, shown in the last two rows of Fig 4-22. For the same input intensity, the main lobe of the Airy beam carrying the highest power ($w_0 = 300 \mu m$, third column of Fig 4-22) shrinks faster than that of the less-powerful Airy beams. Even the secondary lobes of the most powerful Airy beam are significantly reshaped. This trend to self-focus due to the Kerr effect competes with the acceleration of the Airy beam inherited from the properties of linearly propagating Airy beams. Both processes can be viewed as a transfer of power: the acceleration corresponds to a transfer from the secondary lobes to the main lobe and is responsible for the self-healing property of Airy beams [208], whereas self-focusing concentrates the power of a given lobe upon itself.

The left column of Fig 4-23 shows a comparison of the peak intensity and generated plasma density during the nonlinear propagation of the three Airy beams with moderate powers. In these cases, for each propagation distance, intensities and electron densities reported in Fig 4-23 correspond to different positions (x, y) of the peak of the Airy beam because it is turning. However, as shown in Fig 4-22, the initial main lobe remains the most intense all along the propagation distance and the reported electron densities in Fig 4-23 are generated by that lobe. The right column of Fig 4-23 shows iso-intensity surfaces for the three cases, plotted in the (x, y, z) space (central time slice $t = 0$). It can be readily seen that, in these cases, in spite of high intensities and nonlinear effects, the main and the secondary lobes follow the parabolic trajectory which would characterize the linear propagation of the input Airy beam.

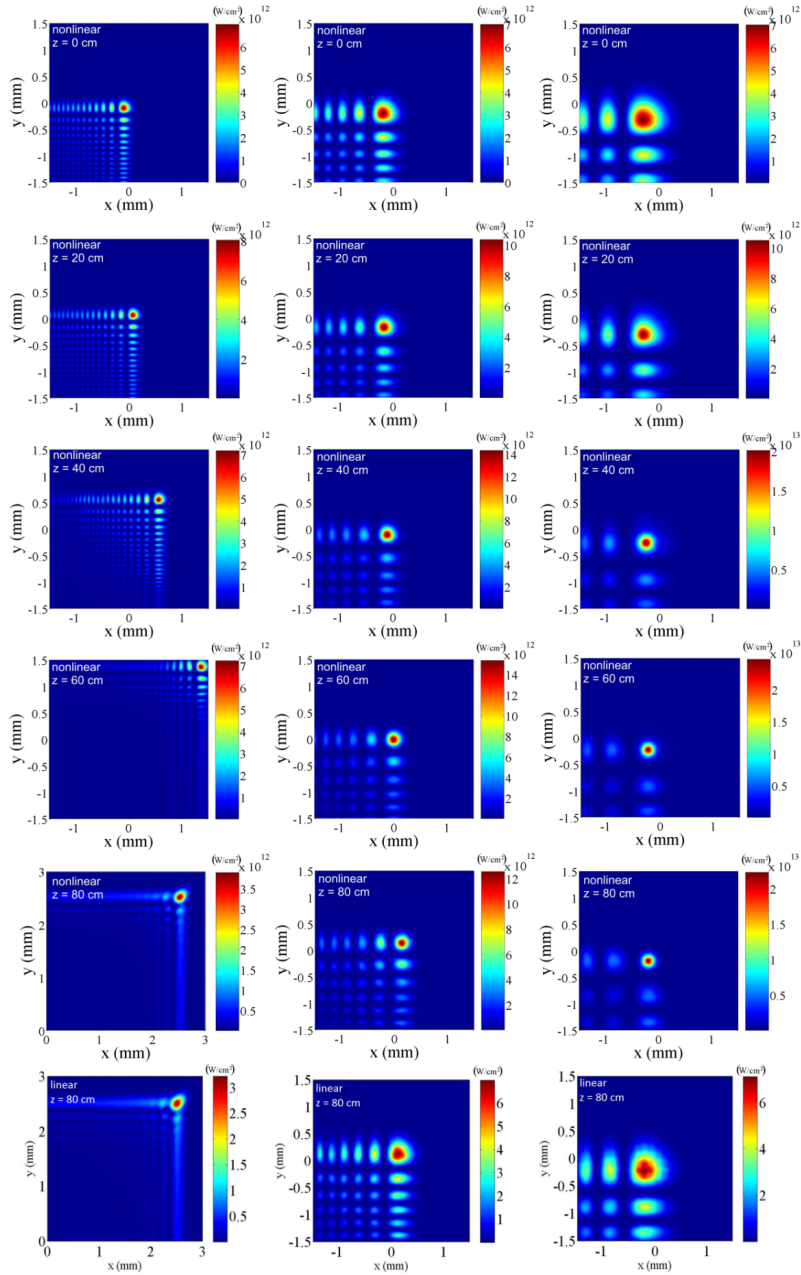


Fig 4-22 (x,y) intensity plots of nonlinear Airy beams with initial peak intensity $7 \times 10^{12} W / cm^2$ and different central lobe size. First column is for $w_0 = 100 \mu\text{m}$, second column is for $w_0 = 200 \mu\text{m}$, and third column is for $w_0 = 300 \mu\text{m}$. The propagation distance varies from $z = 0$ (first line) to $z = 80$ cm (fifth line) by steps of 20 cm. The diaphragm radius for all cases is $r_d = 4.5 \text{ mm}$. The last line shows the beam profiles after linear propagation of the three Airy beams over $z = 80$ cm. Note the larger window used for plotting the cross section in the bottom-left corner.

Airy beams with $w_0 = 200 \mu\text{m}$ and $300 \mu\text{m}$ have $P_A / P_{cr} > 1$. Thus if the most intense Airy lobe behaved like a typical Gaussian beam, it would self-focus and collapse upon itself under the nonlinear action of the optical Kerr effect. Then collapse would be arrested by multiphoton absorption, plasma generation, and plasma defocusing as in ultrashort pulse filamentation. Since these phenomena are high-order processes, they should lead to saturation and prevent intensity to grow above a certain value which can be predicted by simple estimations [77, 219]. However, our simulations show a different behavior that is more similar to that of Bessel filaments [182, 184]. First, no obvious nonlinear focus of the main Airy lobe appears even though we considered propagation distances much larger than the collapse distance estimated from Marburger's formula for Gaussian beams with the same widths and powers as the considered Airy beams (i.e., 7.7 and 8.4 cm for the beams with $200 \mu\text{m}$, $2.6 P_{cr}$ and $300 \mu\text{m}$, $5.5 P_{cr}$, respectively).

Second, for the widest Airy beams with width of $200 \mu\text{m}$ (Fig 4-23(b)) and $300 \mu\text{m}$ (Fig 4-23(c)), the peak intensity reaches values up to $2 \times 10^{13} \text{ W} / \text{cm}^2$ and the electron density exceeds 10^{16} cm^{-3} but no plateau is obtained indicating the absence of a saturation process of the same nature as in filamentation [219]. The intensity profile plotted in Fig 4-23(a) does exhibit a plateau over several tens of centimeters but it corresponds to the smallest Airy beam with width of $100 \mu\text{m}$ Fig 4-23(a), the power of which is below threshold. Its peak intensity is lower than $10^{13} \text{ W} / \text{cm}^2$ and also lower than for a standard filament in air; the electron density of the generated plasma does not exceed a few 10^{12} cm^{-3} , indicating a weakly nonlinear propagation of the Airy beam. The lack of a clear nonlinear focus as well as the absence of intensity plateau in the nonlinear regime suggest that the propagation dynamics of nonlinear Airy beams are governed by the same principles that apply to Bessel filaments.

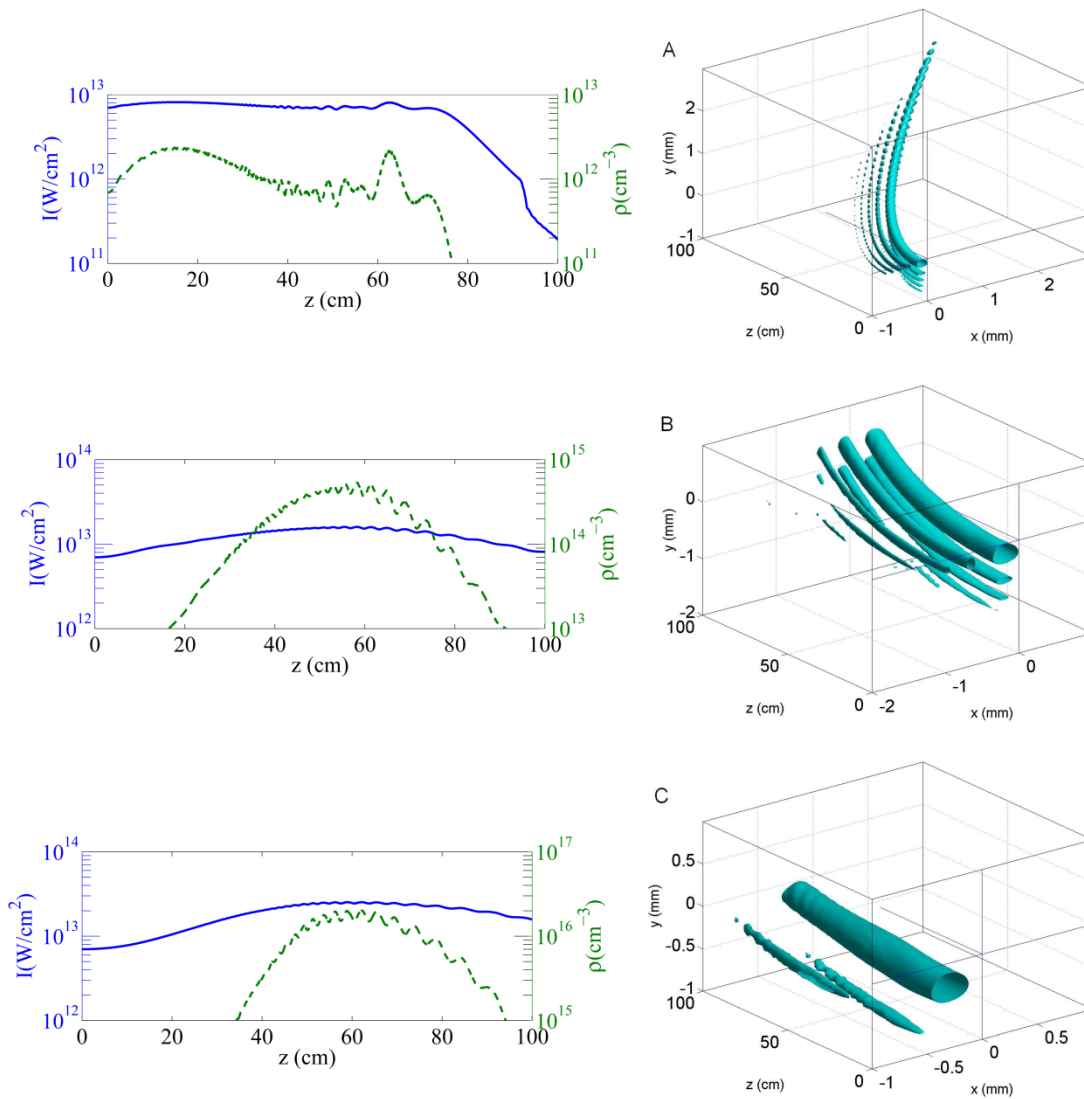


Fig 4-23 Nonlinear propagation of intense Airy beams with initial central lobe width of 100 μm (first line), 200 μm (second line), and 300 μm (third line). Left column is peak intensity (continuous curve, left axis), electron density (dashed curve, right axis). Right column is for isosurfaces of the intensity distribution showing the trajectories of the main and secondary lobes of the Airy beam. The axes crossing at the origin are a guide for the eye so as to evaluate the curvature radius of the main peak trajectory. Note the different box sizes.

The intensity profile is well explained by finite size effects: If the Airy beam was infinitely wide, an energy flux from the tail carrying infinite energy would push the main lobe along the diagonal $x = y$ and could sustain its intensity over extended distances exactly as in the case of Bessel beams [184]. With finite energy, the profile of the peak intensity of a *linearly propagating* Airy beam is known to be governed by finite-size effects and should decrease as $\exp\left[-az^2 / (k^2 w_0^4)\right]$ according to Eq.(4.2-6) (i.e., faster for large Airy beam lobes). This is the behavior we observe in the nonlinear regime [second stage of propagation in Fig 4-23(b) and (c)], in conjunction with an initial self-focusing stage that prevails at the beginning of the propagation. At moderate powers, Airy beams are intense enough to undergo Kerr self-focusing and induce multiphoton absorption; however, the trajectory of the main lobe obtained in the linear regime is preserved in the three cases shown in Fig 4-23. The parabolic trajectory of the Airy beam with the smallest lobe width (Fig 4-23(a)) exhibits the smallest curvature radius. Fig 4-24 shows the projection of the main lobe trajectory in the (x, z) plane and its full width at half maximum (FWHM) diameter. The peak clearly turns as a linear Airy beam would do, following a parabolic trajectory that coincides with that given by Eq.(4.2-7) (dashed curves in Fig 4-24). For the wider input Airy beams (Fig 4-23(b), (c) and Fig 4-24(b), (d)) the nonlinear propagation starts by a Kerr-induced self-focusing stage with a decrease of the FWHM diameter from $z = 0$ cm to $z = 30$ cm. This indicates a competition between Kerr self-focusing and the acceleration of the Airy beam. From this observation, we identified two situations for which the transverse acceleration of the Airy peak is modified by the nonlinear propagation: (i) higher-power Airy beams and (ii) narrower Airy beam truncation.

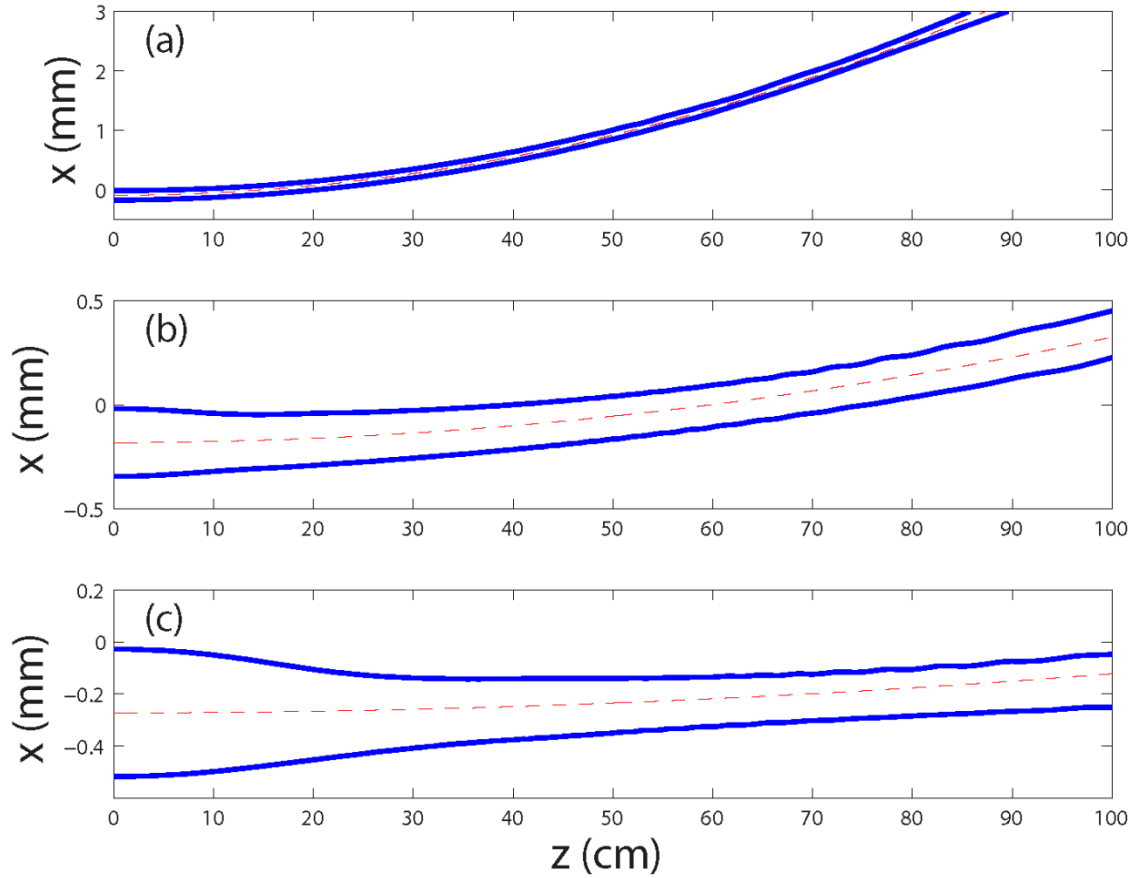


Fig 4-24 Projection of main lobe trajectory and FWHM of Airy beam along the x direction. (a) Input Airy beam with $w_0 = 100 \mu m$. (b) Input Airy beam with $w_0 = 200 \mu m$. (c) Input Airy beam with $w_0 = 300 \mu m$.

4.2.4.1.3 Propagation of intense Airy beams in the strongly nonlinear regime

The Airy peak acceleration is quenched when the power of the main lobe is large enough so that self-focusing of the most intense Airy lobe prevails over the peak acceleration. Increasing the width of the main lobe at constant input intensity does increase its power content; however, it simultaneously increases the curvature radius of the Airy beam trajectory, thus requiring a longer propagation distance to see the effect of acceleration quenching. Increasing the input intensity while keeping the width of the main lobe constant results in intensities approaching $10^{13} W / cm^2$, which ionize air sufficiently to produce a plasma responsible for a defocusing effect. This leads

to an immediate decrease rather than an increase of the intensity in the early stage of propagation. In order to demonstrate the effect of acceleration quenching with a high-power Airy beam having narrow lobes so as to keep propagation distances smaller than 1 m, we arbitrarily increased the Kerr index coefficient by a factor of 10 and used the same input Airy beams as in section 4.2.4.1.2. This keeps the curvature radius of the trajectories of the linearly propagating Airy beams unchanged but increases P_A / P_{cr} by a factor of 10 and allows us to isolate the effect of self-focusing on the beam shape from other nonlinearities, like multiphoton absorption and plasma defocusing. This mimics to some extent an experimental situation in which an Airy beam is formed in vacuum and enters a gas chamber containing pressurized air at 10 atm. Due to the rescaling properties of Eq.(4.2-9), the results also represent the propagation of an input Airy beam with $w_0 = 93 \mu\text{m}$, $I_0 = 1.4 \times 10^{12} \text{ W} / \text{cm}^2$ generated with an infrared (1500 nm), 130 fs pulse, in water (gap $Ui = 6.5 \text{ eV}$, same number of photons $K = 8$ in multiphoton processes at 1500 nm, $n_2 = 2 \times 10^{-16} \text{ cm}^2 / \text{W}$, $\rho_{nt} = 6.7 \times 10^{22} \text{ cm}^{-3}$, $\beta_K = 2 \times 10^{-89} \text{ cm}^{13} / \text{W}^7$, and $\sigma_K = 3 \times 10^{-94} \text{ s}^{-1} \text{ cm}^{16} / \text{W}^8$). There are many other combinations of beam or pulse parameters ensuring that, for water, the ratios L_{Kerr} / L_{Diff} , L_{MPA} / L_{Diff} , and L_{Plasma} / L_{Diff} are equal to their counterparts in air at 10 atm.

Fig 4-25 shows the results of this numerical experiment: The peak intensity displayed on the first line exhibits several cusps which indicate the distances where the intensity of the most intense lobe is decreasing below the intensity of a secondary lobe, which in turn becomes the most intense. Correspondingly, each dashed curve indicates the electron density generated by the most intense peak as a function of propagation distance. Except at the beginning, this electron density is obtained for a different lobe of the Airy beam, which was initially not the most intense. This competition between the different-intensity lobes is illustrated on the iso-intensity plot shown on the second column of Fig 4-25. A general trend of the intensity peaks to follow curved trajectories

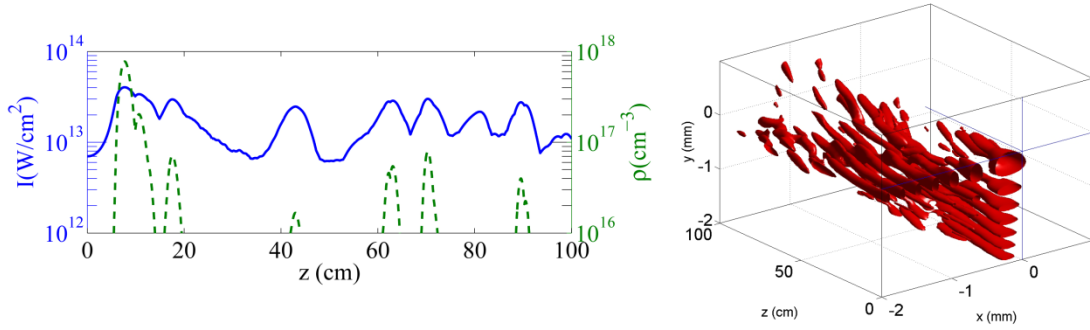


Fig 4-25 Nonlinear propagation of intense Airy beams with initial central lobe width of $200 \mu\text{m}$, $I_0 = 7 \times 10^{12} \text{ W} / \text{cm}^2$ in a highly nonlinear Kerr medium with $n_2 = 3.2 \times 10^{-18} \text{ cm}^2 / \text{W}$. First column is for peak intensity (continuous curve, left axis), electron density (dashed curve, right axis). Second column is for isosurfaces of the intensity distribution.

is observed; however, the initial main lobe clearly undergoes self-focusing over a much shorter distance and disappears after 15 cm. Then the most intense peak is located in a secondary lobe which, after some propagation distance, also disappears. This dynamical process repeats itself until the power in the whole beam is exhausted. The trajectory of the most intense lobe is therefore discontinuous each time a different secondary lobe becomes dominant. The competition between the main and secondary lobes can be followed on the $I(x, y)$ cross sections of the Airy beam as it propagates along z (second column of Fig 4-26). The main lobe width w_0 and its power content P_A are therefore important parameters for characterizing nonlinear Airy beam propagation: We observe from numerical simulations a transition between a regime where the turning ability of the Airy beam is preserved to a regime where nonlinear effects seemingly modify the curvature radius of the Airy peak trajectory due to self-focusing of intense lobes and lobe competition for the available power. This trend is clearly illustrated by the comparison of the second column of Fig 4-26 with the first that shows the $I(x, y)$ cross sections of the same Airy beam propagating in air with nonlinear index coefficient n_2 at 1 atm (also shown in the second column of Fig 4-22). At high powers, the Airy beam eventually undergoes a reshaping into a multi-filamentation pattern with multiple filaments located at the positions of the main secondary lobes of the input Airy beam.

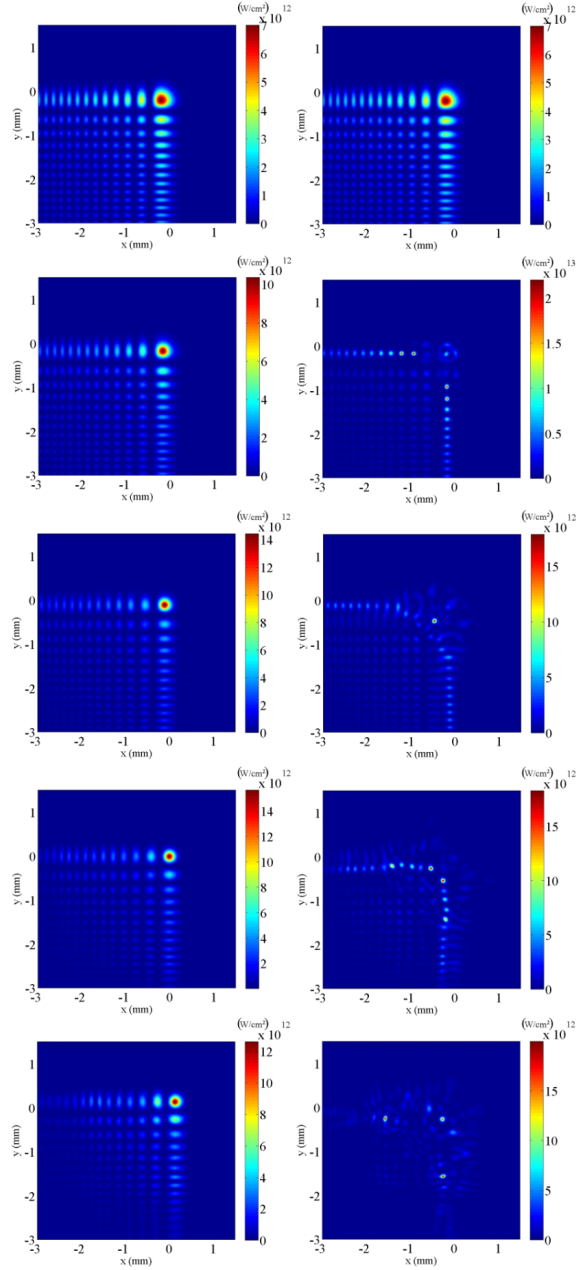


Fig 4-26 (x, y) intensity plots of nonlinear Airy beams with initial peak intensity $I_0 = 7 \times 10^{12} \text{ W} / \text{cm}^2$, with $w_0 = 200 \mu\text{m}$, and a diaphragm of $r_d = 4.5 \text{ mm}$. First column is $n_2 = 3.2 \times 10^{-19} \text{ cm}^2 / \text{W}$ (moderate power regime). Second column is for $n_2 = 3.2 \times 10^{-18} \text{ cm}^2 / \text{W}$ (high-power regime). The propagation distance varies from $z = 0$ (first line) to $z = 80 \text{ cm}$ (fifth line) by steps of 20 cm.

4.2.4.1.4 The significance of the truncation in the nonlinear regime

We identified a second situation of transverse acceleration quenching, that proceeds from the idea of managing the competition between energy fluxes induced by Kerr self-focusing and by peak acceleration. We kept our initial Airy beam parameters $w_0 = 200 \mu\text{m}$, $I_0 = 7 \times 10^{12} \text{ W / cm}^2$ and changed the radius of the circular diaphragm. The input Airy beams we considered so far in our simulations were truncated by a circular diaphragm with a rather large radius ($r_d = 4.5 \text{ mm}$) compared to the main lobe width. This approach makes finite the energy of the input Airy beam while preserving a large number of secondary lobes. Our simulations show that the diaphragm radius has an important effect on the nonlinear propagation of the Airy beam and on its transverse acceleration since the number of secondary lobes controls the energy flux that refills and pushes the main lobe. To facilitate the comparison with previous results, all simulations concerning this topic were conducted for the nonlinear index coefficient n_2 characterizing propagation in air at 10 atm or in water owing to the above-mentioned rescaling.

Fig 4-27 shows a comparison of the propagation of three Airy beams which have identical main lobe width ($200 \mu\text{m}$) but which are truncated differently: the diaphragm radius is $r_d = 4.5 \text{ mm}$ in the first column, $r_d = 2.5 \text{ mm}$ in the second column, and $r_d = 1 \text{ mm}$ in the third column of Fig 4-27. By using Eq.(4.2-8), we obtain Airy zones of 351, 261, and 165 cm which are much larger than the typical distance for self-focusing of the $200\text{-}\mu\text{m}$ -wide lobe containing $26 P_{cr}$. The input peak intensity and beam width are the same for all columns of Fig 4-27; hence the main lobes of the input Airy beams carry the same power.

In the case of the large apodizer, the linear energy flux of the Airy beam is sustained over a larger propagation distance. The beam truncated by the small diaphragm containing only 3 lobes of the input Airy beam propagates under the action of nonlinear effects over a much shorter distance. The linear energy flux responsible for the curved trajectory is in this case not strong enough to bring energy from the tail to the peak of the Airy beam over the whole Airy zone. The small diaphragm quenches the power refilling of the secondary lobes and therefore simultaneously tends to quench the turning ability of the Airy beam. Secondary lobes still undergo self-focusing and form filaments, but they subsequently follow a standard filament interaction process featured by energy exchange with the neighborhood. Their intensity increases

until multiphoton absorption becomes efficient and plasma is generated that eventually participates in beam spreading and nucleation of other filaments from the reservoir. Fig 4-27 shows that, although these multiple filaments are initiated at the same locations regardless of the diaphragm size, the smaller the diaphragm radius the earlier in their propagation they depart from each other. In this case the nonlinear dynamics dominate and seemingly prevent the main lobe to turn. In fact, these nonlinear dynamics require a much shorter distance than the Airy zone, thus the associated energy flux is used to fill the secondary lobes of the Airy beam rather than to induce a curvature of the trajectory of the main lobe. So effectively, the diaphragm radius allows us to switch off the energy flux at a given distance.

Nonlinear Airy beam propagation falls into two separate regimes identified in Fig 4-26 and Fig 4-27, depending on whether the linear acceleration and beam profile is preserved. In the strongly nonlinear regime (i.e., for a large relative strength of the self-focusing nonlinearity), the input Airy beam is effectively destroyed during its propagation. This is clearly demonstrated in Fig 4-27 at $z = 40$ cm (3rd row) for all three apodizers. In the weakly nonlinear regime, the linear dynamics prevails and the parabolic trajectory of the Airy peak is unperturbed. The strongly nonlinear regime, however, may show manifestations of linear dynamics such as the self-healing property reported in [208], where part of a linearly propagating Airy beam profile was obscured and observed to be reconstructed after a few cm. The first column of Fig 4-27 shows this effect (i.e., the destroyed profile at $z = 40$ cm is partially reconstructed at $z = 60$ cm). At this point multiphoton absorption becomes strong enough to gradually destroy once again the beam profile, as we can see at $z = 80$ cm. The outcome of this competition is actually controlled by the size of the apodizer. As the apodizer size is reduced $r_d = 2.5$ mm, the reconstruction ability of the Airy beam is weakened, as can be seen in the second column of Fig 4-27. In the third case (third column), where $r_d = 1$ mm, the Kerr effect completely dominates over all linear dynamics and the Airy profile is entirely ruined after the short Airy zone.

Note that, in all three cases, the strength of the Kerr effect is unchanged and only the apodizer radius (related to the Airy zone length and the self-healing strength) is modified.

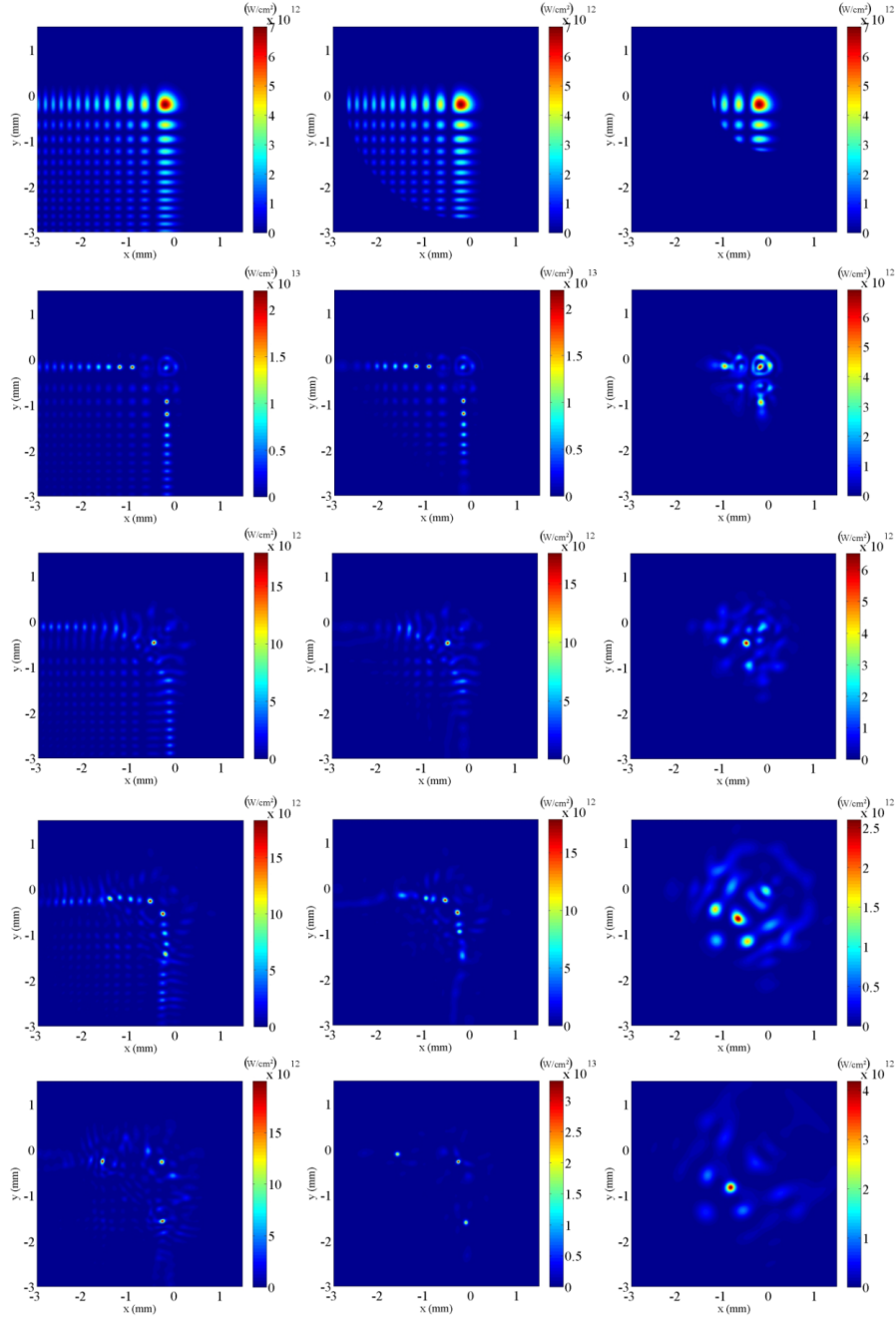


Fig 4-27 Effect of truncation in high-power regime. The three columns correspond to the propagation of nonlinear Airy beams with initial peak intensity $I_0 = 7 \times 10^{12} W / cm^2$, central lobe size $w_0 = 200 \mu m$, diaphragmed by circular apertures of radius $r_d = 4.5 mm$ (first column), $r_d = 2.5 mm$ (second column), and $r_d = 1 mm$ (third column), with nonlinear-index coefficient[220] $n_2 = 3.2 \times 10^{-18} cm^2 / W$. The propagation distance varies from $z = 0$ (first line) to $z = 80 cm$ (fifth line) by steps of 20 cm.

4.2.4.1.5 Energy flux along propagation

In order to study the dynamics of Airy beam propagation in greater detail, the transverse energy flux is evaluated at different position along propagation. A usefull way of presentation is with movies showing the evolution, as a function of the propagation distance z , of the cross section of the intensity $I(x,y)$ superimposed to an arrow plot showing the associated local energy density flux. The transverse components of the energy density flux are simply proportional to the beam intensity and to the phase gradient in the corresponding direction [184, 220-222].

The first movie is associated with the regime of moderate powers [i.e., the propagation of the 200 μm lobe width shown in Fig 4-26(a)], while the second is associated with the high-power regime; that is, the propagation of the same input Airy beam in the medium with larger Kerr coefficient used for Fig 4-26(b). Fig 4-28 shows the main features of the energy flux as identified from the movies. We can observe in the weakly nonlinear regime that the main lobe of the Airy beam is turning because of the energy flux along the symmetry axis $x = y$, from the quadrant ($x < 0, y < 0$) toward the peak, as in the case of linear propagation [Fig 4-28(a) and Fig 4-28(b) and **Video_Flux1.mov**]. In the strongly nonlinear regime, we observe that the main Airy lobe undergoes standard filamentation and part of the energy flux from the tail of the Airy beam is feeding the secondary lobes which in turn undergo self-focusing and nonlinear losses. Upon further propagation the main lobe peak decays while one or several of the secondary peaks becomes dominant, until they too decay [Fig 4-28(c)-(g) and **Video_Flux2.mov**]. Visualization of the energy flux allows us to understand the presence of notches in the curve shown in Fig 4-25(a), which correspond to propagation distances when a secondary lobe with growing intensity takes over the decaying intensity of the main lobe. Similarly to the scenario for spatial replenishment in filaments [223], a notch in the intensity curve in Fig 4-25 is explained as that propagation distance where the increasing secondary peak takes over as the global maximum from the decreasing main lobe peak. This process can repeat itself if the power in the secondary lobe is sufficient to be further transferred to a third-order lobe.

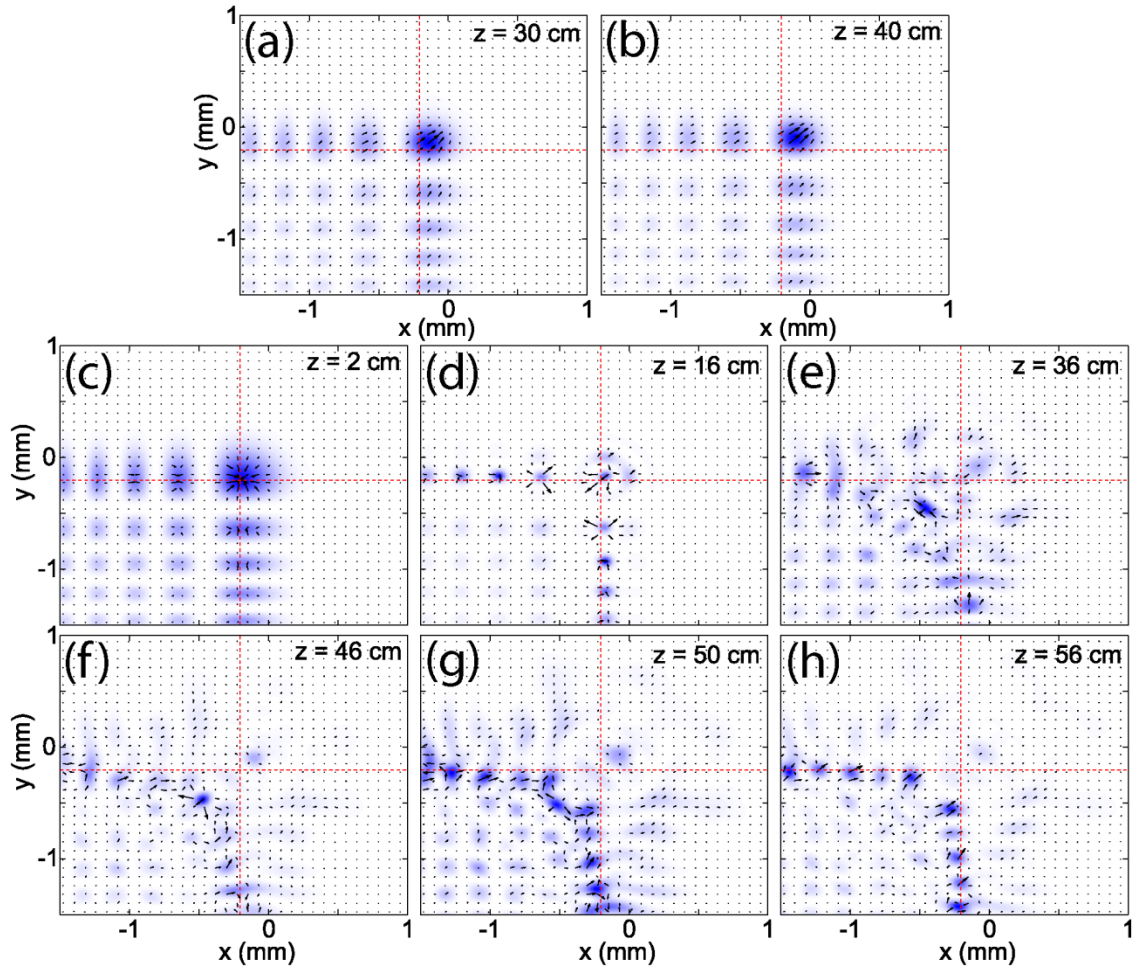


Fig 4-28 First line shows evolution of energy flux during nonlinear propagation of Airy beams with $w_0 = 200 \mu m$ and moderate power. The arrows indicate the direction of the energy flux while its strength is proportional to arrow lengths. The propagation distances are $z = 30$ and $z = 40$ cm. Second and third lines are same as for the first line but for the high-power regime. The propagation distances are $z = 2, 16, 36, 46, 50,$ and 56 cm from left to right and from the second to third line.

4.2.4.1.6 Experimental results

In addition to numerical simulations, laboratory experiments were performed to observe the moderate- and high-power regimes in Airy beam propagation as well as the effect of Airy beam truncation. As shown in Fig 4-29, the laser beam is reshaped into an exponentially apodized 2D Airy beam by using a recently developed technique [204] which exploits coma aberration as a means to imprint a 2D spatial cubic phase onto the initial Gaussian beam followed by spatial Fourier transformation via a spherical lens. The Airy beam is generated at the focus of the Fourier lens, located 2 cm inside a variable length transparent water tank, where an iris is used to truncate the Airy profile to the desired size. Experiments are performed in water to profit from the higher nonlinearity of the medium.

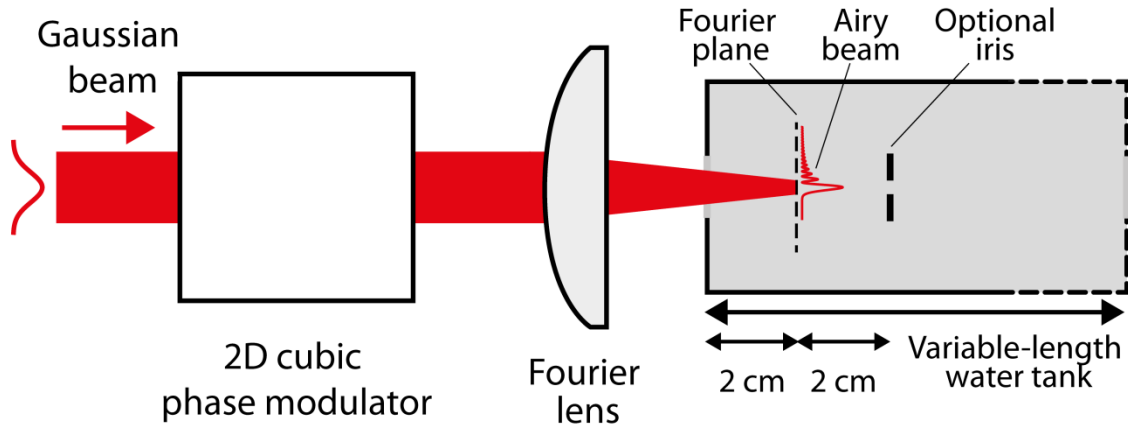


Fig 4-29 Experimental layout.

Fig 4-30 shows the experimentally generated Airy beam with main lobe FWHM of 230 μm , which corresponds to $w_0 \sim 140 \mu\text{m}$ (Fourier lens $f = 50 \text{ cm}$), after propagation over 10 cm in water, for 8 different input energies. The 800 nm laser pulse duration where the Airy beams are generated is 80 fs (as the initial pulse of 35 fs goes through a number of dispersive optical elements). The power contained in the Airy profile, at the point of creation inside the water tank, is increased from $0.03 P_{cr}$ (9.5 nJ), which is essentially linear, up to $94 P_{cr}$ (32 μJ). These values refer to the power contained in the whole Airy beam profile and not only in the main lobe, since

the latter is difficult to accurately measure experimentally. However, from previous studies [153, 204] the power content of the main lobe can be estimated around 7% of the whole beam, and thus the cases for the highest energy are well inside the high-power regime. As the energy of the pulse is increasing, nonlinear dynamics start to act on the beam shape in the same way as predicted by simulations. Self-focusing of the main Airy lobe clearly occurred for $22 P_{cr}$ (total beam). As the beam energy is increased further, secondary lobes start to self-focus and increase in intensity, showing exactly the same trend as predicted by numerical simulations.

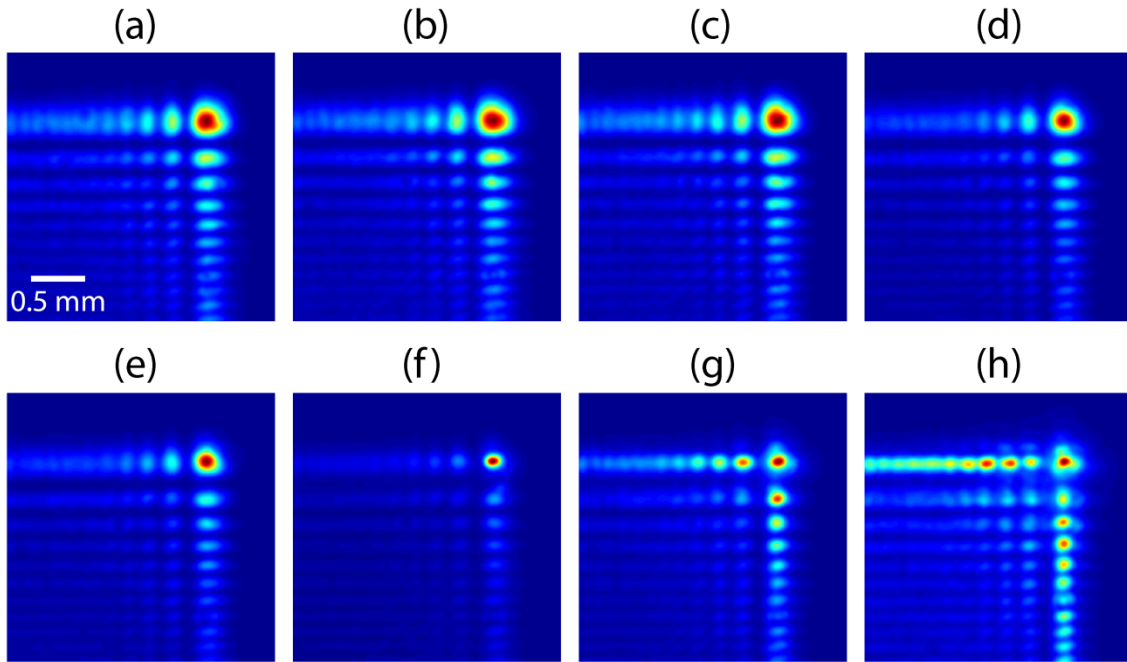


Fig 4-30 Normalized experimentally measured intensity at $z = 10$ cm after the focus, inside the water tank, for different input pulse energies. (a) 9.5 nJ ($0.03 P_{cr}$), (b) 65 nJ ($0.19 P_{cr}$), (c) 507 nJ ($1.75 P_{cr}$), (d) $2.9 \text{ } \mu\text{J}$ ($8.5 P_{cr}$), (e) $5.4 \text{ } \mu\text{J}$ ($16 P_{cr}$), (f) $7.5 \text{ } \mu\text{J}$ ($22 P_{cr}$), (g) $15 \text{ } \mu\text{J}$ ($44 P_{cr}$), (h) $32 \text{ } \mu\text{J}$ ($94 P_{cr}$). $w_0 \sim 140 \text{ } \mu\text{m}$ (FWHM $230 \text{ } \mu\text{m}$).

In Fig 4-31, a close-up of the measured Airy beam profile at $94 P_{cr}$ is shown side by side with the simulated intensity profile of the truncated ideal Airy beam. The input parameters of the simulated Airy beam are matching the ones of the experiment. Since the code operates in frozen time we take an average pulse duration of 160 fs inside the water tank (due to the dispersion of

water). In the simulation, the Airy beam propagates in 10 cm of water with $n_2 = 1.6 \times 10^{-16} \text{ cm}^2 / W$, which corresponds to $P_{cr} \approx 4 \text{ MW}$ at the laser wavelength of 800 nm [19]. The ionization coefficients used for water are $\sigma_K = 1 \times 10^{-54} \text{ s}^{-1} \text{ cm}^{10} / W^5$ for $K = 5$ photons, and neutral atom density $\rho_{nt} = 6.6 \times 10^{22} \text{ cm}^{-3}$ [166]. As we can see in Fig 4-31, the measured and the calculated patterns agree very well. In both cases the main lobe is starting to generate a filament-like structure with an extended reservoir around it. The nearby secondary lobes are strongly perturbed, while the subsequent ones are self-focusing and gaining intensity. Beyond the 6th lobe, the beam shape remains unchanged.

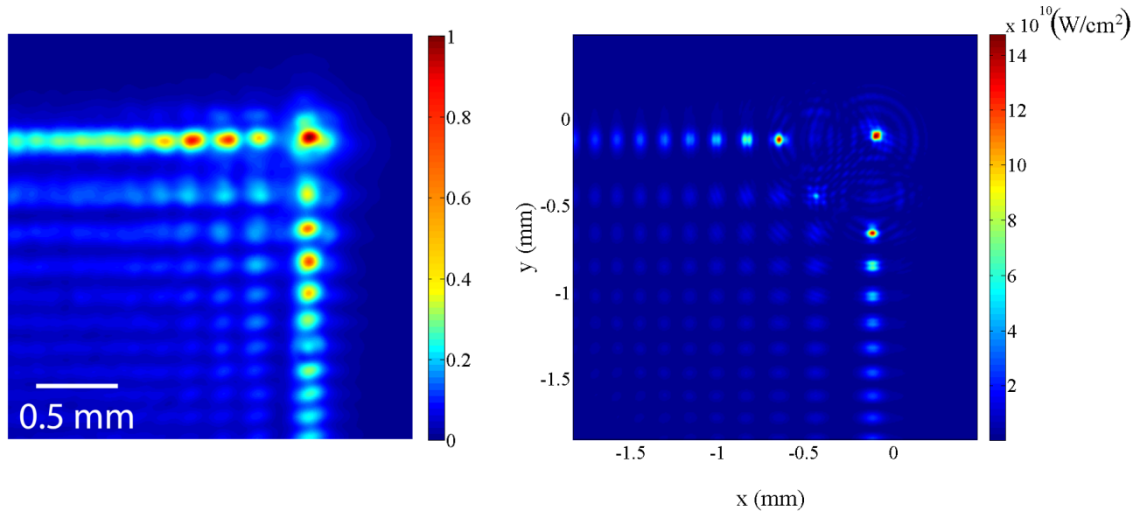


Fig 4-31 Comparison of nonlinear dynamics between experiments and simulations. Left shows normalized experimentally measured intensity at $z = 10 \text{ cm}$ after the focus inside the water tank, for the highest power ($94 P_{cr}$) and $w_0 \sim 140 \mu\text{m}$. Right shows simulated intensity distribution with identical input conditions after propagation of 10 cm in water.

We also studied the effect, previously shown in simulations; of Airy beam truncation on nonlinear propagation. Fig 4-32 shows a comparison between measurements and simulations of two input Airy beams truncated by two different-radius irises. The first line shows the two initial Airy beams used in the experiment. The main lobe size is $w_0 = 30 \mu\text{m}$ (Fourier lens $f = 10 \text{ cm}$) and the apodizer radius is $750 \mu\text{m}$ (left) and $450 \mu\text{m}$ (right). The power contained in the two Airy beams is $35 P_{cr}$ and $20 P_{cr}$ for the large and small apodizer, respectively. After nonlinear

propagation over 4.6 cm in water the beams are reshaped as can be seen in the second line of the same figure. In the case of the large iris, some features of the Airy profile are preserved while the most intense first and nearby secondary lobes show manifestations of filamentation. In the case of the small iris, the Airy profile is almost completely destroyed by the nonlinear dynamics, and a multi-filamentary pattern is formed in its place. These experimental observations are in very good agreement with corresponding simulation results shown in the third line of Fig 4-31.

To summarize this section so far, we have investigated numerically and experimentally the nonlinear dynamics of intense finite energy Airy beams. Nonlinear propagation of Airy beams is found to be governed by the same principles that rules propagation of nonlinear Bessel beams: two regimes are distinguished by the power content of the most intense Airy lobe. At moderate powers, Airy beams propagate smoothly without exhibiting an abrupt increase of intensity that would define a nonlinear focus, even if the power carried by the main lobe is several times above the critical power for self-focusing. The peak intensity does not reach a plateau but slowly increases and eventually drops due to finite size, truncation or apodization effects. The Airy peak is transversely accelerated as in the linear regime. In the high-power regime, the nonlinear dynamics is no longer smooth. The competition between the Kerr effect and the transverse energy flux regulated by the cubic spatial phase of the beam leads to an unsteady propagation featured by the formation and interaction of multiple filaments. If the Kerr effect dominates, multiple lobes will indeed self-focus on themselves and form filaments. This procedure leads to a destruction of the Airy beam profile and as a result the turning ability is lost. Alternatively, when the linear transverse flux dominates, the beam tends to accelerate along the diagonal, even though individual lobe shrinking (due to self-focusing) is still observed. This competition can be observed over an Airy zone, the length of which is determined by apodization or truncation effects. These results apply to transparent media in general: gases liquids or solids and might be useful for engineering optical materials with Airy beams [224].

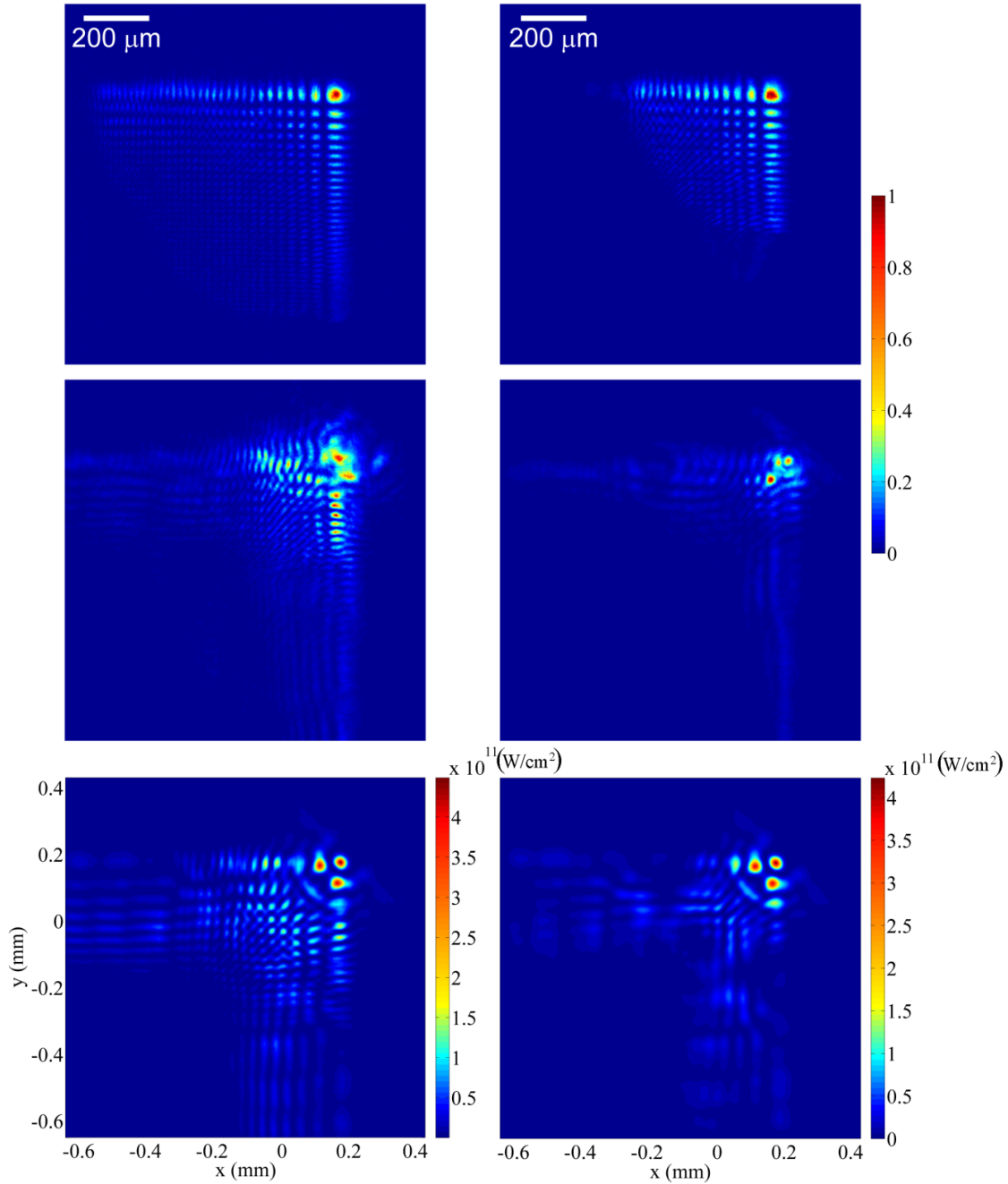


Fig 4-32 Truncation effect for two different apodizers. First line shows normalized experimental input beams. The apodizers used are $r_d = 750 \mu m$ (left) and $r_d = 450 \mu m$ (right), the main lobe FWHM is $w_0 = 30 \mu m$. Input powers are $35 P_{cr}$ (left) and $20 P_{cr}$ (right). Second line is normalized experimental intensity profiles after $z = 4.6$ cm of propagation inside the water tank, for the same pulses as in line one. Last line is simulated intensity profiles at the same position as in line two for identical input conditions.

4.2.4.1.7 Validity of the "frozen time" approximation

The goal of section 4.2.4.1 is to describe the spatial dynamics of nonlinear Airy beams. In the experiments presented, we used femtosecond laser pulses with $t_p = 35 \text{ fs}$ nominal duration propagating in air or passing through various optical elements to generate an Airy beam which results in 80 fs pulses propagating further in water. We assumed that the laser pulse profile remains undistorted along the propagation; that is, we considered that effects associated with changes in the temporal profile are sufficiently weak (or slow) with respect to the spatial effects induced by self-focusing, plasma defocusing, and multiphoton absorption. This approximation requires justification to guarantee the validity of the model to describe the spatial dynamics of propagating nonlinear pulses. This is the goal of this section, where we evaluate the importance of temporal effects by comparing their characteristic lengths.

Taking into account the material parameters, we evaluated the nonlinear lengths $L_{Kerr} = \frac{c}{\omega_0 n_2 I}$, $L_{MPA} = \frac{1}{2\beta_K I^{K-1}}$, and $L_{Plasma} = \frac{2}{\sigma\omega_0\rho\tau_C}$ of the Airy beams used in this work and compared them to the dispersive length of our laser pulse. Since both lengths are a function of the local intensity, they generally vary along z . For propagation in air, the dispersive length of the pulse is $L_{GVD} = \frac{t_p^2}{2k_0''} \sim 30.6 \text{ m}$, for a dispersive coefficient $k_0'' = 0.2 \text{ fs}^2 / \text{cm}$, whereas at their minimum value both nonlinear characteristic lengths decrease down to about 1.6 cm (Kerr) and 0.4 cm (MPA). This is three orders of magnitude shorter than L_{GVD} . Comparison of these lengths justify that the effect of dispersion can be safely neglected compared to nonlinear effects.

For the Airy beams propagating in water, the nonlinear lengths are as short as $L_{Kerr} \sim 110 \mu\text{m}$ and $L_{MPA} \sim 76 \mu\text{m}$ at their minimum, both much shorter than the dispersive length $L_{GVD} = 2.47 \text{ cm}$, for a dispersive coefficient $k_0'' = 360 \text{ fs}^2 / \text{cm}$ [225]. This means that, despite the high dispersion of water, we can still neglect it since the nonlinear effects are much stronger in the high-intensity regime.

Fig 4-33 shows the characteristic lengths for the three main cases (one Airy beam propagating in air and two others in water) in this work along propagation distance. In addition

Table 1 is showing the analytical formulas for all characteristic lengths used for the calculations of the curves in Fig 4-33, and the values that give the minimum for each physical effect.

Dispersion effectively broadens the pulse even in the linear propagation regime, although neglected in Eq.(4.2-9), but for our parameters it has a homogeneous effect on the whole beam which does not seriously affect the much faster spatial dynamics. The laser pulse profile can therefore be safely assumed to remain undistorted along propagation. We used this undistorted profile to calculate the generated plasma density by means of Eq.(4.2-10), where ionization rate depends on the local intensity. The electron density used in the plasma defocusing term in Eq.(4.2-9) is evaluated at the central local time $t = 0$ after calculation by Eq.(4.2-9).

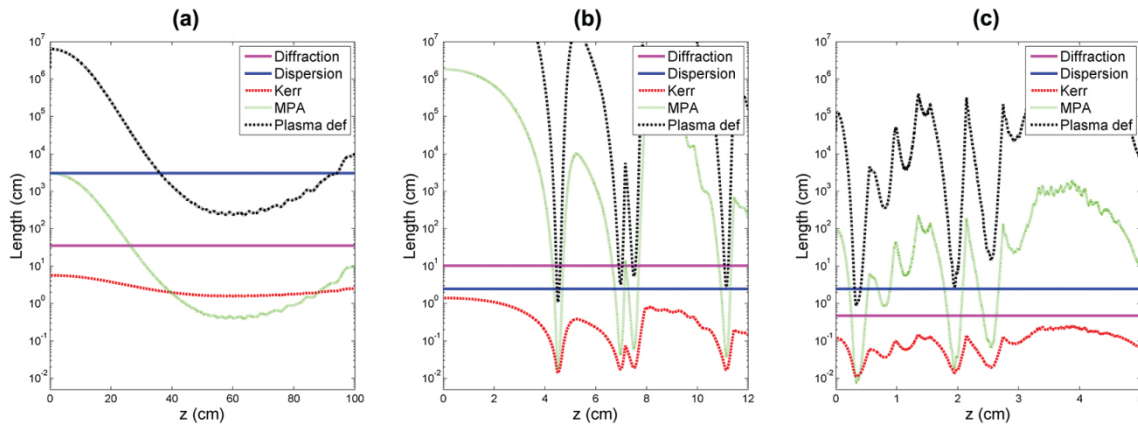


Fig 4-33 Log scale plot of the characteristic lengths of physical effects vs propagation distance for (a) the Airy beam of Fig 4-23(c) propagating in air, (b) the Airy beam of Fig 4-31 propagating in water, and (c) the Airy beam of figure Fig 4-32 propagating in water. The blue and magenta continuous lines that correspond to the characteristic lengths of dispersion and diffraction respectively. Green dotted line is for MPA, red dashed line is for Kerr, and black dash-dotted line is for plasma defocusing.

Our model includes another approximation: we considered multiphoton ionization of a single species in air (i.e., oxygen) with the lowest ionization potential $U_i = 12.06 eV$. This is usually an excellent approximation in the regime of ultrashort laser pulse filamentation since a more complete model taking into account ionization of both oxygen and nitrogen molecules gives a negligible additional contribution to the electron density due the much smaller ionization rate of nitrogen compared to oxygen molecules [29].

The above evaluation of dispersive lengths justifies this assumption and the use of Eq.(4.2-9) [216]. We emphasize that assuming the spatial profile is mainly shaped by spatial dynamics (diffraction, self-focusing, multi-photon absorption, and plasma defocusing) and neglecting the effect of the much weaker temporal dynamics on the beam shape will be further justified by the good agreement between simulation and results and measurements of nonlinear Airy beam profiles.

Table 1 Minimum Characteristic lengths of physical effects.

Physical effect	Length formula *	Fig 4-23(a)		Fig 4-31(b)		Fig 4-32(c)	
		Value that results in the minimum length	Minimum Length (cm)	Value that results in the minimum length	Minimum Length (cm)	Value that results in the minimum length	Minimum Length (cm)
Kerr	$L_{Kerr} = \frac{1}{k_0 n_2 I}$	$I = I_{max} = 2.5 \times 10^{13} \text{ W / cm}^2$	1.6	$I = I_{max} = 4.2 \times 10^{12} \text{ W / cm}^2$	1.4×10^{-2}	$I = I_{max} = 5.3 \times 10^{12} \text{ W / cm}^2$	1.1×10^{-2}
MPA	$L_{MPA} = \frac{1}{2\beta_K I^{K-1}}$	$I = I_{max}$	0.4	$I = I_{max}$	1.9×10^{-2}	$I = I_{max}$	7.6×10^{-3}
Plasma defusing	$L_{plasma} = \frac{2}{\sigma \omega_0 \rho \tau_C}$	$\rho = \rho_{max} = 1.9 \times 10^{16} \text{ cm}^{-3}$	2.3×10^2	$\rho = \rho_{max} = 3.2 \times 10^{18} \text{ cm}^{-3}$	1.0	$\rho = \rho_{max} = 3.9 \times 10^{18} \text{ cm}^{-3}$	0.9
Dispersion	$L_{GVD} = \frac{t^2}{2k_0''}$	$t = 35 \text{ fs}$	3.1×10^3	$t = 35 \text{ fs}$	2.47	$t = 35 \text{ fs}$	2.47
Diffraction	$L_{Diff} = \frac{k_0 R_0^2}{2}$	$R = w_0 = 300 \text{ } \mu\text{m}$	35	$R = w_0 = 140 \text{ } \mu\text{m}$	10	$R = w_0 = 30 \text{ } \mu\text{m}$	0.47

* The characteristic lengths naturally arise when the propagation equation (Eq.(2.1-92)) is made dimensionless.

4.2.4.2 Stationary nonlinear Airy beams

Here we demonstrate the existence of stationary Airy-like solutions in the presence of third-order Kerr nonlinearity of any sign (i.e., focusing or defocusing) and, most importantly, even in the presence of nonlinear losses (NLLs). We perform an detailed analysis that describes the shape and main features of one-dimensional nonlinear Airy wave packets, i.e., monochromatic beams that exhibit a curved trajectory. The Kerr nonlinearity is shown to lead to a compression of the Airy lobes (for a focusing nonlinearity) and nonlinear losses lead to an imbalance of the incoming energy flux toward the main lobe which in turn induces a reduction in the contrast of the Airy oscillations. This finding is then verified in numerical simulations and experiments that show the spontaneous emergence of the main features of stationary nonlinear Airy beams.

We consider the propagation of a monochromatic beam of frequency ω_0 in one spatial dimension. The electric field $E(x, z, t)$ is decomposed into carrier and envelope as $E(x, z, t) = \text{Re}\{\mathcal{E}(x, z, t)\exp[-i\omega t + ik_0 z]\}$, as before. In the presence of nonlinearity, such as the optical Kerr effect and multiphoton absorption, propagation may be described by the nonlinear Schrödinger equation for the complex envelope of the field:

$$\frac{\partial \mathcal{E}}{\partial z} = \frac{i}{2k_0} \frac{\partial^2 \mathcal{E}}{\partial x^2} + ik_0 \frac{n_2}{n_0} |\mathcal{E}|^2 \mathcal{E} - \frac{\beta_K}{2} |\mathcal{E}|^{2K-2} \mathcal{E} \quad (4.2-13)$$

where the nonlinear Kerr modification of the refractive index is $\delta n = n_2 |\mathcal{E}|^2$, while K and β_K are the order and the coefficient of multiphoton absorption, respectively. In the case of linear propagation, Eq.(4.2-13) admits the Airy beam solution $\mathcal{E} = Ai(y) \exp[i\varphi_L(y, \zeta)]$, whose intensity profile is invariant in the uniformly accelerated reference system defined by the normalized coordinates $\zeta = z / k_0 w_0^2$, $y = x / w_0 - \zeta^2 / 4$, with $\varphi_L(y, \zeta) \equiv y\zeta / 2 + \zeta^3 / 24$ and w_0 a typical length scale so that the acceleration or curvature is given by $1 / 2k_0^2 w_0^3$. We are interested in finding stationary nonlinear solutions to Eq.(4.2-13), in the above sense (invariant in

the accelerated reference system), with boundary conditions compatible with the shape and properties of Airy beams, whose asymptotic behavior as $y \rightarrow \pm\infty$ reads [226].

$$Ai(y) \sim |y\pi^2|^{-1/4} \sin(|\rho| + \pi/4) \quad \text{for } y \rightarrow -\infty \quad (4.2-14)$$

$$Ai(y) \sim \frac{(y\pi^2)^{-1/4}}{2} \exp[-|\rho|] \quad \text{for } \rho \rightarrow +\infty \quad (4.2-15)$$

where $\rho = (2/3)\text{sgn}[y]|y|^{3/2}$. We therefore impose the constraints of a weakly localized tail toward $y \rightarrow -\infty$ and an exponentially decaying tail toward $y \rightarrow +\infty$. Solutions, hereafter called nonlinear Airy beams (NABs) must also match Airy beams in the absence of nonlinearity. We thus rewrite Eq.(4.2-13) in normalized units in the accelerated reference frame (ζ, y) as

$$\frac{\partial \mathcal{E}}{\partial \zeta} - \frac{1}{2} \zeta \frac{\partial \mathcal{E}}{\partial y} = \frac{i}{2} \frac{\partial^2 \mathcal{E}}{\partial y^2} + i\gamma |\mathcal{E}|^2 \mathcal{E} - a |\mathcal{E}|^{2K-2} \mathcal{E} \quad (4.2-16)$$

The nonlinear parameters read as $\gamma = k_0^2 n_2 w_0^2 / n_0$ and $a = \beta_K k_0 w_0^2 / 2$. In order to find the shape of NABs, we consider the complex envelope $\mathcal{E} = A(y) \exp[i\varphi(y, \zeta)]$ with a ζ -invariant modulus, substitute into Eq.(4.2-16), separate real and imaginary parts, and require that the ζ dependence of the phase be the same as that of linear Airy beams $\varphi(y, \zeta) = \varphi_L(y, \zeta) + \psi(y)$.

The modulus $A(y)$ and nonlinear phase $\psi(y)$ satisfy

$$A'' - yA - (\psi')^2 A + 2\gamma A^3 = 0 \quad (4.2-17)$$

$$\psi' A^2 = 2a \int_y^{+\infty} A^{2K} dy = N_y \quad (4.2-18)$$

where primes stand for d/dy . The LHS of Eq.(4.2-18) represents the net power flux N_y per unit propagation length through a y boundary of a semi-infinite domain $[y, +\infty)$ in the co-accelerating reference frame. Eq.(4.2-18) imposes the requirement that the flux compensates for the power N_y lost by nonlinear absorption within this domain. In the linear case, i.e., with no nonlinear

losses ($\alpha = 0$), there is no net energy flux ($\psi' = 0$) and phase fronts exhibit the curvature of Airy beams [201]. Nonlinear losses, assumed to be finite, since $K > 2$, increase from $N_{+\infty} = 0$ at

$y \rightarrow +\infty$ to $N_{-\infty} = 2a \int_{-\infty}^{+\infty} A^{2K} dy$ at $y \rightarrow -\infty$, thereby establishing an additional curvature of the

phase front in the weakly decaying tail of the beam, since $\psi' \rightarrow N_{-\infty} / A^2$, whereas the exponentially decaying tail has the curvature of the Airy beam. By introducing the variable

$B(\rho) = A(y)|\rho|^{1/6}$, Eqs.(4.2-17) and (4.2-18) can be combined into a Newton-like equation governing the tail amplitude in the limit $y, \rho \rightarrow \pm\infty$:

$$\frac{\partial^2 B}{\partial \rho^2} \pm B = \frac{N_{\pm\infty}^2}{B^3} \quad \text{for } \rho \rightarrow \pm\infty \quad (4.2-19)$$

Eq.(4.2-19) admits solutions in the form $B \sim \exp(-\rho)$ and $B^2(\rho) \sim B_{-\infty}^2 [1 + C \sin(2|\rho|)]$ as $\rho \rightarrow \pm\infty$. The latter exhibits oscillations of finite amplitude around the mean value $B_{-\infty}$ and contrast

$C \equiv (1 - N_{-\infty}^2 / B_{-\infty}^4)^{1/2}$, decreasing as the amount of total losses increases. In the absence of nonlinear absorption ($N_{-\infty} \rightarrow 0$), it reduces to the asymptotics of Eq.(4.2-14) with maximum contrast $C = 1$. The contrast vanishes for $B_{-\infty}^2 = N_{-\infty}$, showing that no solution exist above a certain threshold of total losses.

In analogy with the physics of nonlinear Bessel beams [227], NABs can be viewed as Airy beams reshaped by nonlinear absorption and the Kerr effect, the former being responsible for the power flux from the weakly decaying tail toward the intense lobes where nonlinear absorption occurs and the latter of a nonlinear phase shift [228]. This is expressed by considering the NAB as an unbalanced superposition of two stationary Hankel beams, each carrying energy in the direction of, or opposite to the main lobe:

$$A(y) \exp[i\psi(y)] = \frac{1}{2} \sqrt{\frac{-y}{3}} \sum_{l=1}^2 a_l \exp[(-l)i\pi/6] H_{1/3}^{(l)}(|\rho|) \quad (4.2-20)$$

The power fluxes associated with each Hankel component exactly compensate for the balanced superposition with $a_1 = a_2 = 1$, which gives the stationary Airy beam with no net power flux. Unbalancing creates a net flux associated with a lowering of the contrast of the oscillating tail.

We numerically integrated Eqs.(4.2-17) and (4.2-18) from $+\infty$ to $-\infty$ starting from the linear asymptotic solution as a boundary condition in order to retrieve the intensity and phase profiles of the NAB. Fig 4-34(a) shows the normalized intensity profiles in the pure Kerr case, i.e., $\alpha = 0$, for focusing ($\gamma > 0$) and defocusing ($\gamma < 0$) Kerr nonlinearity, respectively. The width of the main lobe is narrower or wider depending on the sign of γ . Since the reference system in which we are considering the solutions is always referred to the linear case, the nonlinear solution preserves the same acceleration although the relation between the width of the main lobe and the peak acceleration no longer holds. In Fig 4-34(b) for the $K = 5$ case and $\gamma = 0$ (red dashed line), we show the effect of multiphoton absorption and we observe a reduction of the contrast in the decaying oscillations, which asymptotically goes to C , and this reduction is greater when the total amount of energy lost in absorption (proportional to $N_{-\infty}$) is greater (data not shown). When we have both Kerr nonlinearity and multiphoton absorption, we observe features characteristic of both regimes (blue dotted line). As in the pure Kerr case, the acceleration of linear Airy beams is preserved. We performed a scan in the parameter space in order to derive the region of existence of these stationary solutions.

Fig 4-34(c) shows this domain in the (I_0, w_0) coordinates for water at $\lambda_0 = 800 \text{ nm}$ (we considered $n_2 = 2.6 \times 10^{-16} \text{ cm}^2 / \text{W}$, $n_0 = 1.3286$, $K = 5$, and $\beta_K = 8.3 \times 10^{-50} \text{ cm}^7 / \text{W}^4$ [229]), where I_0 is the maximum intensity of the nonlinear profile and w_0 is the width of the corresponding linear solution, which represents the acceleration as $a(w_0) = 1 / (2k_0^2 w_0^3)$.

A relevant question is whether one is actually able to excite or experimentally observe stationary NABs. The ideal beams described above have infinite energy whereas experiments obviously resort to finite-energy realizations that cannot guarantee perfect stationarity. However, as in the linear case in which finite energy Airy beams still exhibit the main stationary features, e.g., sub-diffractive propagation of the main intensity peak, over a limited distance [203], we may expect the nonlinear Airy beam to emerge during propagation in the nonlinear regime.

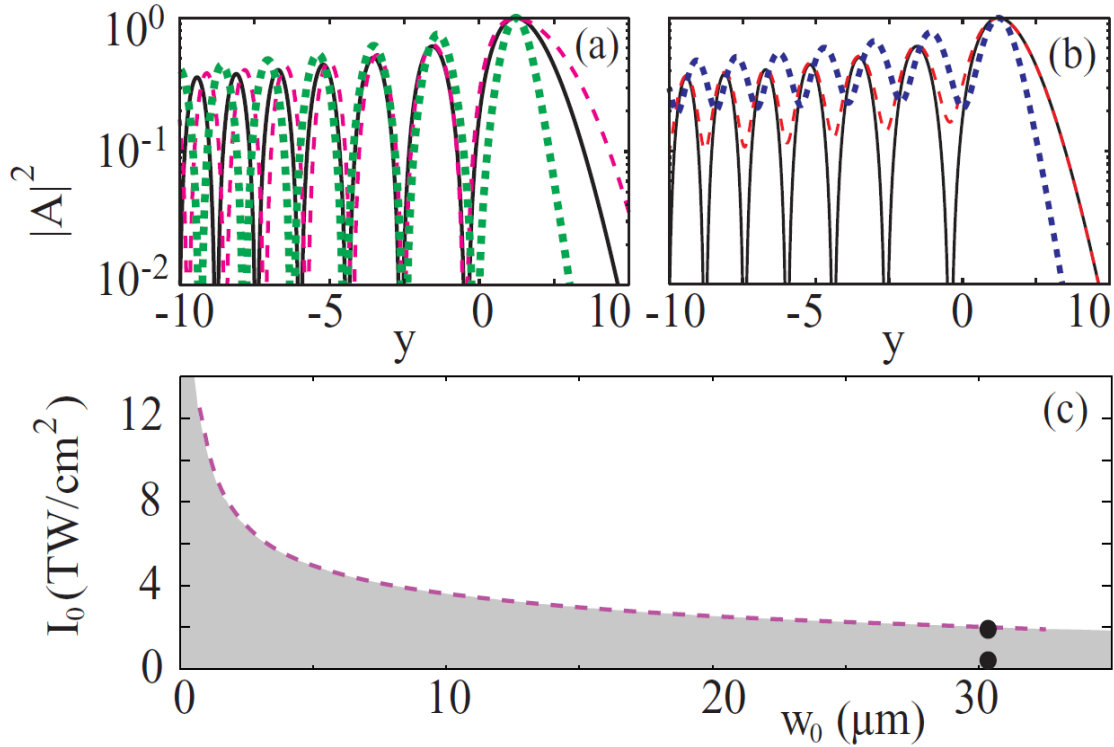


Fig 4-34 Nonlinear Airy wave forms for (a) a pure Kerr focusing (green dotted line) and defocusing (red dashed line) nonlinearity with no NLLs; (b) NLLs alone with $K = 5$ (red dashed line) and Kerr + NLLs (blue dotted line). (c) Domain of existence (shaded region) of the NAB solution in the case of water at $\lambda_0 = 800 \text{ nm}$ as a function of peak intensity and width of the linear solution. The circles indicate the peak intensities at which numerical simulations were performed (Fig 4-35).

The rationale behind this reasoning is also based on the observation that stationary wave forms have been shown to act as attractor states for the dynamical evolution of laser beams and pulses in the nonlinear regime, e.g., dynamically evolving X-waves during ultrashort laser pulse filamentation [68, 230], nonlinear unbalanced Bessel beams during the evolution of high-intensity Bessel beams [182, 227], and the spatial Townes profile during the self-focusing of intense Gaussian pulses [231].

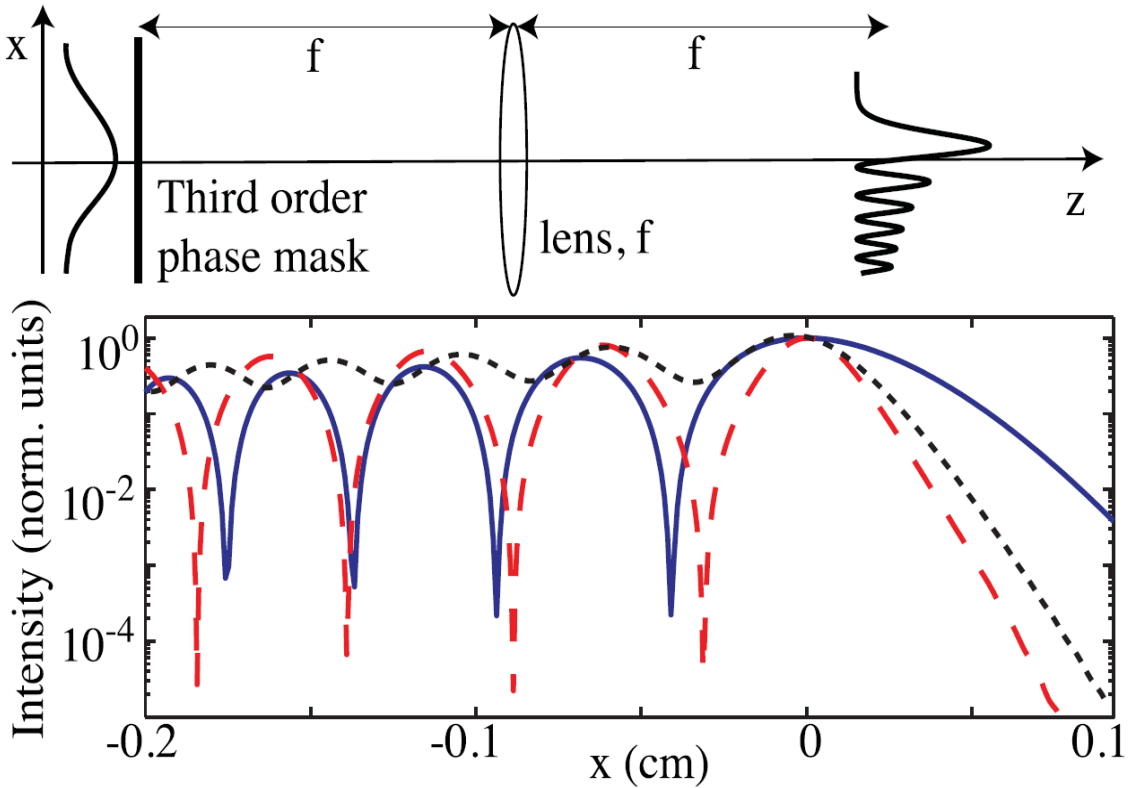


Fig 4-35 Numerical results: propagation in water with focal length $f = 20$ cm. Solid blue line, linear Airy profile; dashed red line, nonlinear Airy profile; black dotted line, nonlinear case with artificially increased NLLs. All profiles are shown in the focal plane of lens f ($z = 20$ cm).

We performed a series of numerical simulations, solving Eq.(4.2-13) for the same material parameters as in Fig 4-34 with an input Airy beam defined as in the linear regime, for various increasing input intensities. The Airy beam was generated by applying a third-phase mask to a Gaussian beam (full width at half maximum of 0.5 mm) followed by a 2- f linear propagation so as to obtain the Fourier transform in the focal plane of the lens (focal length $f = 20$ cm). This layout is shown at the top of Fig 4-35. In Fig 4-35 we show a line-out of the nonlinear profile (dashed red line) obtained by numerical simulations based on Eq.(4.2-13), at $z = 20$ cm from the last focusing lens for $I_0 = 2TW / \text{cm}^2$. The linear Airy profile (solid blue line) is included for comparison. The contraction of the main lobe and the different periodicity of the side lobes is clearly evident, while the effect of NLLs (i.e., loss of contrast in the side-lobe oscillations) is not observed. We therefore performed an additional simulation (black dotted line) at the same peak intensity with an increased nonlinear absorption coefficient,

$\beta_K = 8.3 \times 10^{-45} \text{ cm}^7 / \text{W}^4$: the strong reduction in the contrast of the Airy beam oscillations is now clear, indicating the presence of an inward flux that is stabilizing the energy loss in the main lobe.

We performed two series of experiments by launching one-dimensional Airy beams with increasing input energy into two different nonlinear media: (1) a 2 cm thick cuvette filled with water and (2) a 2.5 cm thick sample of the polymer polymethyl-methacrylate (PMMA). The experimental setup is shown in Fig 4-36(a): a third order spatial phase, together with a quadratic one corresponding to a cylindrical Fourier lens, is impressed onto a Gaussian-shaped beam delivered by an amplified Ti: sapphire laser with 35 fs pulse duration, using a spatial light modulator (Hamamatsu LCOS). The Airy-shaped beam then propagates through the nonlinear sample and the beam profile at the exit surface is imaged onto a CCD camera. Fig 4-36(b) shows the spatial fluence profiles (in logarithmic scale) for three different input energies 25 nJ (linear propagation), 350 μJ , and 530 μJ and for an input phase profile such that the linear Airy main lobe full width at half maximum (FWHM) is 159 μm . The main lobe undergoes an evident contraction that increases with increasing energy, in agreement with the prediction summarized in Fig 4-34(a) for the Kerr-dominated NAB. We then repeated the measurements with an increased input phase such that the Airy main lobe has a FWHM of 182 μm . Fig 4-36(c) shows the results for the same energies as in Fig 4-36(b). The reduced density of the Airy peaks and the correspondingly lower spatial intensity gradients imply that now both self-focusing effects and the energy flux within the beam are weaker. We may therefore expect the effects of NLLs to become more evident. Indeed, while Kerr self-focusing effects are nearly absent, the contrast in the secondary Airy lobes decreases in agreement with the expected behavior of the “unbalanced” Airy beam, as summarized in Fig 4-34(b). These effects are even more pronounced in measurements performed in PMMA which is expected to have higher NLLs due to the lower multiphoton absorption photon number, $K = 3$. As for the case of water, two different Airy widths were tested, 78 μm (Fig 4-34(d)) and 159 μm (Fig 4-34(e)), at three different energies 25 nJ, 78 μJ , and 246 μJ , with similar dynamics as in water and with the larger Airy peak leading to increased NLL effects. We observe an increase of minimum intensity values by nearly an order of magnitude with increasing input energy. Although we do not have the same resolution and dynamic range as in the numerics, the experiments clearly show the predicted trends for the stationary NAB.

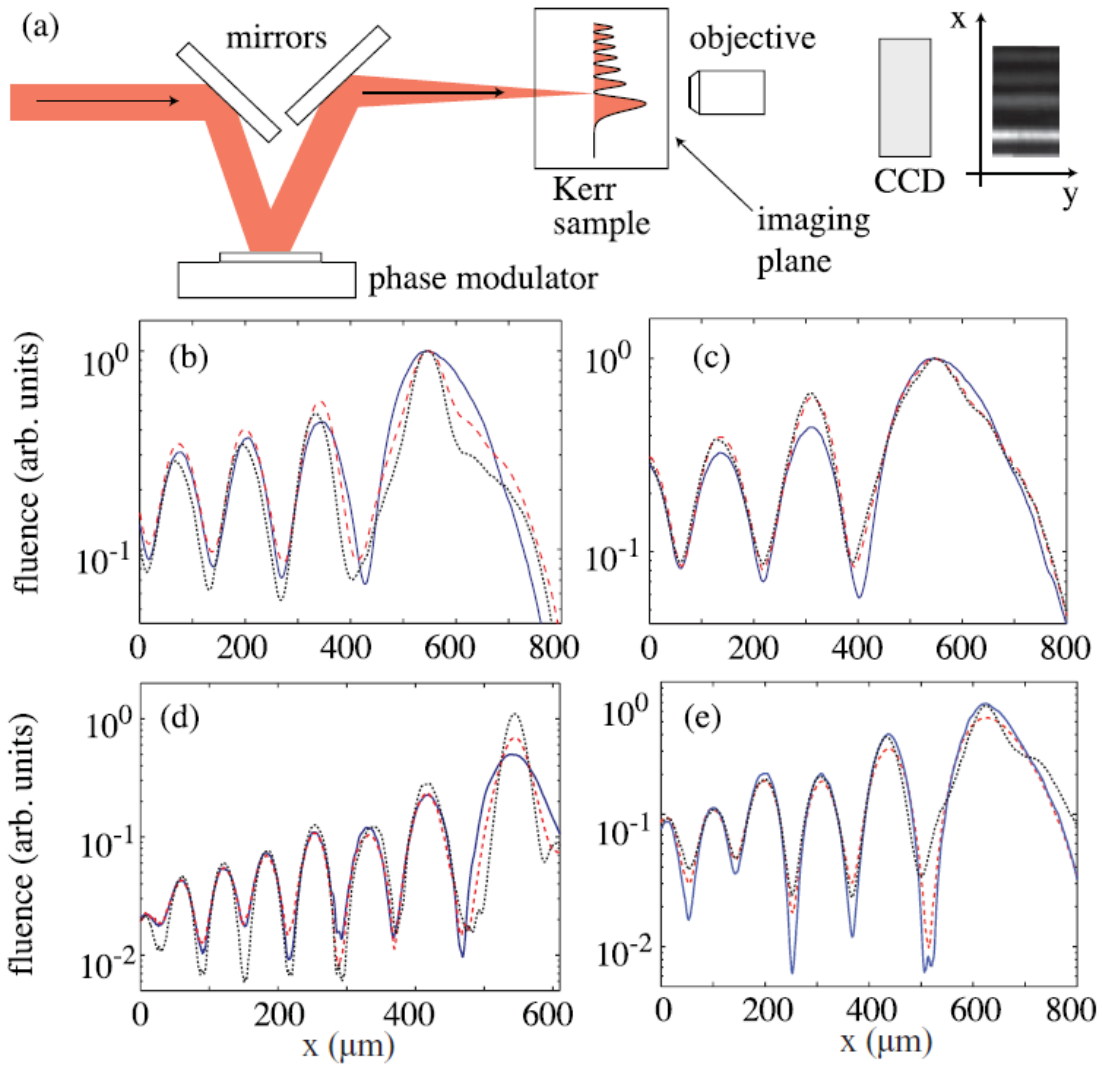


Fig 4-36 Experimental results: (a) Experimental layout. (b)–(e) Output Airy beam fluence profiles in logarithmic scale. (b) Water at three input energies 25 nJ (solid line), 350 μJ (dashed line), and 530 (dotted line) μJ and for an input Airy pulse with a main lobe FWHM of 159 μm. (c) Water at same energies as in (b) and a main lobe FWHM of 182 μm. (d) PMMA at three input energies 25 nJ (solid line), 78 μJ (dashed line), and 196 (dotted line) μJ and for an input Airy main lobe FWHM of 78 μm. (e) PMMA at same energies as in (d) and a main lobe FWHM of 136 μm.

To summarize this section, the existence of a freely accelerating solution in the nonlinear regime that remains stationary even in the presence of nonlinear losses is demonstrated. Clearly these results may be extended to the original quantum context in which Airy wave packets were proposed for the first time [201]. NABs could also find practical applications in a similar fashion

to stationary Bessel beams where the beam stability above ablation intensities has led to technical improvements in micromachining optical materials [232] or soft tissue laser surgery by using them as razor blades with a well-defined curvature. Stationarity is also a critical issue in “analog Hawking” emission experiments [233]: the nonlinear Airy beam may be used to reach huge $\sim 10^{21} m/s^2$ accelerations and thus investigate related photon emission mechanisms [234].

4.2.5 Autofocusing waves

By exploiting the transverse acceleration and the 1D nature of the Airy function, Efremidis *et al.* recently introduced the cylindrically symmetric Airy beam, or ring-Airy wavepacket (RAW), which is able to abruptly autofocus in the linear regime [232]. As shown in a recent work [233], abruptly autofocusing waves are experimentally feasible, and can be used to deliver high energy pulses inside thick transparent samples without damaging the material prior to the focus. The abrupt intensity increase at the focus of the cylindrical symmetric Airy makes it easy to combine a long working distance with a small focal volume. The remarkable abilities of these wavepackets make them ideal candidates for laser ablation applications in previously hard to reach environments.

4.2.5.1 Linear autofocusing waves

The linear RAW that was introduced in [232] is in our case a radial symmetric Airy beam. The electric field envelope follows the function

$$\mathcal{E}_0(r, 0) = Ai\left(\frac{r_0 - r}{w_0}\right) \exp\left[a\left(\frac{r_0 - r}{w_0}\right)\right] \quad (4.2-21)$$

where Ai corresponds to the Airy function from Eq.(4.2-1), r is the radial coordinate, r_0 represents the radius of the primary ring, a is a constant, and w_0 is a scaling factor. The radial fluence distribution of a ring-Airy beam can be seen in Fig 4-37. More precisely, the primary

ring of the beam has its peak intensity at a radius of $R_0 \equiv r_0 - w_0 \cdot g(\alpha)$, where $g(\alpha)$ denotes the position of the first zero of the function $\text{Ai}'(x) + \alpha \cdot \text{Ai}(x)$, while its full width at half maximum (FWHM) is $\sim 2.28 w_0$ [233].

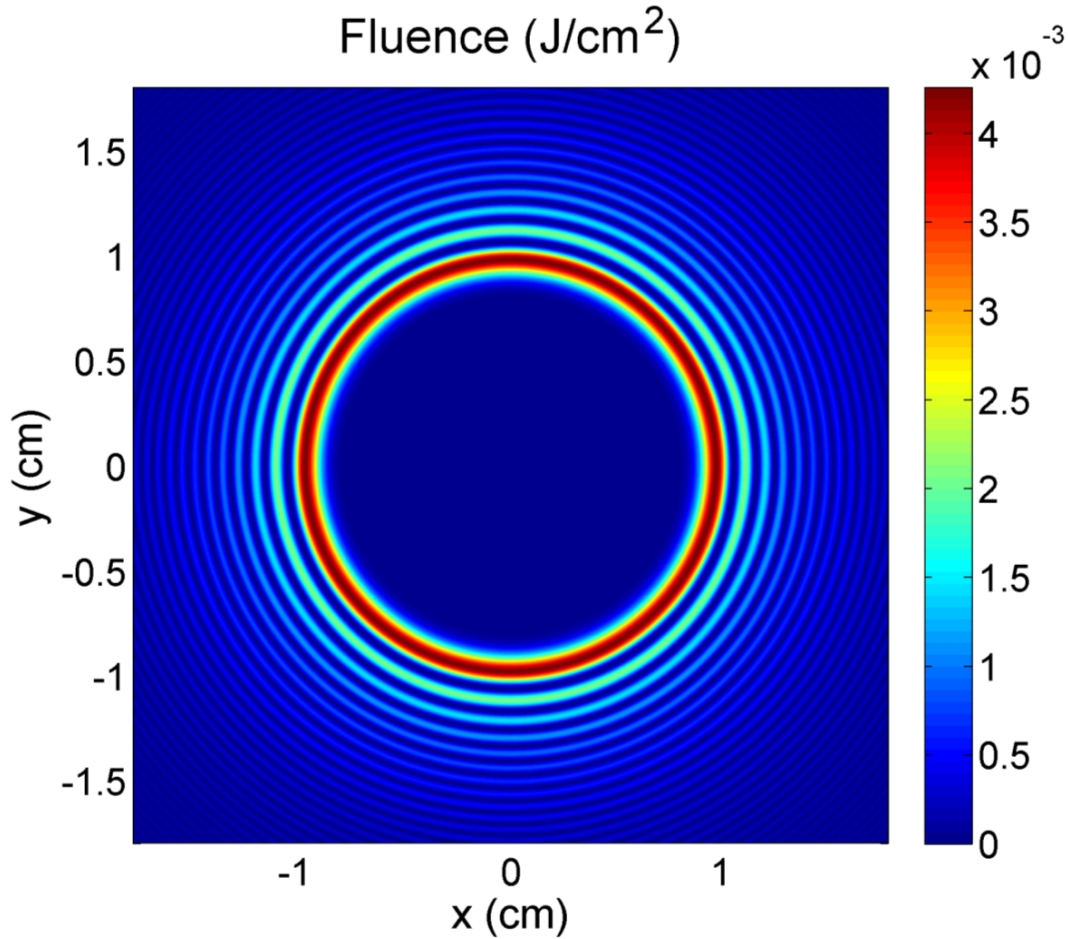


Fig 4-37 Radial fluence distribution of a ring-Airy beam with $a = 0.05$, $r_0 = 921 \mu m$, and $w_0 = 61.4 \mu m$.

Fig 4-38 shows the normalized radial electric field amplitude distribution of a RAW along propagation distance. The normalized coefficients of Eq.(4.2-21) are $a = 0.05$, $r_0 = 10$, and $I_{\max}(z=0) = 1$. As we can see at $z \sim 6$ the beam exhibits an intense autofocus. The maximum intensity inside the auto-focus depends on the beam initial beam characteristics a and

r_0 . The maximum contrast I_{\max} / I_0 was found in [232] to be 156 for $a = 0.05$ and $r_0 = 15$ (dimensionless units), which will be the values used in the next sections.

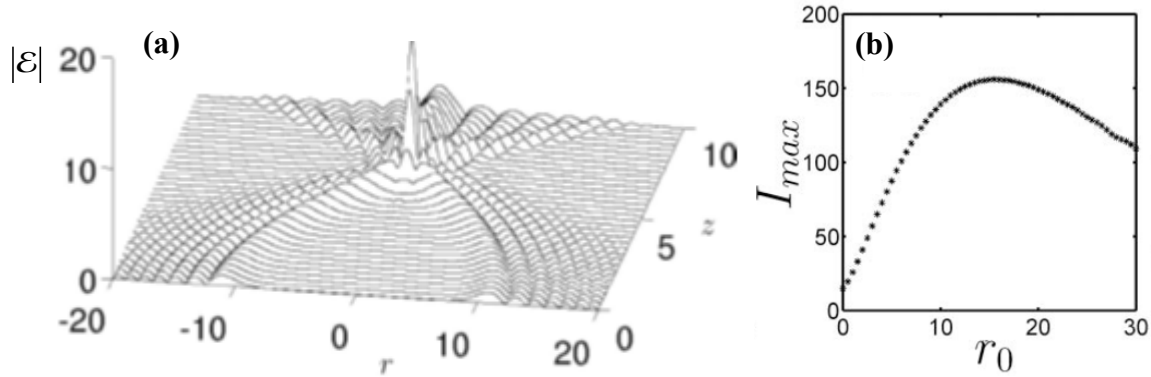


Fig 4-38 (a) Radial field envelope distribution along propagation of a ring-Airy beam with $a = 0.05$, $r_0 = 10$, and $I_{\max}(z = 0) = 1$. (b) Maximum intensity as a function of r_0 . Taken from [232].

The experimental realization of RAWs is utilizing the same approach as is used in the 1D and 2D (x, y) Airy beams, a phase mask in the form of an SLM and a Fourier transformation lens. The experimental setup used in [233] can be seen in Fig 4-39. The phase mask used in this case must be a cylindrical symmetric version of the XY Airy phase mask, as is shown in Fig 4-40. As we can see the experimental result matches the theoretical prediction (Fig 4-40(b), (c)).

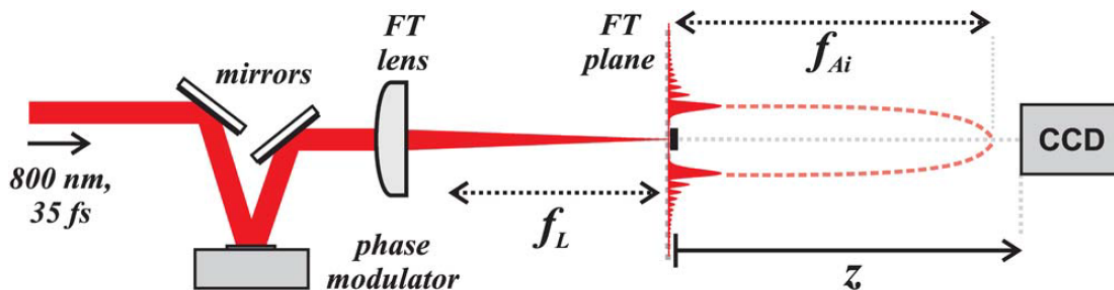


Fig 4-39 Experimental setup for the generation of RAWs. FT, Fourier transform; f_L , FT lens focal length; f_{Ai} , effective focal length of the Airy ring. Taken from [233].

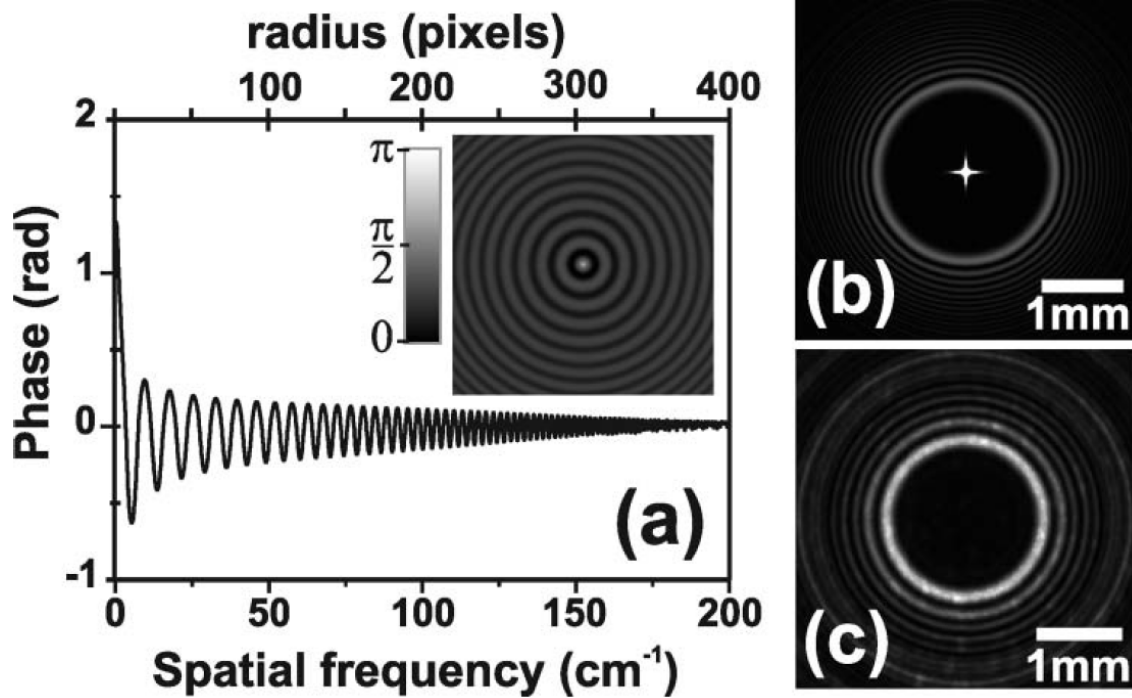


Fig 4-40 (a) Radial profile of the phase mask. Inset, phase mask (b) Theoretical intensity at the FT plane (in the center is the zero order) (c) Experimental intensity profile of the generated Airy ring as captured by the CCD at $z = 200\text{mm}$ (zero order blocked). Taken from [233].

4.2.5.2 Nonlinear autofocusing waves

In this section, we will numerically explore the nonlinear dynamics of high power abruptly autofocusing waves generated with Gaussian laser pulses, hereafter called high power ring-Airy wavepackets (HPRAW). We compare the attributes of HPRAW to those of Gaussian beams carrying the same power and identify a number of very useful and interesting features for practical applications [89, 234-236]. In addition, novel spatio-temporal mechanisms are observed in the high power regime, which are directly related to the RAW wavefront and the electron plasma generated at the focus.

Three different laser beam profiles were used in the simulations, a RAW and two Gaussian beams. All simulations were done in air at atmospheric pressure. The RAW electric field envelope is described by Eq.(4.2-21). The power content carried by the beam is numerically calculated by integration of the starting spatial intensity profile over the whole computational

box (5 mm radius). In our simulations we used $r_0 = 921 \mu\text{m}$, $w_0 = 61.4 \mu\text{m}$ and $\alpha = 0.05$, leading to $g(a) \approx -0.97$. We can see in Fig 4-41, that using these parameters the ring-Airy beam is auto-focusing at a position $z = 23.95 \text{ cm}$.

In order to study nonlinear propagation of HPRAWs, we compare their dynamics to that of Gaussian beams. Following a recent work [233], we consider two types of Gaussian beams that are equivalent to a given ring-Airy beam, i) the equivalent envelope Gaussian beam (EEGB) defined as the Gaussian beam with FWHM equal to the diameter of the ring Airy beam, and ii) the equivalent peak contrast Gaussian beam (ECGB) which in the linear regime reaches the same value of peak intensity contrast at the focus. Both beams are focused at the focus of the ring-Airy using a lens. Both of them carry the same power so the EEGB and the ECGB only differ by their beam width and initial peak intensity. In our simulations, the widths at $1/e^2$ radius of the EEGB and ECGB are $1738 \mu\text{m}$ and $855 \mu\text{m}$, respectively. Fig 4-41(b), (c) show the distribution of the beam amplitude of both Gaussian beams in the (r, z) plane. Regardless the spatial profile of the beams used the temporal profile in our simulations was in all cases Gaussian with a FWHM of 200 fs at a central wavelength of 800 nm.

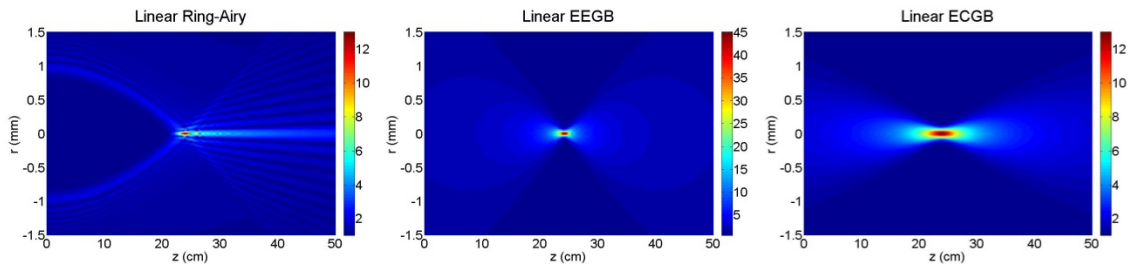


Fig 4-41 Radial distribution of electric field amplitude as a function of the propagation distance in the linear regime. a) ring-Airy wavepacket (RAW), b) Equivalent envelope Gaussian beam (EEGB), and c) Equivalent peak contrast Gaussian beam (ECGB).

4.2.5.2.1 Nonlinear focus shift

We performed numerical experiments by increasing the input power for all beams. As expected, the focus is shifted towards the laser source as the input power is increased. Fig 4-42(a) shows a comparison of the position of the nonlinear focus of the HPRAW with those obtained for the two equivalent Gaussian beams. The focal shift is measured from the linear focus obtained at low power, the position of which, $f = (4\pi w^3 / \lambda)^{1/2} R_0$, is known analytically by considering large HPRAWs as quasi-1D structures, *i.e.* the trajectory of the intensity maximum of the HPRAW in the linear regime is given by the quadratic acceleration for the 1D Airy beams [202, 233]:

$$R(z) = R_0 \sqrt{1 - (z/f)^2} \quad (4.2-22)$$

Interestingly, in the nonlinear regime, the HPRAW focus shifts in a significantly smaller amount compared to the two equivalent Gaussian beams as the beam power increases. For the HPRAW, the focus position moves from 24 cm to roughly 22 cm, while the input power is gradually increased up to $10 P_{cr}$. Further increase in power up to $24 P_{cr}$ seems to have negligible effect on the focus position. For both Gaussian beams, the focus shift is much larger than in the HPRAW case. Especially for the ECGB, the focus position is shifted down to 11 cm for $24 P_{cr}$, which is more than half the initial distance. For the EEGB, the focus shift is not as strong, but still reaches 6 cm, about 3 times more than for the HPRAW case. The difference between the two Gaussian beams is explained by the wider beam width for the EEGB and the fact that the nonlinear focus position is proportional to the Rayleigh length, *i.e.*, scales as w_0^2 [10, 25].

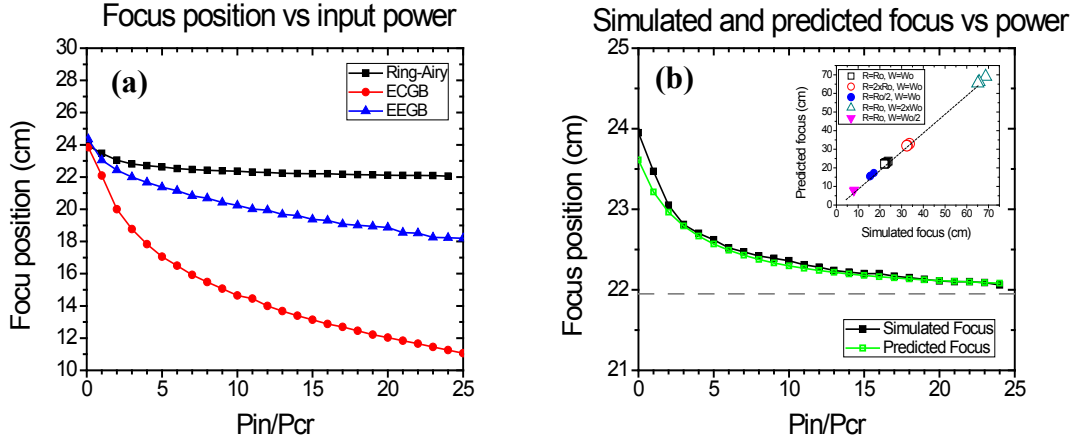


Fig 4-42 (a) Focus position as a function of the input power for the HPRAW (black squares), and the two Gaussian beams with equivalent contrast (red dots), and equivalent envelope (blue triangles). (b) Focus shift for the HPRAW as a function of the input power. Simulation results (black dots), Empirical formula (green line), f_{\min} empirical limiting focus position (blue line). Inset: comparison between expected and simulated focus position.

Since the spatial profile of HPRAW is significantly different from that of a typical Gaussian beam, Marburger's formula [25] cannot be used to predict the collapse distance. Following a similar approach, we attribute the focal shift towards the laser source to the optical Kerr effect. The collapse of a ring-Airy beam is described in two stages: (i) a quasi linear stage during which the ring structure shrinks over a propagation distance f_{\min} , and follows the parabolic trajectory Eq.(4.2-22). (ii) a second stage from f_{\min} to the collapse distance f_{HPRAW} , during which intensity of the HPRAW increases more abruptly and the assumption of a quasi 1D trajectory for the peak intensity no longer holds. This happens when the primary ring becomes sufficiently narrow to induce significant mutual attraction between opposite parts of the ring, in analogy with the mutual attraction and merging of two individual filaments induced by cross Kerr effects when they are separated by less than approximately three typical filament diameters. Pursuing this analogy, we assume that in the case of HPRAWs as well, non-linear effects will take over when the diameter of the primary ring is ~ 3 times larger than the diameter of a typical filament in the medium [171]. Using Eq.(4.2-22) we can estimate the propagation distance f_{\min} from the condition $R(f_{\min}) = 3w_{\alpha} / 2$:

$$f_{\min} = f \sqrt{1 - \frac{3w_\alpha}{2R_0}} \quad (4.2-23)$$

where $w_\alpha \cong 90 \mu\text{m}$ is the typical filament diameter in air and $R_0 \sim 980 \mu\text{m}$. In our case the ring-Airy focus in the linear regime is $f = 23.95 \text{ cm}$. For the second stage, a simple empirical formula that fits nicely the simulation results for the nonlinear focus shift as a function of the power P_{Ring} contained in the primary ring of the HPRAW is given by:

$$f_{\text{HPRAB}} = f - (f - f_{\min}) \left(1 - e^{-\sqrt{P_{\text{Ring}}/P_{cr}}}\right)^2 \quad (4.2-24)$$

where P_{cr} refers to the critical power of a Gaussian beam with the same central wavelength. The quantity $f - f_{\min}$ corresponds to the maximum shift that would be obtained at very large power, i.e. with an extremely abrupt collapse of the ring in the second stage, due to the optical Kerr effect. In order to confirm that Eq.(4.2-24) adequately predicts the non-linear focus position for different HPRAW, we have performed simulations for a range of HPRAWs parameters (different radius and width). The results of these simulations are compared with the predictions from Eq.(4.2-24) and are shown in the inset of Fig 4-42(b). In all cases Eq.(4.2-24) nicely predicts the focus position of HPRAWs.

4.2.5.2.2 Intensity clamping

The peak intensity of the HPRAW is shown in Fig 4-43(a) as a function of the propagation distance for five different input powers. As the input power is increased, the distribution of the peak intensity along the beam propagation changes significantly showing an escalating abrupt increase near the focus. For example, at $5 P_{cr}$, the first peak appears much more abruptly and high peak intensities extend over a longer propagation distance, compared to the linear case. Two additional features appear as the input power is increased. The first, emerging at moderate powers ($2 P_{cr} < P_{in} < 10 P_{cr}$), is a secondary wide (along z) peak of the

intensity profile which initially appears around $z = 40$ cm. This broad feature is strengthened and widened as the input power is increased and is transformed to a plateau at $P_{in} > 10 P_{cr}$. At these powers, the peak intensity is almost constant $\cong 2.5 \cdot 10^{13}$ W/cm² along the plateau, without significantly increasing as the input power is further increased. We attribute this effect to the presence of nonlinear losses, which are strong enough to limit the increase of the peak intensity. The resulting structure is a long filament similar to the filament obtained by propagation of a high power Gaussian beam [10], except that it results from the collapse of a ring Airy beam as detailed below.

The second feature in the peak intensity profile, appearing at very high input powers ($P_{in} > 20P_{cr}$) is an intense sharp peak emerging at the focus. This peak, in contrast to the plateau coming next, monotonically increases as the input power is increased. Fig 4-43(b) shows a detailed view of this sharp peak intensity for various input powers. When the input power is increased above $20P_{cr}$ a sharp peak is clearly visible in the focal region. As the input power is further increased at $24P_{cr}$, this peak gets even sharper reaching an intensity of $\sim 6.46 \times 10^{13}$ W/cm², indicating a peculiar ability of ring-Airy beams to surpass clamping effects at high input powers. Remarkably, this occurs for relatively low numerical apertures whereas reaching high intensity within a short filament requires tight focusing geometries [237]. To our knowledge, this type of intensity spike was obtained at similar numerical apertures only once in numerical simulations [238] and recently in experiments on filamentation in air [239]. In both cases, the spike was obtained at the end of the filament after significant reshaping of the initially Gaussian beam. In contrast, Airy–ring beams carry by construction a spatial phase that drives an energy flux organized to form a spike at the beginning of the filament.

This unique feature of the HPRAWs is clearly demonstrated in Fig 4-43(c) where the maximal peak intensity of equivalent Gaussian and HPRAWs are compared in a range of input powers up to $25 P_{cr}$. In contrast with Gaussian beams, the maximum intensity of the HPRAW keeps increasing as the input power is increased. Interestingly, this process is accelerated for input powers above $20 P_{cr}$, which is exactly the power value at which the sharp peak forms in the focal region. On the other hand, for both Gaussian beams we observe a similar behavior: In the case of the EEGB, the maximal intensity does not increase above $\sim 4.4 \times 10^{13}$ W/cm² at $(21 P_{cr})$.

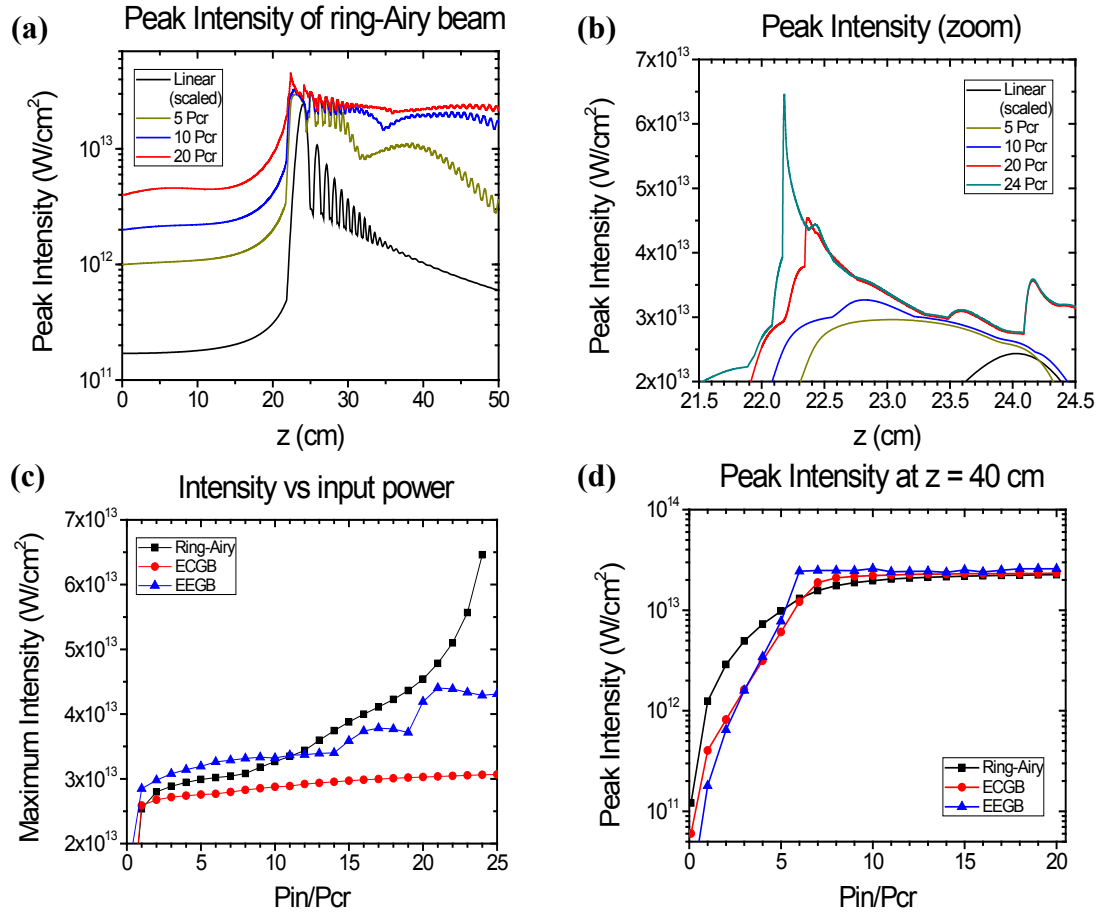


Fig 4-43 a) Peak Intensity distribution of the HPRAW vs. propagation distance for various input powers. c) Peak Intensity distribution in the focal area as a function of the propagation distance for various input powers c) Maximal peak intensity of the HPRAW, and the two Gaussian beams with equivalent contrast (red dots), and equivalent envelope as a function of the input power. d) Maximal peak intensity at the plateau region ($z = 40$ cm) as a function of the input power for the ring-Airy (black squares) and the EEGB (blue triangles)

This regularization of the maximum intensity is referred to as intensity clamping [171], and is usually interpreted as resulting from a balance between self-focusing and plasma defocusing. It is actually the combined action of nonlinear losses and plasma defocusing that effectively prevents the increase of the laser pulse intensity beyond a certain value (typically $3 - 4 \times 10^{13} W/cm^2$) [157]. Likewise, in the case of the ECGB, the maximal peak intensity is marginally increasing as the input power is increased, without exceeding $3 \times 10^{13} W/cm^2$. The smaller value is due to the lower numerical aperture of the ECGB compared to the EEGB beam.

Interestingly, this exciting behavior of the HPRAW is limited to the focal region. Beyond the focal region, nonlinear propagation of HPRAWs is similar to filamentation, like in the case of Gaussian beams, in the sense that the combined action of various non-linear effects regulates the peak intensity. This is clearly demonstrated in Fig 4-43(d) where the peak intensity of a HPRAW at the plateau region ($z = 40$ cm) is shown in comparison to two Gaussian beams, as a function of the input power. The peak intensity for all beams is practically identical for input powers above $5P_{cr}$.

An important question to answer for the purpose of predicting the presence of an intensity spike in a given experimental situation is: what is the mechanism that allows a paraxial beam such as the ring-Airy to surpass the combined limiting action of nonlinear effects and exhibit a region of non-regulated intensity in the highly non-linear regime?

4.2.5.2.3 Plasma focusing mechanism

In order to give an explanation for the intensity increase beyond the clamping value, we carefully examined the spatio-temporal evolution of the optical wave packet at the focal region. Fig 4-44 depicts the spatiotemporal distribution of the intensity (first row), generated plasma (second row) and overall refractive index modulation due to Kerr and plasma, for various propagation distances. We find that the annular shape of the intensity and excited plasma profiles results in a cooperative action of the optical Kerr effect and the plasma, to form the intense sharp peak, in contrast to the situation where the same effects are induced by a Gaussian beam and competing. In a first stage, due to the auto-focusing action, the ring structure shrinks until a central peak emerges, enhanced by cross-Kerr effects (Fig 4-44(a)). This position corresponds to $z = 22$ cm, which in our preceding analysis is referred as f_{min} (Eq.(4.2-23)). As the primary ring structure continues to shrink, the combined action of Kerr self-focusing towards the center and the plasma defocusing from the intense central peak leads to the formation of an intense narrow inner ring (Fig 4-44(b)). This narrow ring is accompanied by a thin plasma tubular structure. As a second stage of this process, this intense ring in turn collapses into a single intense spot. Fig 4-44(c) shows that the defocusing action of the tubular plasma structure splits spatially the trailing part of the wave packet creating conical structures in the space-time intensity

distribution. The cylindrical geometry of this splitting action results in redirecting energy towards the center, acting cooperatively with Kerr self-focusing and linear autofocusing. This unique spatiotemporal behavior leads to the very intense hot spot shown in Fig 4-44(d).

In the paraxial propagation regime, it is unusual that, the peak intensity of this hot spot is not immediately regulated by nonlinear losses (Fig 4-43(c)). The reason behind this behavior lies in the abruptness of the process. The spatiotemporal reshaping of the HPRAW is taking place on a too short propagation distance for allowing nonlinear losses to actually compensate the abrupt energy flux towards the beam center. It is clearly shown in Fig 4-43(b) and Fig 4-44 that the ring-Airy wave packet transfers its energy to the intense central peak in only 140 μm of propagation. Locally in the beam center, multiphoton absorption is not efficient until its

characteristic length $L_{MPA} = \frac{1}{(2\beta_K I^{K-1})}$ decreases below $\sim 140 \mu\text{m}$, as intensity grows. This

occurs for intensities exceeding $\sim 4 \times 10^{13} \text{W} / \text{cm}^2$ (for which $L_{MPA} = 181 \mu\text{m}$). In other words, increasing the power of a HPRAW leads to a ring-collapse bringing more energy to the central peak, without significantly changing the position for the nonlinear focus. This additional energy can be absorbed by MPA over the same distance only if the MPA rate increases, *i.e.* if the peak intensity reaches a substantially higher value. Beyond this intense spike, nonlinear losses and plasma defocusing regulate again the wave packet intensity of the central peak around the clamping value, resulting in the formation of a long filament.

As shown in Fig 4-43(c), this unique nonlinear spatiotemporal reshaping mechanism leads to higher and higher intensities as the input power is increased. This counterintuitive behavior results from the cooperating action of the plasma defocusing and Kerr self-focusing. As input power increases the plasma tubular structure (Fig 4-44(c)) becomes denser and thus more strongly defocusing. This stronger defocusing directs more energy towards the center leading to higher intensities. Does this process have a limit after which the peak intensity at the focus cannot be increased anymore? Actually this limit is reached when the medium is fully ionized, *i.e.* when one electron per molecule is liberated. At this point the excited plasma density saturates since the second level of ionization would require higher intensities in the primary ring, and so does the amount of energy that is redirected towards the center. Furthermore, at much higher input powers ($P_{in} > 100 P_{cr}$) the peak intensity of the ring Airy beam exceeds $2 - 3 \times 10^{13} \text{W} / \text{cm}^2$, even from an early stage of propagation ($z \approx 0$). The combined action of high nonlinear losses

and strong plasma defocusing then depletes the power of the ring-Airy beam and seriously reduces the fraction of energy reaching the focus.

As we can see in the last line of Fig 4-44, where the total refractive index in (r, t) is depicted, the beam is driven by the plasma induced negative Δn almost exclusively. This behavior is the key mechanism that shapes the wavepacket at the nonlinear autofocus, with Kerr and linear autofocusing being much weaker. Before this point however the Kerr contribution is strong, as can be seen at 4 mm and 2 mm before then onset of ionization (at $z = 22$ cm). This can be clearly seen in Fig 4-45, where the total refractive index is plotted again in the (r, t) plane at 21.6 cm, 21.8 cm and 22 cm.

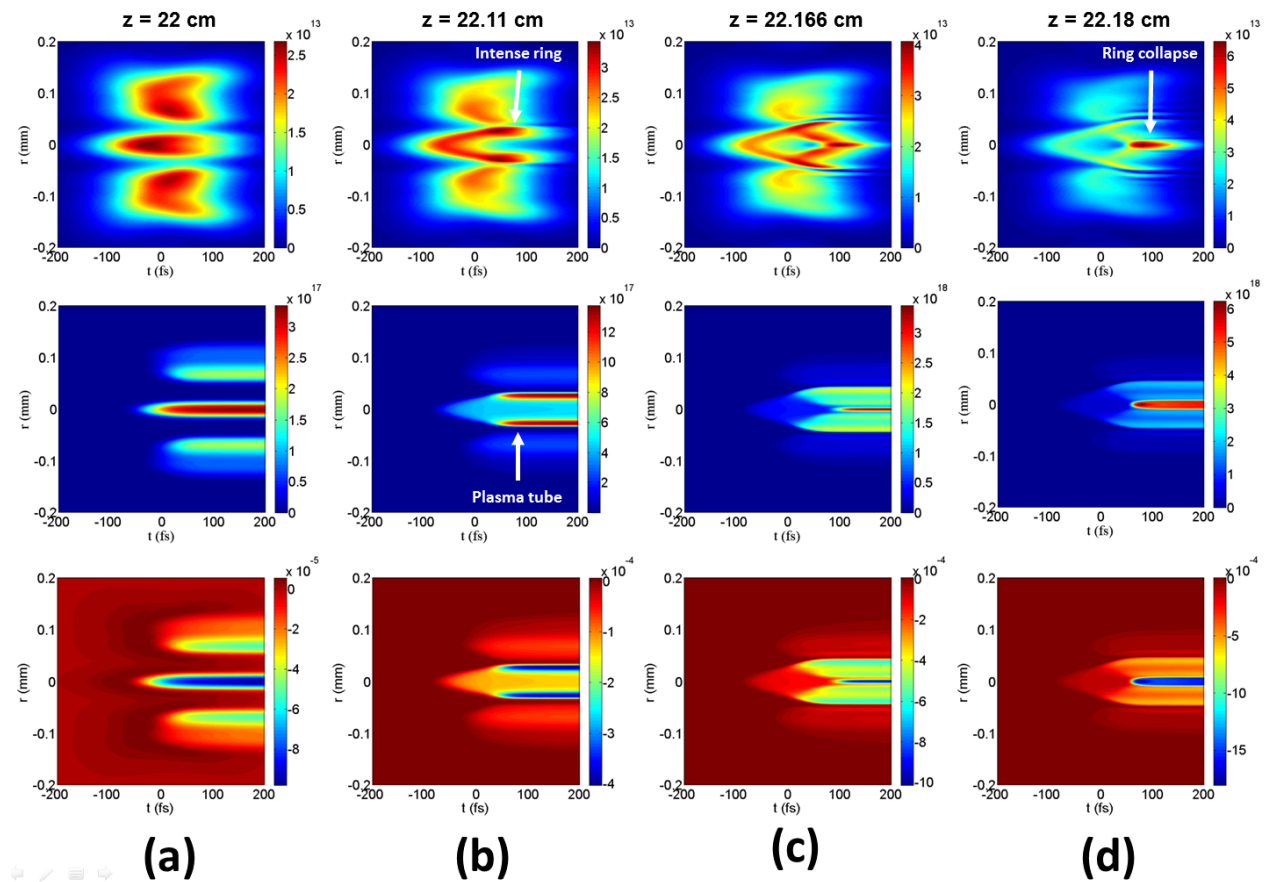


Fig 4-44 (Video_HPRAW_Focus.avi) spatiotemporal distribution of optical wavepacket intensity (first row), plasma density (second row), and total Δn (third row) of an HPRAW carrying 24 Pcr powers for various positions along the propagation.

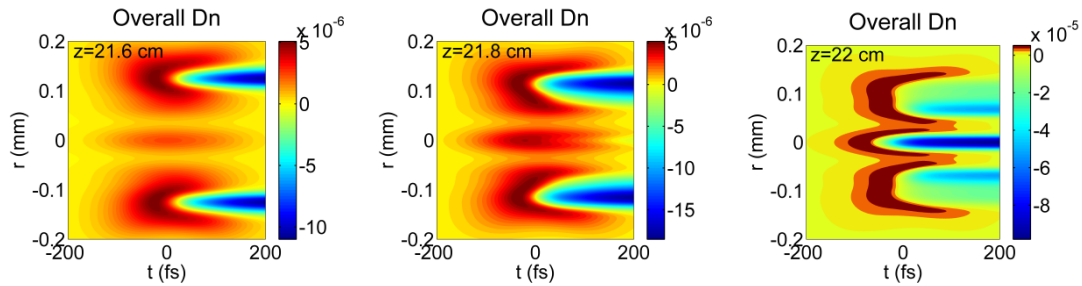


Fig 4-45 Total refractive index before the nonlinear autofocus position of the $24P_{cr}$ HPRAW.

4.2.5.2.4 Quasi light bullet formation

Besides the intense peak at the HPRAW focus, interesting spatiotemporal dynamics take place beyond the focal region. Fig 4-46 depicts the intensity isosurfaces for an EEGB (first row), an ECGB (second row) and HPRAW (third row) for various propagation distances beyond the nonlinear focus. Each of the three wave packets carries 10 critical powers. Due to the different nonlinear dynamics (Fig 4-42(a)) the actual focus position (denoted as 0 cm in Fig 4-46) along the propagation axis is different for each beam. The two Gaussian beams exhibit a typical spatiotemporal reshaping process extensively studied in the literature [10]. As shown in Fig 4-46 the initial Gaussian wavepacket is reshaped into a ring structure with an intense spot that is split in the temporal domain. We can clearly see that for both cases the space and time distributions of the wavepacket are constantly evolving in a complex way, as expected in filamentation of Gaussian pulses. The dynamic reshaping action of nonlinear effects diminishes after ~ 15 cm of propagation. After this point both Gaussian wavepackets spread due to linear diffraction and dispersion

On the other hand, as shown in the last line of Fig 4-46, the spatiotemporal dynamics of the ring-Airy beam are very different. The wavepacket has the form of a ring with an intense core in its center while no pulse splitting occurs in the temporal domain. This nonlinear quasi-light-bullet structure propagates without significant changes over 15 cm. Only after 18 cm of

propagation the nonlinear dynamics are starting to weaken and the ring-Airy wavepacket starts to spread due to the action of diffraction and dispersion.

Note that the ring that surrounds the ring-Airy intense peak at 15 cm after the focus, although resembles to the ring feature formed in the Gaussian wavepacket, is generated by different mechanisms. In the case of the nonlinear ring-Airy beam, the ring is sustained by the combination of the pre-organized energy flux from the tail to the main lobe of the Airy profile [232, 233] and light coming from the nonlinear focus, diffracted by the generated plasma. In the case of the Gaussian beam, the ring is generated by a spontaneous transformation of the Gaussian beam into a Bessel-like beam induced by nonlinear effects [240] and featured by conical emission [222]. The extreme case of two-photon absorption exemplify this type of ring formation [183].

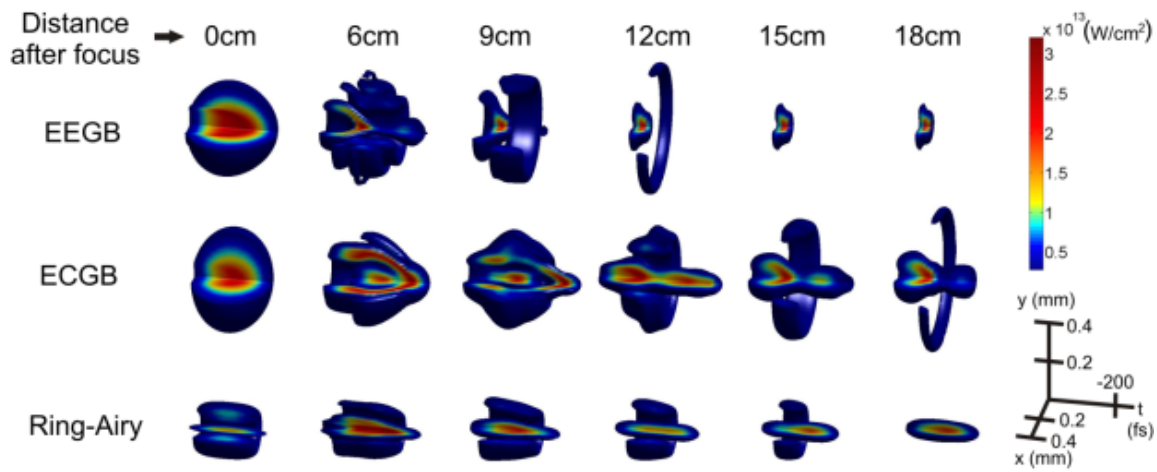


Fig 4-46 (Video_HPRAW_Bullet.avi) Intensity iso-surfaces for a EEGB (first row), a ECGB (second row) and ring-Airy wave packet (third row) at various positions along z after the nonlinear focus. Beam propagation direction is from left to right.

Summarizing this section, we have conducted a numerical study of the spatiotemporal dynamics of high power ring-Airy wave packets (HPRAW). Compared to Gaussians, nonlinear ring-Airy wave packets have unique and unexpected features for paraxial beams. They are able to locally surpass saturating nonlinear effects and exhibit a region of non-regulated intensity in the highly non-linear regime. Our simulations show that this behavior originates from the annular shape of the beam that leads to the cooperative action of plasma defocusing with Kerr self-

focusing and linear auto-focusing of the ring-Airy. Furthermore, the nonlinear focus shift, as the beam power is increased, is much smaller for a ring-Airy beam compared to equivalent Gaussian beams. By attributing this small shift to a Kerr induced ring-collapse, we proposed a simple semi-empirical formula that predicts the position of the non-linear focus for ring-Airy beams. Another exciting feature is that beyond the high intensity focal region, the ring-Airy wave packet is reshaped into a nonlinear quasi-light-bullet. These unique features make ring-Airy wavepackets very promising for applications of filaments that require high intensities, such as harmonic generation, laser micromachining, and remote sensing.

5. Appendix

In this section a simple derivation of the linear paraxial propagation equation will be derived directly from the Maxwell equations.

The Maxwell equations in differential form in SI units are:

$$\nabla \cdot \vec{D} = \rho \quad (5.1-1)$$

$$\nabla \cdot \vec{B} = 0 \quad (5.1-2)$$

$$\nabla \times \vec{E} = -\frac{\partial \vec{B}}{\partial t} \quad (5.1-3)$$

$$\nabla \times \vec{H} = \vec{J} + \frac{\partial \vec{D}}{\partial t} \quad (5.1-4)$$

and:

$$\vec{D} = \epsilon_0 \vec{E} + \vec{P} \quad (5.1-5)$$

$$\vec{B} = \mu_0 \vec{H} + \vec{M} \quad (5.1-6)$$

where:

\vec{E} : electric field

\vec{D} : electric displacement

\vec{P} : electric polarization

\vec{J} : current density

ϵ_0 : permittivity of vacuum

\vec{B} : magnetic field

\vec{H} : magnetic field strength

\vec{M} : magnetization

ρ : charge density

μ_0 : permeability of vacuum

For a non-magnetic material: $\vec{M} = 0 \Rightarrow \vec{H} = \frac{\vec{B}}{\mu_0}$. Eq. (5.1-4) can now be written as:

$$\nabla \times \vec{H} = \nabla \times \frac{\vec{B}}{\mu_0} = \vec{J} + \frac{\partial \vec{D}}{\partial t} \Rightarrow \nabla \times \vec{B} = \mu_0 \vec{J} + \mu_0 \frac{\partial \vec{D}}{\partial t} \quad (5.1-7)$$

We also assume for the time being that no electric polarization is present in the material $\vec{P} = 0$, and Eq. (5.1-5) can be simplified to

$$\vec{D} = \epsilon_0 \vec{E} \quad (5.1-8)$$

Using Eqs. (5.1-7) and (5.1-8), and the assumption that the propagation is taking place in a material without free charges ($\rho = 0$) and currents ($\vec{J} = 0$), the Maxwell equations can now be written in the following way:

$$\nabla \vec{D} = 0 \quad (5.1-9)$$

$$\nabla \vec{B} = 0 \quad (5.1-10)$$

$$\nabla \times \vec{E} = -\frac{\partial \vec{B}}{\partial t} \quad (5.1-11)$$

$$\nabla \times \vec{B} = \mu_0 \epsilon_0 \frac{\partial \vec{E}}{\partial t} \quad (5.1-12)$$

Starting from Eq. (5.1-11) we can write:

$$\begin{aligned} \nabla \times \vec{E} &= -\frac{\partial \vec{B}}{\partial t} \xrightarrow{\nabla \times} \nabla \times \nabla \times \vec{E} = \nabla \times \left(-\frac{\partial \vec{B}}{\partial t} \right) \\ \Rightarrow \nabla \times \nabla \times \vec{E} &= -\frac{\partial}{\partial t} (\nabla \times \vec{B}) \xrightarrow{(1.2-20)} \nabla \times \nabla \times \vec{E} = -\frac{\partial}{\partial t} \left(\mu_0 \epsilon_0 \frac{\partial \vec{E}}{\partial t} \right) \\ \Rightarrow \nabla \times \nabla \times \vec{E} &= -\mu_0 \epsilon_0 \frac{\partial^2 \vec{E}}{\partial t^2} \left. \begin{array}{l} \\ \text{for: } \frac{\partial}{\partial t} = \partial_t \text{ and } \frac{\partial^2}{\partial t^2} = \partial_t^2 \end{array} \right\} \Rightarrow \nabla \times \nabla \times \vec{E} = -\mu_0 \epsilon_0 \partial_t^2 \vec{E} \quad (5.1-13) \end{aligned}$$

From basic vector calculus we know that:

$$\nabla \times \nabla \times \vec{E} = \nabla(\nabla \cdot \vec{E}) - \nabla^2 \vec{E} \quad (5.1-14)$$

Also by definition:

$$\mu_0 \epsilon_0 \equiv \frac{1}{c^2} \quad (5.1-15)$$

By substituting Eqs. (5.1-14) and (5.1-15) in equation (5.1-13) we get:

$$\nabla(\nabla \cdot \vec{E}) - \nabla^2 \vec{E} = -\frac{1}{c^2} \partial_t^2 \vec{E} \quad (5.1-16)$$

We assume that the electric field remains linearly polarized, transverse to the propagation direction. This way the term $\nabla(\nabla \cdot \vec{E})$ can be neglected. Eq. (5.1-16) can now be written in scalar form simplifying calculations:

$$\nabla^2 E = \frac{1}{c^2} \partial_t^2 E \quad (5.1-17)$$

Equation (5.1-17) is the paraxial wave equation in vacuum.

In order to obtain the evolution equation along z we use the method of separation of variables of space and time:

$$E = A(r)T(t) \quad (5.1-18)$$

where $A(r)$ and $T(t)$ are function of r and t .

By substitution of Eq. (5.1-18) in Eq. (5.1-17) we get:

$$\nabla^2 A(r)T(t) = \frac{1}{c^2} \partial_t^2 A(r)T(t)$$

$$\frac{1}{A(r)} \nabla^2 A(r) = \frac{1}{c^2 T(t)} \partial_t^2 T(t) \quad (5.1-19)$$

Note that the left hand side (LHS) of Eq. (5.1-19) is a function of only r, while the right hand side (RHS) is a function of only t. This means that Eq. (5.1-19) can only be valid if both sides are constant for all values of r and t. Let this constant be a function of the wavenumber $k \equiv \frac{2\pi}{\lambda} = \frac{\omega}{c}$, so we can write:

$$\frac{1}{A(r)} \nabla^2 A(r) = \frac{1}{c^2 T(t)} \partial_t^2 T(t) = -k^2 \quad (5.1-20)$$

This gives us two separate equations, one spatial and one temporal:

$$\frac{1}{A(r)} \nabla^2 A(r) = -k^2 \Rightarrow (\nabla^2 + k^2) A(r) = 0 \quad (5.1-21)$$

$$\left. \begin{array}{l} \frac{1}{c^2 T(t)} \partial_t^2 T(t) = -k^2 \\ \omega = kc \end{array} \right\} \Rightarrow (\partial_t^2 + \omega^2) T(t) = 0 \quad (5.1-22)$$

To find the spatial evolution equation we will use the electric field envelope $\mathcal{E}(x, y, z)$

$$A(r, z) = \mathcal{E}(x, y, z) \exp[ikz] \quad (5.1-23)$$

where $r = \sqrt{x^2 + y^2}$.

By substitution of Eq. (5.1-23) in Eq. (5.1-21) we get:

$$(\nabla^2 + k^2)\mathcal{E}(x, y, z)e^{ikz} = 0 \quad (5.1-24)$$

$$\left. \begin{aligned} \Rightarrow \nabla^2 \mathcal{E}(x, y, z)e^{ikz} + k^2 \mathcal{E}(x, y, z)e^{ikz} = 0 \\ \nabla^2 = \frac{\partial^2}{\partial x^2} + \frac{\partial^2}{\partial y^2} + \frac{\partial^2}{\partial z^2} \end{aligned} \right\} \Rightarrow$$

$$\left. \begin{aligned} \Rightarrow \frac{\partial^2}{\partial x^2} \mathcal{E}(x, y, z)e^{ikz} + \frac{\partial^2}{\partial y^2} \mathcal{E}(x, y, z)e^{ikz} + \frac{\partial^2}{\partial z^2} \mathcal{E}(x, y, z)e^{ikz} + k^2 \mathcal{E}(x, y, z)e^{ikz} = 0 \\ \frac{\partial^2}{\partial x^2} + \frac{\partial^2}{\partial y^2} = \nabla_{\perp}^2 \end{aligned} \right\} \Rightarrow$$

$$\nabla_{\perp}^2 \mathcal{E}(x, y, z)e^{ikz} + \frac{\partial^2}{\partial z^2} \mathcal{E}(x, y, z)e^{ikz} + k^2 \mathcal{E}(x, y, z)e^{ikz} = 0 \quad (5.1-25)$$

However, the second term of the LHS can be written as:

$$\frac{\partial^2}{\partial z^2} \mathcal{E}(x, y, z)e^{ikz} = \frac{\partial}{\partial z} \left[\frac{\partial}{\partial z} (\mathcal{E}(x, y, z)e^{ikz}) \right] = \frac{\partial}{\partial z} \left[e^{ikz} \frac{\partial \mathcal{E}(x, y, z)}{\partial z} + \mathcal{E}(x, y, z) \frac{\partial e^{ikz}}{\partial z} \right] \Rightarrow$$

$$\frac{\partial^2}{\partial z^2} \mathcal{E}(x, y, z)e^{ikz} = \frac{\partial}{\partial z} \left[e^{ikz} \frac{\partial \mathcal{E}(x, y, z)}{\partial z} + ik e^{ikz} \mathcal{E}(x, y, z) \right] \Rightarrow$$

$$\frac{\partial^2}{\partial z^2} \mathcal{E}(x, y, z)e^{ikz} = \frac{\partial e^{ikz}}{\partial z} \frac{\partial \mathcal{E}(x, y, z)}{\partial z} + e^{ikz} \frac{\partial^2 \mathcal{E}(x, y, z)}{\partial z^2} + ik \left(\frac{\partial e^{ikz}}{\partial z} \mathcal{E}(x, y, z) + e^{ikz} \frac{\partial \mathcal{E}(x, y, z)}{\partial z} \right) \Rightarrow$$

$$\frac{\partial^2}{\partial z^2} \mathcal{E}(x, y, z)e^{ikz} = ik e^{ikz} \frac{\partial \mathcal{E}(x, y, z)}{\partial z} + e^{ikz} \frac{\partial^2 \mathcal{E}(x, y, z)}{\partial z^2} - k^2 e^{ikz} \mathcal{E}(x, y, z) + ik e^{ikz} \frac{\partial \mathcal{E}(x, y, z)}{\partial z} \Rightarrow$$

$$\frac{\partial^2}{\partial z^2} \mathcal{E}(x, y, z) e^{ikz} = 2ik e^{ikz} \frac{\partial \mathcal{E}(x, y, z)}{\partial z} + e^{ikz} \frac{\partial^2 \mathcal{E}(x, y, z)}{\partial z^2} - k^2 e^{ikz} \mathcal{E}(x, y, z) \quad (5.1-26)$$

By substituting Eq. (5.1-26) in Eq. (5.1-25) we get:

$$\nabla_{\perp}^2 \mathcal{E}(x, y, z) e^{ikz} + 2ik e^{ikz} \frac{\partial \mathcal{E}(x, y, z)}{\partial z} + e^{ikz} \frac{\partial^2 \mathcal{E}(x, y, z)}{\partial z^2} - k^2 e^{ikz} \mathcal{E}(x, y, z) + k^2 \mathcal{E}(x, y, z) e^{ikz} = 0 \Rightarrow$$

$$\nabla_{\perp}^2 \mathcal{E}(x, y, z) e^{ikz} + 2ik e^{ikz} \frac{\partial \mathcal{E}(x, y, z)}{\partial z} + e^{ikz} \frac{\partial^2 \mathcal{E}(x, y, z)}{\partial z^2} = 0 \quad (5.1-27)$$

Now we consider the slowly varying envelope approximation in space (SVEA), which was already mentioned in the previous section, and can now neglect the 3rd term of the RHS of Eq. (5.1-27) since:

$$\left| \frac{\partial^2 \mathcal{E}(x, y, z)}{\partial z^2} \right| \ll \left| \frac{\partial \mathcal{E}(x, y, z)}{\partial z} \right| \quad (5.1-28)$$

This will simplify Eq. (5.1-27) to:

$$\nabla_{\perp}^2 \mathcal{E}(x, y, z) e^{ikz} + 2ik e^{ikz} \frac{\partial \mathcal{E}(x, y, z)}{\partial z} = 0 \quad (5.1-29)$$

which, finally gives us the paraxial evolution equation for the spatial envelope of the electric field of a laser beam in vacuum:

$$\frac{\partial}{\partial z} \mathcal{E}(x, y, z) = \frac{i}{2k} \nabla_{\perp}^2 \mathcal{E}(x, y, z) \quad (5.1-30)$$

6. List of Electronic Files

Video_IDB.mov: Video clip of the 3D iso-surface plots of the intensity distribution for a standard filament (red) and Intense Dynamic Bullet (IDB) of the radial lattice. Plotting was done using as an iso-value the half of the peak intensity at each z position. Found in section 3.4.2.

Video_Flux1.mov: Video clip of the transverse flux along propagation distance for a nonlinear 2D Airy beam with moderate power. Found in section 4.2.4.1.5.

Video_Flux2.mov: Video clip of the transverse flux along propagation distance for a nonlinear 2D Airy beam with very high power. Found in section 4.2.4.1.5.

Video_HPRAW_Focus.avi: Video clip of the 2D spatiotemporal intensity and plasma density distribution of a high power ring-Airy wavepacket (HPRAW) carrying $24 P_{cr}$, along propagation distance. Plotting was done using a varying colormap. Found in section 4.2.5.2.3.

Video_HPRAW_Bullet.avi: Video clip of the 3D spatiotemporal intensity distribution of a high power ring-Airy wavepacket (HPRAW) and its equivalent contrast Gaussian beam (ECGB), both carrying $10 P_{cr}$, along propagation distance. Plotting was done using a constant colormap and a common iso-value of $2.75 \times 10^{12} W / cm^2$. Found in section 4.2.5.2.4.

code_linear_RZ.m: Matlab code solving the linear propagation equation in RZ geometry. Found in section 2.2.1.1.

code_linear_XZ.m: Matlab code solving the linear propagation equation in XZ geometry. Found in section 2.2.1.2.

code_nonlinear_RZ.m: Matlab code solving the nonlinear propagation equation in RZ geometry. Found in section 2.2.2.

7. Index of Symbols

E : Electric field

\mathcal{E} : Electric field envelope of a light beam

r : Radial coordinate

I_0 : Peak intensity in W / cm^2

w_0 : Beam waist at $1/e^2$ radius

t_p : pulse duration at $1/e^2$ radius

$\exp[x]$: the exponential function e^x

$k \equiv \frac{2\pi}{\lambda} = n(\omega) \frac{\omega}{c}$: wavenumber in the medium

$k_0 = \frac{2\pi}{\lambda_0}$: wavenumber in vacuum

λ : wavelength

λ_0 : denotes the central wavelength of broad spectrum laser pulse

$\omega_0 \equiv \frac{2\pi c}{\lambda_0}$: is the central frequency

$c \equiv \frac{1}{\sqrt{\mu_0 \epsilon_0}} = 299792458 \text{ m / s}$ is the speed of light in vacuum

$\pi \approx 3.1415926535$

$\nabla = \left(\frac{\partial}{\partial x}, \frac{\partial}{\partial y}, \frac{\partial}{\partial z} \right)$: Del vector differential operator, also called the Nabla operator

$\Delta = \nabla^2 = \frac{\partial^2}{\partial x^2} + \frac{\partial^2}{\partial y^2} + \frac{\partial^2}{\partial z^2}$: Laplacian differential operator in Cartesian coordinates

$\Delta_{\perp} = \nabla_{\perp}^2 = \frac{\partial^2}{\partial x^2} + \frac{\partial^2}{\partial y^2}$: Spatial Laplacian operator in Cartesian coordinates

$\Delta_r = \frac{\partial^2}{\partial r^2} + \frac{1}{r} \frac{\partial}{\partial r}$: Spatial Laplacian operator in cylindrical coordinates

\vec{E} : electric field

\vec{B} : magnetic field

\vec{D} : electric displacement

\vec{H} : magnetic field strength

\vec{P} : electric polarization

\vec{M} : magnetization

\vec{J} : current density

ρ : charge density

ϵ_0 : permittivity of vacuum

μ_0 : permeability of vacuum

$\partial_t = \frac{\partial}{\partial t}$: first order partial derivative

$\partial_t^2 = \frac{\partial^2}{\partial t^2}$: second order partial derivative

$v_{group} = \frac{\partial \omega(k)}{\partial k}$: group velocity

$v_{phase} = \frac{\omega(k)}{k}$: phase velocity

$\frac{\partial^2 k(\omega)}{\partial \omega^2} = \frac{\partial}{\partial \omega} \left(\frac{1}{v_{group}} \right) = k''$: Group Velocity Dispersion (GVD)

$n^2(\lambda) = 1 + \sum_i \frac{B_i \lambda^2}{\lambda^2 - \lambda_i^2}$: Sellmeier dispersion formula

n_0 : linear refractive index

n_2 : nonlinear refractive index

$L_{Diff} = \frac{k w_0^2}{2} = \frac{\pi n_0 w_0^2}{\lambda_0}$: characteristic length for diffraction

$L_{GVD} = \frac{t^2}{2k_0''}$: characteristic length for dispersion

$L_{Kerr} = \frac{1}{k_0 n_2 I}$: characteristic length for Kerr

$L_{Shock} = \frac{cT}{n_2 I}$: characteristic length for Shock

$L_{Plasma} = \frac{2}{\sigma \omega_0 \rho \tau}$: characteristic length for plasma defocusing

$L_{ABS} = \frac{2}{\sigma\rho}$: characteristic length for plasma absorption

$L_{Latt} = \frac{1}{k_0\Delta n}$: characteristic length related to a periodic lattice

P_{cr} : critical power for self-focusing

L_c : collapse distance

$\chi^{(1)}$: linear optical susceptibility

$\chi^{(2)}, \chi^{(3)}, \dots$: nonlinear optical susceptibilities of a nonlinear medium

$h = 4.1356673310 \times 10^{-15} \text{ eV} \cdot \text{s}$: Planck constant

$\hbar = \frac{h}{2\pi} = 6.58211928 \times 10^{-16} \text{ eV} \cdot \text{s}$: reduced Planck constant

$\langle X \rangle$ integer part of X

$E_{photon} = \hbar\omega$: photon energy

$\rho_c \equiv \frac{\epsilon_0 m_e \omega_0^2}{e^2}$: critical plasma density at which it becomes opaque

ρ_n : density of neutral atoms or molecules

$m_e = 9.1093829140 \times 10^{-31} \text{ kg}$: electron mass

$e = -1.602176565 \cdot 10^{-19} \text{ C}$: electron charge

$NA = \frac{w_0 / 2}{f} n$: numerical aperture of a beam

σ_K : MPI coefficient

$\beta_K = K \hbar \omega_0 \rho_{at} \sigma_K$: MPA coefficient

$\sigma \equiv \frac{e^2 \tau_c}{\epsilon_0 m_e c n_0 (1 + \omega^2 \tau_c^2)}$: cross section for inverse Bremsstrahlung

τ_c : characteristic time for collisions

τ_{rec} : characteristic time for electron recombination

$I \equiv \frac{\epsilon_0 n_0 c}{2} |\mathcal{E}|^2$: Intensity as a function of the envelope

$$\text{Numerical Grids: } \left\{ \begin{array}{l}
 \text{Radial:} \quad r_j = j\Delta r, \quad j = 1, \dots, N_{\perp} \quad \text{where: } N_{\perp} = \frac{r_{\max}}{\Delta r} \\
 \text{Longitudinal:} \quad z_n = n\Delta z, \quad n = 1, \dots, N \quad \text{where: } N = \frac{z_{\max}}{\Delta z} \\
 \text{Temporal:} \quad t_l = t_0 + l\Delta t \\
 \text{Frequency:} \quad \omega_l = \omega_0 + l\Delta \omega
 \end{array} \right.$$

8. Index of Abbreviations

FWHM: Full Width at Half Maximum

SVEA: Slowly Varying Envelope Approximation

LHS: Left Hand Side

RHS: Right Hand Side

GVD: Group Velocity Dispersion

SHG: Second Harmonic Generation

THG: Third Harmonic Generation

CPA: Chirped Pulse Amplification

SPM: Self-Phase Modulation

XPM: Cross Phase Modulation

MPI: Multi-Photon Ionization

MPA: Multi-Photon Absorption

NA: Numerical Aperture

LIDAR: Light Detection And Ranging

LIBS: Laser Induced Breakdown Spectroscopy

FDM: Forward Differencing Method

CDM: Central Differencing Method

C-N: Crank – Nicolson

2D: 2 Dimensional

3D: 3 Dimensional

4D: 4 Dimensional

IDB: Intense Dynamic Bullet

ODE: Ordinary Differential Equation

OPL: Optical Path Length

SF: Self-induced Filament

LF: Lattice Filament

BS: Beam Splitter

NLSE: Non-Linear Schrödinger Equation

NAB: Nonlinear Airy Beam

PMMA: PolyMethyl-MethAcrylate

NLLs: NonLinear Losses

PBB: Pulsed Bessel Beam

FEAB: Finite Energy Airy Beam

NAB: Nonlinear Airy Beam

SLM: Spatial Light Modulator

RAW: Ring-Airy Wavepacket

HPRAW: High Power Ring-Airy Wavepacket

ECGB: Equivalent Contrast Gaussian Beam

EEGB: Equivalent Envelope Gaussian Beam

9. Physical Parameters and coefficients

Table 2 Table of physical parameters for $\lambda = 800$ nm, 35 fs duration, and $E_{800nm} = 1.5498$ eV.

	Air	Water	Fused Silica	BK7
n_0	1	1.33	1.45332 [241]	1.5108
n_2	$3.2 \times 10^{-19} \text{ cm}^2 / W$ [17, 18]	$1.6 \times 10^{-16} \text{ cm}^2 / W$ [19, 20]	$3.2 \times 10^{-16} \text{ cm}^2 / W$ [21]	$\sim 2 \times 10^{-16} \text{ cm}^2 / W$
P_{cr}	3.2 GW	4 MW	2 MW	~ 3.37 MW
k_0''	$0.2 \text{ fs}^2 / \text{cm}$	$248 \text{ fs}^2 / \text{cm}$	$360 \text{ fs}^2 / \text{cm}$ [241]	$506 \text{ fs}^2 / \text{cm}$
U_i	~ 12.063 eV	6.9 eV [242]	9 eV [243-247]	~ 4 eV
K	8	5	6	3
σ_K	$3.4 \times 10^{-96} \text{ cm}^{16} / W^8 / s$ [10, 133, 134]	$1 \times 10^{-54} \text{ cm}^{10} / W^5 / s$ [20, 165]	$1.5 \times 10^{-71} \text{ s}^{-1} \text{ cm}^{12} / W^6$ [245]	$2.4 \times 10^{-27} \text{ cm}^6 W^3 / s$
β_K	$4 \times 10^{-95} \text{ cm}^{13} / W^7$	$8.3 \times 10^{-50} \text{ cm}^7 / W^4$	$\beta_K = K \hbar \omega_0 \rho_{at} \sigma_K$	
ρ_{nt}	$\sim 5 \times 10^{18} \text{ cm}^{-3}$	$\sim 6.6 \times 10^{22} \text{ cm}^{-3}$	$2.1 \times 10^{22} \text{ cm}^{-3}$ [166]	$\sim 2.1 \times 10^{28} \text{ cm}^{-3}$
τ_{rec}	$\gg 35$ fs	~ 150 fs [248]	150 fs [249]	~ 150 fs
σ	$\sim 5.5 \times 10^{-20} \text{ cm}^{-2}$	$\sigma \equiv \frac{e^2 \tau_c}{\epsilon_0 m_e c n_0 (1 + \omega^2 \tau_c^2)}$		$\sim 5.23 \times 10^{-22} \text{ cm}^{-2}$
τ_C	~ 350 fs	10 fs [230]	1 fs [250]	~ 5.5 fs

Dispersion coefficients for Eq.(1.2-10), Eq.(1.2-11), and Eq.(1.2-12). From [251].

- **Air:**

$$n(\lambda) - 1 = 10^{-6} \left(A + \frac{B}{C - \lambda^{-2}} + \frac{D}{E - \lambda^{-2}} \right)$$

A = 80.6051; B = 24809.9; C = 132.274; D = 174.557; E = 39.3295.

From [5]

- **Noble Gases:**

$$n^2(\lambda) - 1 = A + \frac{B}{\lambda^2} + \frac{C}{\lambda^4} + \frac{D}{\lambda^6} + \frac{E}{\lambda^8} + \frac{F}{\lambda^{10}}$$

- **He:**

$$A = 6.927 \times 10^{-5}; B = 2.24 \times 10^{-8}; C = 5.94 \times 10^{-6}; D = 1.72 \times 10^{-8}; E = 0; F = 0;$$

- **Ne:**

$$A = 1.335 \times 10^{-4}; B = 2.24 \times 10^{-3}; C = 8.06 \times 10^{-6}; D = 3.56 \times 10^{-8}; E = 0; F = 0;$$

- **Ar:**

$$A = 5.547 \times 10^{-4}; B = 5.15 \times 10^{-3}; C = 4.19 \times 10^{-5}; D = 4.09 \times 10^{-7}; E = 4.32 \times 10^{-9}; F = 0;$$

- **Kr:**

$$A = 8.377 \times 10^{-4}; B = 6.7 \times 10^{-3}; C = 8.84 \times 10^{-5}; D = 1.49 \times 10^{-6}; E = 2.74 \times 10^{-8};$$
$$F = 5.1 \times 10^{-10};$$

- **Xe:**

$$A = 1.366 \times 10^{-4}; B = 9.02 \times 10^{-3}; C = 1.81 \times 10^{-4}; D = 4.89 \times 10^{-6}; E = 1.45 \times 10^{-7};$$
$$F = 4.34 \times 10^{-9};$$

- **Liquids and condensed media:**

$$n^2(\lambda) = A + \frac{B_1\lambda^2}{\lambda^2 - \lambda_1^2} + \frac{B_2\lambda^2}{\lambda^2 - \lambda_2^2} + \frac{B_3\lambda^2}{\lambda^2 - \lambda_3^2} + D\lambda^2 + F\lambda$$

- **Water**

$$\lambda_1^2 = 1.49119 \times 10^{-2}; B_1 = 6.44277 \times 10^{-3} / \lambda_1^2; A = 1.76004457 - B_1; D = -1.54182 \times 10^{-2};$$

$$F = 4.03368 \times 10^{-3}$$

- **Fused silica:**

$$\lambda_1 = 0.0684043; \lambda_2 = 0.1162414; \lambda_3 = 9.896161; A = 1; B_1 = 0.6961663; B_2 = 0.4079426;$$

$$B_3 = 0.8974794; D = 0; F = 0$$

- **BK7:**

$$\lambda_1^2 = 6.00069867 \times 10^{-3}; \lambda_2^2 = 2.00179144 \times 10^{-2}; \lambda_3^2 = 1.03560653 \times 10^2; A = 1;$$

$$B_1 = 1.03961212; B_2 = 2.31792344 \times 10^{-1}; B_3 = 1.01046945; D = 0; F = 0$$

10. List of Publications

1. A. Averchi, D. Faccio, E. Rubino, H. V. Lukner, P. Panagiotopoulos, P. A. Loukakos, S. Tzortzakis, A. Couairon, and P. D. Trapani, "Linear X-wave generation by means of cross-phase modulation in Kerr media," [Opt. Lett. **33**, 3028-3030 \(2008\)](#).
2. D. Abdollahpour, P. Panagiotopoulos, M. Turconi, O. Jedrkiewicz, D. Faccio, P. Di Trapani, A. Couairon, D. Papazoglou, and S. Tzortzakis, "Long spatio-temporally stationary filaments in air using short pulse UV laser Bessel beams," [Opt. Express **17**, 5052-5057 \(2009\)](#).
3. P. Panagiotopoulos, N. K. Efremidis, D. G. Papazoglou, A. Couairon, and S. Tzortzakis, "Tailoring the filamentation of intense femtosecond laser pulses with periodic lattices," [Phys. Rev. A **82**, 061803\(R\) \(2010\)](#).
4. P. Panagiotopoulos, A. Couairon, N. K. Efremidis, D. G. Papazoglou, and S. Tzortzakis, "Intense dynamic bullets in a periodic lattice," [Opt. Express **19**, 10057-10062 \(2011\)](#).
5. A. Lotti, D. Faccio, A. Couairon, D. G. Papazoglou, P. Panagiotopoulos, D. Abdollahpour, and S. Tzortzakis, "Stationary nonlinear Airy beams," [Phys. Rev. A **84**, 021807 \(2011\)](#).
6. P. Panagiotopoulos, D. Abdollahpour, A. Lotti, A. Couairon, D. Faccio, D.G. Papazoglou, and S. Tzortzakis, "Nonlinear propagation dynamics of finite energy Airy beams", [Phys. Rev. A. **86**, 013842 \(2012\)](#).
7. M. Bellec, P. Panagiotopoulos, D. G. Papazoglou, N. K. Efremidis, A. Couairon, and S. Tzortzakis, " Observation and optical tailoring of photonic lattice filaments", [Phys. Rev. Lett. **109**, 113905 \(2012\)](#).
8. S. Suntsov, D. Abdollahpour, D. G. Papazoglou, P. Panagiotopoulos, A. Couairon, and S. Tzortzakis, "Tailoring femtosecond laser pulse filamentation in water using quasi-periodic plasma lattices", submitted for publication.
9. P. Panagiotopoulos, D. G. Papazoglou, A. Couairon, S. Tzortzakis, " Nonlinear propagation of abruptly autofocusing beams", to be submitted.

11. References

1. E. Hecht, *Optics* (Addison Wesley, 2002).
2. T. Brabec, and F. Krausz, "Nonlinear Optical Pulse Propagation in the Single-Cycle Regime," *Phys. Rev. Lett.* **78**, 3282-3285 (1997).
3. B. E. A. Saleh, and M. C. Teich, *Fundamentals of Photonics* (Wiley, 2007).
4. W. Sellmeier, "Zur Erklärung der abnormen Farbenfolge im Spectrum einiger Substanzen," *Ann. Phys. Chem.* **219**, 272-282 (1871).
5. E. R. Peck, and K. Reeder, "Dispersion of Air," *J. Opt. Soc. Am.* **62**, 958-962 (1972).
6. A. Dalgarno, and A. E. Kingston, "The Refractive Indices and Verdet Constants of the Inert Gases," *Proceedings of the Royal Society of London. Series A. Mathematical and Physical Sciences* **259**, 424-431 (1960).
7. P. A. Franken, A. E. Hill, C. W. Peters, and G. Weinreich, "Generation of Optical Harmonics," *Phys. Rev. Lett.* **7**, 118-119 (1961).
8. T. H. Maiman, "Optical and Microwave-Optical Experiments in Ruby," *Phys. Rev. Lett.* **4**, 564-566 (1960).
9. T. H. Maiman, "Stimulated Optical Radiation in Ruby," *Nature* **187**, 493-494 (1960).
10. A. Couairon, and A. Mysyrowicz, "Femtosecond filamentation in transparent media," *Phys. Rep.* **441**, 47-189 (2007).
11. D. Strickland, and G. Mourou, "Compression of amplified chirped optical pulses," *Opt. Commun.* **56**, 219-221 (1985).
12. R. Boyd, *Nonlinear Optics* (2008).
13. G. Agrawal, *Nonlinear Fiber Optics* (Academic Press, 2001).
14. Y. R. Shen, *Principles of Nonlinear Optics* (Wiley, 2002).
15. J. A. Armstrong, N. Bloembergen, J. Ducuing, and P. S. Pershan, "Interactions between Light Waves in a Nonlinear Dielectric," *Phys. Rev.* **127**, 1918-1939 (1962).
16. P. Weinberger, "John Kerr and his effects found in 1877 and 1878," *Philos. Mag. Lett.* **88**, 897-907 (2008).
17. E. T. J. Nibbering, G. Grillon, M. A. Franco, B. S. Prade, and A. Mysyrowicz, "Determination of the inertial contribution to the nonlinear refractive index of air, N₂, and O₂ by use of unfocused high-intensity femtosecond laser pulses," *J. Opt. Soc. Am. B* **14**, 650-660 (1997).
18. Y. Shimoji, A. T. Fay, R. S. F. Chang, and N. Djeu, "Direct measurement of the nonlinear refractive index of air," *J. Opt. Soc. Am. B* **6**, 1994-1998 (1989).
19. W. L. Smith, P. Liu, and N. Bloembergen, "Superbroadening in H₂O and D₂O by self-focused picosecond pulses from a YAlG: Nd laser," *Phys. Rev. A* **15**, 2396-2403 (1977).
20. S. Minardi, A. Gopal, M. Tatarakis, A. Couairon, G. Tamosauskas, R. Piskarskas, A. Dubietis, and P. Di Trapani, "Time-resolved refractive index and absorption mapping of light-plasma filaments in water," *Opt. Lett.* **33**, 86-88 (2008).
21. T. Olivier, F. Billard, and H. Akhouayri, "Nanosecond Z-scan measurements of the nonlinear refractive index of fused silica," *Opt. Express* **12**, 1377-1382 (2004).
22. M. Sheik-bahae, A. A. Said, and E. W. Van Stryland, "High-sensitivity, single-beam n₂ measurements," *Opt. Lett.* **14**, 955-957 (1989).
23. P. L. Kelley, "Self-Focusing of Optical Beams," *Phys. Rev. Lett.* **15**, 1005-1008 (1965).
24. R. W. Boyd, S. G. Lukishova, and Y. R. Shen, *Self-focusing: Past and Present* (2009).

25. J. H. Marburger, "Self-focusing: Theory," *Prog. Quantum Electron.* **4**, Part 1, 35-110 (1975).
26. G. Fibich, and A. L. Gaeta, "Critical power for self-focusing in bulk media and in hollow waveguides," *Opt. Lett.* **25**, 335-337 (2000).
27. E. L. Dawes, and J. H. Marburger, "Computer Studies in Self-Focusing," *Phys. Rev.* **179**, 862-868 (1969).
28. P. Panagiotopoulos, A. Couairon, N. K. Efremidis, D. G. Papazoglou, and S. Tzortzakis, "Intense dynamic bullets in a periodic lattice," *Opt. Express* **19**, 10057-10062 (2011).
29. A. Couairon, S. Tzortzakis, L. Berge, M. Franco, B. Prade, and A. Mysyrowicz, "Infrared femtosecond light filaments in air: simulations and experiments," *J. Opt. Soc. Am. B* **19**, 1117-1131 (2002).
30. M. D. Feit, and J. A. J. Fleck, "Effect of refraction on spot-size dependence of laser-induced breakdown," *Journal Name: Appl. Phys. Lett.*, v. 24, no. 4, pp. 169-172; Other Information: Orig. Receipt Date: 30-JUN-74, Medium: X (1974).
31. Y. P. Rayzer, "Heating of a gas by a powerful light pulse.," *Sov. Phys. JETP-USSR* **21** (1965).
32. F. DeMartini, C. H. Townes, T. K. Gustafson, and P. L. Kelley, "Self-Steepening of Light Pulses," *Phys. Rev.* **164**, 312-323 (1967).
33. J. E. Rothenberg, "Space-time focusing: breakdown of the slowly varying envelope approximation in the self-focusing of femtosecond pulses," *Opt. Lett.* **17**, 1340-1342 (1992).
34. G. Fibich, and G. C. Papanicolaou, "Self-focusing in the presence of small time dispersion and nonparaxiality," *Opt. Lett.* **22**, 1379-1381 (1997).
35. J. K. Ranka, and A. L. Gaeta, "Breakdown of the slowly varying envelope approximation in the self-focusing of ultrashort pulses," *Opt. Lett.* **23**, 534-536 (1998).
36. S. L. Chin, S. A. Hosseini, W. Liu, Q. Luo, F. Theberge, N. Akozbek, A. Becker, V. P. Kandidov, O. G. Kosareva, and H. Schroeder, "The propagation of powerful femtosecond laser pulses in optical media: physics, applications, and new challenges," *Can. J. Phys.* **83**, 863-905 (2005).
37. P. Sprangle, J. R. Peñano, and B. Hafizi, "Propagation of intense short laser pulses in the atmosphere," *Phys. Rev. E* **66**, 046418 (2002).
38. F. Courvoisier, V. Boutou, J. Kasparian, E. Salmon, G. Mejean, J. Yu, and J. P. Wolf, "Ultraintense light filaments transmitted through clouds," *Appl. Phys. Lett.* **83**, 213-215 (2003).
39. M. Kolesik, and J. V. Moloney, "Self-healing femtosecond light filaments," *Opt. Lett.* **29**, 590-592 (2004).
40. A. Dubietis, E. Kucinskas, G. Tamosauskas, E. Gaizauskas, M. A. Porras, and P. Di Trapani, "Self-reconstruction of light filaments," *Opt. Lett.* **29**, 2893-2895 (2004).
41. W. Liu, J. F. Gravel, F. Theberge, A. Becker, and S. L. Chin, "Background reservoir: its crucial role for long-distance propagation of femtosecond laser pulses in air," *Appl. Phys. B* **80**, 857-860 (2005).
42. M. Mlejnek, M. Kolesik, J. V. Moloney, and E. M. Wright, "Optically turbulent femtosecond light guide in air," *Phys. Rev. Lett.* **83**, 2938-2941 (1999).
43. G. Mechain, C. D'Amico, Y. B. Andre, S. Tzortzakis, M. Franco, B. Prade, A. Mysyrowicz, A. Couairon, E. Salmon, and R. Sauerbrey, "Range of plasma filaments created in air by a multi-terawatt femtosecond laser," *Opt. Commun.* **247**, 171-180 (2005).
44. M. Rodriguez, R. Bourayou, G. Méjean, J. Kasparian, J. Yu, E. Salmon, A. Scholz, B. Stecklum, J. Eislöffel, U. Laux, A. P. Hatzes, R. Sauerbrey, L. Wöste, and J.-P. Wolf, "Kilometer-range nonlinear propagation of femtosecond laser pulses," *Phys. Rev. E* **69**, 036607 (2004).
45. G. Méchain, "Study of filamentation of femtosecond laser pulses in air.," (École Polytechnique, Palaiseau, France, 2005).
46. A. Braun, G. Korn, X. Liu, D. Du, J. Squier, and G. Mourou, "Self-channeling of high-peak-power femtosecond laser-pulses in air," *Opt. Lett.* **20**, 73-75 (1995).

47. J. Kasparian, R. Sauerbrey, and S. L. Chin, "The critical laser intensity of self-guided light filaments in air," *Appl. Phys. B* **71**, 877-879 (2000).
48. A. Becker, N. Akozbek, K. Vijayalakshmi, E. Oral, C. M. Bowden, and S. L. Chin, "Intensity clamping and re-focusing of intense femtosecond laser pulses in nitrogen molecular gas," *Appl. Phys. B* **73**, 287-290 (2001).
49. F. Vidal, and T. W. Johnston, "Electromagnetic Beam Breakup: Multiple Filaments, Single Beam Equilibria, and Radiation," *Phys. Rev. Lett.* **77**, 1282-1285 (1996).
50. V. P. Kandidov, N. Akozbek, M. Scalora, O. G. Kosareva, A. V. Nyakk, Q. Luo, S. A. Hosseini, and S. L. Chin, "Towards a control of multiple filamentation by spatial regularization of a high-power femtosecond laser pulse," *Appl. Phys. B* **80**, 267-275 (2005).
51. G. Fibich, S. Eisenmann, B. Ilan, and A. Zigler, "Control of multiple filamentation in air," *Opt. Lett.* **29**, 1772-1774 (2004).
52. A. Dubietis, G. Tamogauskas, G. Fibich, and B. Ilan, "Multiple filamentation induced by input-beam ellipticity," *Opt. Lett.* **29**, 1126-1128 (2004).
53. G. Mechain, A. Couairon, M. Franco, B. Prade, and A. Mysyrowicz, "Organizing multiple femtosecond filaments in air," *Phys. Rev. Lett.* **93**, 035003 (2004).
54. G. Mechain, G. Mejean, R. Ackermann, P. Rohwetter, Y. B. Andre, J. Kasparian, B. Prade, K. Stelmaszczyk, J. Yu, E. Salmon, W. Winn, L. A. Schlie, A. Mysyrowicz, R. Sauerbrey, L. Woste, and J. P. Wolf, "Propagation of fs TW laser filaments in adverse atmospheric conditions," *Appl. Phys. B* **80**, 785-789 (2005).
55. R. R. Alfano, *The Supercontinuum Laser Source* (Springer, 2006).
56. J. E. Greivankamp, *Field Guide to Geometrical Optics* (SPIE Field Guides, 2004).
57. V. P. Kandidov, I. S. Golubtsov, and O. G. Kosareva, "Supercontinuum sources in a high-power femtosecond laser pulse propagating in liquids and gases," *Quantum Electron.* **34**, 348-354 (2004).
58. S. Petit, A. Talebpour, A. Proulx, and S. L. Chin, "Some consequences during the propagation of an intense femtosecond laser pulse in transparent optical media: a strongly deformed white-light laser," *Laser Phys.* **10**, 93-100 (2000).
59. J. Kasparian, R. Sauerbrey, D. Mondelain, S. Niedermeier, J. Yu, J. P. Wolf, Y. B. Andre, M. Franco, B. Prade, S. Tzortzakis, A. Mysyrowicz, M. Rodriguez, H. Wille, and L. Woste, "Infrared extension of the supercontinuum generated by femtosecond terawatt laser pulses propagating in the atmosphere," *Opt. Lett.* **25**, 1397-1399 (2000).
60. I. Golub, "Optical characteristics of supercontinuum generation," *Opt. Lett.* **15**, 305-307 (1990).
61. E. T. J. Nibbering, P. F. Curley, G. Grillon, B. S. Prade, M. A. Franco, F. Salin, and A. Mysyrowicz, "Conical emission from self-guided femtosecond pulses in air," *Opt. Lett.* **21**, 62-64 (1996).
62. O. G. Kosareva, V. P. Kandidov, A. Brodeur, C. Y. Chien, and S. L. Chin, "Conical emission from laser-plasma interactions in the filamentation of powerful ultrashort laser pulses in air," *Opt. Lett.* **22**, 1332-1334 (1997).
63. O. G. Kosareva, V. P. Kandidov, A. Brodeur, and S. L. Chin, "From filamentation in condensed media to filamentation in gases," *J. Nonlinear Opt. Phys.* **6**, 485-494 (1997).
64. Q. Xing, K. M. Yoo, and R. R. Alfano, "Conical emission by four-photon parametric generation by using femtosecond laser pulses," *Appl. Opt.* **32**, 2087-2089 (1993).
65. G. G. Luther, A. C. Newell, J. V. Moloney, and E. M. Wright, "Short-pulse conical emission and spectral broadening in normally dispersive media," *Opt. Lett.* **19**, 789-791 (1994).
66. P. Di Trapani, G. Valiulis, A. Piskarskas, O. Jedrkiewicz, J. Trull, C. Conti, and S. Trillo, "Spontaneously Generated X-Shaped Light Bullets," *Phys. Rev. Lett.* **91**, 093904 (2003).
67. C. Conti, S. Trillo, P. Di Trapani, G. Valiulis, A. Piskarskas, O. Jedrkiewicz, and J. Trull, "Nonlinear electromagnetic X waves," *Phys. Rev. Lett.* **90**, 170406 (2003).

68. D. Faccio, M. A. Porras, A. Dubietis, F. Bragheri, A. Couairon, and P. Di Trapani, "Conical emission, pulse splitting, and x-wave parametric amplification in nonlinear dynamics of ultrashort light pulses," *Phys. Rev. Lett.* **96**, 193901 (2006).
69. A. C. Daniele Faccio, Paolo Di Trapani, *Conical Waves, Filaments and Nonlinear Filamentation Optics* (Ed. Aracne, Roma, 2007).
70. S. L. Chin, "The physics and the challenge of the propagation of powerful femtosecond laser pulses in optical media.," *Phys. Can.* **60**, 273-281 (2004).
71. A. Mysyrowicz, A. Couairon, and U. Keller, "Self-compression of optical laser pulses by filamentation," *New J. Phys.* **10**, 025023 (2008).
72. L. T. Vuong, R. B. Lopez-Martens, C. P. Hauri, and A. L. Gaeta, "Spectral reshaping and pulse compression via sequential filamentation in gases," *Opt. Express* **16**, 390-401 (2008).
73. A. Couairon *, J. Biegert, C. P. Hauri, W. Kornelis, F. W. Helbing, U. Keller, and A. Mysyrowicz, "Self-compression of ultra-short laser pulses down to one optical cycle by filamentation," *J. Mod. Opt.* **53**, 75-85 (2006).
74. L. Berge, and S. Skupin, "Self-channeling of ultrashort laser pulses in materials with anomalous dispersion," *Phys. Rev. E* **71**, 065601 (2005).
75. A. Couairon, M. Franco, A. Mysyrowicz, J. Biegert, and U. Keller, "Pulse self-compression to the single-cycle limit by filamentation in a gas with a pressure gradient," *Opt. Lett.* **30**, 2657-2659 (2005).
76. C. P. Hauri, W. Kornelis, F. W. Helbing, A. Heinrich, A. Couairon, A. Mysyrowicz, J. Biegert, and U. Keller, "Generation of intense, carrier-envelope phase-locked few-cycle laser pulses through filamentation," *Appl. Phys. B* **79**, 673-677 (2004).
77. A. Couairon, H. S. Chakraborty, and M. B. Gaarde, "From single-cycle self-compressed filaments to isolated attosecond pulses in noble gases," *Phys. Rev. A* **77**, 053814 (2008).
78. H. S. Chakraborty, M. B. Gaarde, and A. Couairon, "Single attosecond pulses from high harmonics driven by self-compressed filaments," *Opt. Lett.* **31**, 3662-3664 (2006).
79. H. Hamster, A. Sullivan, S. Gordon, W. White, and R. W. Falcone, "Subpicosecond, electromagnetic pulses from intense laser-plasma interaction," *Phys. Rev. Lett.* **71**, 2725-2728 (1993).
80. D. J. Cook, and R. M. Hochstrasser, "Intense terahertz pulses by four-wave rectification in air," *Opt. Lett.* **25**, 1210-1212 (2000).
81. J. L. Skinner, "Following the Motions of Water Molecules in Aqueous Solutions," *Science* **328**, 985-986 (2010).
82. P. Haring Bolívar, M. Nagel, F. Richter, M. Brucherseifer, H. Kurz, A. Bosserhoff, and R. Büttner, "Label-free THz sensing of genetic sequences: towards 'THz biochips'," *Philosophical Transactions of the Royal Society of London. Series A: Mathematical, Physical and Engineering Sciences* **362**, 323-335 (2004).
83. P. C. Ashworth, E. Pickwell-MacPherson, E. Provenzano, S. E. Pinder, A. D. Purushotham, M. Pepper, and V. P. Wallace, "Terahertz pulsed spectroscopy of freshly excised human breast cancer," *Opt. Express* **17**, 12444-12454 (2009).
84. H. T. Chen, J. F. O'Hara, A. K. Azad, A. J. Taylor, R. D. Averitt, D. B. Shrekenhamer, and W. J. Padilla, "Experimental demonstration of frequency-agile terahertz metamaterials," *Nat. Photonics* **2**, 295-298 (2008).
85. H. G. Roskos, M. D. Thomson, M. Kreß, and T. Löffler, "Broadband THz emission from gas plasmas induced by femtosecond optical pulses: From fundamentals to applications," *Laser & Photonics Review* **1**, 349-368 (2007).
86. J. M. Manceau, M. Massauti, and S. Tzortzakis, "Strong terahertz emission enhancement via femtosecond laser filament concatenation in air," *Opt. Lett.* **35**, 2424-2426 (2010).

87. J. M. Manceau, A. Averchi, F. Bonaretti, D. Faccio, P. Di Trapani, A. Couairon, and S. Tzortzakis, "Terahertz pulse emission optimization from tailored femtosecond laser pulse filamentation in air," *Opt. Lett.* **34**, 2165-2167 (2009).
88. P. Rairoux, H. Schillinger, S. Niedermeier, M. Rodriguez, F. Ronneberger, R. Sauerbrey, B. Stein, D. Waite, C. Wedekind, H. Wille, L. Wöste, and C. Ziener, "Remote sensing of the atmosphere using ultrashort laser pulses," *Appl. Phys. B* **71**, 573-580 (2000).
89. J. Kasparian, M. Rodriguez, G. Mejean, J. Yu, E. Salmon, H. Wille, R. Bourayou, S. Frey, Y. B. Andre, A. Mysyrowicz, R. Sauerbrey, J. P. Wolf, and L. Woste, "White-Light Filaments for Atmospheric Analysis," *Science* **301**, 61-64 (2003).
90. G. Agakichiev, M. Appenheimer, R. Averbeck, F. Ballester, R. Baur, A. Brenschede, J. Diaz, A. Drees, U. Faschingbauer, J. L. Ferrero, P. Fischer, Z. Fraenkel, M. Franke, C. Fuchs, E. Gatti, P. Glässel, T. Günzel, C. P. de los Heros, F. Hess, R. Holzmann, V. Iourevitch, D. Irmscher, C. Jacob, W. Kühn, B. Lenkeit, H. Löhner, A. Marin, F. M. Marques, G. Martinez, V. Metag, M. Notheisen, R. Novotny, L. H. Olsen, R. Ostendorf, Y. Panebrattsev, A. Pfeiffer, I. Ravinovich, P. Rehak, M. Sampietro, A. Schön, J. Schukraft, Y. Schutz, S. Shimansky, A. Shor, R. S. Simon, H. J. Specht, V. Steiner, S. Tapprogge, G. Tel-Zur, I. Tserruya, T. Ullrich, H. Wilschut, and J. P. Wurm, "Systematic study of low-mass electron pair production in p-Be and p-Au collisions at 450 GeV/<i>c</i>," *The European Physical Journal C - Particles and Fields* **4**, 231-247 (1998).
91. G. Méjean, J. Kasparian, E. Salmon, J. Yu, J. P. Wolf, R. Bourayou, R. Sauerbrey, M. Rodriguez, L. Wöste, H. Lehmann, B. Stecklum, U. Laux, J. Eisloffel, A. Scholz, and A. P. Hatzes, "Towards a supercontinuum-based infrared lidar," *Appl. Phys. B* **77**, 357-359 (2003).
92. R. Bourayou, G. Mejean, J. Kasparian, M. Rodriguez, E. Salmon, J. Yu, H. Lehmann, B. Stecklum, U. Laux, J. Eisloffel, A. Scholz, A. P. Hatzes, R. Sauerbrey, L. Woste, and J. P. Wolf, "White-light filaments for multiparameter analysis of cloud microphysics," *J. Opt. Soc. Am. B* **22**, 369-377 (2005).
93. H. L. Xu, J. F. Daigle, Q. Luo, and S. L. Chin, "Femtosecond laser-induced nonlinear spectroscopy for remote sensing of methane," *Appl. Phys. B* **82**, 655-658 (2006).
94. K. Stelmaszczyk, P. Rohwetter, G. Mejean, J. Yu, E. Salmon, J. Kasparian, R. Ackermann, J. P. Wolf, and L. Woste, "Long-distance remote laser-induced breakdown spectroscopy using filamentation in air," *Appl. Phys. Lett.* **85**, 3977-3979 (2004).
95. P. Rohwetter, K. Stelmaszczyk, L. Wöste, R. Ackermann, G. Méjean, E. Salmon, J. Kasparian, J. Yu, and J. P. Wolf, "Filament-induced remote surface ablation for long range laser-induced breakdown spectroscopy operation," *Spectrochimica Acta Part B: Atomic Spectroscopy* **60**, 1025-1033 (2005).
96. P. Rohwetter, J. Yu, G. Mejean, K. Stelmaszczyk, E. Salmon, J. Kasparian, J. P. Wolf, and L. Woste, "Remote LIBS with ultrashort pulses: characteristics in picosecond and femtosecond regimes," *J. Anal. At. Spectrom.* **19**, 437-444 (2004).
97. S. Tzortzakis, D. Anglos, and D. Gray, "Ultraviolet laser filaments for remote laser-induced breakdown spectroscopy (LIBS) analysis: applications in cultural heritage monitoring," *Opt. Lett.* **31**, 1139-1141 (2006).
98. R. Ackermann, G. Méchain, G. Méjean, R. Bourayou, M. Rodriguez, K. Stelmaszczyk, J. Kasparian, J. Yu, E. Salmon, S. Tzortzakis, Y. B. André, J. F. Bourrillon, L. Tamin, J. P. Cascelli, C. Campo, C. Davoise, A. Mysyrowicz, R. Sauerbrey, L. Wöste, and J. P. Wolf, "Influence of negative leader propagation on the triggering and guiding of high voltage discharges by laser filaments," *Appl. Phys. B* **82**, 561-566 (2006).
99. S. Tzortzakis, B. Prade, M. Franco, A. Mysyrowicz, S. Huller, and P. Mora, "Femtosecond laser-guided electric discharge in air," *Phys. Rev. E* **64**, 057401 (2001).

100. M. Rodriguez, R. Sauerbrey, H. Wille, L. Woste, T. Fujii, Y. B. Andre, A. Mysyrowicz, L. Klingbeil, K. Rethmeier, W. Kalkner, J. Kasparian, E. Salmon, J. Yu, and J. P. Wolf, "Triggering and guiding megavolt discharges by use of laser-induced ionized filaments," *Opt. Lett.* **27**, 772-774 (2002).
101. G. Mejean, R. Ackermann, J. Kasparian, E. Salmon, J. Yu, J. P. Wolf, K. Rethmeier, W. Kalkner, P. Rohwetter, K. Stelmaszczyk, and L. Woste, "Improved laser triggering and guiding of meqavolt discharges with dual fs-ns pulses," *Appl. Phys. Lett.* **88**, 021101 (2006).
102. J.-C. Diels, Bernstein, R., Stahlkopf, K.E., Zhao, X.M., "Lightning control with lasers.," *Sci. Am.* **277**, 50-55 (1997).
103. J. Qiu, "Femtosecond laser-induced microstructures in glasses and applications in micro-optics," *The Chemical Record* **4**, 50-58 (2004).
104. K. M. Davis, K. Miura, N. Sugimoto, and K. Hirao, "Writing waveguides in glass with a femtosecond laser," *Opt. Lett.* **21**, 1729-1731 (1996).
105. D. Homoelle, S. Wielandy, A. L. Gaeta, N. F. Borrelli, and C. Smith, "Infrared photosensitivity in silica glasses exposed to femtosecond laser pulses," *Opt. Lett.* **24**, 1311-1313 (1999).
106. C. B. Schaffer, A. Brodeur, J. F. García, and E. Mazur, "Micromachining bulk glass by use of femtosecond laser pulses with nanojoule energy," *Opt. Lett.* **26**, 93-95 (2001).
107. Y. Kondo, K. Nouchi, T. Mitsuyu, M. Watanabe, P. G. Kazansky, and K. Hirao, "Fabrication of long-period fiber gratings by focused irradiation of infrared femtosecond laser pulses," *Opt. Lett.* **24**, 646-648 (1999).
108. L. Sudrie, M. Franco, B. Prade, and A. Mysyrowicz, "Writing of permanent birefringent microlayers in bulk fused silica with femtosecond laser pulses," *Opt. Commun.* **171**, 279-284 (1999).
109. E. N. Glezer, M. Milosavljevic, L. Huang, R. J. Finlay, T. H. Her, J. P. Callan, and E. Mazur, "Three-dimensional optical storage inside transparent materials," *Opt. Lett.* **21**, 2023-2025 (1996).
110. K. Yamada, W. Watanabe, T. Toma, K. Itoh, and J. Nishii, "In situ observation of photoinduced refractive-index changes in filaments formed in glasses by femtosecond laser pulses," *Opt. Lett.* **26**, 19-21 (2001).
111. Y. Shimotsuma, P. G. Kazansky, J. Qiu, and K. Hirao, "Self-Organized Nanogratings in Glass Irradiated by Ultrashort Light Pulses," *Phys. Rev. Lett.* **91**, 247405 (2003).
112. V. R. Bhardwaj, E. Simova, P. P. Rajeev, C. Hnatovsky, R. S. Taylor, D. M. Rayner, and P. B. Corkum, "Optically Produced Arrays of Planar Nanostructures inside Fused Silica," *Phys. Rev. Lett.* **96**, 057404 (2006).
113. A. Couairon, and A. Mysyrowicz, "Femtosecond filamentation in air.," in *Progress in Ultrafast Intense Laser Science I*(Springer, 2006), pp. 235-258.
114. G. Mechain, A. Couairon, Y. B. Andre, C. D'Amico, M. Franco, B. Prade, S. Tzortzakis, A. Mysyrowicz, and R. Sauerbrey, "Long-range self-channeling of infrared laser pulses in air: a new propagation regime without ionization," *Appl. Phys. B* **79**, 379-382 (2004).
115. G. Fibich, and B. Ilan, "Optical light bullets in a pure Kerr medium," *Opt. Lett.* **29**, 887-889 (2004).
116. D. Mihalache, D. Mazilu, L. C. Crasovan, I. Towers, B. A. Malomed, A. V. Buryak, L. Torner, and F. Lederer, "Stable three-dimensional spinning optical solitons supported by competing quadratic and cubic nonlinearities," *Phys. Rev. E* **66**, 016613 (2002).
117. M. Segev, B. Crosignani, A. Yariv, and B. Fischer, "Spatial solitons in photorefractive media," *Phys. Rev. Lett.* **68**, 923-926 (1992).
118. E. Yablonovitch, and N. Bloembergen, "Avalanche Ionization and Limiting Diameter of Filaments Induced by Light-Pulses in Transparent Media," *Phys. Rev. Lett.* **29**, 907 (1972).
119. W. H. Press, S. A. Teukolsky, W. T. Vetterling, and B. P. Flannery, *Numerical Recipes* (Cambridge University Press, New York, 2007).

120. J.-P. Berenger, "Three-Dimensional Perfectly Matched Layer for the Absorption of Electromagnetic Waves," *J. Comput. Phys.* **127**, 363-379 (1996).
121. F. Calegari, C. Vozzi, S. Gasilov, E. Benedetti, G. Sansone, M. Nisoli, S. De Silvestri, and S. Stagira, "Rotational Raman effects in the wake of optical filamentation," *Phys. Rev. Lett.* **100**, 123006 (2008).
122. D. N. Christodoulides, and R. I. Joseph, "Discrete Self-Focusing in Nonlinear Arrays of Coupled Wave-Guides," *Opt. Lett.* **13**, 794-796 (1988).
123. H. S. Eisenberg, Y. Silberberg, R. Morandotti, A. R. Boyd, and J. S. Aitchison, "Discrete spatial optical solitons in waveguide arrays," *Phys. Rev. Lett.* **81**, 3383-3386 (1998).
124. V. Mezentsev, S. Musher, I. Ryzhenkova, and S. Turitsyn, "Two-dimensional solitons in discrete systems," *JETP LETTERS C/C OF PIS'MA V ZHURNAL EKSPERIMENTAL'NOI TEORETICHESKOI FIZIKI* **60**, 829-829 (1994).
125. S. Flach, K. Kladko, and R. S. MacKay, "Energy Thresholds for Discrete Breathers in One-, Two-, and Three-Dimensional Lattices," *Phys. Rev. Lett.* **78**, 1207-1210 (1997).
126. N. K. Efremidis, J. Hudock, D. N. Christodoulides, J. W. Fleischer, O. Cohen, and M. Segev, "Two-dimensional optical lattice solitons," *Phys. Rev. Lett.* **91**, 213906 (2003).
127. J. W. Fleischer, M. Segev, N. K. Efremidis, and D. N. Christodoulides, "Observation of two-dimensional discrete solitons in optically induced nonlinear photonic lattices," *Nature* **422**, 147-150 (2003).
128. N. K. Efremidis, S. Sears, D. N. Christodoulides, J. W. Fleischer, and M. Segev, "Discrete solitons in photorefractive optically induced photonic lattices," *Phys. Rev. E* **66**, 046602 (2002).
129. F. Lederer, G. I. Stegeman, D. N. Christodoulides, G. Assanto, M. Segev, and Y. Silberberg, "Discrete solitons in optics," *Phys. Rep.* **463**, 1-126 (2008).
130. S. Suntsov, D. Abdollahpour, D. G. Papazoglou, and S. Tzortzakis, "Femtosecond laser induced plasma diffraction gratings in air as photonic devices for high intensity laser applications," *Appl. Phys. Lett.* **94**, 251104 (2009).
131. X. Yang, J. Wu, Y. Peng, Y. Tong, P. Lu, L. e. Ding, Z. Xu, and H. Zeng, "Plasma waveguide array induced by filament interaction," *Opt. Lett.* **34**, 3806-3808 (2009).
132. M. Leibscher, I. S. Averbukh, and H. Rabitz, "Molecular Alignment by Trains of Short Laser Pulses," *Phys. Rev. Lett.* **90**, 213001 (2003).
133. L. V. Keldysh, *Sov. Phys. JETP-USSR (Zh. Eksp. Teor. Fiz.* **47**, (1945)) **20**, 1307 (1964).
134. F. A. Ilkov, J. E. Decker, and S. L. Chin, "Ionization of atoms in the tunnelling regime with experimental evidence using Hg atoms," *J. Phys. B: At. Mol. Opt. Phys.* **25**, 4005 (1992).
135. A. Szameit, J. Burghoff, T. Pertsch, S. Nolte, A. Tünnermann, and F. Lederer, "Two-dimensional soliton in cubic fs laser written waveguide arrays in fused silica," *Opt. Express* **14**, 6055-6062 (2006).
136. A. M. Boris, M. Dumitru, W. Frank, and T. Lluís, "Spatiotemporal optical solitons," *Journal of Optics B: Quantum and Semiclassical Optics* **7**, R53 (2005).
137. Y. Silberberg, "Collapse of optical pulses," *Opt. Lett.* **15**, 1282-1284 (1990).
138. A. Hasegawa, and F. Tappert, "Transmission of stationary nonlinear optical pulses in dispersive dielectric fibers. I. Anomalous dispersion," *Appl. Phys. Lett.* **23**, 142-144 (1973).
139. L. F. Mollenauer, R. H. Stolen, and J. P. Gordon, "Experimental Observation of Picosecond Pulse Narrowing and Solitons in Optical Fibers," *Phys. Rev. Lett.* **45**, 1095-1098 (1980).
140. P. Möbius, "Hasegawa, A.; Kodama, Y.: Solitons in Optical Communications. Oxford, Clarendon Press 1995. XIV, 320 pp., £ 60,00. ISBN 0-19-856507-0 (Oxford Series in Optical and Imaging Sciences 7)," *ZAMM - Journal of Applied Mathematics and Mechanics / Zeitschrift für Angewandte Mathematik und Mechanik* **77**, 502-502 (1997).
141. E. Iannone, *Optical communications; Nonlinear optics* (Wiley, New York, 1998).

142. J. S. Aitchison, A. M. Weiner, Y. Silberberg, M. K. Oliver, J. L. Jackel, D. E. Leaird, E. M. Vogel, and P. W. E. Smith, "Observation of spatial optical solitons in a nonlinear glass waveguide," *Opt. Lett.* **15**, 471-473 (1990).
143. G. C. Duree, Jr., J. L. Shultz, G. J. Salamo, M. Segev, A. Yariv, B. Crosignani, P. Di Porto, E. J. Sharp, and R. R. Neurgaonkar, "Observation of self-trapping of an optical beam due to the photorefractive effect," *Phys. Rev. Lett.* **71**, 533-536 (1993).
144. W. E. Torruellas, Z. Wang, L. Torner, and G. I. Stegeman, "Observation of mutual trapping and dragging of two-dimensional spatial solitary waves in a quadratic medium," *Opt. Lett.* **20**, 1949-1951 (1995).
145. L. Torner, and A. Barthelemy, "Quadratic solitons: recent developments," *Quantum Electronics, IEEE Journal of* **39**, 22-30 (2003).
146. G. Fibich, and B. Ilan, "Optical light bullets in a pure Kerr medium," *Opt. Lett.* **29**, 887-889 (2004).
147. D. Mihalache, D. Mazilu, F. Lederer, Y. V. Kartashov, L. C. Crasovan, and L. Torner, "Stable three-dimensional spatiotemporal solitons in a two-dimensional photonic lattice," *Phys. Rev. E* **70**, 055603 (2004).
148. O. Bang, W. Krolikowski, J. Wyller, and J. J. Rasmussen, "Collapse arrest and soliton stabilization in nonlocal nonlinear media," *Phys. Rev. E* **66**, 046619 (2002).
149. D. Mihalache, D. Mazilu, F. Lederer, B. A. Malomed, Y. V. Kartashov, L. C. Crasovan, and L. Torner, "Stable Spatiotemporal Solitons in Bessel Optical Lattices," *Phys. Rev. Lett.* **95**, 023902 (2005).
150. D. E. Edmundson, and R. H. Enns, "Robust bistable light bullets," *Opt. Lett.* **17**, 586-588 (1992).
151. L. Torner, and Y. V. Kartashov, "Light bullets in optical tandems," *Opt. Lett.* **34**, 1129-1131 (2009).
152. A. Chong, W. H. Renninger, D. N. Christodoulides, and F. W. Wise, "Airy-Bessel wave packets as versatile linear light bullets," *Nat Photon* **4**, 103-106 (2010).
153. D. Abdollahpour, S. Suntsov, D. G. Papazoglou, and S. Tzortzakis, "Spatiotemporal Airy Light Bullets in the Linear and Nonlinear Regimes," *Phys. Rev. Lett.* **105**, 253901 (2010).
154. S. Tzortzakis, G. Mechain, G. Patalano, M. Franco, B. Prade, and A. Mysyrowicz, "Concatenation of plasma filaments created in air by femtosecond infrared laser pulses," *Appl. Phys. B* **76**, 609-612 (2003).
155. A. Szameit, D. Blömer, J. Burghoff, T. Schreiber, T. Pertsch, S. Nolte, A. Tünnermann, and F. Lederer, "Discrete Nonlinear Localization in Femtosecond Laser Written Waveguides in Fused Silica," *Opt. Express* **13**, 10552-10557 (2005).
156. G. G. Luther, J. V. Moloney, A. C. Newell, and E. M. Wright, "Self-focusing threshold in normally dispersive media," *Opt. Lett.* **19**, 862-864 (1994).
157. A. Couairon, E. Gaizauskas, D. Faccio, A. Dubietis, and P. Di Trapani, "Nonlinear X-wave formation by femtosecond filamentation in Kerr media," *Phys. Rev. E* **73**, 016608 (2006).
158. S. Tzortzakis, L. Sudrie, M. Franco, B. Prade, A. Mysyrowicz, A. Couairon, and L. Berge, "Self-guided propagation of ultrashort IR laser pulses in fused silica," *Phys. Rev. Lett.* **87**, 213902 (2001).
159. D. N. Nikogosyan, *PROPERTIES OF OPTICAL AND LASER-RELATED MATERIALS: A Handbook* (J. Wiley and Sons, 1997).
160. P. Liu, W. L. Smith, H. Lotem, J. H. Bechtel, N. Bloembergen, and R. S. Adhav, "Absolute two-photon absorption coefficients at 355 and 266 nm," *Phys. Rev. B* **17**, 4620-4632 (1978).
161. V. Nathan, A. H. Guenther, and S. S. Mitra, "Review of multiphoton absorption in crystalline solids," *J. Opt. Soc. Am. B* **2**, 294-316 (1985).
162. M. Mlejnek, E. M. Wright, and J. V. Moloney, "Dynamic spatial replenishment of femtosecond pulses propagating in air," *Opt. Lett.* **23**, 382-384 (1998).

163. F. Chen, M. Stepi, C. Rüter, D. Runde, D. Kip, V. Shandarov, O. Manela, and M. Segev, "Discrete diffraction and spatial gap solitons in photovoltaic LiNbO₃ waveguide arrays," *Opt. Express* **13**, 4314-4324 (2005).
164. T. Pertsch, U. Peschel, F. Lederer, J. Burghoff, M. Will, S. Nolte, and A. Tünnermann, "Discrete diffraction in two-dimensional arrays of coupled waveguides in silica," *Opt. Lett.* **29**, 468-470 (2004).
165. S. Minardi, A. Gopal, A. Couairon, G. Tamoasuskas, R. Piskarskas, A. Dubietis, and P. Di Trapani, "Accurate retrieval of pulse-splitting dynamics of a femtosecond filament in water by time-resolved shadowgraphy," *Opt. Lett.* **34**, 3020-3022 (2009).
166. P. K. Kennedy, "A first-order model for computation of laser-induced breakdown thresholds in ocular and aqueous media. I. Theory," *Quantum Electronics, IEEE Journal of* **31**, 2241-2249 (1995).
167. D. N. Christodoulides, F. Lederer, and Y. Silberberg, "Discretizing light behaviour in linear and nonlinear waveguide lattices," *Nature* **424**, 817-823 (2003).
168. R. R. Gattass, and E. Mazur, "Femtosecond laser micromachining in transparent materials," *Nat Photon* **2**, 219-225 (2008).
169. S. Alexander, and N. Stefan, "Discrete optics in femtosecond-laser-written photonic structures," *J. Phys. B: At. Mol. Opt. Phys.* **43**, 163001 (2010).
170. Y. Zhao, G. Mu, and X. Zhu, "Nonlinear imaging of embedded microstructures inside transparent materials with laser-induced ionization microscopy," *Opt. Lett.* **31**, 2765-2767 (2006).
171. S. Tzortzakis, L. Berge, A. Couairon, M. Franco, B. Prade, and A. Mysyrowicz, "Breakup and fusion of self-guided femtosecond light pulses in air," *Phys. Rev. Lett.* **86**, 5470-5473 (2001).
172. P. Panagiotopoulos, N. K. Efremidis, D. G. Papazoglou, A. Couairon, and S. Tzortzakis, "Tailoring the filamentation of intense femtosecond laser pulses with periodic lattices," *Phys. Rev. A* **82**, 061803(R) (2010).
173. J. Durnin, "Exact solutions for nondiffracting beams. I. The scalar theory," *J. Opt. Soc. Am. A* **4**, 651-654 (1987).
174. J. H. McLeod, "The Axicon: A New Type of Optical Element," *J. Opt. Soc. Am.* **44**, 592-592 (1954).
175. D. G. Papazoglou, and S. Tzortzakis, "In-line holography for the characterization of ultrafast laser filamentation in transparent media," *Appl. Phys. Lett.* **93**, 041120 (2008).
176. S. Varma, Y. H. Chen, and H. M. Milchberg, "Trapping and Destruction of Long-Range High-Intensity Optical Filaments by Molecular Quantum Wakes in Air," *Phys. Rev. Lett.* **101**, 205001 (2008).
177. C. Alpmann, R. Bowman, M. Woerdemann, M. Padgett, and C. Denz, "Mathieu beams as versatile light moulds for 3D micro particle assemblies," *Opt. Express* **18**, 26084-26091 (2010).
178. C. L. Tsangaris, G. H. C. New, and J. Rogel-Salazar, "Unstable Bessel beam resonator," *Opt. Commun.* **223**, 233-238 (2003).
179. M. Abramowitz, and I. Stegun, *Handbook of Mathematical Functions* (1965).
180. A. Vasara, J. Turunen, and A. T. Friberg, "Realization of general nondiffracting beams with computer-generated holograms," *J. Opt. Soc. Am. A* **6**, 1748-1754 (1989).
181. V. P. Koronkevich, I. A. Mikhaltsova, E. G. Churin, and Y. I. Yurlov, "Lensacon," *Appl. Opt.* **34**, 5761-5772 (1995).
182. P. Polesana, A. Couairon, D. Faccio, A. Parola, M. A. Porras, A. Dubietis, A. Piskarskas, and P. Di Trapani, "Observation of conical waves in focusing, dispersive, and dissipative Kerr media," *Phys. Rev. Lett.* **99**, 223902 (2007).
183. D. Faccio, M. Clerici, A. Averchi, O. Jedrkiewicz, S. Tzortzakis, D. G. Papazoglou, F. Bragheri, L. Tartara, A. Trita, S. Henin, I. Cristiani, A. Couairon, and P. Di Trapani, "Kerr-induced spontaneous

- Bessel beam formation in the regime of strong two-photon absorption," *Opt. Express* **16**, 8213-8218 (2008).
184. P. Polesana, M. Franco, A. Couairon, D. Faccio, and P. Di Trapani, "Filamentation in Kerr media from pulsed Bessel beams," *Phys. Rev. A* **77**, 043814 (2008).
 185. S. Akturk, B. Zhou, M. Franco, A. Couairon, and A. Mysyrowicz, "Generation of long plasma channels in air by focusing ultrashort laser pulses with an axicon," *Opt. Commun.* **282**, 129-134 (2009).
 186. P. Polynkin, M. Kolesik, A. Roberts, D. Faccio, P. Di Trapani, and J. Moloney, "Generation of extended plasma channels in air using femtosecond Bessel beams," *Opt. Express* **16**, 15733-15740 (2008).
 187. S. Tzortzakis, M. A. Franco, Y. B. Andre, A. Chiron, B. Lamouroux, B. S. Prade, and A. Mysyrowicz, "Formation of a conducting channel in air by self-guided femtosecond laser pulses," *Phys. Rev. E* **60**, R3505-R3507 (1999).
 188. F. Chen, *Introduction to plasma physics and controlled fusion* (Springer, 2006).
 189. J. Y. Lu, and J. F. Greenleaf, "Experimental verification of nondiffracting X waves," *Ultrasonics, Ferroelectrics and Frequency Control, IEEE Transactions on* **39**, 441-446 (1992).
 190. J. Y. Lu, and J. F. Greenleaf, "Nondiffracting X waves-exact solutions to free-space scalar wave equation and their finite aperture realizations," *Ultrasonics, Ferroelectrics and Frequency Control, IEEE Transactions on* **39**, 19-31 (1992).
 191. L. Jian-Yu, and J. F. Greenleaf, "A study of two-dimensional array transducers for limited diffraction beams," *Ultrasonics, Ferroelectrics and Frequency Control, IEEE Transactions on* **41**, 724-739 (1994).
 192. J. Salo, J. Fagerholm, A. T. Friberg, and M. M. Salomaa, "Nondiffracting Bulk-Acoustic X waves in Crystals," *Phys. Rev. Lett.* **83**, 1171-1174 (1999).
 193. P. R. Stepanishen, "ACOUSTIC BESSEL BULLETS," *Journal of Sound and Vibration* **222**, 115-143 (1999).
 194. P. R. Stepanishen, and J. Sun, "Acoustic bullets: Transient Bessel beams generated by planar apertures," *The Journal of the Acoustical Society of America* **102**, 3308-3318 (1997).
 195. J. Salo, J. Fagerholm, A. T. Friberg, and M. M. Salomaa, "Unified description of nondiffracting X and Y waves," *Phys. Rev. E* **62**, 4261-4275 (2000).
 196. K. Reivelt, and P. Saari, "Optical generation of focus wave modes," *J. Opt. Soc. Am. A* **17**, 1785-1790 (2000).
 197. P. Saari, and K. Reivelt, "Evidence of X-Shaped Propagation-Invariant Localized Light Waves," *Phys. Rev. Lett.* **79**, 4135-4138 (1997).
 198. M. Kolesik, and J. V. Moloney, "Perturbative and non-perturbative aspects of optical filamentation in bulk dielectric media," *Opt. Express* **16**, 2971-2988 (2008).
 199. D. Faccio, P. Di Trapani, S. Minardi, A. Bramati, F. Bragheri, C. Liberale, V. Degiorgio, A. Dubietis, and A. Matijosius, "Far-field spectral characterization of conical emission and filamentation in Kerr media," *J. Opt. Soc. Am. B* **22**, 862-869 (2005).
 200. D. Faccio, A. Averchi, A. Couairon, M. Kolesik, J. V. Moloney, A. Dubietis, G. Tamosauskas, P. Polesana, A. Piskarskas, and P. Di Trapani, "Spatio-temporal reshaping and X Wave dynamics in optical filaments," *Opt. Express* **15**, 13077-13095 (2007).
 201. M. V. Berry, and N. L. Balazs, "Nonspreading wave packets," *American Journal of Physics* **47**, 264-267 (1979).
 202. G. A. Siviloglou, and D. N. Christodoulides, "Accelerating finite energy Airy beams," *Opt. Lett.* **32**, 979-981 (2007).
 203. G. A. Siviloglou, J. Broky, A. Dogariu, and D. N. Christodoulides, "Observation of Accelerating Airy Beams," *Phys. Rev. Lett.* **99**, 213901 (2007).

204. D. G. Papazoglou, S. Suntsov, D. Abdollahpour, and S. Tzortzakis, "Tunable intense Airy beams and tailored femtosecond laser filaments," *Phys. Rev. A* **81**, 061807(R) (2010).
205. D. M. Cottrell, J. A. Davis, and T. M. Hazard, "Direct generation of accelerating Airy beams using a $3/2$ phase-only pattern," *Opt. Lett.* **34**, 2634-2636 (2009).
206. J. A. Davis, M. J. Mitry, M. A. Bandres, I. Ruiz, K. P. McAuley, and D. M. Cottrell, "Generation of accelerating Airy and accelerating parabolic beams using phase-only patterns," *Appl. Opt.* **48**, 3170-3176 (2009).
207. T. Ellenbogen, N. Voloch-Bloch, A. Ganany-Padowicz, and A. Arie, "Nonlinear generation and manipulation of Airy beams," *Nat Photon* **3**, 395-398 (2009).
208. J. Broky, G. A. Siviloglou, A. Dogariu, and D. N. Christodoulides, "Self-healing properties of optical Airy beams," *Opt. Express* **16**, 12880-12891 (2008).
209. G. A. Siviloglou, J. Broky, A. Dogariu, and D. N. Christodoulides, "Ballistic dynamics of Airy beams," *Opt. Lett.* **33**, 207-209 (2008).
210. J. E. Morris, M. Mazilu, J. Baumgartl, T. Ciháček, and K. Dholakia, "Propagation characteristics of Airy beams: dependence upon spatial coherence and wavelength," *Opt. Express* **17**, 13236-13245 (2009).
211. I. M. Besieris, and A. M. Shaarawi, "Accelerating Airy wave packets in the presence of quadratic and cubic dispersion," *Phys. Rev. E* **78**, 046605 (2008).
212. J. Parravicini, P. Minzioni, V. Degiorgio, and E. DelRe, "Observation of nonlinear Airy-like beam evolution in lithium niobate," *Opt. Lett.* **34**, 3908-3910 (2009).
213. P. Polynkin, M. Kolesik, J. V. Moloney, G. A. Siviloglou, and D. N. Christodoulides, "Curved Plasma Channel Generation Using Ultraintense Airy Beams," *Science* **324**, 229-232 (2009).
214. P. Polynkin, M. Kolesik, and J. Moloney, "Filamentation of Femtosecond Laser Airy Beams in Water," *Phys. Rev. Lett.* **103**, 123902 (2009).
215. A. Lotti, D. Faccio, A. Couairon, D. G. Papazoglou, P. Panagiotopoulos, D. Abdollahpour, and S. Tzortzakis, "Stationary nonlinear Airy beams," *Phys. Rev. A* **84**, 021807 (2011).
216. A. Couairon, E. Brambilla, T. Corti, D. Majus, O. D. Ramirez-Gongora, and M. Kolesik, "Practitioner's guide to laser pulse propagation models and simulation," *Eur. Phys. J.-Spec. Top.* **199**, 5-76 (2011).
217. I. Kaminer, M. Segev, and D. N. Christodoulides, "Self-Accelerating Self-Trapped Optical Beams," *Phys. Rev. Lett.* **106**, 213903 (2011).
218. J. Diels, J. Yeak, D. Mirell, R. Fuentes, S. Rostami, D. Faccio, and P. di Trapani, "Air filaments and vacuum," *Laser Phys.* **20**, 1101-1106 (2010).
219. A. Couairon, "Dynamics of femtosecond filamentation from saturation of self-focusing laser pulses," *Phys. Rev. A* **68**, 015801 (2003).
220. D. Faccio, A. Lotti, A. Matijosius, F. Bragheri, V. Degiorgio, A. Couairon, and P. Di Trapani, "Experimental energy-density flux characterization of ultrashort laser pulse filaments," *Opt. Express* **17**, 8193-8200 (2009).
221. A. Lotti, A. Couairon, D. Faccio, and P. D. Trapani, "Energy-flux characterization of conical and space-time coupled wave packets," *Phys. Rev. A* **81**, 023810 (2010).
222. D. Faccio, A. Averchi, A. Lotti, P. Di Trapani, A. Couairon, D. Papazoglou, and S. Tzortzakis, "Ultrashort laser pulse filamentation from spontaneous X Wave formation in air," *Opt. Express* **16**, 1565-1570 (2008).
223. M. Mlejnek, E. M. Wright, and J. V. Moloney, "Power dependence of dynamic spatial replenishment of femtosecond pulses propagating in air," *Opt. Express* **4**, 223-228 (1999).
224. L. Froehly, F. Courvoisier, A. Mathis, M. Jacquot, L. Furfaro, R. Giust, P. A. Lacourt, and J. M. Dudley, "Arbitrary accelerating micron-scale caustic beams in two and three dimensions," *Opt. Express* **19**, 16455-16465 (2011).

225. A. G. Van Engen, S. A. Diddams, and T. S. Clement, "Dispersion Measurements of Water with White-Light Interferometry," *Appl. Opt.* **37**, 5679-5686 (1998).
226. M. Abramowitz, and I. Stegun, *Handbook of Mathematical Functions* (Dover, New York, 1972).
227. M. A. Porras, A. Parola, D. Faccio, A. Dubietis, and P. Di Trapani, "Nonlinear unbalanced Bessel beams: Stationary conical waves supported by nonlinear losses," *Phys. Rev. Lett.* **93**, 153902 (2004).
228. P. Polesana, A. Dubietis, M. A. Porras, E. Kucinskas, D. Faccio, A. Couairon, and P. Di Trapani, "Near-field dynamics of ultrashort pulsed Bessel beams in media with Kerr nonlinearity," *Phys. Rev. E* **73**, 056612 (2006).
229. A. Dubietis, A. Couairon, E. Kucinskas, G. Tamosauskas, E. Gaizauskas, D. Faccio, and P. Di Trapani, "Measurement and calculation of nonlinear absorption associated with femtosecond filaments in water," *Appl. Phys. B* **84**, 439-446 (2006).
230. M. Kolesik, E. M. Wright, and J. V. Moloney, "Dynamic nonlinear X waves for femtosecond pulse propagation in water," *Phys. Rev. Lett.* **92**, 253901 (2004).
231. K. D. Moll, A. L. Gaeta, and G. Fibich, "Self-similar optical wave collapse: Observation of the Townes profile," *Phys. Rev. Lett.* **90**, 203902 (2003).
232. N. K. Efremidis, and D. N. Christodoulides, "Abruptly autofocusing waves," *Opt. Lett.* **35**, 4045-4047 (2010).
233. D. G. Papazoglou, N. K. Efremidis, D. N. Christodoulides, and S. Tzortzakis, "Observation of abruptly autofocusing waves," *Opt. Lett.* **36**, 1842-1844 (2011).
234. M. K. Bhuyan, F. Courvoisier, P. A. Lacourt, M. Jacquot, R. Salut, L. Furfaro, and J. M. Dudley, "High aspect ratio nanochannel machining using single shot femtosecond Bessel beams," *Appl. Phys. Lett.* **97**, 081102 (2010).
235. M. K. Bhuyan, F. Courvoisier, P. A. Lacourt, M. Jacquot, L. Furfaro, M. J. Withford, and J. M. Dudley, "High aspect ratio taper-free microchannel fabrication using femtosecond Bessel beams," *Opt. Express* **18**, 566-574 (2010).
236. S. Juodkazis, K. Nishimura, S. Tanaka, H. Misawa, E. G. Gamaly, B. Luther-Davies, L. Hallo, P. Nicolai, and V. T. Tikhonchuk, "Laser-Induced Microexplosion Confined in the Bulk of a Sapphire Crystal: Evidence of Multimegabar Pressures," *Phys. Rev. Lett.* **96**, 166101 (2006).
237. P. P. Kiran, S. Bagchi, C. L. Arnold, S. R. Krishnan, G. R. Kumar, and A. Couairon, "Filamentation without intensity clamping," *Opt. Express* **18**, 21504-21510 (2010).
238. M. B. Gaarde, and A. Couairon, "Intensity Spikes in Laser Filamentation: Diagnostics and Application," *Phys. Rev. Lett.* **103**, 043901 (2009).
239. X. Sun, S. Xu, J. Zhao, W. Liu, Y. Cheng, Z. Xu, S. L. Chin, and G. Mu, "Impressive laser intensity increase at the trailing stage of femtosecond laser filamentation in air," *Opt. Express* **20**, 4790-4795 (2012).
240. A. Dubietis, E. Gaizauskas, G. Tamosauskas, and P. Di Trapani, "Light filaments without self-channeling," *Phys. Rev. Lett.* **92**, 253903 (2004).
241. M. A. Khashan, and A. Y. Nassif, "Accurate Measurement of the Refractive Indices of Solids and Liquids by the Double-Layer Interferometer," *Appl. Opt.* **39**, 5991-5997 (2000).
242. P. C. d. Couto, and B. J. C. Cabral, "Electronically excited water aggregates and the adiabatic band gap of water," *The Journal of Chemical Physics* **126**, 014509-014509 (2007).
243. M. V. Fischetti, D. J. DiMaria, S. D. Brorson, T. N. Theis, Kirtley, and R. J., "Theory of high-field electron transport in silicon dioxide," *Phys. Rev. B* **31**, 8124-8142 (1985).
244. M. R. Junnarkar, "Short pulse propagation in tight focusing conditions," *Opt. Commun.* **195**, 273-292 (2001).
245. M. Li, S. Menon, J. P. Nibarger, and G. N. Gibson, "Ultrafast Electron Dynamics in Femtosecond Optical Breakdown of Dielectrics," *Phys. Rev. Lett.* **82**, 2394-2397 (1999).

246. M. Lenzner, J. Krüger, S. Sartania, Z. Cheng, C. Spielmann, G. Mourou, W. Kautek, and F. Krausz, "Femtosecond Optical Breakdown in Dielectrics," *Phys. Rev. Lett.* **80**, 4076-4079 (1998).
247. B. C. Stuart, M. D. Feit, S. Herman, A. M. Rubenchik, B. W. Shore, and M. D. Perry, "Nanosecond-to-femtosecond laser-induced breakdown in dielectrics," *Phys. Rev. B* **53**, 1749-1761 (1996).
248. F. Docchio, "Lifetimes of Plasmas Induced in Liquids and Ocular Media by Single Nd:YAG Laser Pulses of Different Duration," *EPL (Europhysics Letters)* **6**, 407 (1988).
249. D. G. Papazoglou, and S. Tzortzakis, "Physical mechanisms of fused silica restructuring and densification after femtosecond laser excitation [Invited]," *Opt. Mater. Express* **1**, 625-632 (2011).
250. A. Q. Wu, I. H. Chowdhury, and X. Xu, "Femtosecond laser absorption in fused silica: Numerical and experimental investigation," *Phys. Rev. B* **72**, 085128 (2005).
251. M. Polyanskiy, "<http://refractiveindex.info/>."

